Magnetic, Dielectric and Physicomechanical Properties of Rubber Ferrite Nanocomposites

Thesis submitted to

Cochin University of Science and Technology

in partial fulfilment of the requirements

for the award of the degree of

Doctor of Philosophy

by

Prema K.H

Department of Polymer Science and Rubber Technology
Cochin University of Science & Technology
Cochin- 682 022, India.

September 2007

CERTIFICATE

This is to certify that the thesis entitled *"Magnetic, Dielectric and Physicomechanical Properties of Rubber Ferrite Nanocomposites"* is based on the authentic research work carried out by Mrs. Prema K.H under my guidance, in the Department of Polymer Science and Rubber Technology, Cochin University of Science and Technology, Cochin-682 022, and no part of the work reported in this thesis has been presented for the award of any other degree from any other institution.
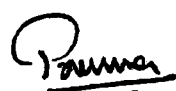
Dr. Philip Kurian
Professor
Department of Polymer Science and
Rubber Technology
Cochin University of Science and
Technology

Cochin-22
13 September 2007

Declaration

I hereby declare that the work presented in this thesis entitled *"Magnetic, Dielectric and Physicomechanical Properties of Rubber Ferrite Nanocomposites"* is based on the original research work carried out by me under the guidance and supervision of Dr. Philip Kurian, Professor, Department of Polymer Science and Rubber Technology, Cochin University of Science and Technology, Cochin-682 022 and no part of the work reported in this thesis has been presented for the award of any other degree from any other institution.

Prema. K. H

Cochin-22
13.09.07

Acknowledgements

PREMA K.H

Preface

Incorporation of ferrites into elastomers like natural or synthetic rubber results in rubber ferrite composites (RFCs). In RFCs mechanical properties of elastomer are combined with characteristic properties of ferrites. The non flexible ceramic magnets are converted to flexible magnets. At the same time all the characteristic properties of ferrites are retained in RFCs. Ferrites as well as RFCs are technologically important materials for transformer cores, magnetic resonance imaging and microwave absorbers. They find extensive use in stealth technology.

Mechanical properties of RFCs mainly depend on the nature of the matrix used for the preparation of RFCs. Elastomers used can be polar or non polar. Other factors that determine the performance of RFCs include the nature of ferrite and its interaction with the matrix and percolation limit. Moreover the physicomechanical properties of the RFCs are greatly influenced by the size of the ferrite particles incorporated into it.

Dielectric behaviour of the matrix can be modified with the incorporation of ferrites. Incorporation of carbon black along with nickel ferrite can further modify the dielectric and microwave properties of RFCs. So the effect of ferrite and carbon black on mechanical, magnetic, dielectric and microwave properties of RFCs opened a new scope for the present study.

Spinel ferrites like nickel ferrite and gamma ferric oxide are characterised with high saturation magnetisation, low coercivity, low eddy current loss and high resistivity. They are important microwave absorbing materials and are largely used as isolators and phase shifters. They have potential applications in computer chip memories and data storage applications. They exhibit size depended magnetic properties. These magnetic particles in the nano metric dimension exhibit magnetic behaviour which is quite different from the bulk counter part. Thus the magnetic properties of these materials can be modified by appropriate preparative techniques and heat treatment.

In the present study the preparation and characterisation of rubber ferrite composites containing nickel ferrite and gamma ferric oxide have been dealt with.

Synthetic rubbers viz. ethylene propylene diene rubber and neoprene rubber were used for the incorporation of nickel ferrite and gamma ferric oxide for the synthesis of RFCs. Incorporation of ferrites were carried out according to a specific recipe for various loadings of the magnetic fillers. The ferrites used for the preparation of RFCs were synthesised using sol-gel method and structural characterisation was carried out. Experimental techniques like X-ray diffraction, Transmission electron microscopy and other analytical techniques were used for this. Precharaterised ferrites were then incorporated at different loading into rubber according to conventional mixing methods. The cure characteristics, mechanical, dielectric, magnetic and microwave properties of these composites were evaluated. The effect of carbon black on these properties of RFCs were carried out. The results are correlated.

The results of the investigation on the 'Magnetic, Dielectric and Physicomechanical Properties of Rubber Ferrite Nanocomposites' in this thesis are divided into ten chapters.

Chapter 1 presents an introduction to magnetic rubber composites and a brief report on literature review in the field of elastomers, magnetic fillers and magnetism, ferrites and rubber ferrite composites.

The experimental methods adopted for the preparation of nickel ferrite, gamma ferric oxide and EPDM and CR based rubber ferrite composites are presented in **Chapter 2**. It deals with analytical techniques like X-ray diffraction and Transmission electron microscopy (TEM) used for the structural characterisation of the ferrites. This chapter also discusses the experimental methods used for the physicomechanical analysis of RFCs. Theoretical and experimental aspects of dielectric, magnetic and microwave measurements are also explained in this chapter.

Chapter 3 explains the synthesis of nickel ferrite and gamma ferric oxide by sol-gel method. Techniques like TEM and X-ray diffraction are employed to study the crystal structure, size and shape. The findings of these studies are discussed in this chapter.

Cure characteristics, processability and mechanical properties of EPDM based rubber ferrite composites are discussed in **Chapter 4**. This chapter also presents the cure kinetic studies and morphology of the RFCs.

Chapter 5 discusses the cure characteristics, processability, mechanical properties and morphology of neoprene based RFCs. This chapter also deals sorption kinetic studies of the RFCs.

The results of dielectric studies of nickel ferrite based RFCs are dealt in **Chapter 6**. The dielectric properties of RFCs are measured in the frequency range 0.1 – 8 MHz in the temperature range 303-393 K and the results are presented in this chapter. Effect of ferrite fillers on the dielectric properties of RFCs is also studied and they are given in this chapter. Different theoretical equations are tried to fit the experimental data and the results are also presented.

Effect of temperature, frequency and loading dependence on the dielectric properties of gamma ferric oxide based RFCs are discussed in detail in **Chapter 7**.

Results of microwave attenuation measurements on nickel ferrite filled RFCs are described in **Chapter 8**. Dielectric behaviour of these RFCs in X and S band frequencies are also discussed.

Chapter 9 explains the results of room temperature magnetisation of ferrites as well as RFCs. The hysteresis loop parameters like saturation magnetisation, coercivity and magnetic remanence are evaluated and are discussed in this chapter.

Chapter 10 is the concluding chapter with emphasis on the major findings of the present work. This chapter also looks for the scope for further work.

Contents

Chapter 4

Studies on the Physicomechanical Properties of EPDM based Rubber Ferrite Composites

Chapter 5

Evaluation of Processability and Mechanical Properties of Neoprene Based Rubber Ferrite Composites

Chapter 9

Magnetic Properties of NiFe$_2$O$_4$ and γ-Fe$_2$O$_3$ Based Rubber Ferrite Composites

Chapter 10

Conclusion   257

List of Abbreviations

List of Symbols

List of Publications

Chapter 1

Introduction

Polymers and polymer based composites are playing a crucial role in the day to day life of human beings. With the advent of nanotechnology aided by the capacity to modify the electrical, mechanical and magnetic properties of polymers, polymer composites are increasingly playing a lead role in everyday life. Hence research on these materials is pursued world wide by chemists, physicists and engineers alike. One such realm where abundant amount of efforts are invested is in the area of new products based on natural and synthetic rubber. This is because of the scope for devicing new materials based on rubber and its potential to synthesise materials for various applications such as flexible magnets, microwave absorbers and magneto-rheological materials. Rubber ferrite composites (RFCs) belong to this class of materials derived by the incorporation of ferrite fillers in elastomer matrices. Elastomers, which are otherwise nonmagnetic, are made into magnetic when ferrites are incorporated into it. These magnetic fillers modify the mechanical, dielectric and other physical properties of the elastomer. Significant changes in magnetic and dielectric properties are observed for ferrites when the particle size is brought down to nano metric dimensions. When ferrite nanoparticles are incorporated into rubber, tremendous improvement in physicomechanical properties of the elastomer is realised.

Magnetism and magnetic materials have profound influence on human life. Magnetic materials are employed in the development of most modern electronic devices like computer chip memories, random access memory (RAM), electromagnetic interference (EMI) shields, high density storage media, television set, cell phone, refrigerator and washing machine. So, nanoscale magnetism and magnetic materials are going to play a very dominant role in developing the technology of the 21st century.

On the other side, polymers and polymer composites have established an inevitable position in the area of material research. The presence of both natural and synthetic rubber composites in different facets of human life such as transportation, communication, development of space vehicles and satellites, as well as in other daily use materials, chairs, automobile spare parts, pipes and toys, increase the importance of these materials in material world. The useful properties of polymers and magnetic materials pave the way for their combination to produce new composite materials with improved characteristics.

The central theme of this thesis is the study on rubber ferrite composites with special reference to the effect of nano ferrites on the physicomechanical properties and on the dielectric, magnetic and microwave properties of RFCs. Therefore, a general introduction is provided in the ensuing sections about elastomers, magnetic fillers and magnetism, ferrites and rubber ferrite composites. Magnetic and dielectric properties of ferrites are mainly dependent on their crystal structure. Structure of ferrites resembles the crystal structure of $MgAl_2O_4$ and hence these types of ferrites are called spinel ferrites. An overview of spinel structure is also given in the forthcoming sections. Since the ferrite used for the preparation of RFCs in the present study is of nano dimension, a short note is also given about the general methods of synthesis of nano ferrites. Finally, the motivation and objectives of the present study are listed.

1.1 Elastomers

Different types of elastomers such as natural /synthetic and polar/non polar are used for the preparation of rubber ferrite composites.

1.1.1 Natural rubber

Chemically, it is *cis* poly-isoprene characterised with low hysteresis, high resilience and low water absorption. High tensile strength, tear strength, resilience and high elongation at break are the major attractive features of natural rubber over synthetic rubbers. Poor resistance to sunlight, oxygen and ozone are the drawbacks of natural rubber compared to some synthetic rubbers. Compared to synthetic rubbers, it is inexpensive. Synthetic rubbers have their own characteristic properties, which make them special purpose rubbers and are used for the preparation of RFCs.

1.1.2 Ethylene propylene diene rubber

Ethylene propylene diene rubber (EPDM) is one of the most widely used synthetic elastomers, having both special and general-purpose applications. It is a copolymer of ethylene and propylene with a few percent of a third monomer namely a diene. The termonomer can introduce unsaturation to the otherwise saturated polymer. The commonly employed comonomers for introducing unsaturation are,
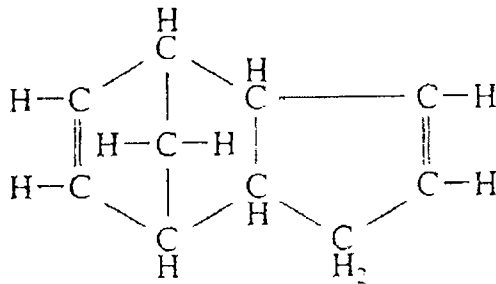
Dicyclopentadiene (DCPD)
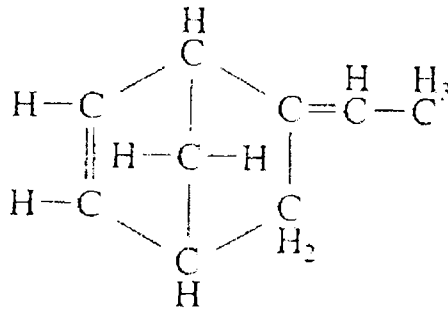
Ethylidene norbornene (ENB)

$$CH_2 = CH - CH_2 - CH = CH - CH_3$$
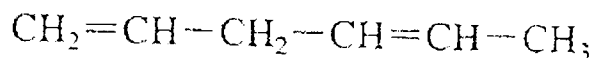
1,4 Hexadiene

The structure of EPDM with ENB as the third monomer is given in figure 1.1. Ethylene propylene diene terpolymer vulcanisate has been used extensively in high frequency power cables, automotive radiator hose and white side walls of tyres because of the exceptional capability to accept high loading of fillers and their

excellent ozone, heat and weathering resistance [1-4]. EPDM vulcanisates exhibit excellent electrical and mechanical properties when properly formulated [5].
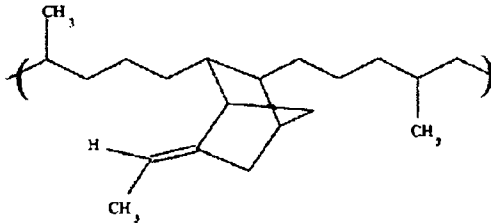
Figure 1.1 Structure of EPDM with ENB as the third monomer

EPDM has found wide acceptance in wire and cable applications. Unsaturation in the side chain renders it ozone resistant. It is also resistant to heat, cold and moisture.

EPDM rubber can be vulcanised using either sulphur or peroxide as the crosslinking agent. Peroxide cure gives better heat and ageing properties and low compression set and better electrical properties. A number of factors such as the ethylene/propylene ratio, nature and amount of the termonomer used, molecular weight distribution, peroxide used and the type of fillers, influence the efficiency of peroxide curing of EPDM [6,7]. The crosslink provided by peroxide vulcanisation is a carbon–carbon bond which is similar in strength to every other bond in the polymer back bone. Thus peroxide cured EPDM vulcanisate exhibits better compression set resistance and resistance to heat and chemical attack compared to sulphur cured vulcanisate. Moisture uptake and staining are less for the finished product prepared by peroxide curing [8]. In the present study, EPDM based RFCs are prepared by peroxide vulcanisation.

1.1.3 Chloroprene rubber

Polychloroprene (CR), commercially known as neoprene is one of the widely used synthetic rubbers with excellent heat, chemical and medium oil resistance [9]. Chloroprene monomer is used for the preparation of neoprene and structure of neoprene is given in figure 1.2. There are three general purpose neoprene rubber, G, W, and T types. Within each type, a number of grades of polymers are available with

varying mooney viscosity, rate of crystallisation and other features. W type CR has excellent raw polymer stability and better heat resistance. Their broad molecular weight distribution imparts better processability [10]. CR has good flame resistance, weather and ozone resistance. Because of its crystallising nature, neoprene gum vulcanisate has inherent high tensile strength, elongation at break and wear resistance.
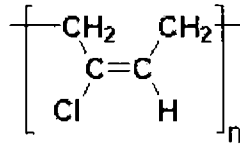
Figure 1.2 Structure of chloroprene rubber

Chloroprene rubbers are generally vulcanised by the action of metal oxides [11-13]. The primary crosslinking agent is zinc oxide, which is used along with magnesium oxide. Lead oxide is also used where high water resistance is required.

1.2 Magnetic fillers

Magnetism has fascinated humans for thousands of years. Nano scale magnetic materials are increasingly used in diverse fields of applications. Synthesis of magnetic materials with nano metric dimension helps in designing newer materials with novel chemical, magnetic and electrical properties. Different types of magnetic materials such as ferrites can be used for the preparation of magnetic composites. Since the central theme of this thesis is magnetic nanocomposites based on ferrites and rubbers, an introduction to different types of magnetism is provided below. Magnetic materials are classified into different types based on their response to an external magnetic field.

1.2.1 Magnetism

Magnetism is a result of moving charges. From an atomic view of matter, there are two electronic motions: orbital and spin motion of electrons. These two electronic motions are the source of macroscopic magnetic phenomena exhibited by materials. Magnetic moment per unit volume or magnetisation M of a substance and the magnetic flux density is related by the equation

$$B = \mu_0 (M + H) \qquad\qquad 1.1$$

where H is the applied field and μ_0 is the magnetic permeability of free space. The ratio

$$\frac{B}{H} = \mu \qquad\qquad 1.2$$

is called absolute permeability and

$$\frac{M}{H} = \chi \qquad\qquad 1.3$$

is called absolute susceptibility. μ and χ are related by the expression

$$\mu = \mu_0 (1 + \chi) \qquad\qquad 1.4$$

The magnetic susceptibility χ is a useful property for characterising magnetic materials.

Magnetism exhibited by different materials can be classified into five, depending upon the value of χ and the response of the materials towards an external field [14-19].

1.2.1.1 Diamagnetism

Diamagnetism occurs when the induced magnetic field opposes the external applied magnetic field. In diamagnetic materials, the constituent atoms or molecules have their electrons paired up in so as to cancel the magnetic dipole moments. In a diamagnetic material, the presence of an external magnetic field induces a change in the magnitude of inner atomic currents. An applied external magnetic field accelerates or decelerates the orbiting electrons, such that their magnetic moment is in the opposite direction from the external field. The response of the orbiting valence electrons counteracts the external field and thus shields the inner electrons from an external magnetic field. For a diamagnetic material, H = -4πM, where H is the external magnetic field applied and M is the magnetisation of the material in the presence of the external field H.

The atomic/magnetic behaviour of diamagnetic materials is as shown in figure 1.3.
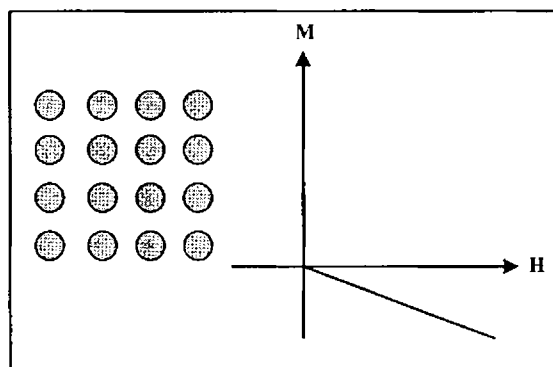
Figure 1.3 Atomic/magnetic behaviour of diamagnetic materials

1.2.1.2 Paramagnetism

Paramagnetic substances are characterised by their intrinsic permanent magnetic moments. Atoms or ions with one or more unpaired electrons exhibit paramagnetism. An external magnetic field tries to turn the unfavourably oriented spin moments in the direction of the external field. This results in an overall magnetic moment that adds to the external magnetic field. The atomic/magnetic behaviour of paramagnetic materials is represented in figure 1.4. Paramagnetic susceptability is independent of the applied field and is temperature dependent. Curie's law governs the temperature dependence of paramagnetic material. The magnetic susceptibility χ is related to the temperature in degree absolute by the equation $\chi = \dfrac{C}{T}$. χ is small and positive for paramagnetic substances. In materials obeying Curie's law, magnetic moments are localised at the atomic or ionic sites. There is no interaction between neighbouring magnetic moments.

Paramagnetism is usually exhibited by transition or rare earth metal compounds that possess unpaired electrons and it is known as spin paramagnetism. In most of the solids, spin paramagnetism is observed. In crystals, the electron orbits are essentially coupled to the lattice, which prevents the orbital magnetic moments from turning into the field direction. Under such circumstances the orbital moments are said to be quenched. Exceptions to this are the rare earth elements and their derivatives with unpaired electrons in the deep lying '4f orbitals'. As the outer electrons from the crystalline field of neighbouring ions shield these electrons, the orbital magnetic

moments of the f electrons may turn into the external field direction and contribute to electron-orbit paramagnetism. The fraction of the total magnetic moment due to the orbital motion to that of the spin motion is defined as the g-factor, which is given by the expression

$$g = 1 + \frac{J(J+1) + S(S+1) - L(L+1)}{2J(J+1)} \qquad 1.5$$

where J is the total angular momentum, S is the total spin angular momentum and L is the total orbital angular momentum.
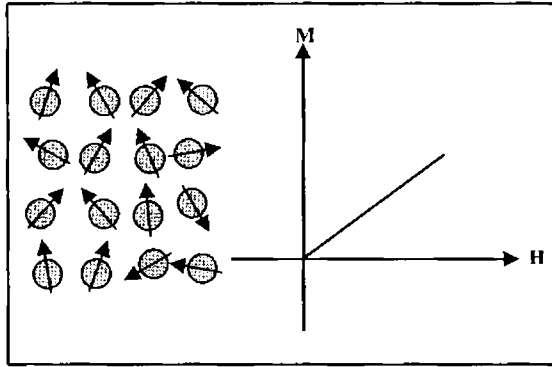
Figure 1.4 Atomic/magnetic behaviour of paramagnetic materials

1.2.1.3 Ferromagnetism

A ferromagnetic substance has a net magnetic moment even in the absence of an external magnetic field. Like paramagnetism, ferromagnetism involves the magnetic dipoles associated with the spins of the unpaired electrons. The interaction between nearby dipoles differentiates ferromagnetism from paramagnetism. If the many individual magnetic dipoles produced in a material are appreciable, there can be long range interactions. This leads to large scale areas of magnetism called domains. In ferromagnetic materials, the dipoles within a domain are all aligned and the domains tend to align with an applied field. The atomic/magnetic behaviour of ferromagnetic materials is represented in figure 1.5.

8
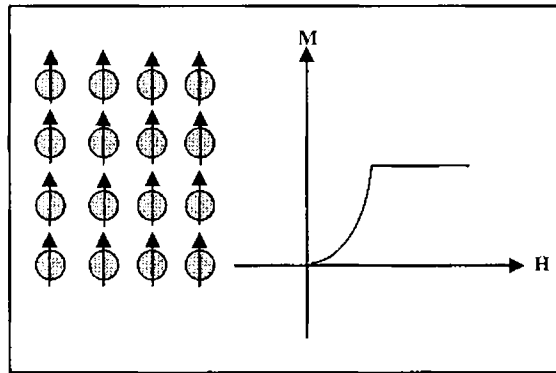
Figure 1.5 Atomic/magnetic behaviour of ferromagnetic materials

A characteristic feature of a ferromagnetic substance is the magnetic hysteresis. The energy expended in reorienting the domains from the magnetised state back to the demagnetised state manifests into a lag in response to an applied magnetic field, known as hysteresis. Another important property of ferromagnets is the Curie temperature. For ferromagnetic materials, susceptibility χ is large and positive and varies with the absolute temperature. They obey the Curie-Weiss law, $\chi = C/ (T-\theta)$, where C and θ are Curie Weiss constants. Above Curie temperature, ferromagnets become paramagnets, since there is sufficient thermal energy to destroy the interaction between atoms that create domain. Iron, cobalt and nickel are examples of ferromagnetic materials. Gadollinium (Gd) which belongs to the rare earth family also exhibit ferromagnetism. The curie temperature of Gd is 295 K. Chromium oxide is another example of a ferromagnet.

1.2.1.4 Antiferromagnetism

In an antiferromagnet, exchange coupling exists between neighbouring moments that causes the moments to align in an antiparallel fashion. This anti parallel alignment causes the system to have a small positive susceptibility, because an applied magnetic field tends to align the spins and this induced alignment is larger than the diamagnetism of the electron orbital. Figure 1.6 shows the atomic/magnetic behaviour of antiferromagnetic materials. Similar to ferromagnets, the exchange energy can be defeated at high temperatures and then the system becomes paramagnetic. The temperature above which a ferromagnetic substance becomes paramagnetic is known

as Neel temperature (T_N). For temperatures greater than T_N, the susceptibility of a ferromagnetic substance follows a paramagnetic Curie-Weiss law with a negative θ, χ = $C/(T+\theta)$. Most antiferromagnetics are found among ionic compounds such as metallic oxides, sulfides and chlorides. Oxides of manganese and chromium are some other examples of antiferromagnetic substances.
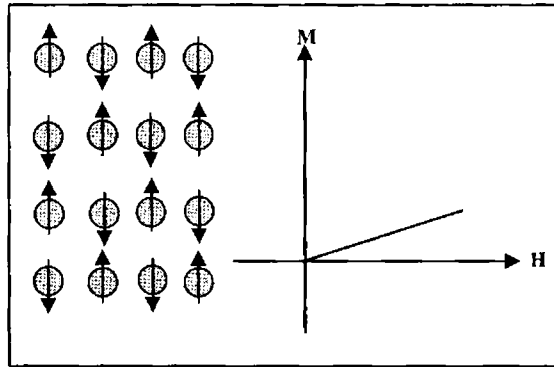
Figure 1.6 Atomic/magnetic behaviour of antiferromagnetic materials

1.2.1.5 Ferrimagnetism

Ferrimagnetism is observed in compounds which exhibit complex crystal structures. Within these materials, the exchange interactions lead to parallel alignment of atoms in some of the crystal sites and anti-parallel alignment in the other sites. The material breaks down into magnetic domains, just like in a ferromagnetic material. The magnetic behaviour is very similar, although ferrimagnetic materials usually have lower saturation magnetisation. Ferrimagnets are similar to antiferromagnets in which the opposing dipoles are not equal, so they do not cancel out. Therefore, these materials exhibit a spontaneous magnetic moment and display hysteresis below Curie temperature. Ferrimagnets are generally ceramic materials and they are good insulators, making them very useful in preventing energy losses due to eddy currents in transformers. Ferrites are typical examples of ferrimagnets and naturally occurring magnetite and maghemite are examples of ferrimagnetic materials. The atomic/magnetic behaviour of ferrrimagnetic materials is depicted in figure 1.7.
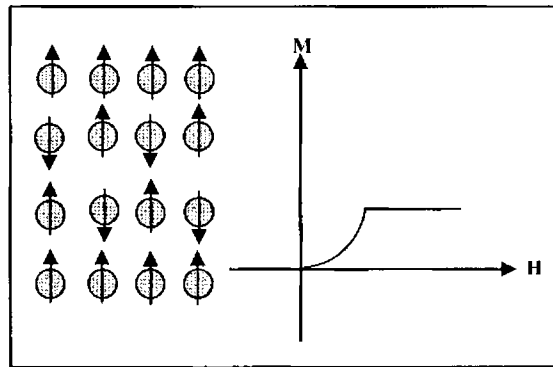
Figure 1.7 Atomic/magnetic behaviour of ferrimagnetic materials

1.2.2 Nano scale magnetism

Nanomaterials exhibit altogether different electrical, magnetic, optical, electrochemical, catalytic, structural and mechanical properties with respect to their coarser sized cousins. Nano magnetic materials display unusual properties like superparamagnetism, single domain behaviour and spin glass phenomenon. Nano scale magnetism is fascinating because of their tremendous potential in finding technological applications. The unusual behaviour exhibited by nanoparticles is mainly due to two major reasons, finite size effects [20] and surface effects [21,22]. For magnetic particles, the latter is more significant since the ratio of surface atoms to bulk atoms is sufficiently high.

Nano magnetic particles are characterised by enhanced magnetic moments [23], exchanged coupled dynamics [24], quantisation of spin waves [25,26] and giant magnetoresistance [27]. These new properties can lead to potential applications in permanent magnets, data storage devices [28], new magnetic refrigeration systems [29], enhancing agents for magnetic resonance imaging, catalysis and targeted drug delivery systems.

Nano magnetic materials also exhibit interesting magneto-optical properties such as large Faraday rotation and Kerr rotation and they are potential materials for many magneto-optical applications.

Key features such as single domain particles and superparamagnetism dominate the magnetism of small ferromagnetic particles. For single domain particles,

magnetisation reversal takes place through spin rotation where as in other cases, it occurs due to the spin wall movement. Greater energy is required for spin rotation resulting in higher coercivity for single domain system [30].

1.2.3 General methods employed for the synthesis of nanomaterials

The primary step in any investigation in material science is the preparation and characterisation of materials. Any suitable method can be adopted for the preparation of micron sized particles. However, the preparation of nanoparticles requires some special methods that may be unique with respect to a particular material. There are mainly two approaches for the synthesis of nanomaterials viz. bottom up and top down approach.

In the bottom up approach, nanostructures are created, atom by atom or by assembly of components consisting of a few thousand atoms or molecules. Processes such as self organisation, self assembly or templating can be used to build a multitude of nano architectures. Examples for bottom up approach are vapour phase processing like physical and chemical vapour deposition, inert gas condensation and sputtering. Chemical synthesis like sol-gel method, precipitation method and electrochemical synthesis are based on bottom up principle.

Top down approach involves the use of conventional bulk starting materials that include solid state processing like mechanical attrition, severe plastic deformation, crystallisation of amorphous precursors and liquid-phase processing. High energy ball milling (HEBM) is employed for attrition which can impart high momentum to the milled powder through the high speed of rotation and revolution of the vials which helps in obtaining high efficiency in low milling times.

Between the two methods, bottom up process is more advantageous. Surface imperfections and strain will be less in bottom up process as it involves the formation of nano structured materials via atom by atom growth. Careful control of the preparative conditions in bottom up process ensures systematic tuning of the grain size and other characteristics of the nanoparticles. Nanomaterials produced by these methods mostly require further processing, sintering or thermal spraying to produce useful structural materials.

Several physical aerosol methods have been reported for the synthesis of nano size particles of ceramic materials. These include gas condensation techniques [31,32], spray pyrolysis [33-35] and thermochemical decomposition of metal-organic precursors in flame reactors [36,37]. On the other hand, most widely used liquid phase chemical method is sol-gel method [38,39]. Other wet chemical methods, including microemulsion [40,41] and co-precipitation have also been widely used [42].

1.2.3.1 Vapour condensation method

In this method, a super saturated vapour of the metal is condensed under inert convection of gas inside a chamber. A high pressure of inert gas is usually needed to achieve super saturation. Frequent collision with the gas atom decreases the diffusion rate of atoms from the vapour source region and cools the atoms. The powder is oxidised by allowing oxygen into the chamber. This post oxidation must be carried out slowly. Due to the highly exothermic reaction, particles heat up for short times to temperature as high as $1000°C$ resulting in their agglomeration into large particles by rapid diffusion processes. A subsequent annealing process at higher temperature is often required to complete the oxidation.

Advantages of this method over other techniques are versatility, ease of performance and analysis and production of high-purity products. This method is also employed to produce films and coatings. The disadvantages are high production cost and low yield. Heating techniques have other disadvantages like the possibility of reaction between the metal vapors and the heat source materials. This method can not be used to prepare a wide variety of materials as the operating temperatures are limited by the choice of the source material.

1.2.3.2 Spray pyrolysis

In this method, precipitation from a concentrated solution of cations can be performed by solvent evaporation. The starting precursor for this method is sol or suspension of appropriate salts. From this, aerosol droplets are prepared by nebulisation or atomisation of the starting sol at high pressure. The solvent is rapidly evaporated by an upward stream of hot gas. The microporous particles thus produced are compacted and calcined to produce the ceramic powders.

Advantages of this method include the formation of high purity and homogeneous products with nano metric dimensions. Since each particle/droplet undergo the same reaction conditions, no subsequent milling is necessary. Major disadvantages of this process are the requirement of large amount of solvents and difficulty in scaling up of the process. Use of nonaqueous solvents increases the cost of production, so this process is limited to the aqueous systems.

1.2.3.3 Thermochemical/flame decomposition of metal organic precursors

This is an effective method for the preparation of ceramic nanoparticles. This process is also referred to as chemical vapor condensation (CVC). The starting materials are liquid chemical precursors which are vapourised and then oxidised in a combustion process using a fuel oxidant mixture. The process involves the rapid thermal decomposition of a precursor carrier gas stream at reduced pressures with simultaneous decomposition of the condensed product particles on substrates. Organometallic based synthesis, carried out at high temperatures, facilitates the removal of crystalline defect and results in high quality magnetic nanoparticles.

1.2.3.4 Reverse microemulsion method

This is one of the promising methods for the preparation of nano crystalline materials. In this method, micelles are formed by adding surfactants, dissolved in organic solvents to the aqueous solution of reactive precursors. Nanoparticle synthesis inside the micelles can be achieved by hydrolysis of reactive precursors or by precipitation reactions of metal salts. Solvent removal and subsequent calcination lead to the final product. The final properties of the product such as particle size, particle size distribution, agglomeration and final phase formation of the ceramics are affected by several parameters such as the concentration of the reactive precursor in the micelle and mass percentage of the aqueous phase in microemulsion. Microemulsion techniques are often carried out at low temperatures but with the disadvantage that the particles are less crystalline and more polydispersed.

1.2.3.5 Sol- gel method

Sol-gel method is widely used for the preparation of a large number of inorganic and inorganic/organic composite materials. The process involves the

preparation of a sol and typically used for the preparation of metal oxide via the hydrolysis of reactive metal precursors. The sol of the metal salt is prepared by mixing concentrated solutions containing the cations of interest, with an organic solvent (usually alcohol) as the dispersion medium. The solution is then destabilised by adding water. The presence of water modifies the pH of the sol and reduces the repulsion between particles. This results in a large increase in the viscosity of the system, leading to the formation of a gel.

Addition of water to alcoholic solution of alkoxide results in the formation of corresponding hydroxide. Condensation of hydroxide molecules by elimination of water leads to the formation of a network of metal hydroxide. When all hydroxide species are linked in one network structure, gelation is achieved and a dense porous gel is obtained. The gel is a polymer of three dimensional skelton surrounding interconnected pores. Removal of the solvents and appropriate drying of the gel results in an ultrafine powder of the metal hydroxide. Further heat treatment of the hydroxide leads to the corresponding ultrafine powder of the metal oxide.

Solvent removal from the gel is achieved by two ways. Drying is achieved by evapouration under normal conditions and the gel network shrinks as a result of capillary pressure and the hydroxide obtained is known as xerogel. Aerogels are obtained when drying is being done using a high pressure autoclave at temperatures higher than the critical temperature of solvents. Aerogel powders have higher porosities and larger surface areas than analogous xerogel powders [19].

1.2.4 Application of magnetic materials

It is well known that magnetism and magnetic materials have unprecedented role in data storage and magnetic recording. A novel substitute for the conventional magnetic materials in these fields is magnetic nano wires. For long term storage, magnetic materials should have a reasonably high coercivity, because external magnetic fields should not alter the magnetisation. At the same time it should not be too large if the medium is to be reusable. Ferromagnetic nano wires encapsulated within carbon nano tubes provide an ideal system for recording. Small size anisotropy and the single isolated domain nature of the encapsulated iron crystals provide higher coercivity. Due to the graphite protecting cover, the magnetic properties of entrapped

nano wires do not degrade with time [43,44]. Magnetic nanocomposites should also find applications in the fabrication of fine particle magnets, for use in magnetic inks and as toners in xerography.

Magnetoelastic materials are another class of technologically important magnetic materials. These materials give the possibility of converting very small mechanical stress into electrical voltage. Magnetic devices for detecting parked vehicles are developed based on the principle of magnetoelastic resonance. Coding devices are developed based on magnetoelastic resonators which rely on the variation of the Youngs modulus with the bias field [45]. Frequency dependence of permeability of the nanocrystalline ribbons have been made use in devices such as current-compensated chokes, saturable reactors and inverter transformers for integrated services digital network (ISDN) telecommunications [46].

Magnetorheological elastomers composed of ferromagnetic particles dispersed in a non-ferromagnetic elastomer matrix susceptible to elastic deformations constitute a very interesting group of magnetic materials [47]. Magnetorheological elastomers are used for the production of controlled vibration dampers [48].

Superparamagnetism is a unique feature of magnetic nanoparticles and is crucially related to many modern technologies like ferrofluid technology [49], magnetocaloric refrigeration [50] magnetic resonance imaging (MRI) [51] and magnetically guided drug delivery. Ferrofluids are stable suspensions of nano magnetic particles in a suitable base fluid like oil or water. They are of great research interest because of their numerous physical, engineering and medical applications. These smart fluids show many interesting magneto-optical properties. Some of the engineering applications of these rheological fluids are in making rotary seals, pressure sensors and loud speakers. Ferrofluids can serve as contaminant exclusion seals, vacuum seals and dampers in stopper motors. With improvement in performance and production cost, nano ferrofluids may find applications as cooling fluids, nano scale bearings and in magnetically controlled heat conductivity [52]. They are also widely used in bio medical fields especially in cancer therapy [53].

Tumor specific nanocomposites are developed and the technique is named as magnetic hyperthermia. Magnetic nanoparticles are specifically attached to the cancer

cells and under the application of an ac electric field, the particles become selectively heated, damaging (hyperthermia) or destroying (thermoablation) the attached tumor cell. This method has immediate effect without any side effects. Magnetic nanoparticles can also be used for controlled drug delivery at a predetermined site within the body [54-56].

Ferromagnetic semiconductors are obtained by doping magnetic impurities in host semiconductors. They are key materials for spin electronics (spintronics) in which the correlation between the charge and spin of electron is used to bring about spin dependant electronic functionality such as giant magneto resistance (GMR) and spin field effect.

Magnetic particles coated with protective and functional materials such as silica can easily be prepared by sol-gel method or liquid phase coating process [57]. Magnetic particles embedded in polymer matrices have been synthesised for the fabrication of conductive, superparamagnetic plastic films [58-63]. Deposition of conductive polymer chains and magnetic nanoparticles in a layer by layer fashion may lead to new properties such as GMR and novel organic based nano structured GMR materials. Other than serving as a lossless transformer, the nano magnets can act as miniature switches or sensors. Polymer based nanocomposites can be used as a dielectric layer in electronic packing applications.

A new class of flexible magnetic composites can be prepared by incorporating ferrite materials into elastomer medium which are named as rubber ferrite composites. Rubber ferrite composites find applications in many devices because of their easy mouldability and microwave absorbing properties [64,65].

1.3 Ferrites

Ferrites are mixed metal oxides with Iron (111) oxides as their main component. Based on their crystal structures, ferrites are classified into three types namely spinels, garnets and magnetoplumbites. They are shown in table1.1.

Simplest among the ferrites are the spinel ferrites. The structure of ferrites resembles that of the mineral spinel $MgAl_2O_4$. Spinel ferrites can again be categorised into two namely normal and inverse spinels. The unit cell of a spinel structure consists

Table 1.1 Different types of ferrites

Type	General formula	Structure	Example
Spinel	$M^{II}Fe_2O_4$	Cubic	M^{II} = Cd, Co, Mg, Ni and Zn
Garnet	$Ln_3^{II}Fe_2O_{12}$	Cubic	Ln^{II} = Y, Sm, Eu, Gd, Tb, Dy, Ho, Er, Tm and Lu
Magnetoplumbite	$M^{II}Fe_{12}O_{19}$	Hexagonal	$BaFe_{12}O_{19}$

of eight formula units ($8 \times MFe_2O_4$). The 32 oxygen ions form a face centered cubic lattice in which two kinds of interstitial sites are present, namely tetrahedral sites (A sites) and octahedral sites (B sites) (figure 1.8).
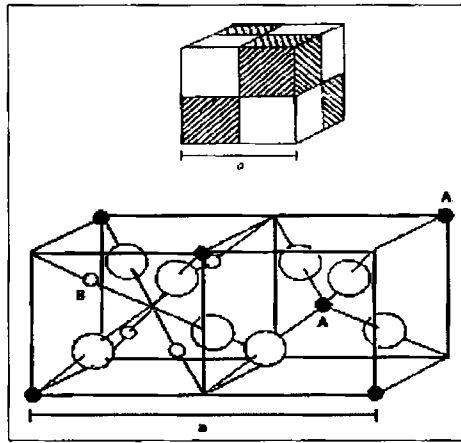
Figure 1.8 Crystal structure of a cubic ferrite: O – Oxygen ion • – Metal ion

The interesting and useful electrical and magnetic properties of the spinel ferrites are governed by the distribution of the iron and the divalent metal ions among the tetrahedral and octahedral sites of the spinel lattice. Generally a spinel ferrite can be represented by the formula $M_\delta^{2+}Fe^{3+}_{1-\delta}[M_{1-\delta}^{2+}Fe^{3+}_{1+\delta}]O_4$ [66]. Ions within the square bracket represent octahedral sites and ions outside the bracket represent tetrahedral sites. The limiting case where $\delta = 1$ is called normal spinel and $\delta = 0$ is called inverse spinel.

Site preference of the cations between the octahedral site and tetrahedral site are explained using crystal field theory by Dunitz and Orgel [67] and also by McClure [68] where as Blasse [69] has used a simplified molecular orbital approach. According to the crystal field theory, the five degenerate 3d orbitals in an octahedral field are split into a lower triplet (t_{2g}) and higher doublet (e_{2g}). These two levels are separated by an energy difference of 10 Dq. This splitting of orbitals is reversed when the cations occupy a tetrahedral site. In this case, e_{2g} orbitals become lower and t_{2g} orbitals become higher energy levels. Thus, the crystalfield stabilisation energy of a cation will be different in both tetrahedral and octahedral coordination. This determines the cation distribution in ferrites [70].

In the case of $NiFe_2O_4$, Ni^{2+} ion with d^8 configuration contains two unpaired electrons irrespective of the A or B site. But crystal field stabilisation energy is more in B site, hence preferably occupies octahedral site, thus forming an inverse spinel structure. In addition to simple binary spinels, a number of mixed ferrites are also possible by partial substitution of cations, either in A or B site. As the properties of mixed ferrites are highly dependant on the composition, ferrites with predetermined material characteristics can be designed by properly adjusting the composition. A large number of mixed ferrites are studied and reported, among this the extensively studied one is Ni-Zn ferrite.

In addition to the above mentioned forms, some ferrites exhibit distorted spinel structures. Examples are magnetite (Fe_3O_4) and maghemite (γ-Fe_2O_3). γ-Fe_2O_3 has a cation deficient spinel structure with a fraction of octahedral sites occupied by vacancies at all temperatures.

1.3.1 Magnetic properties of ferrites

Ferrites are important ferrimagnetic materials. In ferrites, the metallic ions occupy two crystallographic sites; octahedral sites and tetrahedral sites. Three kinds of magnetic interactions are possible between the metallic ions, through the intermediate O^{2-} ions, by super exchange mechanisms namely A-A, B-B and A-B interactions. These interaction energies are negative and induce an anti parallel orientation (as proposed by Neel in 1948). In ferrites, A-B interaction predominates. Thus spins of A

site and B site ions in ferrite are oppositely magnetised with a resultant magnetic moment equal to the difference between those of A and B site ions.

Ferrites such as $MnFe_2O_4$, $NiFe_2O_4$, $FeFe_2O_3$ and $CoFe_2O_4$ have high curie temperatures and have reasonable saturation magnetisations in agreement with Neels theory. In these ferrites, Fe^{3+} ions are found in equal numbers on A and B sites. Hence, saturation magnetic moment should correspond to that of the metallic ion. In $NiFe_2O_4$, the net magnetisation is 2 μ_B magneton as shown below, consistent with Neel's two sublattice theory.

A site	B site
$8Fe^{3+}$	$8Fe^{3+}$ $8Ni^{2+}$
↑↑↑↑↑	↓↓↓↓↓ ↓↓
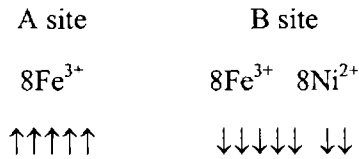
Thus the magnetic properties of ferrites can be tuned by distributing different cations in A and B sites and is highly significant for mixed ferrites.

1.3.2 Electrical properties of ferrites

Ferrites are considered as magnetic semiconductors and the conductivity can be attributed to the presence of Fe^{2+} and M^{3+} ions. The presence of Fe^{2-} results in n-type behaviour and presence of M^{3+} results in p-type behaviour. Conduction process is due to the hopping of extra electrons (from Fe^{2+}) or the positive hole (M^{3+}) through the crystal lattice.

Temperature dependence of the electrical conductivity is given by the relationship $\sigma = \sigma_0\, e^{-E_a/kT}$ where E_a is the activation energy for conduction, which is the energy required for hopping of the electron or hole and σ_0 is a constant. k is the Boltzmann constant and T is the temperature in Kelvin. Conduction mechanism in ferrites is entirely different from that of the conventional semi conductors where in charge carriers occupy states in wide energy band. The charge carriers in ferrites are localised at the magnetic atoms. Temperature dependence of electrical conductivity of ferrites is mainly due to the variation in mobility of the charge carriers where as the concentration of charge carrier is almost temperature independent.

Dielectric properties of ferrites depend on several factors including the method of preparation, chemical composition and grain structure and size. Dielectric properties of solids can be explained based on phenomenon like polarisation. In polycrystalline ferrites, three principle mechanisms of polarisation exist within a frequency spectrum extending from zero frequency to frequencies corresponding to ultra violet radiations. The electronic contribution arises from the displacement of electron shell relative to the nucleus. Ionic polarisation comes from the displacement of charged ion with respect to other ions and dipolar polarisation due to the orientation of electric dipole in an external field. In addition to this, in heterogeneous materials interfacial polarisation occurs due to the accumulation of charges at structural interfaces. Frequency dependence on the polarisability due to several contributions is represented in figure 1.9.
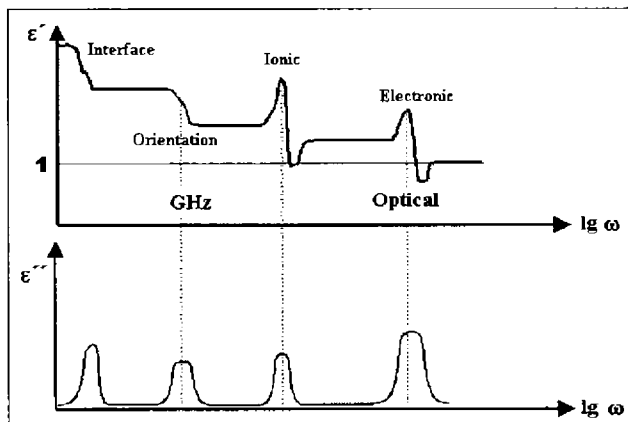
Figure 1.9 Frequency dependence of the several contributions to the dielectric polarisability.

1.3.3 Different methods for the preparation of ferrites

A number of chemical methods such as micro emulsion or reverse micelle method, co-precipitation method, sol-gel method and synthesis from different organic precursors are reported for the preparation of nano ferrites.

1.3.3.1 Ceramic method

This is one of the earliest and most popular methods used for the synthesis of ferrite materials. The particle size of the materials prepared by this method is often found to be of micrometric dimension. Required precursors are mixed in appropriate

molar ratio and sintered at very high temperature which results in the formation of crystalline materials [71-74].

The disadvantage of ceramic method is that it is highly difficult to control the stoichiometirc composition and final structure. Since this technique requires prolonged heating at very high temperatures, some of the constituents may evapourate thereby resulting in alteration of the desired stoichiometry [75].

1.3.3.2 Co-precipitation method

In cold co-precipitation method, the precursors are taken in the appropriate molar ratio in an aqueous medium at an appropriate pH and temperature. The precipitate is then heated at high temperatures to obtain crystalline ferrite materials [76].

Nano crystalline ferrite materials can successfully be prepared from different organic precursors. Citrate and oxalate precursors are used for the synthesis of ferrite nanoparticle. This solution method allows the atomic scale mixing of the constituent cations and allows the formation of ferrite particles at low temperatures [77,78]. C. Caizer and M. Stefanescu had reported the preparation of Ni-Zn ferrite powder from the glyoxylate precursor. It is practically a low temperature method. The reaction efficiency is nearly 100% and high purity products are formed [79].

1.3.3.3 Sol-gel technique

This is one of the easiest routes for the synthesis of nanomaterials [80-82]. In this method, reactants, preferably, metal nitrates or acetates are completely dissolved in a suitable organic solvent and the solution is allowed to react at low temperature until a gel is formed. The gel is then heated at high temperature to obtain the desired final product. The detailed mechanism and sol-gel chemistry is provided in section 1.2.3.5.

1.3.3.4 High energy ball milling

In this method, mechanical energy is utilised for the synthesis of nanoparticles from micro particles. Here, due to the very high rotation and revolution, the energy

imparted to the material is very high. The properties of nano phase materials synthesised by this method are dependant on ball milling conditions [83].

1.3.4 Applications of ferrites

Polycrystalline ferrites are good dielectric materials with low conductivity and have a wide field of technological applications. Ferrites are used extensively in many electronic devices, because of their high permeability in the radio frequency region, high electrical resistivity, mechanical hardness and chemical stability [84,85].

Hexagonal ferrites based on barium ferrite are efficient replacements for the metallic magnets in recording media and in microwave devices [86]. High stability in air, non metallic electrical properties, corrosion resistance and sharp switching fields make hexagonal ferrites superior to metallic magnets [87]. Among the different types of hexaferrites, M-type barium hexaferrite has been intensively studied as a material for permanent magnet, high density magnetic recording media and microwave devices [88,89]. Anisotropic hexaferrites are highly used in loud speakers and in dc motors. Stepping motors based on ferrite materials are needed in floppy-disc drivers, printers and other computer peripherals.

Ferrites are also used in antennas to transform an electromagnetic signal transmitted through the air into an electric signal. The application of ferrites at microwave frequencies (1-300 GHz) is based on electromagnetic wave propagation phenomena. Ferrite isolators are typically employed to isolate source from load in microwave systems. Circulators and phase shifters based on ferrites are typically used in microwave antenna systems. As microwave absorbers, ferrites can be used to suppress electromagnetic interference [90-92].

Ferrite nanoparticles possess superior magnetic properties when compared to their bulk counter parts. In ferrite nanoparticles, a strong decrease in saturation magnetisation and an enhancement in coercivity in comparison to the bulk material have been reported [93]. Property enhancement of ferrite nanoparticles makes them suitable for applications in electronics, bioprocessing, magnetic resonance imaging and ferrofluids [94].

Mixed ferrites based on Ni-Zn and Mn-Zn are the most widely used materials for different applications. These types of ferrites are used in magnetic cores of read-write heads for high-speed digital recording. Zn-Mn ferrites are important electronic ceramic materials because of their high magnetisation polarisations and electrical resistivity. These are the main constituents of transformer cores, inductors, converters and yokes [95]. High resistivity and low eddy current loss of Ni-Zn ferrite makes them adaptable for high frequency applications [96]. Mg-Zn ferrites are used as materials for coil cores like deflection coils for picture tubes in TV and computer memories [97].

1.4 Rubber ferrite nanocomposites

Development of magnetic nanocomposites leads to new composite materials such as plastic magnets or magneto polymers [45,98]. Incorporation of magnetic fillers into a polymer matrix produces plastic magnets. Rubber ferrite composites are magnetic polymer composites, prepared by the incorporation of ferrites into rubber [99,100]. They have wide range of technological applications. These flexible magnetic materials have excellent performance characteristics and often on par with ceramic magnetic materials. The unique advantages of RFCs are their easy processability and mouldability into convoluted structures. This makes them superior in many respects over conventional ceramic magnets. The degradation of the polymeric matrix limits the application potential of these materials at temperature above 200°C. However, polymer magnets are increasingly used as special purpose composites.

Addition of magnetic fillers to a polymer host medium affects its processability and mechanical properties; where as the magnetic properties of the fillers are also affected by encapsulating them with polymeric medium. Magneto polymers with tailored properties are made with suitable selection of magnetic fillers and host medium [101]. The concentration and orientation of the magnetic particles and degree of interaction of the filler with the matrix are important factors of concern in tailor making materials. In selecting the matrix, the mechanical, viscoelastic and chemical properties of the matrix must be taken into consideration. The compatibility of the matrix with magnetic particles is a significant factor. Advantages of plastic magnets over their metallic and ceramic counterparts include light weight and low

cost, resistance to corrosion, ease of machining and preparation and capability of high production rates [102,103].

Polymer composites are important commercial materials, which find application in vibration damping, electrical insulations, thermal insulations and high performance composites for use in aircraft. Rubber ferrite composites are one such special purpose composite in which the flexibility and mechanical properties of an elastomer and magnetic properties of ferrite filler have been effectively utilised.

The impregnation of magnetic fillers in the matrix imparts magnetic properties and appreciably modifies the physical properties of the matrix. Proper selection of the elastomer as well as the ferrite is important for achieving the desired properties. The polymer must have appropriate physical properties and reasonable stability. Factors like percolation limits, nature of the matrix namely saturation/ unsaturation/ polarity all influence the final properties of the composites. Both natural and synthetic rubbers can be used as the host matrix for RFCs.

Magnetic properties of the RFCs like saturation magnetisation, coercivity and remanant magnetisation can easily be controlled by proper selection of the magnetic filler. Both hard and soft ferrites are used as filler. Soft ferrites like nickel-zinc ferrite and manganese zinc ferrite are incorporated in the polymer matrices (both natural and synthetic) to produce RFCs [104-106]. Rubber ferrite composites based on natural /synthetic rubbers and hard ferrites like strontium ferrite and barium ferrite are also reported [107-109].

One of the important factors that determines the processability and properties of RFCs is the particle size of the filler. When the size of the filler is in the nano regime, greater enhancement of mechanical properties can be anticipated. Smaller the particle size, larger the surface area and greater is the polymer-filler interface interaction. Thus, ferrite particles can act as a semi reinforcing filler, though the main intention of incorporation of these fillers is to modify the magnetic and dielectric properties of the elastomer.

Addition of fillers to rubber has a strong impact on its static and dynamic behaviour. Surface interactions between a reinforcing filler and rubber molecules involve a range of bond energies from relatively weak Vander-Waal interaction to

very strong chemical interaction. Physical adsorption of polymers on filler surface occurs to varying degree depending on the filler surface and nature of the polymer segments [110,111]. Chemical interaction is possible when specific functional groups like -OH, -COOH, -NH$_2$ etc. are available on the filler surface. Since, such functional groups are absent in ferrites; the reinforcement may be due to some physical interactions [112].

Nanocomposite magnets, with both particle and matrix systems being magnet have received much attention, because they may have high remanance, associated with exchange coupling at interfaces separating hard and soft magnetic phases and large energy product, (BH)$_{max}$ relative to conventional magnetic materials [113,114]. The resistance of RFCs to mutual demagnetisation is as good as that of sintered isotropic ferrite. RFCs have enormous application potential in electrical and electronic industries where flexibility is a desired factor. Microwave absorbing characteristics of ferrites make these magnetic composites applicable in microwave and radar applications [115,116].

Carbon black, the unique and most widely used reinforcing filler, can improve the mechanical properties of RFCs. Incorporation of carbon black along with ferrite filler can modify mechanical, dielectric and microwave properties of elastomers [117-121].

1.5 Motivation for the present study

Incorporation of ultrafine ferrite fillers like nickel ferrite and gamma ferric oxide in matrices like EPDM and CR results in rubber ferrite nanocomposites. It is important that the incorporation of these fillers in definite loadings in the host matrix is according to a specific recipe. Hence specific recipes are to be formulated for preparing ferrite polymer nanocomposites. The processability of these polymer composites is to be determined by evaluating the cure characteristics. Incorporation of fillers along with other compounding ingredients in the polymer matrix should normally result in a homogeneous composite without agglomeration and segregation. Morphology study using Scanning electron microscopy (SEM) is an ideal tool for assessing the homogeneity of these composites.

Ferrites are commercially important materials due to their unique properties like appropriate magnetic characteristics, high resistivity and low eddy current lossess. They are important microwave absorbing materials and are also employed as isolators, circulators and phase shifters, where they are in the form of ceramic materials. The inherent draw back of ceramic materials is their lack of flexibility and mouldability into complex shapes. This can overcome by incorporating these materials into flexible medium like rubber.

In the present study, nickel ferrite and gamma ferric oxide are used as the magnetic fillers for the preparation of the composites. Nickel ferrite is an important member of the family of ferrites. It is an ideal template for the preparation of a number of mixed ferrites such as nickel zinc ferrites. Gamma ferric oxide is a commercially important magnetic material extensively used in audio/video recording. It is rather difficult to synthesise pure γ-Fe_2O_3 without traces of alpha ferric oxide. Precise preparative conditions are to be maintained for the synthesis of pure γ-Fe_2O_3. The synthetic route adopted for the preparation, generally influences properties of ferrites. In the present study, sol-gel method is employed for the preparation of the ferrite nanoparticles. Sol-gel method is adopted as this is one of the simplest and economic methods for the preparation of nano scale materials. This is a low temperature method and ensures the formation of pure and crystalline particles.

Before incorporation, fillers are characterised so that comparison and correlation of various physical properties after the preparation becomes less difficult. Since the fillers possess high surface area, they contribute a larger interphase and reinforce the elastomer. They also modify the electrical and magnetic properties of the composites. So investigations on the mechanical, magnetic and electrical properties of these composites assume significance. These investigations are necessary to delve into the fundamental aspects involving fine particle fillers and their interaction with the matrix.

Mechanical properties of the elastomer are a major concern in the designing of composite materials for specific applications. The extensibility of the elastomer should be high so that higher amount of magnetic fillers can be incorporated without any processing difficulty. Outdoor application of composite materials demands

appreciable ageing characteristics. The composite materials must be resistant to heat, weather, oils and chemicals, oxygen and ozone attack and a number of other factors. Compared to natural rubber, synthetic rubbers proved to have excellent resistance to all these factors. Thus, the choice of synthetic rubbers like EPDM and CR for the preparation of RFCs in the present study is mandatory.

It is also necessary that composites should have appropriate magnetisation and the required coercivity. So the loading percentage of the magnetic filler was varied to have optimal properties. Carbon black was incorporated in to the composite having optimum magnetic and electric properties. This was carried out to study the microwave absorption property of these RFCs so that the band width of absorption can be tuned. This is attempted from an application point of view. A systematic investigation in to the various fundamental aspects involving the modification of physical properties viz. mechanical, magnetic and electrical is undertaken. For the preparation of nano fillers new techniques or the modification of the existing ones are attempted. Specific recipes are formulated depending upon the nature of the host matrix. Finally attempts are made to correlate the various results and model them using simple existing models. The objectives of the present work are shown in a nutshell.

Objectives of the present work:

- Synthesis of nanosized nickel ferrite and gamma ferric oxide by sol-gel method.

- Structural characterisation of sol-gel synthesised nano ferrites using X-ray diffractometry and Transmission electron microscopy.

- Preparation of rubber ferrite composites by incorporating precharacterised nano ferrites at different loading into ethylene propylene diene rubber and neoprene rubber.

- Evaluation of cure characteristics of the RFCs and determination of kinetics of the cure reaction.

- Evaluation of mechanical properties of the RFCs.

- Morphological studies of the RFCs using Scanning electron microscopy and Electron spin resonance spectroscopy (ESR).

- Evaluation of dielectric properties of ferrites and the RFCs in 0.1-8 mega hertz frequencies (MHz) and at different temperatures.

- Microwave absorption studies of the RFCs in X and S band frequencies.

- Determination of magnetic properties of ferrite nanoparticles and RFCs.

- Study on the effect of carbon black on processing, mechanical, dielectric, magnetic and microwave properties of the RFCs.

- Correlation of results.

References

1. Maurice Morton, Rubber Technology, 3rd Edition, Van Nostrand Reinhold, NewYork (1999).

2. M.N. Ismail and G.M. Turky, Poym. Plast. Technol. Eng., **40** (2001) 635.

3. Zhenghong Tao, Nantiya Viriyabanthorn, Bhavjtt Ghumman, Carol Barry and Joey Mead, Rubber Chem. Technol.,**78** (2005) 489.

4. G.H. Zohuri, M. Vakili, R. Jamjah, S. Ahmadjo and M. Nekomanesh, Rubber Chem. Technol., **78** (2005) 682.

5. M. Ehsani, H. Borsi, E. Gockenbach, J. Morshedian, G.R. Bakhshandeh, and A.A. Shayegani International Conference on Solid Dielectrics, Toulouse, France, (2004) 5-9.

6. Martin Van Duin and Herman G. Dikland, Rubber Chem. Technol., **76** (2003) 132.

7. Peter R. Dluzneski, Rubber Chem. Technol., **74** (2001) 451.

8. Kinsuk Naskar and JacquesW.M. Noordermeer, Rubber Chem. and technol., **77** (2004) 955.

9. M.S. Pinho, M. Dezzoti, M.M. Gorelova and B.G. Soares, J. Appl. Polym. Sci., **71** (1999) 2329.

10. Encyclopedia of Polymer Science and Engineering, Volume 3, Wiley Interscience Publications, New York, (1985)

11. Abi Santhosh Aprem, Kuruvilla Joseph and Sabu Thomas, Rubber Chem. Technol., **78** (2005) 458.

12. Yoshiaki Miyata and Masao Atsumi, Rubber Chem. Technol., **62** (1989) 1.

13. R.S. Rajeev and S.K. De, Rubber Chem. Technol., **75** (2002) 475.

14. Rolf E. Hummel, Electronic properties of materials, 2nd Edition, Narosa Publishing House, New Delhi (1985).

15. J. Smit, and H.P.J. Wijn, Ferrites, Philips Technical Library Netherlands (1959).

16. Charles Kittel, Introduction to Solid State Physics, 7th Edition, John Wiley & Sons, Inc., Singapore (1996).

17. B.D. Cullity, Introduction to Magnetic Materials, Addison-Wesley Publishing Company Inc., Philippines (1972).

18. A.R. West, Solid State Chemistry and Its Applications, John Wiley & Sons, Singapore (2003).

19. Kenneth J. Klabunde, Nanoscale Materials in Chemistry, Wiley Interscience, New York (2001).

20. C.N. Chinnasamy, A. Narayanasamy, N. Ponpandian, R. Justin Joseyphus, B. Jeyadevan, K.Tohji and K. Chattopadhyay, J. Magn. Magn. Mater., **238** (2002) 281.

21. E.C. Sousa, C.R. Alves, R. Aquino, M.H. Sousa, G.F. Goya, H.R. Rechenberg, F.A. Tourinho and J. Depeyrot, J. Magn. Magn. Mater., **289** (2005) 118.

22. M.H. Sousa, E. Hasmonay, J. Depeyrot, F.A. Tourinho, J.C. Bacri, E. Dubois, R. Perzynski and Yu.L. Raikher, J. Magn. Magn. Mater., **242-245** (2002) 572.

23. J.P. Bucher, D.C. Douglass and L.A. Bloomfield, Phys. Rev. Lett., **66** (1991), 3052.

24. E.E. Fullerton, J.S. Jiang, C.H. Sowers, J.E. Pearson and S.D. Bader, Appl. Phys. Lett., **72** (1998) 380.

25. S. Jung, B. Watkins, L. DeLong, J.B. Ketterson and V. Chandrasekhar, Phys.Rev. B, **66** (2002) 132401.

26. U. Ebels, J. L. Duvail, P. E. Wigen, L. Piraux, L.D. Buda and K. Ounadjela, Phys. Rev. B, **64** (2001) 14421.

27. John Q. Xiao, J. Samuel Jiang and C.L. Chien, Phys. Rev. B., **46** (1992) 9266.

28. D. Waller and A. Moser, IEEE Trans. Mag., **35** (1999) 4423.

29. R.D. Shull, IEEE Trans. Mag., **29** (1993) 2614.

30. Yoshiaki Kinemuchi, Kazuhiro Ishizaka, Hisayuki Suematsu, Weihua Jiang and Kiyoshi Yatsui, Thin Solid Films, **407** (2002) 109.

31. R.W. Siegel, S. Ramasamy, H. Hahn, L. Zongquan, L. Ting and R. Gronsky, J. Mater. Res., **3** (1988) 1367.

32. M.S. EI-Shall, W. Slack, W. Vann, D. Kane and D. Hanley, J. Phys. Chem., **98** (1994) 3067.

33. G.L. Messing, S.C. Zhang and G.V. Jayanthi, J. Am. Ceram. Soc., **76** (1993) 2707.

34. Takao Tani, Lutz Madler and Sotiris E. Pratsinis, Journal of Nanoparticle Research, 4 (2002) 337

35. T.T. Kodas, A. Datye, V. Lee and E. Engler, J. Appl. Phys., **65** (1989) 2149.

36. G.D. Ulrich and J.W. Riehl, Journal of Colloid Interface Sci. Technol., **87** (1982) 257.

37. G. Skanadan, Y.J. Chen, N. Glumac and B.H. Kear, Nanostruct. Mater., **11** (1999) 149.

38. V.R. Palkar, Nanostruct. Mater., **11** (1999) 369.

39. F. Hatakeyama and S. Kanzaki, J. Am. Ceram. Soc., **73** (1990) 2107.

40. L.M. Gan, L.H. Zhang, H..S.O. Chan, C.H. Chew and B.H. Loo, J. Mater.Sci., **31** (1996) 1.

41. J. Wang, S.E. Lee, S.C.Ng and L.M. Gan, Mater. Lett., **30** (1997), 119.

42. Qi Chen, Adam J. Rondinone, Bryan C. Chakoumakos and Z. John Zhang, J. Magn. Magn. Mater., **194** (1999) 1.

43. T. M. Whitney, J.S. Jiang, P. C. Searson and C.L. Chien, Science, **261** (1993) 1316.

44. S.Y. Chou, Proc. IEEE, **85** (1997) 652.

45. B. Martorana, G. Carotenuto, D. Pullini, K. Zvezdin, G. La Peruta, P. Perlo and L.Nicolais, Sensors and Actuators A, **129** (2006) 176.

46. P. Martin and A. Hernando, J. Magn. Magn. Mater., **215-216** (2000) 729.

47. Liliana Borcea and Oscar Bruno, Journal of the Mechanics and Physics of Solids, **49** (2001) 2877.

48. Stanislaw Bednarek, Materials Science and Engineering, **B55** (1998) 201.

49. K. Raj, R. Moskowitz and R. Casciari, J. Magn. Magn. Mater., **149** (1995), 174.

50. R.D. McMichael, R.D. Shull, L.J. Swartzendruber and L.H. Bennett, J. Magn. Magn. Mater., **111** (1992) 29.

51. D.G. Mitchell, J. Magn. Reson. Imaging, **7** (1997) 1.

52. C.N.R. Rao, A. Muller and A.K. Cheetham, The Chemistry of Nanomaterials Synthesis, Properties and Applications, Volume-1, WILEY-VCH Verlag GmbH & Co. KgaA, Weinheim (2004).

53. V.S. Abraham, S. Swapna Nair, S. Rajesh, U.S. Sajeev and M.R. Anantharaman, Bull. Mater. Sci., **27** (2004) 155.

54. Q.A. Pankhurst, J. Conolly, S.K. Jones and J. Dobson, J. Phys. D: Appl. Phys., **36** (2003) R167.

55. I. Hilger, R. Hergt and W.A. Kaiser, J. Magn. Magn. Mater. **293** (2005) 314.

56. Rudolf Hergt, Silvio Dutz, Robert Muller and Matthias Zeisberger, J. Phys: Condens. Matter, **18** (2006) S2919.

57. Senoy Thomas, D. Sakthikumar, P.A. Joy, Yasuhiko Yoshida and M.R.Anantharaman, Nanotechnology, **17** (2006) 5565.

58. H. Srikanth, R. Hajndl, C. Chirinos, J. Sanders, A. Sampath and T.S. Sudharshan, Applied Physics Letters, **79** (2001) 3503.

59. Cecilia Savii, Mihaela Popovici, Corina Enache, J. Subrt, D. Niznansky, Snejana Bakarzieva, C. Caizer and I. Hrianca, Solid State Ionics, **151** (2002) 219.

60. C. Baker, S. Ismat Shah and S.K. Hasanain, J. Magn. Magn. Mater., **280** (2004) 412.

61. Juan Carlos Aphesteguy and Silvia E. Jacobo, Physica B, **354** (2004) 224.

62. D.E. El-Nashar, S.H. Mansour and E. Girgis, J. Mater. Sci., **41** (2006) 5359.

63. N.E. Kazantseva, Yu.I. Bespyatykh, I. Sapurina, J. Stejskal, J. Vilcakova and P. Saha, J. Magn. Magn. Mater., **301** (2006) 155.

64. V. Provenzano and R.L. Holtz, J. Material Science and Engineering, **A204** (1995) 125.

65. Maurice Gell, J. Material Science and Engineering, **A204** (1995) 246.

66. N. Ponpandian, P. Balaya and A. Narayanasamy, J. Phys: Condens. Matter, **14** (2002) 3221.

67. J.D. Dunitz and L.E. Orgel, J. Phys. Chem. Solids, **3** (1957) 318.

68. D.S. McClure, J. Phys. Chem. Solids., **3** (1957) 311.

69. G. Blasse, Philips Res: arch Repl. Supplement, **3** (1964) 13.

70. Raul Valenzuela, Magnetic Ceramics, Cambridge University Press, Cambridge (1994).

71. M.A. Ahmed and M.A. El Hiti, J. Phys. 111 France, **5** (1995) 775.

72. A.M. Shaikh, S.S. Bellad and B. K. Chougule, J. Magn. Magn. Mater., **195** (1999) 384.

73. S.J. Ahns, C.S. Yoon, S.G. Yoon, C.K. Kim, T.Y. Byun and K.S. Hong, Materials Science Engineering, **B84** (2001) 146.

74. G. Ranga Mohan, D. Ravinder, A.V. Ramana Reddy and B.S. Boyanov, Materials Letters, **40** (1999) 39.

75. A.C.F.M. Costa, E. Tortella, M.R. Morelli, M. Kaufman and R.H.G.A. Kiminami, J. Mater. Sci., **37** (2002) 3569.

76. A.S. Albuquerque, J.D. Ardisson, W.A.A. Macedo, J. L. Lopez, R. Paniago and A.I.C Persiano, J. Magn. Magn. Mater., **226-230** (2001) 1379.

77. Anjali verma and Ratnamala Chatterjee, J. Magn. Magn. Mater., **306** (2006) 313.

78. R.M. More, T.J. Shinde, N.D. Choudhari and P.N. Vasembekar, J. Mater. Sci., **16** (2005) 721.

79. C. Caizer and M. Stefanescu, J.Phys. D: Appl. Phys., **35** (2002) 3035.

80. Jae-Gwang Lee, Hi Min Lee, Chul Sung Kim and Young-Jei Oh, J. Magn. Magn. Mater., **177-181** (1998) 900.

81. Mathew George, Asha Mary John, Swapna S. Nair, P.A. Joy and M.R. Anantharaman, J. Magn. Magn. Mater., **302** (2006) 190.

82. Souilah Zahi, Mansor Hashim and A.R. Daud, Materals Letters, **60** (2006) 2803.

83. M.H. Mahmoud, H.H. Hamdeh, J.C. Ho, M.J. O'Shea and J.C. Walker, J. Magn. Magn. Mater. **220** (2000) 139.

84. T. Nakamura and E. Hankui, J. Magn. Magn. Mater., **257** (2003) 158.

85. S.A. Ghodake, U.R. Ghodake, S.R. Sawant, S.S. Suryavanshi and P.P. Bakare, J. Magn. Magn. Mater., **305** (2006) 110.

86. Miha Drofenik, Matjaz Kristl, Andrey Znidarsic, Darko Hanzel and Darja Lisjak, J. Am. Ceram. Soci., **90** (2007) 2057.

87. K.B. Paul, Physica B Condensed Matter, **388** (2007) 337.

88. Mukesh C. Dimri, Subhash C. Kashyap and D.C. Dube, Ceramic International, **30** (2004) 1623.

89. Wei Zhang, Weiping Ding, Yumei Jiang, Liang Wang, Ning Zhang, Shiyuan Zhang, You Wei Du and Qijie Yan, J. Appl. Phy., **85** (1999) 5552.

90. Hong-Mei Xiao, Xian-Ming Liu and Shao-Yun Fu, Composites Science and Technology, **66** (2006) 2008.

91. A. Verma, R.G. Mendiratta, T.C. Goel and D.C. Dube, Journal of Electroceramics, **8** (2002) 203.

92. Xiangcheng Li, Rongzhou Gong, Zekun Feng, Junbing Yan, Xiang Shen and Huahui He, J. Am. Ceram. Soc., **89** (2006) 1450.

93. R.H. Kodama, A.E. Berkowitz, E.J. McNiff Jr. and S. Foner, Phys. Rev. Lett., **77** (1996) 394.

94. S. Gubbala, H. Nathani, K. Koizol and R.D.K. Misra, Physica B, **348** (2004) 317.

95. Guoxi Xi, Li Yang and Maixi Lu, Mater. Lett., **60** (2006) 3582.

96. Ramesh Peelamedu, Craig Grimes, Dinesh Agrawal, Rustum Roy and Purushotham Yadoji, J. Mater. Res., **18** (2003) 2292.

97. B. Skolyszewska, W. Tokarz, K. Przybylski, Z. Kakol, Physica C **387** (2003) 290.

98. Courtney Marrett, Alexander Moulart and Jonathan Colton, Polymer Engineering and Science, **43** (2003) 822.

99. M.R. Anantharaman, S. Jagathesan, S. Sindhu, K.A. Malini, C.N Chinnasamy, A. Narayanasamy, P. Kurian and K.Vasudevan, Plast. Rubber Comps. Process Appl., **27** (1998) 77.

100. K.A. Malini, P. Kurian and M.R. Anantharaman, Materials Letters, **57** (2003) 3381.

101. J. Matutes-Aquino, D. Rios-Jara, O. Ayala-Valenzuela, P. Sifuwentes Gallardo, L.F. Ramos De Valle, and O.S. Rodriguez Fernandez, Polym. Comps., **21** (2000) 734.

102. J. Ormerod and S. Constantinides, J. Appl. Phys., **81** (1997) 4816.

103. J. Xiao and J.U. Otaigbe, Polym. Comps., **21** (2000) 332.

104. S. Sindhu, M.R. Anantharaman, Bindu P Thampi, K.A. Malini and Philip Kurian, Bull. Mater. Sic., **25** (2002) 599.

105. E.M. Mohammed, K.A. Malini, P.A. Joy, S.D. Kulkarni, S.K. Date, P. Kurian and M.R. Anantharaman, Plastics, Rubber and Composites, **31** (2002) 106.

106. Mathew George, Ph.D Thesis, Dept. of Physics, Cochin University of Science and Technology, Cochin, India, (2004).

107. M.A. Soloman, Philip Kurian and M.R. Anantharaman, Progress in Rubber, Plastics and Recycling Technology, 18 (2002) 269.

108. S. Hamdan, D.M.A. Hashim and M. Yusop, AJSTD, **21** (2004) 69.

109. D.R. Saini, V.M. Nadkarini, P.D. Grover and K.D.P. Nigam, J. Mater. Sci., **21** (1986) 3710.

110. J.B. Donnet, Rubber Chem. Technol., **71** (1998) 323.

111. A. Blanchard, Rubber Journal, **153** (1971) 44.

112. N. Dishovsky, K. Ruskova and I. Radulov, Materials Research Bulletin, **36** (2001) 35.

113. R. Skomski and J.M.D. Coey, Phys. Rev. B, **48** (1993) 15812.

114. H. Fukunaga, J. Kuma and Y. Kanai, IEEE Trans. Magn., **35** (1999) 3235.

115. S.M. Abbas, A. K.Dixit, R. Chatterjee and T.C. Goel, J. Magn. Magn. Mater., **309** (2006) 20.

116. FENG Yongbao, QIU Tai, SHEN Chunying and LI Xiaoyun, IEEE APMC 2005 Proceedings.

117. P. Annadurai, A. K. Mallic and D.K. Tripathy, Journal of Applied Polymer Science, **83** (2002) 145.

118. Gerard Kraus. Rubber Chem. and Technol., **51** (1978) 297.

119. Zhuangjun Fan, Guohua Luo, Zengfu Zhang, Li Zhou and Fei Wei, Materials Science and Engineering B, **132** (2006) 85.

120. Anna A. Barba, Gaetano Lamberti, Matteo d'Amore and Domenico Acierno, Polymer Bulletin, **57** (2006) 587.

121. M.A. Soloman, Philip Kurian, M.R. Anantharaman and P.A. Joy, Journal of Applied Polymer Science, **89** (2003) 769.

Chapter 2

Experimental Techniques

Successful investigations in material science demand synthesis of phase pure materials. A detailed characterisation at various stages is highly essential to ensure that the materials prepared are pure. Evaluation of structural parameters, determination of cure characteristics and computing the magnetic properties are also highly essential. The chapter on experimental techniques will be incomplete without the detailed description of preparative methods adopted for the synthesis of materials. A description of the various analytical techniques employed for characterisation at various stages is also very essential for continuity and comprehension.

2.1 Experimental Methods

Various methods generally employed for the synthesis of ferrites are the conventional ceramic method [1-4] high energy ball milling [5,6], co-precipitation [7,8], reverse micelle technique [9-11], hydrothermal synthesis [12,13] and synthesis from organo-metallic precursors [14,15]. Each method has its own advantages and disadvantages. Sol-gel method is an important one that can be adopted for the synthesis of nano materials. This method guarantees the formation of pure crystalline phases if the preparative conditions are adequately controlled. Hence, this method of synthesis has been placed on a high pedestal by material scientists. Sol-gel method was adopted here for the synthesis of ferrite nanoparticles [16,17].

2.1.1 Sol-gel method for the preparation of ferrite fillers

Ultrafine particles of nickel ferrite were prepared by the sol-gel method using analytical grade nickel nitrate [$Ni(NO_3)_2.7H_2O$] and ferric nitrate [$Fe(NO_3)_3.9H_2O$]. Ferric nitrate and nickel nitrate were dissolved in pure ethylene glycol at $40^{\circ}C$ and were mixed in the molar ratio 2:1. This solution was then heated to $60^{\circ}C$ and the

temperature was kept constant till a wet gel of the metal nitrates was obtained. The gel was then dried at 100°C, it self-ignited to produce a fluffy and voluminous product. The chemical reaction leading to the formation of nickel ferrite is as follows.

$$Ni(NO_3)_2.7H_2O + 2Fe(NO_3)_3.9H_2O \rightarrow NiFe_2O_4 + \text{volatilities}$$
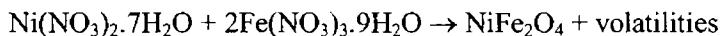
The fluffy products were ground to a fine powder using a mortar and a pestle, and homogenised using a high energy ball mill (HEBM). Fritsch Pulverisette 7 planetory micro mill with tungsten carbide balls and bowls was employed for the ball milling. Milling was carried out after wetting the powder with acetone, at 300 rotations per minute (rpm) speed and for 20 minutes. The ball to powder ratio was maintained at 1:10 to impart a high momentum to these fine particles. Final homogenisation and removal of any traces of volatile impurities or solvents were carried out by heating the sample at 200°C for 2 hours.

A similar method was employed for the preparation of gamma ferric oxide by dissolving analytical grade ferric nitrate in ethylene glycol. The solution was heated to 60°C and kept at this temperature till a wet gel was obtained. The obtained gel was then heated to 100°C, when it self-ignited and resulted in fluffy gamma ferric oxide. Final homogenisation was carried out by wet milling the powdered samples for 10 minutes at 300 rpm speed in HEBM.

2.1.2 Preparation of rubber ferrite composites

Incorporation of ferrites into ethylene propylene diene rubber and neoprene rubber was carried out by choosing an appropriate recipe and the mixing was carried out in a Brabender Plasticorder. It is a torque rheometer which is widely used for mixing, blending and to study processability of polymers such as mixing and extrusion and evaluation of the rheological properties of the polymer melts [18-21]. It is used to measure the torque generated due to the resistance offered by the material to mastication or flow under preselected conditions of shear and temperature. The heart of the torque rheometer is a jacketed mixing chamber with horizontal rotors connected to a shaft. The volume of the chamber is approximately 40 cm^3 for the model used (PL 3S). The resistance due to the mixing of the test material within the mixing chamber is measured with the help of dynamometer balance. A dc thyrister controlled drive is used to control the speed of rotation of the rotors. The temperature of the mixing

chamber can be varied up to 300°C which can be controlled and measured with the aid of a temperature controller and a recorder. Different types of rotors can be employed depending upon the nature of polymer used. After selecting the temperature and rotor speed, the rubber was charged into mixing chamber. When the nerve of the rubber had disappeared, compounding ingredients were added as per the sequence given in ASTM D 3182 (1982). Mixing was carried out at 60°C and at 50 rpm speed. Homogenisation of the compound was carried out using a laboratory (15× 33 cm) two roll mill at a friction ratio 1: 1.25. The temperature of the roll was maintained at 60°C and the compound was homogenised by passing the compound six times through the tight nip and finally made into a sheet at a nip gap of 3 mm.

2.1.3 Determination of cure characteristics

Cure characteristics of the mixed compounds were determined using a rubber process analyser (RPA). It is an advanced dynamical mechanical and rheological test instrument designed to measure the properties of polymers and rubber compounds. This can be employed to investigate the physicomechanical properties of polymers before, after or during the process of curing. RPA measures the viscoelastic properties of rubber compounds providing comprehensive data on key parameters such as processability and cure characteristics. It is a microprocessor controlled rotorless cure meter with a quick temperature control mechanism and well defined homogeneous temperature distribution in the test chamber. It uses two directly heated low mass biconical dies. The required starting temperature for the test is set and controlled by heating and /or forced air cooling. The temperature can be varied during the test or maintained at a constant value within ± 0.5°C.

The RPA is equipped with a direct drive servo motor system that can vary the oscillation angle and frequency. A circular shaped test specimen is kept in the lower half of the cavity, which is oscillated through a small deformation angle. The frequency of oscillation is maintained at 50 cycles/min. The torque is transmitted through the sample from the oscillating lower die to a highly sensitive torque transducer positioned in the upper die. The measurements made by the torque transducer are fed into the system computer. The selected sample properties are calculated and the results are displayed and the data is available for further analysis.

In the present study, cure characteristics of the RFCs were determined using a rubber process analyser (RPA 2000 of Alpha technology), at a temperature of $160^\circ C$ by measuring modulus and torque against time at a pre-programmed strain. Different cure parameters were obtained from the RPA results. They are:

- Minimum torque

  Torque obtained by the mix after homogenising at the test temperature and before the onset of cure.

- Maximum torque

  Maximum torque recorded at the completion of cure.

- Optimum cure time (t_{90})

  This is the time taken for obtaining 90% of the maximum torque

- Scorch time (t_{10})

  It is the time taken for two unit rise above minimum torque (that is about 10% vulcanisation)

- Cure rate index

  Cure rate index is calculated using the equation

  Cure rate index = $100 / (t_{90} - t_{10})$

2.1.4 Moulding

The test specimens for determining the physical properties were prepared in standard moulds by compression moulding on an electrically heated press having 45 × 45 cm platens at a pressure of 140 Kg cm^{-2} to the respective cure times. After completing the cure, pressure was released and the sheet was stripped out from the mould and cooled by immersing in cold water. Samples were matured for 24 hours prior to testing.

2.2 Structural characterisations

It is essential that the right characterisation techniques have to be employed for the evaluation of physicomechanical properties of the composites. Some of the analytical methods employed for the characterisation are,

- X-ray diffraction technique (XRD)
- Transmission electron microscopy (TEM)
- Inductively coupled plasma-atomic electron spectrometry (ICP)
- Brunauer-Emmet-Teller (BET) nitrogen adsorption.

2.2.1 X-ray diffraction technique

Powder X-ray diffraction pattern provides the finger print of a crystalline material as it gives information on the structure, phase and purity of a material.

The X-ray diffractograms of the powder samples were recorded on X-ray diffractometer, Rigaku D-Max using Cu K_α ($\lambda = 1.5418$ A°). From the recorded diffractograms, parameters like relative intensity (I/I_0) and inter atomic spacing 'd' were obtained. Interplanar spacings were evaluated using the Bragg's equation [22]

$$n\lambda = 2dSin\theta \qquad 2.1$$

where λ is the wavelength of the X-radiation, n is an integer and θ is known as diffraction angle. The lattice parameter was then computed by assuming cubic symmetry and combining equations $2dSin\theta = n\lambda$ and

$$d_{hkl} = \frac{1}{\sqrt{\dfrac{h^2}{a^2} + \dfrac{k^2}{b^2} + \dfrac{l^2}{c^2}}} \quad \text{when a = b = c}$$

$$d_{hkl} = \frac{a}{\sqrt{h^2 + k^2 + l^2}} \qquad 2.2$$

Width of a diffraction peak increases when the crystallite size is reduced below a certain limit. The broadening of the lines can be used to estimate the average size of the particles. The average particle size was determined from the measured width of the diffraction peak, using Debye-Sherrer formula [23,24]

$$t = \frac{0.9\lambda}{\beta \cos\theta} \qquad 2.3$$

where 't' is the thickness of the crystallite (particle size), λ is the wavelength of the X-radiation, β is the angular width (in radians) which is equal to the full width at half maximum.

The X-ray density of the prepared ceramic samples was then calculated using the relation

$$\rho_x = \frac{nM}{a^3 N} \qquad\qquad 2.4$$

where n is the number of molecules /unit cell, M is the molecular weight, 'a' is the lattice parameter and N is the Avogadro number.

The apparent density (ρ_a) was calculated by making cylindrical pellets, using the relation

$$\rho_a = \frac{m}{V} = \frac{m}{\pi r^2 h} \qquad\qquad 2.5$$

where m, r and h are the mass, radius and thickness of the pellet respectively.

From the calculated values of the apparent density and X-ray density (ρ_x), porosity P was calculated by using the relation

$$P = \frac{\rho_x - \rho_a}{\rho_x} \qquad\qquad 2.6$$

The surface area was calculated from these data using the relation [25]

$$S = \frac{6000}{D\rho} \qquad\qquad 2.7$$

where 'D' is the diameter of the particle in nm 'ρ' is the density of the particle in g/cc.

2.2.2 Transmission electron microscopy

Transmission electron microscopy provides detailed structural information at levels down to atomic dimensions. It is an imaging technique analogous to light microscopes, where an electron beam illuminates the specimen. This is one of the useful technique for determining the size, shape and size distribution of the particles. Here a thin specimen is irradiated with an electron beam of uniform current density. Electrons emitted from an electron gun illuminate the specimen through a two or three stage condenser lens system. The electron intensity distribution behind the specimen is magnified with a three or four stage lens system and viewed on a fluorescent screen. The image can be recorded by direct exposure to a photographic film [26,27]. Various imaging modes exist, ranging from conventional bright-field and dark field to high resolution images.

Selected area electron diffraction (SAED) is another technique, which is highly useful for the determination of the lattice planes, and the detection of atomic scale defects in areas of few square nanometers. The 'd' spacing between lattice planes of crystalline materials can be calculated using the relationship

$$dr = \lambda L \qquad\qquad 2.8$$

where L is the distance between the specimen and the photographic plate, λL is known as the camera constant and r is the radius of the diffracted rings. 'r' can be measured directly from the diffraction in the photographic plate. λL can be determined from the instrument by calibrating it with a standard material. Hence from equation 2.8, 'd' can be calculated. Since each d value corresponds to a specific lattice plane for a specific crystal structure, a minimum description of the crystal structure of a crystalline specimen can be obtained from the diffraction pattern [28,29]. Lattice planes could also be identified using a high resolution transmission electron microscope image (HRTEM) [30].

The synthesised ferrite particles were analysed for their grain size and grain size distribution using Transmission electron microscope model Joel JEM 2200 FS applying an accelerating voltage of 200 kV.

2.2.3 Inductively coupled plasma-atomic electron spectrometry

Elemental analysis of the samples was carried out with the help of Inductively coupled plasma-atomic electron spectroscopy. Thermo Electron Corporation, IRIS INTREPID II XSP model was used for ICP measurement. This is a very powerful tool for elemental analysis upto the parts per million (ppm) level. In this method, a plasma or gas consisting of ions, electrons and neutral particles are formed from an Argon gas. The plasma is used to atomise and ionise the elements in a sample. The resulting ions are then passed through a series of apertures (cones) into the high vacuum mass analyser. The elements are identified by their mass-to-charge ratio (m/e) and the intensity of a specific peak in the mass spectrum is proportional to the amount of that element in the original sample.

2.2.4. Surface area determination by BET method

Specific surface area of the powder samples was estimated by Brunauer-Emmet-Teller method using TriStar 3000 V6.03A surface area analyser. N_2 gas was

used as the adsorbate at the liquid nitrogen temperature. BET method is generally used for analysing the surface area of the catalysts. The BET equation can be represented as

$$\frac{P}{V(P_0 - P)} = \frac{1}{V_m C} + \left[\frac{(C-1)}{V_m C}\right]\left(\frac{P}{P_0}\right) \qquad 2.9$$

where C is a constant for a given system and is dependant on adsorbent-adsorbate interaction.

P is the adsorption equilibrium pressure, P_0 is the saturation vapour pressure of the adsorbate, V is the volume of adsorbate required for monolayer adsorption.

A plot of $\frac{P}{V(P_0 - P)}$ against $\left(\frac{P}{P_0}\right)$ gives a straight line with slope $\left[\frac{(C-1)}{V_m C}\right]$ and

intercept $\frac{1}{V_m C}$. From these two, surface area can be obtained by applying the value of V_m in the equation,

$$\text{surface area} = V_m N_A A_m / 22414$$

where N_A is Avogadro number and A_m is cross-sectional area of the adsorbate molecule in A^0 and 22414 is the volume in cm^3, corresponding to Avogadro number of particles.

Prior to measurements, samples were activated for two hours at the appropriate temperature and then degassed at 200°C under nitrogen flow. The degassed samples were subjected to N_2 adsorption at 77 K using liquid nitrogen.

2.2.5 Fourier Transform infrared spectroscopy

Fourier transform infrared spectra (FTIR) are generated by the absorption of electromagnetic radiation in the frequency range 400 to 4000 cm^{-1} by organic molecules. Different functional groups and structural features in the molecules absorb energy at characteristic frequencies. The frequency and intensity of absorption are the indication of the bond strength and structural geometry in the molecule.

Infrared spectroscopic analysis was used for the characterisation of the gel prepared for the synthesis of ferrites using sol-gel method. FTIR spectra of the samples were taken using the spectrometer model Bruker Tensor 27.

2.2.6 Scanning electron microscopy

Scanning electron microscopy is a very useful tool to gather information about topography, morphology, composition and micro structural information of materials. The image is formed by scanning a probe of focused electron beam across the specimen. The electron beam interacts with a thin surface layer of the specimen resulting in back scattering of electrons of high energy, generation of secondary electrons of low energy and X-rays. These signals are monitored by detectors (photo multiplier tubes) and magnified. An image of the investigated microscopic region of the specimen is thus observed in cathode ray tube and photographed using photographic film. Due to the manner in which the image is created, SEM image have a characteristic three dimensional appearance and are useful in judging the surface structure of the sample [31].

In the present study, morphological characterisation of the fractured surfaces of the tensile test specimens was carried out using Scanning electron microscope (Cambridge Instruments S 360 stereo scanner version VO2-01, England). The specimens were mounted on a metallic stab and the sample was placed in an E-101 ion sputtering unit for gold coating, which make the sample conducting. The gold coated sample was then subjected to take SEM image.

2.2.7 Electron spin resonance spectroscopy

Electron spin resonance spectroscopy also called electron paramagnetic resonance (EPR) spectroscopy is used to investigate the nature of bonding within molecules by identifying unpaired electrons and their interaction with immediate surroundings. In the case of filled elastomers, ESR spectroscopy throws light into many of the structural informations. It is a useful method to understand the filler distribution and dispersion within the matrix.

An electron has a magnetic moment when placed in an external magnetic field of strength B_0, this magnetic moment can align itself parallel or antiparallel to the external field (Zeeman effect). The former is of lower energy state than the latter and the difference in energy is given by $\Delta E = g_e \mu_B B_0 = h\gamma$. Where g_e is Lande g-factor and μ_B is the Bohr magneton. Application of an oscillating field

perpendicular to the direction of B_0 induces transitions between the two sub-energy levels. The value of g_e depends on the electron environment of the unpaired electron. The value of g_e for a free electron is 2.0023.

The ESR spectrum of the ferrites and filled elastomers were recorded on a Varian E-like century series (E-112), which consists of an electromagnet with power supplies to generate and modulate a uniform magnetic field of several thousand Gauss, as well as the components that generate and detect microwave power. A hall probe, driven from a stable constant-current power system, with a digital multimeter, reading the hall voltage, is used to measure the value of the magnetic field between the poles of the magnet.

The microwave system consists of a microwave power supply that uses klystron. The output of the power supply is connected via rectangular wave guides (9.12 GHz) and through a circulator to a high-Q resonant cavity. The samples to be investigated are mounted in the middle of the cavity, where magnetic component of the microwave power is maximum and is oriented perpendicular to the static field. A microwave diode, which detects the microwave power, resides inside the same box as the power supply. The higher the quality of the resonant cavity, the greater the microwave field that can be obtained on the sample.

Tetra cyano ethylene (TCNE) free radical is used as the standard for the accurate determination of g value.

2.3 Mechanical properties

Mechanical properties such as stress-strain properties, tear strength, hardness, resilience, abrasion resistance and sorption kinetics of the rubber ferrite composites were measured using standard test methods' [25,32-34] and according to ASTM standards.

2.3.1 Stress-strain properties

Tensile strength, modulus and elongation at break are some of the most important indications of the strength of a composite material. The stress-strain properties such as tensile strength, modulus and elongation at break were determined using a Shimadzu, Universal testing machine (UTM model SPL 10

kN). It has a fixed or a stationary part carrying one grip and a movable part carrying a second grip. Stress-strain measurements were carried out as per ASTM D 412-98a (2002). Tests were carried out at 23 ± 1°C of temperature and 65 ± 5% relative humidity. Dumbbell shaped test specimens were punched out from the compression moulded sheets along the mill grain direction using a standard die (Type D). The sample is held between the two grips on the UTM and a uniform rate of grip separation of 500 ± 50 mm/min. was applied. The tensile strength, elongation at break and modulus at different elongations were recorded and evaluated after each measurement by the microprocessor.

2.3.2 Tear strength

The tear of a rubber is a mechanical rupture process initiated and propagated at a site of high stress concentration caused by a cut, defect or localised deformation. In a tear test, the force is not applied evenly, but concentrated onto a deliberate flaw or sharp discontinuity and the force to continuously create a new surface is measured.

Tear strength of the samples were measured as per ASTM D 624-2000 using standard test specimens with 90° angle on one side and tab ends (type-C die), which were punched out from the moulded sheets along the mill grain direction. The test was carried out using a Universal testing machine (model SPL 10 kN) at a crosshead speed of 500 mm per minute.

2.3.3 Hardness

Hardness can generally be defined as the resistance of a material to deformation which gives a measure of elastic modulus at low strain of the sample and can be measured by determining its resistance to indentation by a rigid indenter.

Durometer hardness tester is used for measuring the relative hardness of soft materials. It consists of a pressure foot, an indenter and a dial gauge. The indenter is spring loaded and the point of the indenter protrudes through the opening in the base. Several instruments are used to measure the hardness of materials ranging from soft sponge to ebonite type materials. The most commonly used are durometer Type A and Type D. The basic difference between these two is the shape and dimension of the

indenter. The hardness numbers derived from either scale are just numbers without any units ranging from 0 to 100. Type A Durometer is used for measuring the hardness of relatively soft materials and Type D Durometer is used for measuring the hardness of harder materials. The hardness measured using Type A Durometer is expressed in Shore A unit.

The hardness of the moulded samples was tested by using Zwick 3114 hardness tester in accordance with ASTM D 2240-03. The tests were carried out on a mechanically unstressed sample of 12 mm diameter and minimum 6 mm thickness. The test is conducted by first placing the specimen on a hard, flat surface and the pressure foot of the instrument is pressed onto the specimen. A load of 12.5 N was applied after ensuring firm contact with the specimen; the readings were taken after 10 seconds of indentation.

2.3.4 Rebound resilience

Rebound resilience is a dynamic test in which the test piece is subjected to one half cycle of deformation only. The strain is applied by impacting the test piece with an indenter which is free to rebound after the impact. Rebound resilience is defined as the ratio of the energy of the indenter after impact to its energy before impact expressed as percentage.

Resilience of the samples was measured according to the ASTM D 2632-2001 with vertical rebound resiliometer. Using this method, resilience was determined, which is the ratio of rebound height to drop height of a metal plunger of prescribed mass and shape that is allowed to fall on the rubber specimen. The rubber samples used were of cylindrical shapes of 16 mm diameter and 6 mm thickness. The resilience measurement includes means for suspending a plunger at a given height above the specimen, its release, and measuring the subsequent rebound height. The top of the plunger should be in line with 100 on the scale when the plunger is locked in the elevated position so that the rebound height is equal to the resilience in percentage.

2.3.5 Abrasion resistance

The abrasion resistance of the samples was determined using a DIN abrader (DIN 53516). The abrasion resistance was measured by moving a test piece across the surface of an abrasive sheet mounted to a revolving drum, and is expressed as volume loss. Cylindrical samples of 15 mm diameter and 20 mm length was kept on a rotating sample holder and 10 N load was applied. Initially a pre run was given for the sample and its weight taken. The weight after the final run was also noted. The difference in weight is the weight loss on abrasion. It was expressed as the volume loss of the test piece when it is abraded by traveling through 42 m on a standard abrasive surface. The volume loss on abrasion was calculated as follows:

$$V = \Delta M / \rho \qquad\qquad 2.10$$

where V = volume loss in mm^3, ΔM = mass loss in g and ρ = density of the sample in g/ mm^3.

Abrasion resistance is the reciprocal of volume loss on abrasion.

2.3.6 Crosslink density and swelling studies

The crosslink density (CLD) of vulcanised samples was determined by the equilibrium swelling method and using Florey-Rehner equation [25]. Approximately 0.3 g samples were accurately weighed and kept in toluene solvent taken in an airtight container for 24 hrs. The surface of the swollen samples was then gently wiped using filter paper and weighed. The samples were placed again in the solvent and weights were recorded at regular intervals, usually one hour, till equilibrium weight was obtained. The swollen samples were heated at 60°C for 24 hours in an oven to remove the solvent. The deswollen weight was then determined. The volume fraction of rubber in the deswollen network was then calculated using the equation [35,36]

$$V_r = \frac{(D-FT)\rho_r^{-1}}{(D-FT)\rho_r^{-1} + A_0\rho_s^{-1}} \qquad\qquad 2.11$$

where T = weight of test specimen, D = de swollen weight, F = weight fraction of the insoluble component, A_0 = weight of the absorbed solvent corrected for the swelling increment, ρ_r = density of the test specimen, ρ_s = density of the solvent.

In order to analyse the interaction between the components of the system, equilibrium swelling studies were carried out in toluene. Circular samples of diameter 20 mm were punched from the vulcanised sheet and were allowed to swell in toluene at room temperature. At different intervals, the amount of solvent entering the sample was assessed gravimetrically until equilibrium was reached, as evidenced by the constant weight of the sample. The mole% uptake of solvent was calculated using the equation; [37]

$$Q_t = \frac{\left(\dfrac{M_{c(m)}}{M_{r(m)}}\right) \times 100}{M_{i(s)}} \qquad 2.12$$

where $M_{c(m)}$ is the mass of solvent at a given time, $M_{r(m)}$ is the molecular weight of the solvent and $M_{i(s)}$ is the initial weight of the specimen. At equilibrium swelling, Q_t was taken as Q_∞, the mole% uptake at infinite time. Sorption curves were obtained by plotting mole% uptake against square root of time. The effective diffusivity, D of the elastomer-solvent system was calculated from the initial portion of the sorption curves using the equation:

$$D = \pi \left(\frac{h\theta}{4Q_\infty}\right)^2 \qquad 2.13$$

where θ is the slope of the initial portion of the sorption curve.

Another parameter called sorption coefficient was calculated from the equilibrium swelling using the relation,

$$S = \frac{M_\infty}{M_0} \qquad 2.14$$

where M_∞ is the mass of the penetrant sorbed at infinite time and M_0 is the initial weight of the polymer sample. Sorption coefficient describes both initial penetration and dispersal of penetrant molecules into elastomer network.

The permeation coefficient which is a characteristic parameter reflecting the collective processes of diffusion and sorption was calculated using the equation [38].

$$P = DS \qquad 2.15$$

2.3.7 Thermogravimetric analysis

Thermogravimetric analysis was carried out using TGA Q50 instrument at a heating rate of 5°C/minute. Thermograms were recorded from room temperature to 800°C. The onset of degradation, the temperature at which maximum weight loss is observed and the residual weight in percentage were evaluated.

2.4 Dielectric measurements

Evaluation of dielectric properties is important in any material science related study. Incorporation of fillers in polymer matrices modifies the dielectric properties to a great extent. Parameters like dielectric permittivity, loss and ac conductivity can be evaluated by employing Inductance, capacitance and resistance (LCR) meter.

2.4.1 Dielectric constant

The ability of an insulator to resist the passage of alternating current or serve as a capacitor is determined by the permittivity (dielectric constant) and the dissipation factor. These properties are measured using low voltage so that bound charges are displaced but not ruptured. Dielectric permittivity is a measure of the energy stored in a material subjected to electrical stress. It is defined as the ratio of the field strength in vacuum to that in the material for the same distribution of charges. A number of parameters like temperature, grain size and orientation, molecular structure of the material and frequency of the applied field affect the dielectric permittivity of the materials.

An electrical conductor charged with a quantity of electricity q at a potential V is said to have a capacitance C = q/V. The capacitance of a sample parallel plate capacitor is given by

$$C = \frac{\varepsilon A}{d} \qquad\qquad 2.16$$

where A is the area of the parallel plates, d is the separation between the plates and ε is the absolute permittivity.

When a parallel plate capacitor with a dielectric in between is charged, the capacitance is given by

$$C = \frac{\varepsilon_0 \varepsilon_r A}{d} \qquad\qquad 2.17$$

where A is the area of the parallel plates, d is the separation between the plates and ε_0 is the permittivity of free space and ε_r is the dielectric permittivity of the material between the plates.

The dielectric properties of the ceramic samples and the RFCs were studied using a dielectric cell and an impedance analyser (Model: HP 4285A) in the frequency range 0.1-8 MHz. A schematic diagram of the dielectric cell is shown in figure 2.1.

1. BNC	9. Copper Electrodes
2. Neoprine O Ring	9. Sample
3. MS Chamber	10. Fixing Screws
4. SS Pipe	11. MS Flange
5. Sample Holder	12. To Vacuum pump
6. Liq. Nitrogen Cavity	13. Thermo couple
7. Optical Window	14. Spring
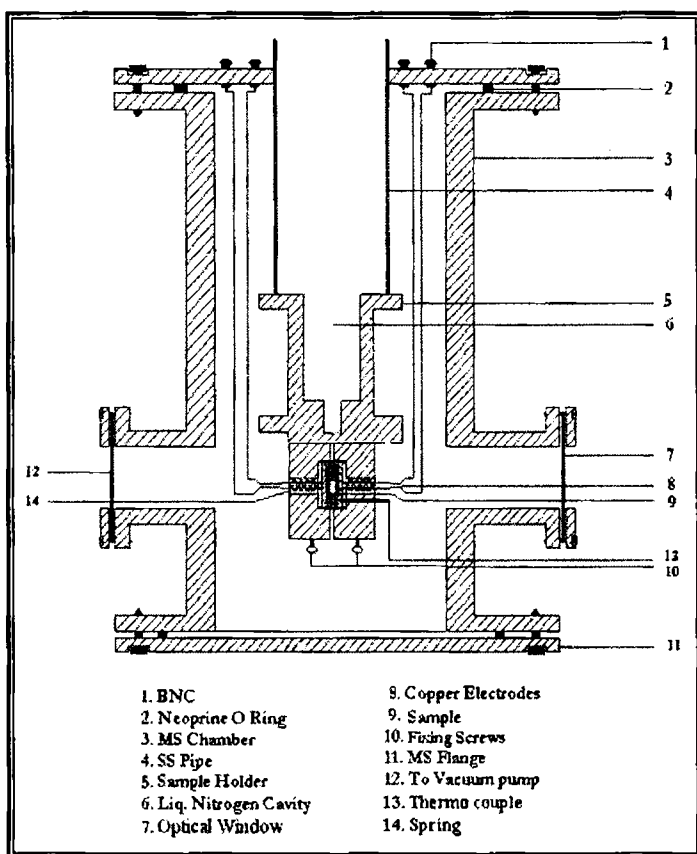
Figure 2.1 Schematic representation of dielectric cell

Pellet shaped samples of 12 mm diameter and about 2 mm thickness were used for the measurements. The data acquisition was automated by interfacing the

impedance analyser with a computer. For this, a virtual instrumentation package, based on a graphical programme was employed. This package is called LabVIEW, a base software package developed by National Instruments for implementing virtual instrumentation and G programming. LabVIEW is a programming language for data acquisition, analysis, simulation or computer control of instruments and techniques or processes. Appropriate modifications were incorporated in the software so as to enable the data acquisition automatic and visual observation of the graphs on the computer screen. The characteristic feature of this automatic data acquisition is that it has been possible to acquire 20,000 data points or more in a matter of 5 to 10 minutes. By using the modified package, the data can be plotted and analysed.

2.4.2 ac conductivity measurements

The ac electrical conductivity of the ferrite materials and rubber ferrite composites were calculated utilising the dielectric parameters. The dielectric studies of both ceramic and rubber ferrite composites were carried out using a dielectric cell and a HP 4285A impedance analyser. Using disc shaped samples, capacitance and dielectric loss were measured and dielectric constant and relative permittivity of the samples were calculated using equation 2.17. The ac conductivity of these samples were then evaluated using the relation

$$\sigma_{ac} = 2\pi f \tan \delta \varepsilon_0 \varepsilon_r \qquad\qquad 2.18$$

where f is the frequency of the applied field and tanδ is the loss factor. The principle and theory underlying the evaluation of σ_{ac} from dielectric measurements are based on a treatment dealt by Goswamy [39]. The measured values of ε_r and tanδ from the dielectric measurements for both ceramic and RFCs were used for the calculation of the ac conductivity.

2.5 Magnetic measurements

The magnetic characterisation of the ferrites and rubber ferrite composites were carried out using Vibrating sample magnetometer (VSM), model:EG & G PAR 4500. Parameters like saturation magnetisation (M_s), magnetic remanance or retentivity (M_r) and coercivity (H_c) were evaluated from the hysteresis loops obtained at room temperature.

51

When a sample material is placed in a uniform magnetic field, a dipole moment is induced in the sample. The moment of magnetic flux linked to any coil placed in the vicinity of this magnetic moment is given by

$$\phi = \mu_0 n \alpha M \qquad\qquad 2.19$$

where μ_0 is the permeability of free space, n is number of turns per unit length of coil, M is the magnetic moment of the specimen and α is the geometric moment decided by position of moment with respect to the coil as well as shape of the coil.

A harmonic oscillator of the type

$$Z = Z_0 + A \exp (j\omega t) \qquad\qquad 2.20$$

induces an emf in the stationary detection coil. The induced emf is given by

$$V = -\frac{d\phi}{dt} = -j\omega\mu_0 n M A \left(\frac{\partial \alpha}{\partial z}\right) e^{j\omega t} \qquad 2.21$$

If amplitude of vibration (A), frequency and $\partial\alpha/\partial z$ are constants over the sample zone then the induced voltage is proportional to the magnetic moment of the sample. This is the basic idea behind VSM [40-42].

In model PAR 4500 VSM, the material under study is contained in a sample holder, which is centered in the region between the pole pieces of a laboratory electromagnet. A slender vertical sample rod connects the sample holder with a transducer assembly located above the magnet. The transducer converts a sinusoidal ac drive signal into a sinusoidal vertical vibration of the sample rod and the sample is thus made to undergo a sinusoidal motion in a uniform magnetic field. Coils mounted on the pole pieces of the magnet pick up the signal resulting from the sample motion. This ac signal at the vibrating frequency is proportional to the magnitude of the moment induced in the sample. However, it is also proportional to the vibration amplitude and frequency. This vibration amplitude and frequency are kept constant by a servo system. Thus the pickup coil output accurately gives an account of the moment level of the sample.

2.6 Microwave measurements

Permittivity studies of ferrite materials and rubber ferrite composites at microwave frequencies assume significance, both in fundamental and application point of views. Different methods including cavity resonant and cavity perturbation techniques were used for microwave measurements. Among this, cavity perturbation method has been widely used to study the dielectric parameters in the microwave frequency region.

In the cavity perturbation technique, generally rectangular or cylindrical wave guide resonators are employed. When a dielectric material is introduced into a cavity resonator at the position of maximum electric field, the resonant frequencies of the cavity are perturbed. The contribution of magnetic field for the perturbation is minimal at this position. So from the measurement of the perturbation due to the sample, the dielectric parameters can be determined.

Permittivity measurements were carried out using a vector network analyser HP 8510 C. The permittivity measurements of the samples were done both in X (8 -12 GHz) and S (2-4 GHz) frequencies. The dimensions of the rectangular wave guides used in the measurement is given in table 2.1.

Table 2.1 Design parameters of S and X band rectangular wave guides.

Dimensions of the Cavity (cm)	S band	X band
Length	34.5	14.1
Breadth	7.2	2.3
Height	3.4	1.1

For measuring permittivity values, the following procedure was employed. The quality factor Q_c of the cavity and resonance frequency f_c in the unperturbed conditions were measured. The sample in the form of a strip was then inserted and positioned at the maximum electric field. The resonance frequencies f_s and loaded quality factor Q_s of the samples were measured. Permittivity values were then calculated using the following equations:

$$\varepsilon_r{}' = \left(\frac{V_c}{2V_s}\right)\left[\left(\frac{f_c}{f_s}\right) - 1\right] + 1 \qquad 2.22$$

$$\varepsilon_r{}'' = \left(\frac{V_c}{4V_s}\right)\left[\frac{1}{Q_s} - \frac{1}{Q_c}\right] \qquad 2.23$$

The procedure was repeated for all the available resonant frequencies. From the dielectric parameters $\varepsilon_r{}'$ and $\varepsilon_r{}''$, loss tangent and heating coefficient (J) of the samples were calculated using the following equations $\tan\delta = \varepsilon_r{}'' / \varepsilon_r{}'$ and $J = \frac{1}{\varepsilon_r} \tan\delta$.

Microwave attenuation behavior of the RFCs was determined from insertion loss of the samples by closely inserting the samples between the two waveguides to coaxial adapters. The values were reported in –dB/cm.

References

1. G. Ranga Mohan, D. Ravinder, A.V. Ramana Reddy and B.S. Boyanov, Matterials Letters, **40** (1999) 39.

2. S.R. Murthy, Bull. Mater. Sci., **24** (2001) 379.

3. K. Haneda and H. Kojima, J. Am. Ceram. Soc., **57** (1974) 68.

4. A.N. Patil, M.G. Patil, K.K. Patankar, V.L. Mathe, R.P. Mahajan and S.A. Patil, Bull. Mater. Sci., **23** (2000) 447.

5. M.H. Mahmoud, H.H. Hamdeh, J.C. Ho. M.J. O'Shea and J.C. Walker, J. Magn. Magn. Mater., **220** (2000) 139.

6. V. Sepelak, D. Baabe, D. Mienert, D. Schultze, F. Krumeich, F.J. Litterst and K.D. Becker, J. Magn. Magn. Mater., **257** (2003) 377.

7. W. Roos, J. Am. Ceram. Soc., **63** (1980) 601.

8. Kajal K. Mallick, Philip Shepherd and Roger J. Green, Journal of the European Ceramic Society, **27** (2006) 2045.

9. A. Kale, S. Gubbala and R.D.K. Misra, J. Magn. Magn. Mater., **277** (2004) 350.

10. Christy R. Vestal and Z. John Zhang, Int. J. of Nanotechnology, **1** (2004) 240.

11. V. Pillai and D.O. Shah, J. Magn. Magn. Mater., **163** (1996) 243.

12. J.F. Wang, C.B. Ponton and I.R. Harris, J. Magn. Magn. Mater., **234** (2001) 233.

13. C.H. Lin, Z.W. Shin, M.L. Wang and Y.C. Yu, IEEE Trans. Magn., **26** (1990) 15.

14. A. Verma, O.P. Thakur, C. Prakash, T.C. Goel and R.G. Mendiratta, Materials Science and Engineering B, **116** (2005) 1.

15. A. Verma, T.C. Goel, R.G. Mendiratta and R.G. Gupta, J. Magn. Magn. Mater., **192** (1999) 271.

16. Tal Meron, Yuri Rosenberg, Yossi Lereah and Gil Markovich, J. Magn. Magn. Mater., **292** (2005) 11.

17. Joong-Hee Nam, Sang Jin Park, and Won Ki Kim, IEEE Transactions on magnetics, **39** (2003) 3139.

18. Z. Bartha, P. Erdos and J. Maits, Int. Polym. Sci. Technol., **10** (1983) T/50.

19. N.V. Zakharenko and F.B. Yremchuk, Int. Polym. Sci. Technol., **12** (1985) T/23.

20. H.P. Schreiber and Olguin, Polym. Eng. Sci., **23** (1983) 129.

21. G.C.N. Lee and J.R. Purdon, Polym. Eng. Sci., **9** (1969) 360.

22. Charles Kittel, Introduction to Solid State Physics, John Wiley and Sons, New York (1997).

23. H.V. Keer, Principles of Solid State Physics, Wiley Eastern Ltd., New Delhi (1993).

24. B.D. Cullity, Elements of X-ray diffraction, Philippines, Addison-Wesley Publishing Company, Inc., 2nd Edition. California (1978).

25. C.M. Blow and C. Hepburn, Rubber Technology and Manufacture, 2nd Edition, Butterworth Publishers, London (1985).

26. M. Watt, The Principles and Practice of Electron Micrscopy, 2nd Edition., Cambridge university press, Cambridge (1997).

27. Encyclopedia of Polymer Science and Engineering, Volume 5, Wiley Interscience Publications, New York (1985).

28. D. Campbell and J.R. White, Polymer Characterisation Physical Techniques, Chapman and Hall, London (1989).

29. C.T. Schamp, W.A. Jesser, Ultramicroscopy, **103** (2005) 165

30. A. Subramanian, L.D. Marks, Ultramicroscopy, **98** (2004) 151.

31. Linda C. Sawyer and David T. Grubb, Polymer Microscopy, 2nd Edition., Chapman and Hall, London (1987).

32. Vishu Shah, Handbook of Plastic Testing Technology, John Wiley and Sons, New York (1984).

33. Roger Brown, Physical Testing of Rubber, 3rd Edition, Chapmann & Hall, London (1996).

34. John S. Dick, Rubber Technology Compounding and Testing for Performance, Hanser Publishers, Munich (2001).

35. Soney C. George and Sabu Thomas, Journal of Macromolecular Science, Part B Physics, **39** (2000) 175.

36. Cattaleeya Pattamaprom, Duangkamol Dechojarassri and Worsak Kanok- Nukulchai, Rubber Chem. Technol., **78** (2005) 724.

37. G. Mathew, R.P. Singh, N.R. Nair and S. Thomas, Journal of Materials Science, **38** (2003) 2469.

38. S.B. Harogoppad and T.M. Aminabhavi, Macromolecules, 24 (1991) 2595.

39. A. Goswami, Thin Film Fundamentals, New age International Publishers Ltd., New Delhi (1996).

40. Simon Foner, Rev. Sci. Instrum., **30** (1959) 548.

41. Joseph A. Pesch, Rev. Sci. Instrum., **54** (1983) 480.

42. R.V. Krishnan and A. Banerjee, Rev. Sci. Instrum., **70** (1999) 85.

Synthesis and Characterisation of Nickel Ferrite and Gamma Ferric oxide Nanoparticles

Preparation of phase pure materials is a prerequisite for any study in material science. The purity of the synthesised compound can be established only by a systematic and thorough characterisation using various analytical techniques at different intermediate stages. For the synthesis of rubber ferrite composites, preparation of phase pure precursors assumes importance. The history of precursor samples, the nature of heat treatment and the method of preparation are all vital inputs for a proper correlation and correct interpretation of data after an exhaustive study. This chapter emphasises the importance of synthesising pristine compounds and their characterisation for incorporation into matrices like ethylene propylene diene and neoprene rubber.

Since the focal theme of this particular investigation is on the influence of nano ferrite fillers in polymer composites like RFCs, emphasis is laid in preparing ultrafine ferrites. Nano nickel ferrite and maghemite (γ-Fe_2O_3) are chosen as fillers for synthesising RFCs because they find applications in a horde of devices ranging from transformer cores, to high density recording [1], magnetocaloric refrigeration [2], contrast enhancement in magnetic resonance imaging [3], magneto-optical devices and ferrofluid technology [4]. Normally, they are employed in the form of ceramic components. It is known from literature that different methods of preparation are in vogue for the synthesis of ferrites in the nano regime. Methods such as co-precipitation [5] micelle/reverse micelle [6,7], hydrothermal [8,9], high energy ball milling [10] and sol-gel [11-13] method are employed for the synthesis of ferrite nanoparticles.

A. Kale et al. utilised the technique of reverse micelle for the synthesis of nickel ferrite nanoparticles and were found to exhibit superparamagnetism [14]. Well crystallised ultrafine particles of zinc ferrite were prepared by Shu-Hong Yu et al.

using a low temperature hydrothermal method [15,16]. Nickel ferrite nanoparticles were synthesised by Yoshiaki Kinemuchi by pulsed wire discharge of iron and nickel in an oxygen rich environment [17]. However, the final product was contaminated with traces of nickel oxide impurities. Zhang et al. prepared nanorods of nickel ferrite by employing polyethylene glycol [18].

A low temperature technique, namely sol-gel method is adopted here for the preparation of spinel ferrites. It is also important that the crystal structure of the prepared compounds is evaluated and the particle size and particle size distribution are estimated properly. Powder X-ray diffraction is an effective tool for the precise determination of the crystal structure and evaluation of lattice parameters. This technique can also be employed for the particle size evaluation. However, particle size determination using the phenomenon of line broadening and employing Debye-Sherrer equation is not without uncertainities. Hence, alternate and complimentary techniques like Transmission electron microscopy are to be adopted. The employment of electron microscopy reveals information about shape and size of the particles. Electron microscopy aided by SAED/EDS will also reveal compositional details of the compounds. The structural details of the inorganic fillers for impregnation also assume significance. A wealth of information on bonding and existence of functional groups can be obtained by carrying out Fourier transform infrared spectroscopy on these samples. Spectral studies can be considered as the first step in fingerprinting the samples.

Thermal studies on precursor samples are useful in determining the exact decomposition temperature. Thermogravimetry reveals information on the temperature at which thermal decomposition or degradation of different groups occurs and the corresponding weight losses. These are crucial parameters for preparing the fillers in bulk.

The synthesis and characterisation of nanosized nickel ferrite and gamma ferric oxide is explained in this chapter.

3.1 Synthesis of nickel ferrite and gamma ferric oxide

Nickel ferrite and gamma ferric oxide nanoparticles were prepared by sol-gel technique. In this method, nitrate precursors were employed and ethylene glycol was

used as solvent. Chemical and structural changes that take place during combustion of gel precursors can be followed by infrared spectroscopy supported by thermogravimetric analysis.

The gel obtained during the preparation of nickel ferrite was subjected to thermogravimetric analysis. The thermogam is shown in figure 3.1. It can be seen that the weight loss occurring at around 200°C corresponds to the complete escape of ethylene glycol. The onset of decomposition is at around 260°C and the completion of this process is noticeable at around 370°C. Thermogravimetric studies provide information about phase formation. The dried gel samples were then heat treated corresponding to the decomposition temperature for further studies.

Figure 3.1 Thermogram of the dried gel obtained in the preparation of NiFe₂O₄
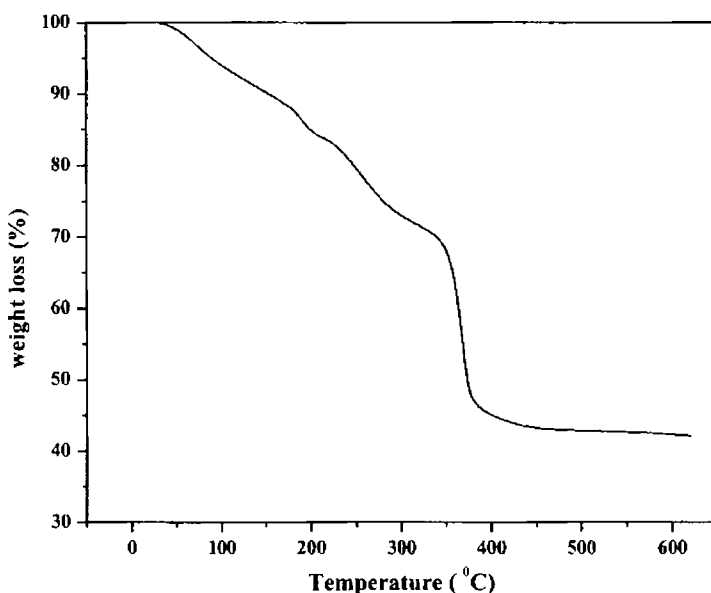
Figure 3.1 Thermogram of the dried gel obtained in the preparation of $NiFe_2O_4$

Chemical and structural changes that take place during combustion can be ascertained by recording the IR spectrum. The FTIR spetra of the dried gel of nickel ferrite precursor was recorded and a typical spectrum is shown in figure 3.2a.
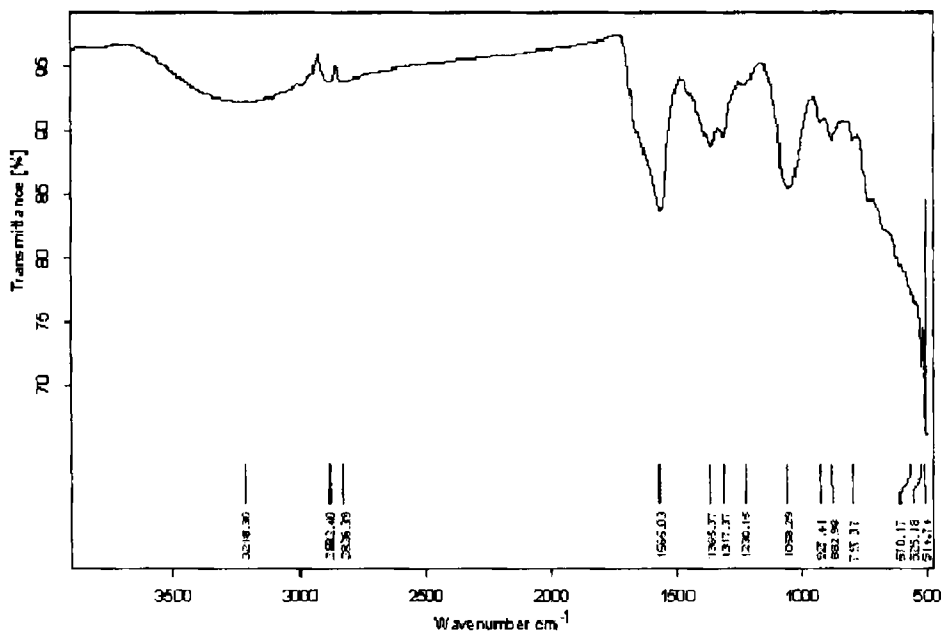
Figure 3.2a FTIR spectrum of dried gel precursor for nickel ferrite synthesis

Characteristic bands at 3218 cm^{-1}, 2882 cm^{-1} and 1565 cm^{-1} corresponding to -OH, -CH$_2$ and (NO$_3^-$) functional groups are observed in the spectrum. The band at 1059cm^{-1} is attributable to C-O deformations. The presence of the band at 1565 cm^{-1} indicates that metal ions and the nitrate ions are trapped in the gel structure, which on further ignition, converts to nickel ferrite.

The spectrum corresponding to the ignited sample is also shown in figure 3.2b. It can be seen that except the band at 540 cm^{-1} all bands which are present in the spectrum corresponding to the dried gel sample vanishes. The disappearance of characteristic bands corresponding to –CH$_2$ and NO$_3$ $^-$ ions in the IR spectrum indicates that these groups play an active role in the reaction process during combustion leading to the formation of nickel ferrite. The combustion can be considered as thermally induced redox reaction of the gel wherein ethylene glycol acts as a reducing agent. The nitrate ion acts as an oxidant. Nitrate ion provides an in situ oxidising environment for the decomposition of the organic component [19,20].
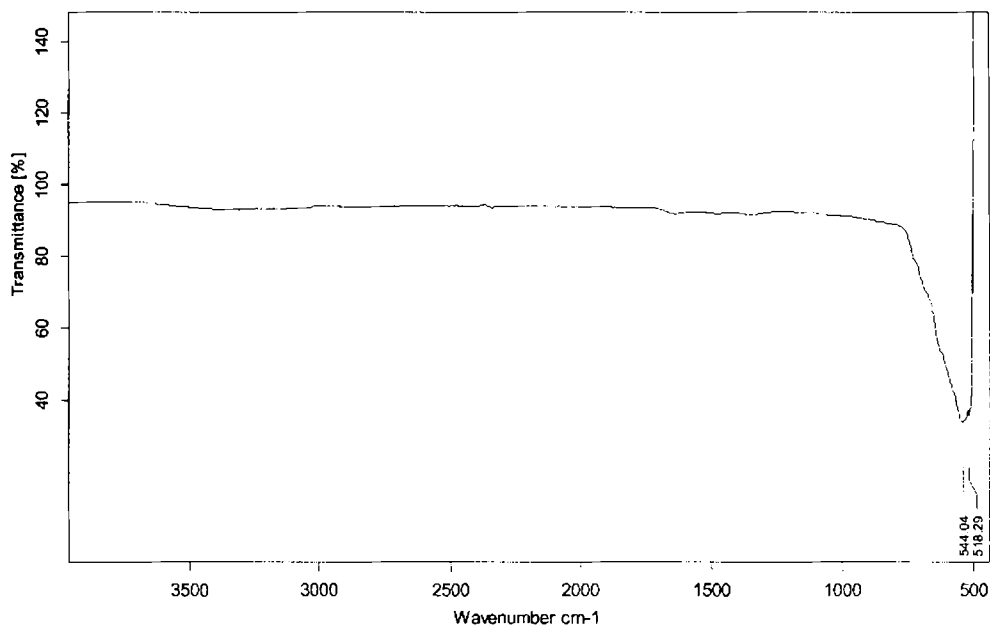
Figure 3.2b FTIR spectrum of the ignited sample (nickel ferrite)

Compounds having spinel structure should posses four IR bands γ_1, γ_2, γ_3 and γ_4 at 550 cm^{-1}, 630 cm^{-1}, 268 cm^{-1} and 178 cm^{-1} respectively. In the spinel lattice, every oxygen anion is bonded to three octahedral cations and one tetrahedral cation. These two give rise to two modes of vibration; γ_1 (550 cm^{-1}) and γ_2 (630 cm^{-1}). Two other modes γ_3 and γ_4 are related to displacement of cations in the lattice and these bands are reported to be at 268 cm^{-1} and 178 cm^{-1}. The IR absorption band obtained at 540 cm^{-1} (figure 3.2b) may be assigned to the stretching vibrations of octahedral groups.

The IR spectrum of the dried gel precursor for gamma ferric oxide synthesis is shown in figure 3.3a. The identical nature of IR spectrum of the dried gel obtained in both the cases suggests a similar mechanism for the preparation of gamma ferric oxide particles.
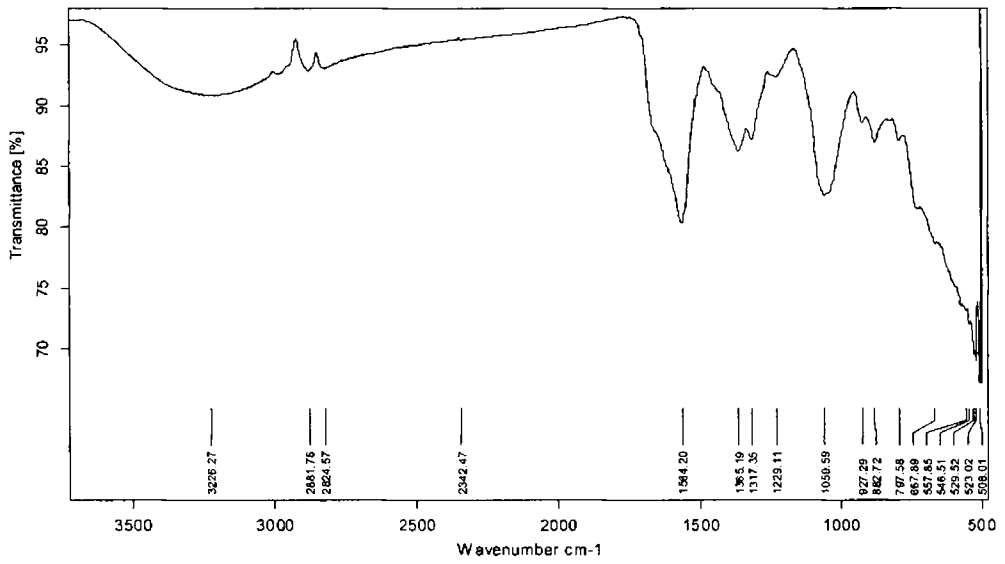
Figure 3.3a FTIR spectrum of dried gel precursor for gamma ferric oxide synthesis.
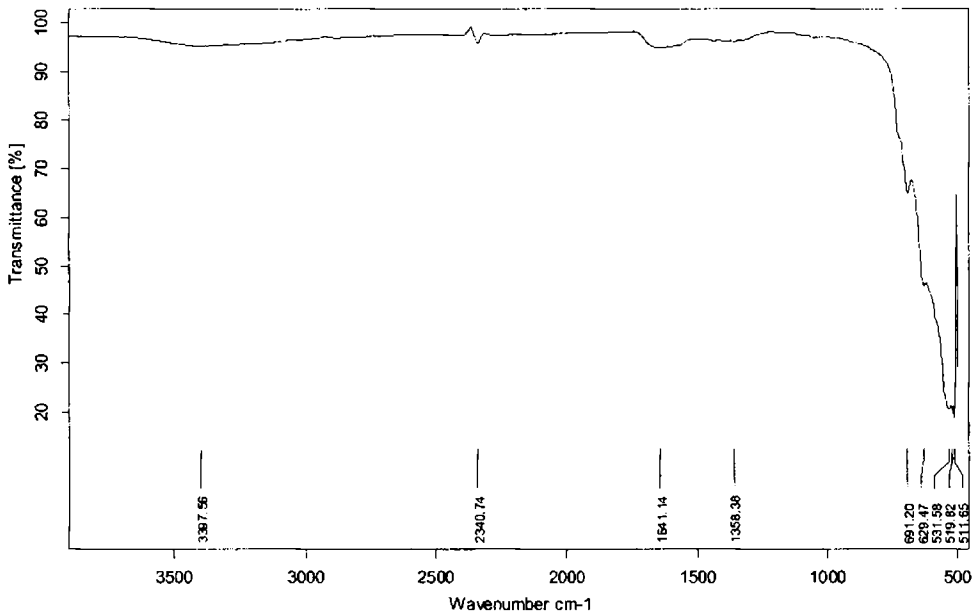
Figure 3.3 b FTIR spectra of ignited gel (gamma ferric oxide)

FTIR spectrum of the ignited gel (gamma ferric oxide) is shown in figure 3.3b. The bands observed in the IR spectrum of gamma ferric oxide at 630 cm^{-1} (γ_2) and 536 cm^{-1} (γ_1) are assigned to the stretching vibrations of tetrahedral and octahedral groups respectively.

3.2 Structural studies of nickel ferrite

Nickel ferrite prepared by the method of sol-gel was then subjected to X-ray powder diffraction studies using Rigaku Dmax-C and employing Cu Kα radiations (λ = 1.5418A°). The diffractogram is depicted in figure 3.4.
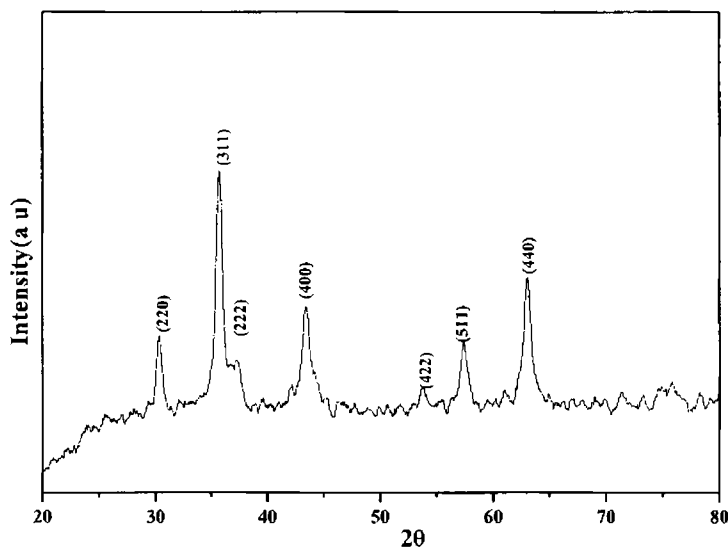
Figure 3.4 X-ray powder diffractogram for NiFe₂O₄ prepared by sol-gel method

The d values and the corresponding relative intensities are then compared with a standard spectrum of nickel ferrite (JCPDS No. 74-2081). Lattice parameter is then evaluated assuming cubic symmetry and found to be 8.329 Å. The powder diffractogram is characteristic of an inverse spinel and prominent planes are identified. This is shown in figure 3.4. Average particle size estimated using Debye-Sherrer formula is 19 nm.

Transmission electron micrograph of NiFe$_2$O$_4$ was recorded on a Joel JEM 2200 FS electron microscope using an accelerating voltage of 200 kV. The micrograph and the electron diffraction diagram are shown in figures 3.5 and 3.6.
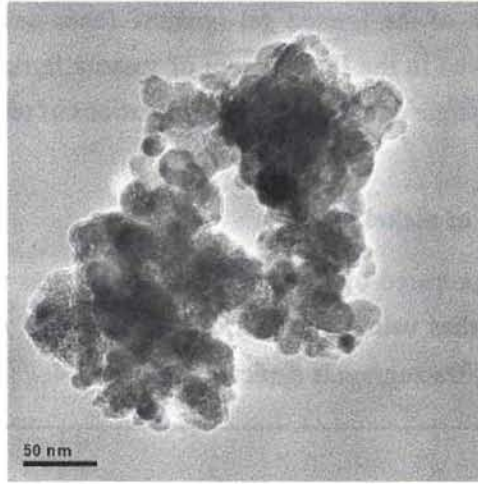
Figure 3.5 TEM image of $NiFe_2O_4$

Figure 3.6 Selected area diffraction pattern of $NiFe_2O_4$

The histogram representing the particle size distribution is given in figure 3.7. Transmission electron micrograph reveals that the nickel ferrite samples are pure and polycrystalline in nature and have wide particle size distribution in the range 15-26 nm. The average particle size obtained from the histogram is about 19 nm. These results match well with the results obtained from X-ray diffraction studies.
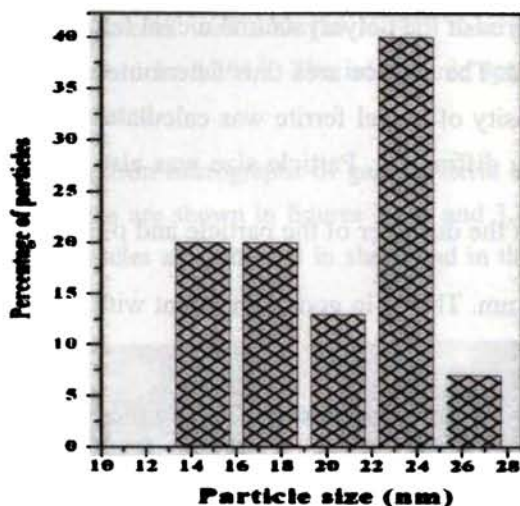
Figure 3.7 Histogram of particle size distribution of NiFe₂O₄

Mapping picture of the nickel ferrite is shown in figure 3.8. The identical nature of the mapping diagram of iron, nickel and oxygen shows the phase formation of nickel ferrite particles and also shows the homogeneous nature of the prepared sample.
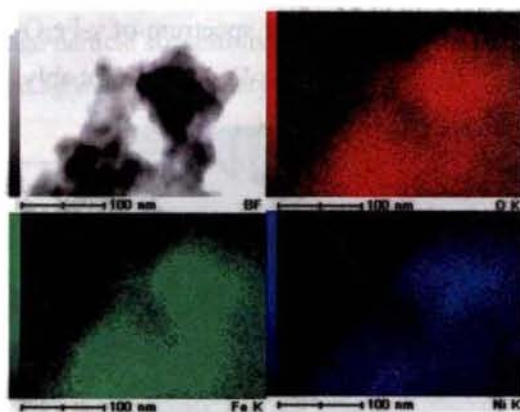
Figure 3.8 Mapping picture of NiFe₂O₄

Stoichiometric formation of nickel ferrite can be evidenced from the mapping picture which is further supported by data collected from experiments using inductively coupled plasma analysis. The iron/nickel ratio obtained from ICP analysis is 1.78. From this, the actual stoichiometry of the nickel ferrite can be written as $Ni_{1.0894}Fe_{1.9404}O_4$.

The surface area of the polycrystalline nickel ferrite is measured by **Brunauer-Emmet-Teller** method. The surface area thus determined is found to be 53 m^2/g. The theoretical **X-ray** density of nickel ferrite was calculated using the lattice parameters evaluated from X-ray diffraction. Particle size was also estimated using the relation $S = \dfrac{6000}{D\rho}$ where D is the diameter of the particle and ρ is the theoretical density. D is found to be about 20 nm. This is in good agreement with the results obtained from X-ray diffraction results.

Porosity of the sample was calculated using the equation $(\rho_x - \rho_a)/\rho_x$ where ρ_x is the theoretical density and ρ_a is the actual density of the sample. Porosity of the sample is 39%.

3.3 Structural studies of gamma ferric oxide

Structural parameters of gamma ferric oxide are evaluated using the data from X-ray diffraction and electron diffraction. A typical X-ray diffractogram for gamma ferric oxide is shown in figure 3.9. All the planes are identified and the crystal planes are indexed. On comparison with standard spectrum of γ-Fe_2O_3, peaks corresponding to α-Fe_2O_3 are found. The formation α-Fe_2O_3 is probably because of the high temperature during the reaction.
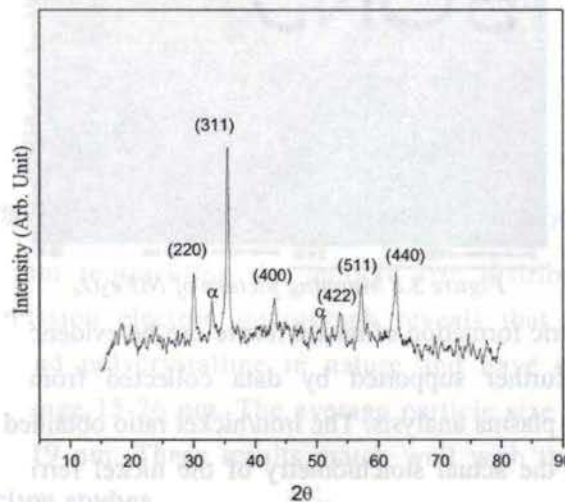
Figure 3.9 X-ray diffraction diagram of gamma ferric oxide

The average particle size calculated using Debye Sherrer formula is about 24 nm. The XRD pattern matches well with the JCPDS data (No.391346) [21]. The lattice parameter is found to be 8.361Å. The interatomic spacing and their relative intensities were also estimated.

Transmission electron micrographs of gamma ferric oxide are recorded and representative micrographs are shown in figures 3.10a and 3.10b. It is evident from micrographs that the particles are spherical in shape and in the range of 8-28 nm in size.
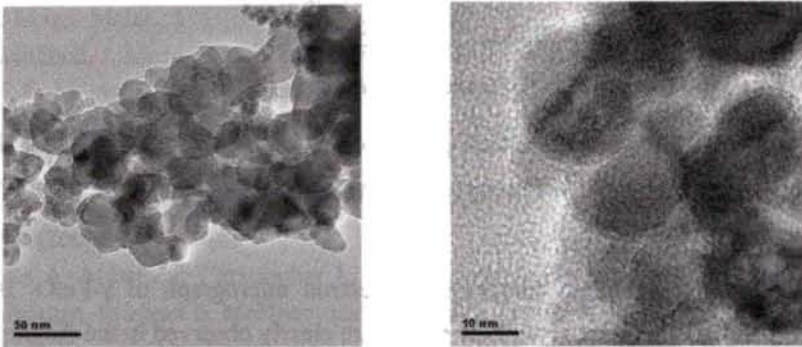
Figure 3.10 TEM image of γ-Fe₂O₃ (a) at 50 nm scale (b) at 10 nm scale

The average particle size estimated from these micrographs is found to be 20 nm. This is in good agreement with that of results obtained from X-ray diffraction.

Figure 3.11 Selected area electron diffraction of γ-Fe₂O₃

67
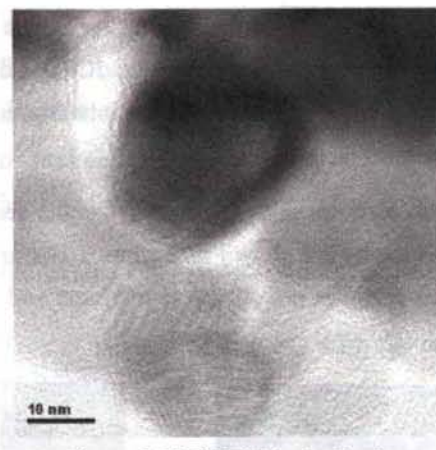
Figure 3.12 HRTEM of γ-Fe₂O₃

The electron diffraction pattern of γ-Fe_2O_3 is shown in figure 3.11. Bright spots observed in the diffraction pattern confirm the formation of poly crystalline gamma ferric oxide.

High resolution transmission electron micrograph of γ-Fe_2O_3 is shown in figure 3.12. Prominent crystalline planes are clearly observed in the diagram.

Surface area of the powdered sample was determined by BET nitrogen adsorption method. Surface area of the sample is found to be 36 m^2/g. Porosity of the sample is calculated as explained in section 3.2 and is found to be 21%.

3.4 Conclusion

Phase pure nano nickel ferrite was prepared by using the sol-gel method. The particle size was evaluated by different complimentary techniques and was found to be 19 nm. The results obtained using different techniques were in good conformity. Gamma ferric oxide was also prepared using the sol-gel technique. However, traces of α-Fe_2O_3 were found along with γ-Fe_2O_3. Thermal and infrared spectroscopic studies carried out on gel precursors for nickel ferrite and gamma ferric oxide, confirm the belief that metal ions do not have any active role leading to the formation of their corresponding gels. Particle size evaluated using X-ray diffraction and Transmission electron microscopy indicate that γ-Fe_2O_3 particles are in the nano regime and lie in the range 24 nm. Consistency in particle size and structural parameters were obtained

for various batches prepared in identical condition. Samples prepared in various batches were further homogenised using high energy ball milling and used for making rubber ferrite composites.

References

1. Martha Pardavi-Horvath, J. Magn. Magn. Mater., **203** (1999) 57.
2. R.D. McMichael, R.D. Shull, L. J. Swartzendruber and L.H. Bennett and R.E. Watson, J. Magn. Magn. Mater., **111** (1992) 29.
3. D.G. Mitchell, J. Magn. Reson. Imaging, **7** (1997) 1.
4. K. Raj, R. Moskowitz and R. Casciari, J. Magn. Magn. Mater., **149** (1995) 174.
5. A. Verma, T.C. Goel, R.G. Mendiratta and R.G. Gupta, J. Magn. Magn. Mater., **192** (1999) 271.
6. Hironori Iida, Takuya Nakanishi, Harumi Takada and Tetsuya Osaka, Electrochimica Acta, **52** (2006) 292.
7. Shannon A. Morrison, Christopher L. Cahill, Everett E. Carpenter, Scott Calvin, Raja Swaminathan, Michael E. McHenry and Vincent G. Harris, J. Appl. Phy., **95** (2004) 6392.
8. Shu-Hong Yu, Takahiro Fujino and Masahiro, J. Magn. Magn. Mater., **256** (2003) 420.
9. Miha Drofenik, Matjaz Kristal, Andrej Znidarsic, Darko Hanzel and Darja Lisjak, J. Am. Ceram. Soci., **90** (2007) 2057.
10. G.F. Goya and H.R. Rechenberg, J. Magn. Magn. Mater., **203** (1999) 141.
11. Adriana S. Albuquerque, Jose D. Aedisson and Waldemar A.A. Macedo, J. Magn. Magn. Mater., **192** (1999) 277.
12. Souilah Zahi, Mansor Hashim and A.R. Daud, Materals Letters, **60** (2006) 2803.
13. Dong-Hwang Chen and Xin-Rong He, Materials Research Bulletin, **36** (2001) 1369.
14. A. Kale, S. Gubbala and R.D.K. Misra, J. Magn. Magn. Mater., **277** (2004) 350.
15. Shu-Hong Yu, Takahiro Fujino and Masahiro Yoshimura, J. Magn. Magn. Mater., **256** (2003) 420.
16. Jun Zhou, Junfeng Ma, Chong Sun, Lijin Xie, Zhongqiang Zhao and Hua Tian, Yanggang Wang, Jiantao Tao and Xiaoyi Zhu, J. Am. Ceram. Soc., **88** (2005) 3535.
17. Yoshiaki Kinemuchi, Kazuhiro Ishizaka, Hisayuki Suematsu, Weihua Jiang and Kiyoshi Yatsui, Thin Solid Films, **407** (2002) 109.
18. D.E. Zhang, X.J. Zhang, X.M. Ni, H.G. Zheng and D.D. Yang, J. Magn. Magn. Mater., **292** (2005) 79.
19. S.V. Chavan, K.T. Pillai and A.K. Tyagi, Materials Science and Enginering B, **132** (2006) 266.
20. Zhenxing Yue, Ji Zhou, Longtu Li, Hongguo Zhang and Zhilun Gui, J. Magn. Magn. Mater., **208** (2000) 55.
21. D. Schulz and G. Mcarthy, ICDD (1987).

Studies on the Physicomechanical Properties of EPDM based Rubber Ferrite Composites

Rubber ferrite composites can be prepared by the incorporation of ferrites into natural/synthetic rubber according to a specific recipe. Malini et al. conducted a detailed study on processing, magnetic and dielectric properties of rubber ferrite composites containing nickel zinc ferrite [1]. A similar study was carried out by Mohammed and others using manganese zinc ferrite as the filler and natural rubber as the matrix [2,3]. Inclusion of hard ferrites like barium and strontium ferrites into natural and synthetic rubbers were performed by Soloman et al. [4,5]. All these cited studies clearly indicate that the processability and properties of RFCs depends on both the nature of matrix like polar/non polar and the type of elastomer viz. natural or synthetic. Processability of these composites also depends on the type of the ferrites incorporated into it. Determination of processability and cure characteristics are indispensable for the evaluation of physical and mechanical properties of RFCs.

In this investigation, EPDM based RFCs were prepared using nickel ferrite $(NiFe_2O_4)$ and gamma ferric oxide $(\gamma\text{-}Fe_2O_3)$ as the filler. EPDM is being selected as the host matrix because of its superlative performance characteristics like high extensibility and excellent heat and weather resistance [6]. EPDM used for the preparation of RFCs were Royalene 512 supplied by Herdillia Unimers Ltd. with the undermentioned specifications. The ethylene propylene weight ratio is 68/32 with four weight percentage of the third monomer, ethylidene norbornene. This chapter deals with the synthesis of RFCs based on EPDM and nanoparticles of nickel ferrite and gamma ferric oxide. The compounding recipe is very important in the preparation of a polymer composite. Hence emphasis is also laid in the design of right recipe keeping in view of the nature of the filler and the speciality of the matrix.

Ferrites as well as rubber ferrite composites are important dielectric materials and find applications as microwave absorbers. Dielectric and microwave absorbing properties of RFCs can be improved by the incorporation of carbon black. Hence along with fillers like nickel ferrite and gamma ferric oxide, carbon black was also added for the preparation of RFCs. These studies were conducted to investigate the improvement in the reinforcing properties of the composites as well as the enhancement in the microwave absorption properties. The details regarding the microwave absorption studies will be dealt in chapter 8.

4.1 Preparation of nickel ferrite and gamma ferric oxide based RFCs

4.1.1 Incorporation of ferrites in rubber matrix

Precharacterised $NiFe_2O_4$ and γ-Fe_2O_3 were incorporated into the EPDM matrix according to the recipe given in table 4.1. Compounds were prepared with filler loadings ranging from 20 to 120 phr in steps of 20. A set of carbon black (HAF) loaded composites were also prepared and evaluated along with the RFCs, under identical experimental conditions for comparing them with the RFCs. The carbon black loaded compounds were prepared using the same recepie, given in table 4.1.

Table 4.1 Recipe used for compounding of EPDM rubber with nickel ferrite, gamma ferric oxide and carbon black

Material	Loading (phr)
EPDM	100
Stearic acid	1
Filler	X
Paraffinic oil	10% of X
DCP	3

X is 20,40,60,80,100 and 120 parts of $NiFe_2O_4$ or γ-Fe_2O_3 per hundred parts of EPDM. The corresponding composites are represented as En and Eg for nickel ferrite and gamma ferric oxide based RFCs. The carbon black loaded compounds are represented as Eb.

The mixing was carried out using Brabender Plasticorder at 60°C for ten minutes at 50 rpm rotor speed. The compounds were finally homogenised using a two roll mill (15×33 cm) as per ASTM D 3182-1982.

Carbon black loaded RFCs were prepared as per the recipe given in table 4.2. High abrasion furnace black (N330) was used for the study. RFCs were prepared with 100 parts per hundred rubber (phr) of nickel ferrite and carbon black loading was varied from 20 to 80 phr in steps of 20.

Table 4.2 Recipe used for compounding of EPDM rubber containing 100 phr nickel ferrite and different loadings of carbon black.

Material	Loading (phr) $E_{100,Y}$
EPDM	100
Stearic acid	1
Nickel ferrite	100
HAF (N330)	Y
Paraffinic oil	10% of (100+Y)
DCP	3

$E_{100,Y}$ represents RFCs with 100 phr of nickel ferrite and 20,40,60 or 80 phr of carbon black. The mixed compounds were matured for a period of 24 hrs and the cure characteristics like cure time, scorch time, maximum torque and minimum torque were determined using a Rubber process analyser at a temperature of 160°C.

From the respective cure curves, the optimum cure time of the RFCs were determined. Sheets for preparing the test specimens were prepared by moulding to a thickness of 2 mm using an electrically heated hydraulic press at 160°C upto their respective cure times. For determining the abrasion resistance, cylindrical shaped test specimens with 16 mm diameter and 6 mm thickness were prepared using suitable moulds.

4.2 X-ray diffraction studies of RFCs

X-ray diffraction spectra of $NiFe_2O_4$ as well as that of the RFCs were recorded and the structural parameters were evaluated. The spectra are compared to find out any structural changes taking place on incorporation of fillers in the matrix.

Figure 4.1 represents the X-ray diffraction patterns of nickel ferrite and nickel ferrite filled RFCs.
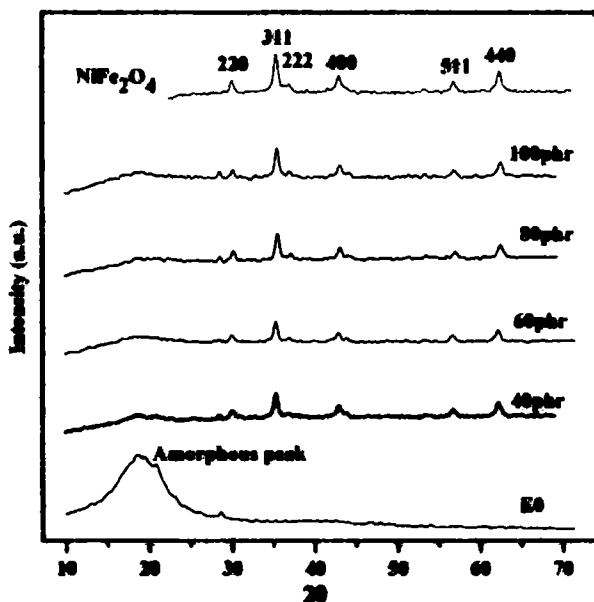
Figure 4.1 XRD of nickel ferrite and nickel ferrite loaded RFCs

All the characteristic peaks of nickel ferrite are present in the XRD of the RFCs. It may be noted that no shift in the peak positions is observed. This indicates that the nickel ferrite do not under go any structural change during the different stages of processing of the RFCs. Further, the intensity of the amorphous peak is found to decrease as the ferrite loading increases. Hence it can be inferred that the characteristic properties of ferrite are not at all affected by its incorporation into EPDM matrix.

4.3 Cure characteristics

4.3.1 Cure time curves for RFCs

Cure characteristics of the prepared composites were determined using a Rubber process analyser, RPA 2000 of Alpha technology, at a temperature of 160°C. Using these measurements parameters like optimum cure time and scorch time were determined along with the maximum and minimum torque values.
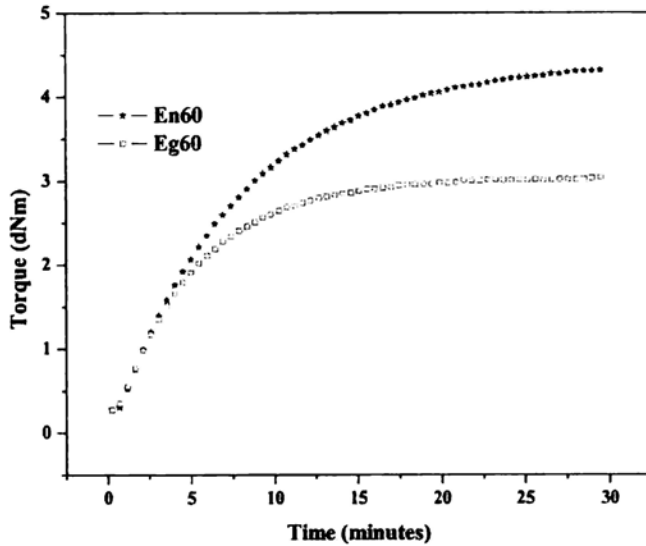
Figure 4.2 Cure time curves of RFCs containing 60 phr NiFe₂O₄ and γ-Fe₂O₃

Figure 4.2 shows the representative cure graphs of $NiFe_2O_4$ and γ-Fe_2O_3 filled RFC. From figure 4.2, it is evident that the nature of cure curve is similar for the RFCs containing $NiFe_2O_4$ and γ-Fe_2O_3, which indicates that spinel ferrites in EPDM matrix react identically.

4.3.2 Cure time and Scorch time

Table 4.3 shows the effect of filler loading on cure time of the composites with $NiFe_2O_4$, γ-Fe_2O_3 and HAF black. In all these three set of composites, cure time is found to decrease with increase in filler content.

For nickel ferrite filled RFCs, cure time increases marginally at a loading of 20 phr and then decrease with further increase in filler loading. This decrease in cure time indicates that filler incorporation activates the cure reaction of EPDM rubber. This is supported by cure kinetic studies and cure rate index values of cure reactions which are discussed elsewhere.

It is noteworthy here that among the three set of composites, RFCs containing γ-Fe_2O_3 are found to have a lower cure time. This point to the fact that γ-Fe_2O_3 has a much stronger influence on the cure reaction with respect to $NiFe_2O_4$.

Table 4.3 Effect of filler loading on cure time of composites with
NiFe$_2$O$_4$, γ-Fe$_2$O$_3$ and HAF black

Filler loading (phr)	Optimum cure time (minutes)		
	En	Eg	Eb
0	19.94	19.94	19.94
20	20.24	17.48	19.04
40	18.95	14.83	18.65
60	17.26	13.76	16.59
80	17.06	10.8	15.94
100	15.59	9.76	14.78
120	14.22	7.8	10.74

Table 4.4 Scorch time of NiFe$_2$O$_4$, γ-Fe$_2$O$_3$, and HAF filled composites

Filler loading (phr)	Scorch time (minutes)		
	En	Eg	Eb
0	1.58	1.58	1.58
20	1.65	1.41	1.52
40	1.52	1.18	1.29
60	1.44	1.07	1.04
80	1.42	0.95	0.74
100	1.28	0.84	0.91
120	1.17	0.6	0.176

Variation of the scorch time of NiFe$_2$O$_4$ and γ-Fe$_2$O$_3$ filled RFCs along with carbon black composites are represented in table 4.4. Scorch time of the composites decreases with loading. Here it is to be noted that such a decrease in scorch time is attributable to the heat of mixing resulting in the premature curing of the compounds.

From table 4.4 it can be noted that among the three fillers incorporated in EPDM viz. NiFe$_2$O$_4$, γ-Fe$_2$O$_3$ and HAF, composites with NiFe$_2$O$_4$ are having a higher scorch safety.

4.3.3 Minimum and maximum torque

The maximum and minimum torque values of the RFCs and carbon black loaded composites were evaluated and shown in table 4.5. Maximum torque is a measure of the shear modulus of the fully vulcanised rubber at the vulcanisation temperature. In both set of RFCs, the maximum torque decreases slightly with filler loading. At the same time maximum torque value is found to increase with carbon

Table 4.5 Maximum and minimum torque values of NiFe$_2$O$_4$ and γ-Fe$_2$O$_3$ filled RFCs and carbon black composites

Loading (phr)	Maximum torque (dNm)			Minimum torque (dNm)		
	En	Eg	Eb	En	Eg	Eb
0	4.83	4.83	4.83	0.17	0.17	0.17
20	4.67	4.38	5.05	0.18	0.19	0.19
40	4.64	3.15	5.82	0.21	0.23	0.31
60	4.33	3.04	7.77	0.23	0.25	0.68
80	4.34	2.59	10.61	0.26	0.31	1.61
100	4.34	2.51	13.48	0.31	0.39	3.15
120	4.11	2.46	13.31	0.35	0.58	2.75

black loading. These values are a reflection on the filler-polymer interaction. There is no evident chemical interaction is taking place between the ferrite fillers and the matrix. Where as, carbon black is a known reinforcing filler and the high torque values in the case of carbon black filled composites are the result of bound rubber formation. In the case of NiFe$_2$O$_4$ impregnated composites, the maximum torque is not reduced substantially probably because of the porous nature of the filler.

Minimum torque, which is a measure of the viscosity of the compound, is found to increase with ferrite loading. It can be considered as a measure of the stiffness of the unvulcanised compound. Even though the minimum torque is found to increase with loading of ferrite, it does not affect the processability of the compound. The increase in viscosity with the addition of fillers is because of the occlusion of rubber within and between the filler aggregates and immobilisation of a layer of elastomer at the surface of the filler.

4.3.4 Cure characteristics of RFCs containing carbon black

Cure characteristics of the RFCs containing 100 phr $NiFe_2O_4$ and different loadings of carbon black are given in table 4.6.

Table 4.6 Cure parameters of RFCs with different loading of carbon black

Sample	Scorch time t_{10}(minutes)	Optimum cure time t_{90}(minutes)	Maximum torque D_{max} (dNm)	Minimum torque D_{min} (dNm)
E_{100}	1.58	19.94	4.34	0.31
$E_{100.20}$	0.97	13.89	4.25	0.39
$E_{100,40}$	0.79	13.35	6.19	0.75
$E_{100,60}$	0.57	12.97	8.50	1.65
$E_{100,80}$	0.29	10.81	16.07	6.65

From table 4.6, it is clear that the scorch time and cure time of RFCs containing different loadings of carbon black decreases with increase in carbon black content. Maximum and minimum torque values are found to increase with loading of carbon black.

4.3.5 Distribution of filler aggregates-by Lee's treatment of torque values

The dispersion of filler within the matrix and formation of filler agglomerates were studied in detail by B.L. Lee [7,8]. This method is applicable for carbon black composites. Even in well dispersed filler-rubber systems, differences in the degree of filler agglomeration in the cured and uncured state can be observed. In Lee's approach, a new parameter L is introduced which is defined as

$$L = \eta_r - M_r \qquad\qquad 4.1$$

where $\eta_r = D^f_{min}/D^0_{min}$ and $M_r = D^f_{max}/D^0_{max}$. Where D^f_{max} and D^f_{min} are the maximum and minimum torque of the filled composites and D^0_{max} and D^0_{min} are the maximum and minimum torque of the unfilled composites respectively. For an ideal dispersion of fillers, $\eta_r = M_r$. This occurs when the Poisson ratio of the matrix material is equal to 0.5 and when the individual particles are well dispersed in the matrix. Adhesion between the filler and the polymer matrix also has to be perfect.

In the case of non ideal dispersion of fillers, the value of L changes less rapidly at low filler loadings but above a certain limit it increases sharply. Thus a plot of L with filler loading along X-axis can be approximated by two straight lines having different slopes. The abrupt rise of the index L at high filler loadings may be ascribed to the predominance of agglomerates that remain relatively undispersed in the rubber matrix.

Lee's approach is adopted here. The variation of L for the nickel ferrite and gamma ferric oxide are plotted in figure 4.3. From the figure, it is very clear that there is no sharp increase in L even at a concentration of 120 phr for both the ferrites. The value of L is found to be higher for gamma ferric oxide compared to nickel ferrite. This indicates poor dispersion of gamma ferric oxide particles compared to nickel ferrite particles in EPDM matrix.
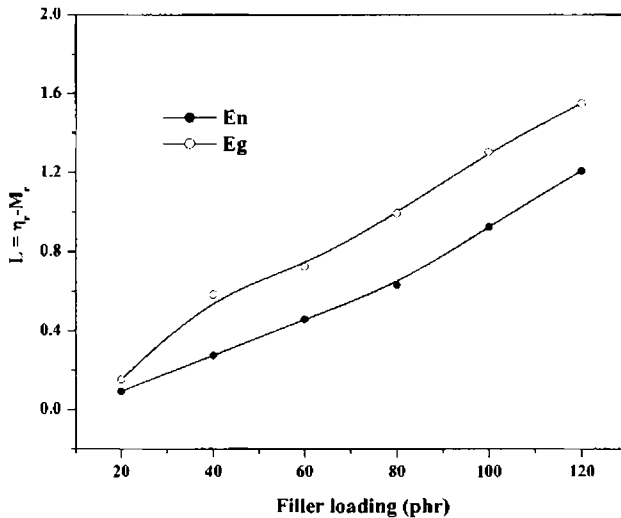
Figure 4.3 Variation of parameter L with NiFe$_2$O$_4$ and γ-Fe$_2$O$_3$ loading

In the case of γ-Fe_2O_3 composites, large deviation in L is observed above 60 phr where as for $NiFe_2O_4$ composites the sharp increase in the value of L is observed above 80 phr. Thus it can be assumed that the percolation limit of γ-Fe_2O_3 filled composites is between 60 and 80 phr and that of $NiFe_2O_4$ is between 80 and 100 phr loading.

It can be seen in figure 4.4 that when compared to carbon black loaded composites, the ferrite filled composites show better dispersion of fillers. Even the RFCs with carbon black, possess lower values of L when compared with carbon black filled composites, except for the one with 80 phr carbon black and 100 phr nickel ferrite. Thus, the incorporation of carbon black along with nickel ferrite shows better processability compared to the carbon black filled EPDM composites.
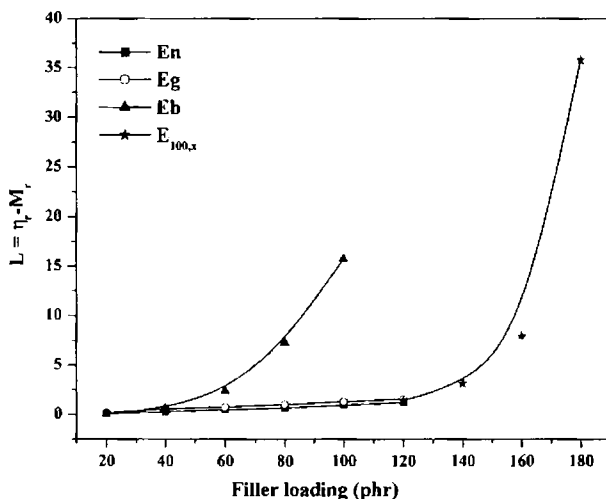
Figure 4.4 Variation of parameter L for the ferrite filled RFCs, carbon black loaded RFCs and carbon black filled composites

4.4 Cure rate index and cure kinetics of RFCs

The cure rate index (CRI) [9,10], a parameter which indicates the speed of a curing reaction and rate constant of the cure reactions were determined from the rheometric data. CRI is calculated using the relation

$$CRI = 100/(curetime\text{-}scorch\ time) \qquad 4.2$$

The kinetics of a first order chemical reaction can be expressed by the following equation [11-13]

$$\ln(a-x) = -kt + \ln a \qquad 4.3$$

where a is the initial concentration of the reactant, x is the concentration at any instant of time t and k is the reaction constant

For the vulcanisation of rubber, crosslinking can be considered as a first order chemical reaction and the rate of reaction can be monitored by measuring the torque developed during vulcanisation. The torque obtained is proportional to the modulus of the rubber. The following substitutions in equation 4.3 are made,

$$(a-x) = M_h - M_t \qquad 4.4$$

$$a = M_h - M_0 \qquad 4.5$$

where M_h is the maximum torque, M_0 is minimum torque and M_t is the torque at time t.

So the equation 4.3 can be rewritten as

$$\ln(M_h - M_t) = -kt + \ln(M_h - M_0) \qquad 4.6$$

If the plot of $\ln(M_h - M_t)$ against time is a straight line, then it indicates that the cure reaction follows first order kinetics. The rate constant (k) of the cure reaction is directly obtained from the slope of the straight line.

The energy of activation E_a for curing also can also be determined using the Arrhenius equation

$$k = A \exp(-E_a/RT) \qquad 4.7$$

where A is the Arrhenius constant, R is the universal gas constant and T is the temperature in absolute scale [14].

4.4.1 Cure rate index

Cure rate index of cure reactions of different composites were estimated as per equation 4.2 and shown in figure 4.5.

Cure rate index is found to increase with loading for all the composites which indicates that the incorporation of fillers increases the rate of cure reaction.

Both carbon black and nickel ferrite loaded composites exhibit almost the same cure rate index at lower filler loadings and deviations are observed only at 100 phr and above.
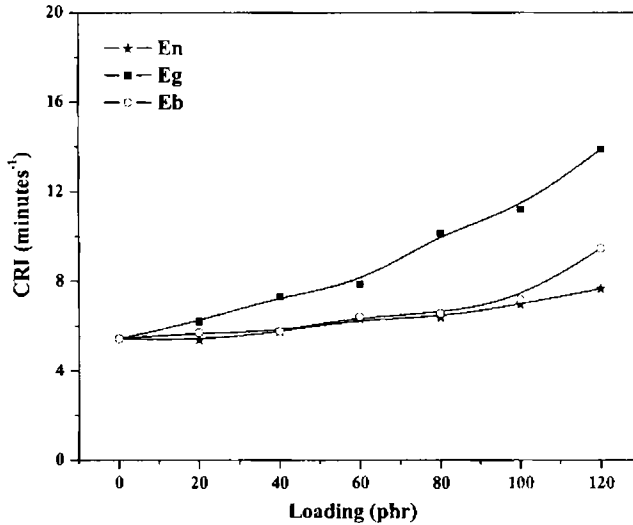
Figure 4.5 Cure rate indexes of NiFe₂O₄ and γ-Fe₂O₃ filled RFCs and carbon black filled composites.

Among the three fillers, gamma ferric oxide has the highest CRI values; pointing to the fact that gamma ferric oxide activates the cure reaction of EPDM rubber higher than the other two fillers. This is supported by the lower cure times obtained for the RFCs with γ-Fe₂O₃ as given in table 4.3.

4.4.2 Cure kinetics

The plot of $\ln(M_h-M_t)$ versus time t of the elastomer compounds is shown in figure 4.6. They are found to be linear which proves that the cure reactions proceed according to first order kinetics. From the slope of the straight lines, the corresponding rate constants were computed.

Cure rate constant is found to increase with ferrite content. A comparison of cure rate index and cure reaction constant is given in figure 4.7. Both cure rate index and cure reaction constant, increase with NiFe₂O₄ loading. The increase in CRI and cure reaction constant with ferrite loading indicates the activation of cure reaction [15-17].
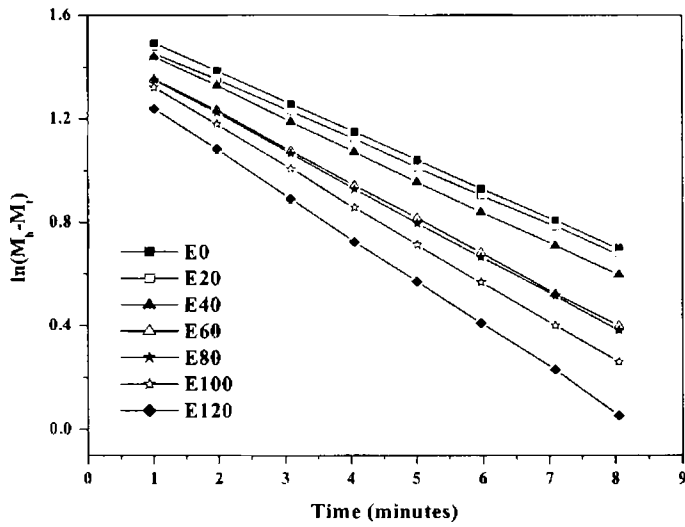
Figure 4.6 ln(M_h-M_t) vs time of RFCs with NiFe_2O_4 as the filler
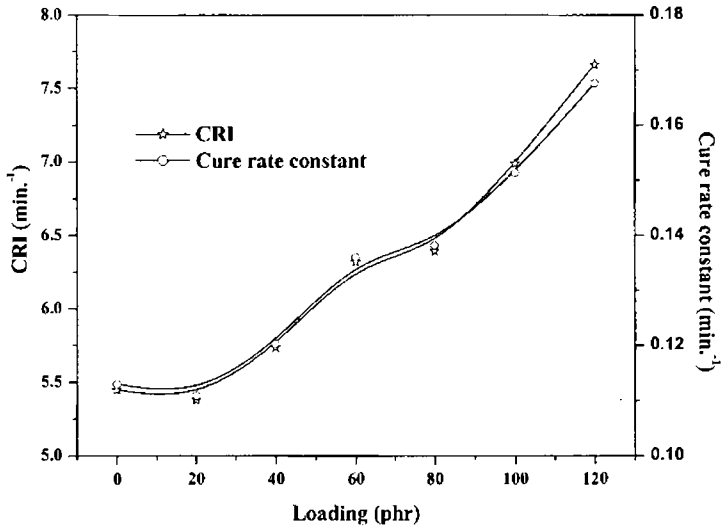
Figure 4.7 Cure rate index and cure reaction constant of NiFe_2O_4 filled RFC

Cure kinetics of carbon black filled RFCs were also determined from the rheometric torque values and are plotted in figure 4.8. The plot of $\ln(M_h-M_t)$ vs time is found to be a straight line. Thus the cure reaction of EPDM based RFCs does not deviate from first order kinetics even with the additional loadings of carbon black.
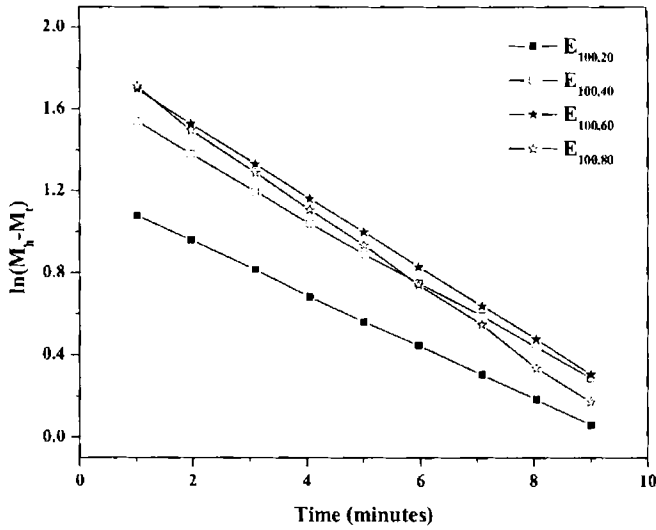
*Figure 4.8 ln(M_h-M_t) vs time of RFCs containing 100 phr NiFe_2O_4
and various loadings of carbon blacks*

The cure rate index and cure reaction constants of carbon black filled RFCs are plotted and shown in figure 4.9. Both the cure rate index and cure reaction constant increases with increase in carbon black loading.
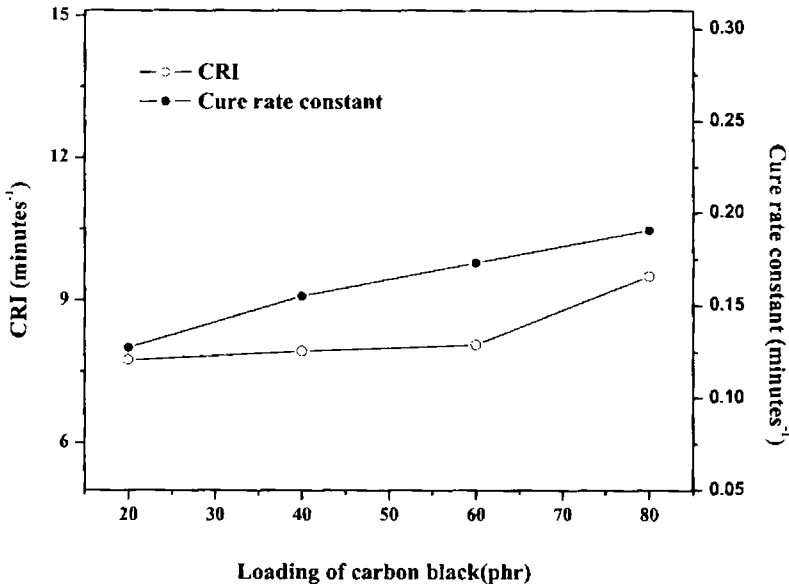
*Figure 4.9 Cure rate index and cure reaction constant of RFCs
with different loadings of carbon black*

4.4.3 Cure kinetics and energy of activation of γ-Fe₂O₃ filled RFCs

The plot of $\ln(M_h-M_t)$ of γ-Fe$_2$O$_3$ filled RFCs versus time t of the EPDM compounds at three different temperatures (150°C, 160°C and 170°C) is shown in figures 4.10 to 4.12. Cure reaction constants were determined from the slope of these lines. The straight line graphs are indicative of first order kinetics of cure reaction. The cure reaction constants obtained at the three different temperatures are shown in table 4.7. As the temperature increases, the cure rate constant also increases.
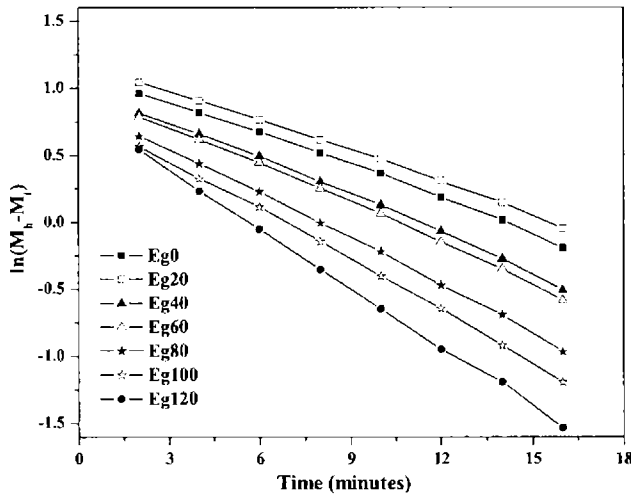
Figure 4.10 ln(M$_h$-M$_t$) vs time of γ-Fe$_2$O$_3$ filled RFCs at 150 °C
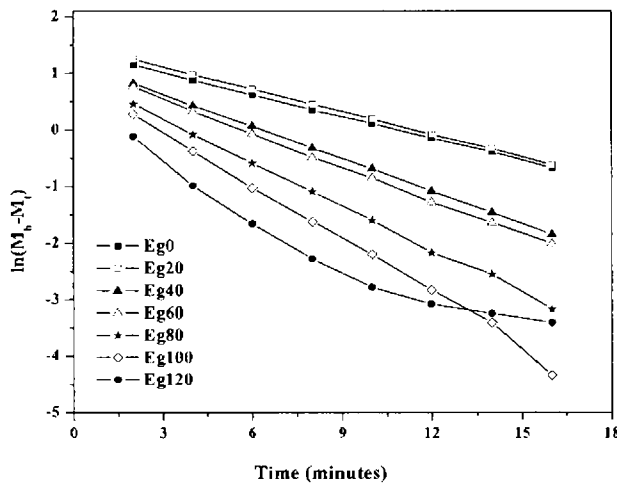
Figure 4.11 ln(M$_h$-M$_t$) vs time of γ-Fe$_2$O$_3$ filled RFCs at 160 °C
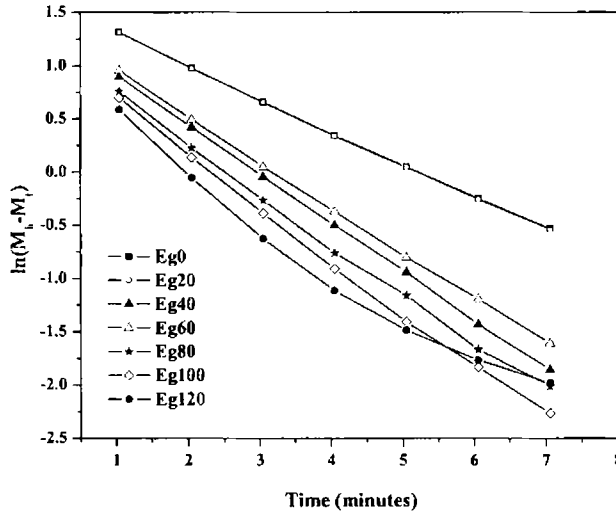
Figure 4.12 ln(M_h-M_t) vs time of γ-Fe_2O_3 filled RFCs at 170 °C

From the Arrhenius equation, the energy of activation is calculated by plotting log k against 1/T according to the equation,

$$\log k = \log A - E_a/2.303RT \qquad\qquad 4.8$$

The plot of log k versus 1/T is shown in figure 4.13. From the slope of the straight lines, the corresponding activation energies were calculated according to equation 4.8. The energy of activation at different loadings is tabulated in table 4.7.
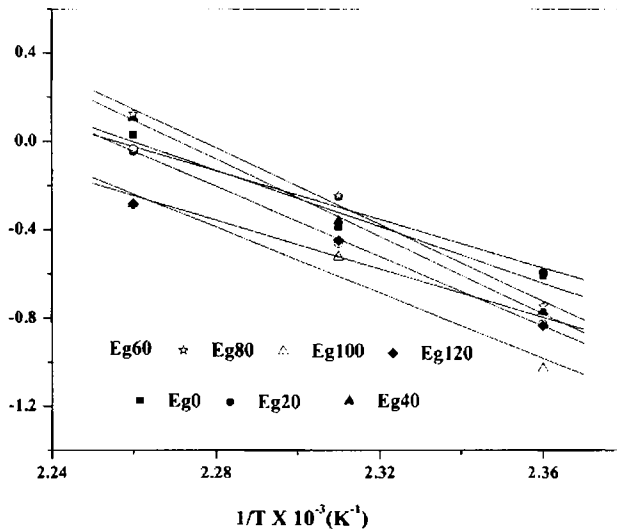
Figure 4.13 log k versus 1/T of the RFCs

*Table 4.7 Cure rate constants at different temperatures and activation
energy of γ-Fe₂O₃ filled RFCs*

Sample	Cure rate constant (min.⁻¹)			E_a (KJ/mol)
	150°C	160°C	170°C	
Eg0	0.0816	0.1293	0.3065	103
Eg20	0.0769	0.1830	0.3079	108
Eg40	0.0937	0.1903	0.4252	118
Eg60	0.0975	0.1979	0.4579	120
Eg80	0.1145	0.2560	0.4634	109
Eg100	0.1254	0.3182	0.4938	107
Eg120	0.1467	0.3572	0.5204	99

Upto 60 phr loading, the activation energy is found to increase with increase in filler content and then decreases. Normally, faster reactions (higher k) yield lower values of activation energy. Initial increase in activation energy can be attributed to the decrease in volume fraction of the rubber on which the rate of reaction depends. But at higher concentrations of the filler, contrary to the expectations, a decreasing trend is observed. One of the reasons would be the outweighing effect of cure activation by the fillers over the decrease in volume fraction of the matrix.

4.5 Mechanical properties of RFCs

The properties and performance of a rubber product depend on many factors including the chemical nature of the rubber, the amount and kinds of ingredients incorporated into the rubber compound, processing and vulcanising conditions, design of the product and service conditions. Among different ingredients, fillers play an important role in determining the final vulcanisate properties. Fillers can be either reinforcing or nonreinforcing. The crucial characteristics that decide the reinforcing capability of the fillers are size, shape, specific surface area and a combination of the size distribution and shape [9,18].

Earlier studies conducted on natural rubber based RFCs revealed the semi reinforcing nature of ferrite fillers on the matrix [19,20]. The mechanical properties of RFCs based on EPDM and nickel ferrite/gamma ferric oxide were studied and analysed in the following sections.

4.5.1 Stress-strain properties of RFCs

4.5.1.1 Tensile strength

Mechanical properties namely tensile strength, 300% modulus and elongation at break were determined using a Shimadzu, Universal testing machine (model SPL 10 kN) at a cross head speed of 500 mm/min. Stress-strain measurements were carried out as per ASTM D 412-98a (2002).

The variation of tensile strength of $NiFe_2O_4$ and γ-Fe_2O_3 filled EPDM based RFCs is shown in Figure 4.14. In both the set of composites, tensile strength increases with filler loading, reaches a maximum value and then decreases.
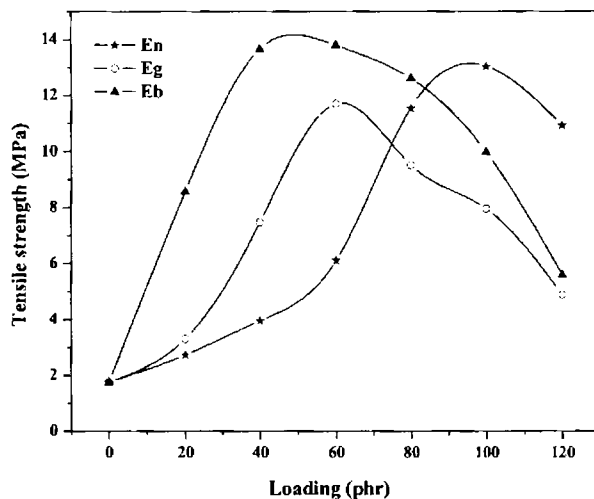
Figure 4.14 Variation of tensile strength with loading of $NiFe_2O_4$, γ-Fe_2O_3 and HAF filled EPDM based composites

For $NiFe_2O_4$ filled composites, maximum value of 13.03 MPa is obtained for 100 phr loading and for γ-Fe_2O_3 composites the maximum value is 11.7 MPa at 60 phr loading. The increase in tensile strength of the composites, speaks of the reinforcing nature of the filler. The enhancement in tensile strength is due to the larger surface area of the fillers since both the fillers are in the ultrafine regime (size ~20 nm). As the particle size decreases, the interface area between the filler and the elastomer increases which leads to better reinforcement characteristics.

For comparison, tensile strength of carbon black loaded composites are plotted with that of RFCs and are shown in figure 4.14. Carbon black filled composites have high tensile values at lower loadings and maximum tensile strength is attained between 40 to 60 phr loading. Almost the same tensile strength is obtained for nickel ferrite filled RFCs at 100 phr loading.

The reinforcing index (RI) is calculated as per the equation [21]

$$RI = \frac{N \times 100}{N_0 \times filler\%} \qquad 4.9$$

where N and N_0 are nominal values of the mechanical properties of the composites with and without the filler, respectively. Reinforcing index is an empirical parameter and represents reinforcement effect on a mechanical property.
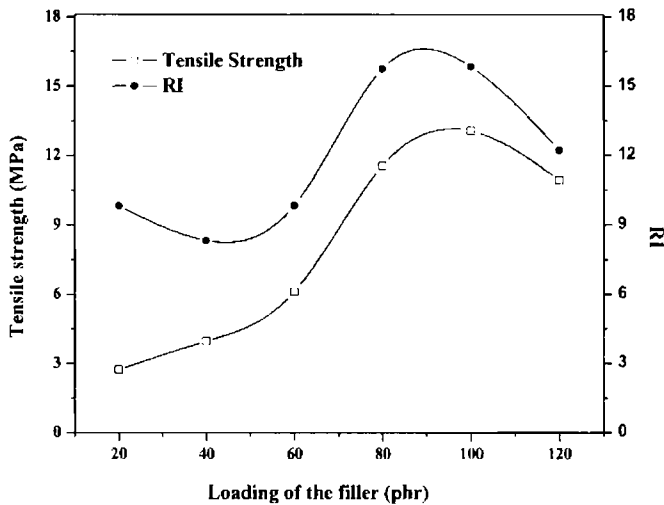
Figure 4.15 Comparison of tensile strength and RI of NiFe₂O₄ composites

Figures 4.15 and 4.16 depicts the comparison of reinforcing index with the tensile strength values of $NiFe_2O_4$ and γ-Fe_2O_3 filled EPDM based RFCs.

In both sets of RFCs, the variation of reinforcing index with filler loading is identical to the variation of tensile strength with filler loading. For $NiFe_2O_4$ based composites, a maximum reinforcing index and tensile strength value lies in between
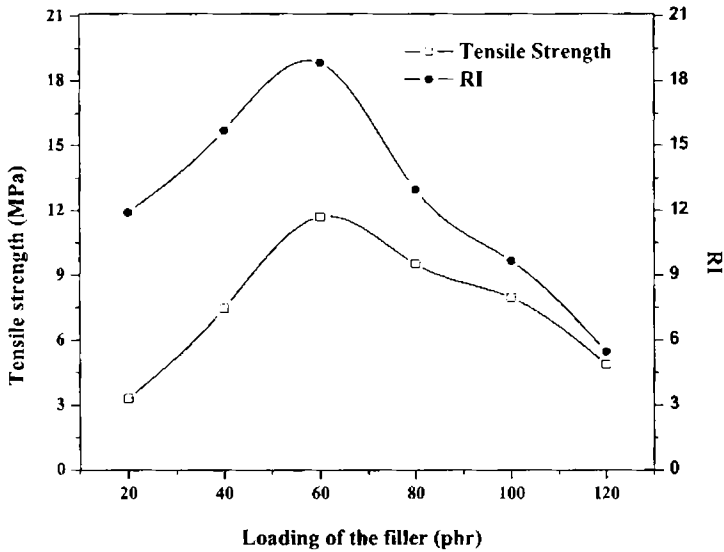
Figure 4.16 Comparison of tensile strength and RI of γ-Fe₂O₃ composites

80 and 100 phr loading. Where as in the case of γ-Fe$_2$O$_3$ based RFCs, the maximum value obtained is at 60 phr loading. This indicates that the percolation limit for NiFe$_2$O$_4$ is approximately 100 phr and that for γ-Fe$_2$O$_3$ is about 60 phr. These observations are well supported by the Lees approach discussed in section 4.4.5.

4.5.1.2 Tear strength

Figure 4.17 shows the variation in tear strength of NiFe$_2$O$_4$ and γ-Fe$_2$O$_3$ filled RFCs with filler loading. Tear strength of RFCs increases with loading, proclaiming the reinforcing qualities of the ferrites in EPDM matrix. In a matrix containing fillers, the filler interacts with the elastomer chains and create a barrier for the tear path. Filler particles present at the propagation tip arrest the propagating cracks and thus increase the tear strength [22]. Gamma ferric oxide filled RFCs show higher tear strength values indicating better reinforcing nature of this filler than nickel ferrite particles.
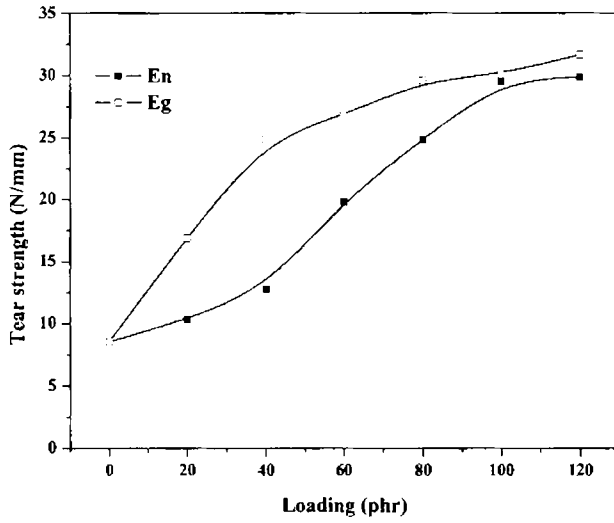
Figure 4.17 Tear strength of NiFe₂O₄ and γ-Fe₂O₃ filled RFCs.

4.5.1.3 Elongation at break

For RFCs with $NiFe_2O_4$/ γ-Fe_2O_3, elongation at break were estimated and shown in figure 4.18. RFCs containing gamma ferric oxide display higher elongation at break values when compared to nickel ferrite filled RFCs.
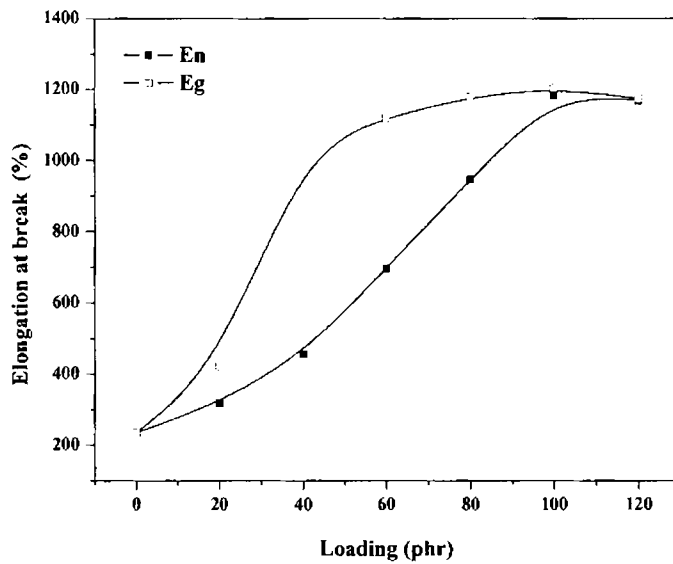
Figure 4.18 Variation of elongation at break of NiFe₂O₄ and γ-Fe₂O₃ filled RFCs.

Elongation at break increases with filler loading in both types of RFCs. Increase in elongation at break with filler loading is due to the increase in the stress bearing capacity of the filler-matrix interface. This again supports the reinforcing nature of ferrite fillers.

4.5.1.4 Modulus

Modulus at 300% elongation is plotted against filler loading, in figure 4.19. For both set of RFCs, modulus values are found to increase gradually with filler loading. Lower modulus values obtained for the γ-Fe_2O_3 filled RFCs can be accounted for, by the reduced porosity of γ-Fe_2O_3 particles. Nickel ferrite particles are more porous and provides higher modulus compared to gamma ferric oxide.
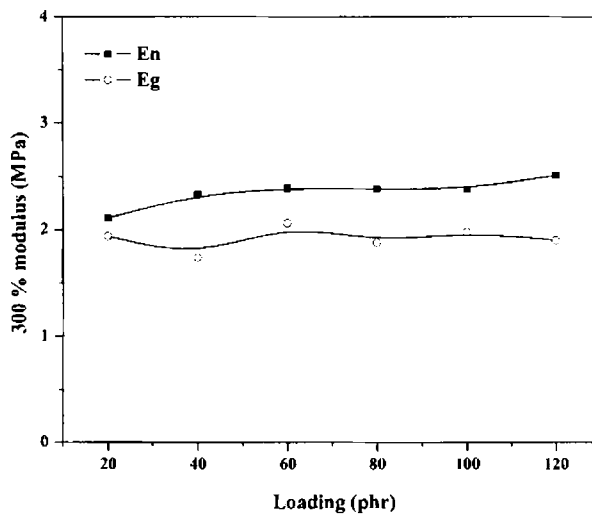
Figure 4.19 Variation of modulus at 300% elongation of NiFe₂O₄ and γ-Fe₂O₃ filled RFCs

4.5.2 Hardness

Variation of hardness for nickel ferrite and gamma ferric oxide filled RFCs with filler loading is depicted in figure 4.20. Hardness values increase with filler concentration. $NiFe_2O_4$ filled RFCs are found to give higher hardness than γ-Fe_2O_3 composites. Since hardness represents a measure of modulus at low strains, comparatively lower values are as expected for γ-Fe_2O_3 composites.
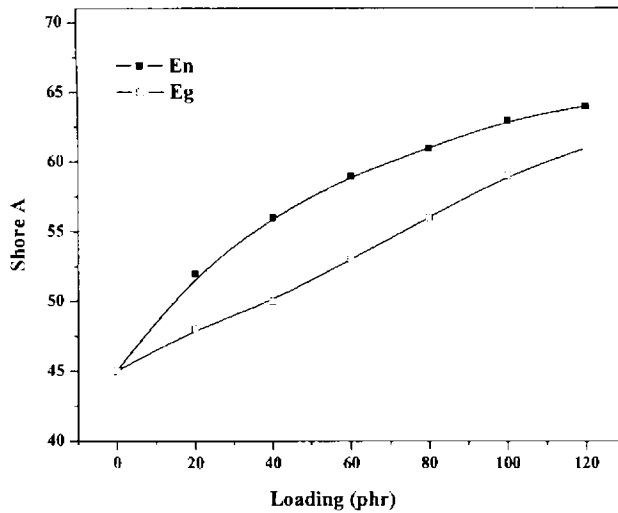
Figure 4.20 Variation of hardness of NiFe₂O₄ and γ-Fe₂O₃ filled RFCs

4.6 Mechanical properties of carbon black filled composites

The mechanical properties of EPDM based composites with carbon black filler is shown in table 4.8. These composites display better stress strain properties as well as other mechanical properties like tear strength and hardness. Percolation limit of these composites is found to be at about 40 phr loading. On comparing the mechanical properties of the RFCs with the carbon black filled composites, it can be observed that ferrite filled composites exhibit semi reinforcing characteristics.

Table 4.8 Mechanical properties of carbon black filled composites

Loading (phr)	Tensile strength (MPa)	Elongation at break (%)	Tear strength (N/mm)	Modulus at 100% elongation (MPa)	Hardness (Shore A)
20	8.56	426	32.3	1.18	50
40	13.66	362	43.4	2.01	55
60	13.8	339	46.3	2.96	60
80	12.62	234	47.8	4.59	65
100	9.98	104	32.8	7.56	70
120	5.59	148	31.8	4.42	75

Mechanical properties of RFCs with 100 phr nickel ferrite and different loadings of carbon black are represented in table 4.9.

Table 4.9 Mechanical properties of RFCs containing 100 phr NiFe₂O₄
and different loadings of carbon black

Sample	Tensile strength (MPa)	Elongation at break (%)	Tear strength (N/mm)	Modulus at 100% elongation (MPa)	Hardness (Shore A)
E_{100}	13.05	1091	29.5	1.35	63
$E_{100,20}$	8.04	687	39.3	2.4	67
$E_{100,40}$	7.84	566	40.4	2.28	73
$E_{100,60}$	6.52	376	36.5	3.03	79
$E_{100,80}$	5.21	-	23.2	-	89

Tensile strength and elongation at break values of RFCs with carbon black decrease with increase in carbon black content, where as tear strength, modulus and hardness values are found to be enhanced. It can be noticed that, when carbon black alone is used as the filler, the maximum tensile strength is 13.8 MPa for 60 phr loading. In RFCs with carbon black, total loading of the filler ranges from 100 to 180 phr. So the dilution effect outweighs the reinforcing effect of the carbon black. At this high loading sufficient amount of elastomer may not be available for wetting the fillers. More over, at very high loading filler-filler interaction will be very high leading to filler agglomeration. The mechanical properties of the carbon black loaded RFCs are lower compared to EPDM composites with carbon black/ferrite filler alone. The carbon black filled RFCs are found to be good microwave absorbers, which justify the preparation of RFCs with carbon black.

4.7 Swelling studies of RFCs

Swelling studies of the RFCs were carried out as explained in section 2.4.6, using toluene as the penetrant solvent. The diffusion, sorption and permeation coefficients were calculated according to the equations 2.13, 2.14 and 2.15.

The sorption curves of the EPDM gum and nickel ferrite filled vulcanisates at room temperature are presented in figure 4.21. It can be seen from the sorption curves of the samples that the initial swelling rate is very high owing to the large concentration gradient. This keeps the polymer sample under intense solvent stress. As the concentration gradient decreases with advancing swelling, the swelling rate decreases and the concentration difference becomes negligible at equilibrium swelling. The equilibrium mole% uptake decreases with increase in loading of the

filler as evident from the figure 4.21. The decrease in mole% uptake is due to the decrease in volume fraction of elastomer with loading.
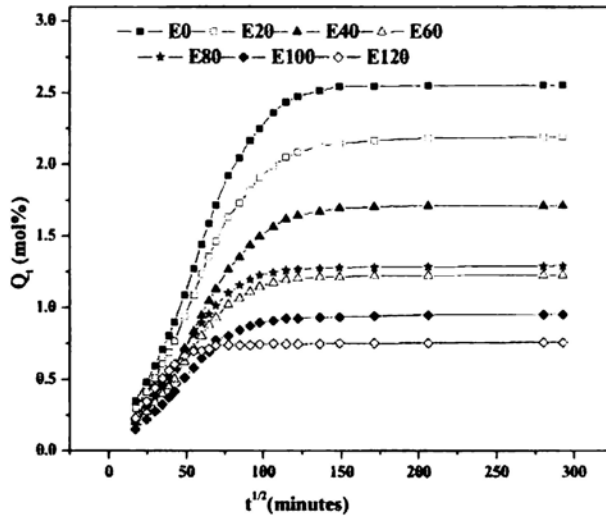
Figure 4.21 Sorption curves of NiFe$_2$O$_4$ composites

The mechanism of penetrant transport into the elastomer network can be analysed using an empirical relation of the form [23]

$$\log Q_t/Q_\infty = \log k + n \log t \qquad\qquad 4.10$$

where Q_t is the mole % uptake at time t, Q_∞ is the equilibrium mole % uptake and k is a constant. Value of n determines the mode of transport of solvent through rubber compound which depends upon many factors such as chemical nature of rubber and vulcanising agents [24], dimension and shape of the filler particles, rubber-filler compatibility and interfacial adhesion. The liquid diffusion can be Fickian, non-Fickian or anomalous, depending upon the value of 'n'. When n is 0.5, the mechanism is known as Fickian. Here, the rate of polymer chain relaxation is higher compared to the diffusion rate of penetrant. When n = 1, the transport process corresponds to a mechanism where chain relaxation is slower than liquid diffusion, which is expected for rigid polymers. When the value of n is in between 0.5 and 1, transport behaviour is termed as anomalous where rearrangement of polymer molecules occurs at a comparable rate to that of the change of concentration [25].

The parameter 'n' for $NiFe_2O_4$ composites is shown in table 4.10. The value of n is found to be greater than 0.5, which indicates anomalous behaviour.

Table 4.10 The values of 'n' for NiFe₂O₄ composites

Sample	n
E0	0.55
E20	0.53
E40	0.51
E60	0.50
E80	0.56
E100	0.57
E120	0.58

As filler loading increases, the value of n decreases upto 60 phr loading and then increases. The initial decrease in n indicates that the polymer relaxation is higher compared to the rate of diffusion of the penetrant, which is due to the intervene effect of fillers between polymer chains. Polymer chain mobility may be restricted at higher concentration due to the increased population of filler particles in between the chains.
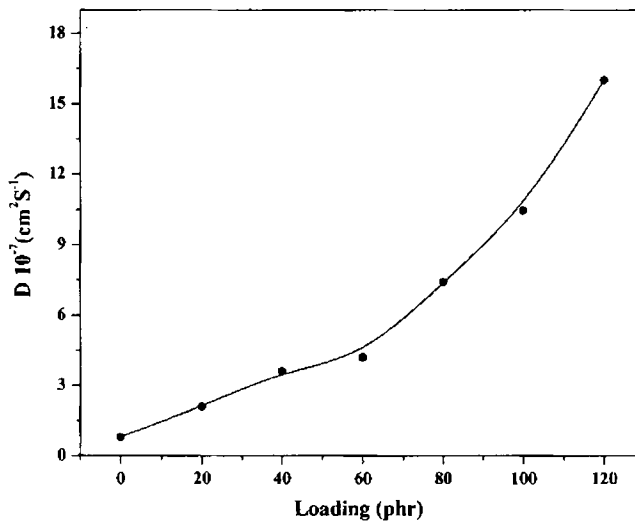
Figure 4.22 Variation of diffusion coefficient of NiFe₂O₄ composites with loading

During diffusion, the polymer swells and mass flow takes place in addition to the molecular diffusion. Diffusion coefficients which have been corrected for mass flow are termed as intrinsic diffusion. Figure 4.22 shows the variation of intrinsic diffusion coefficient of the nickel ferrite filled composites. As the loading increases, the diffusion coefficient increases. The increase is gradual at lower filler concentration and becomes higher above 60 phr loading.

Transport of penetrant molecules through polymer proceeds via a two stage sorption and diffusion process. At first, the penetrant molecules are sorbed by the polymer followed by diffusion. Diffusivity is a kinetic parameter which depends on the polymer segmental mobility. Incorporation of fillers separate the polymer chains allowing the diffusion of penetrant molecules through the rubber phase. This can increase the diffusion coefficient. The larger diffusion coefficient at higher filler
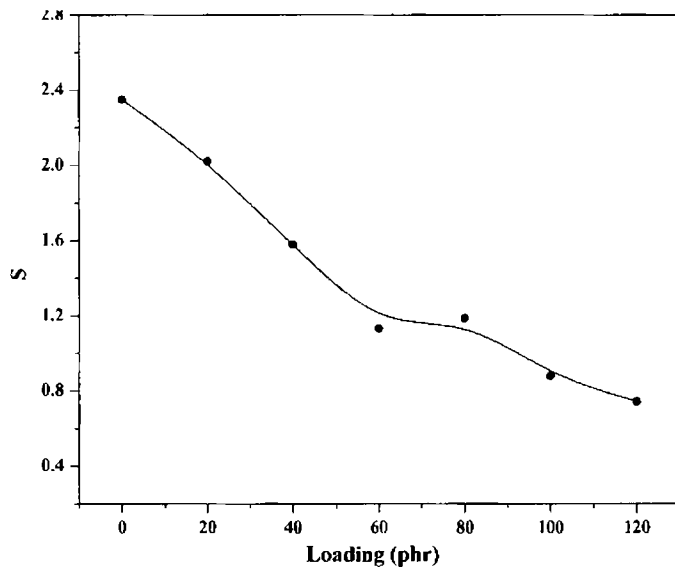
Figure 4.23 Variation of sorption coefficient of NiFe₂O₄ composites with loading

loadings may be due to the formation of some channels, which promote diffusion through the filler aggregates. Moreover, the non polar nature of both the penetrant and rubber support the diffusion of the solvent through the medium.

The variation of sorption coefficient is plotted in figure 4.23 which decreases with loading. As the loading increases, the volume fraction of polymer

decreases. Consequently, sorption decreases as the available polymer surface for diffusion decreases.
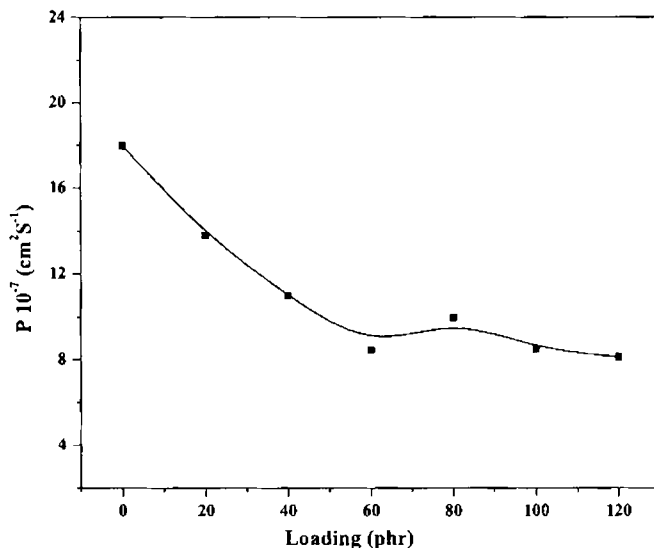
Figure 4.24 Permeation coefficients of NiFe₂O₄ composites

Figure 4.24 shows the variation of permeation coefficient of the RFCs with loading. Permeation coefficient decreases with loading as in the case of sorption coefficient. Permeation coefficient is a characteristic parameter, reflecting collective processes of diffusion and sorption. Hence, it can be concluded that in nickel ferrite filled EPDM based RFCs, permeability is controlled significantly by the process of sorption.

4.8 Morphology

Morphology of RFCs were studied using Scanning electron microscopy and Electron spin resonance technique or Electron paramagnetic resonance spectroscopy. Figure 4.25 shows the first derivative EPR spectrum of nickel ferrite and figure 4.26 shows the EPR spectra of gum vulcanisate of EPDM. Representative EPR signals of RFCs are given in figures 4.27 to 4.29.
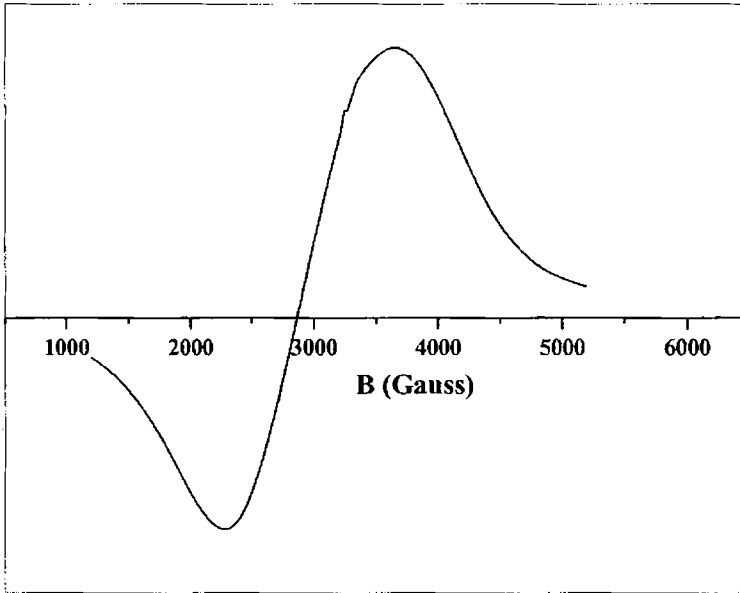
Figure 4.25 EPR spectra of nickel ferrite
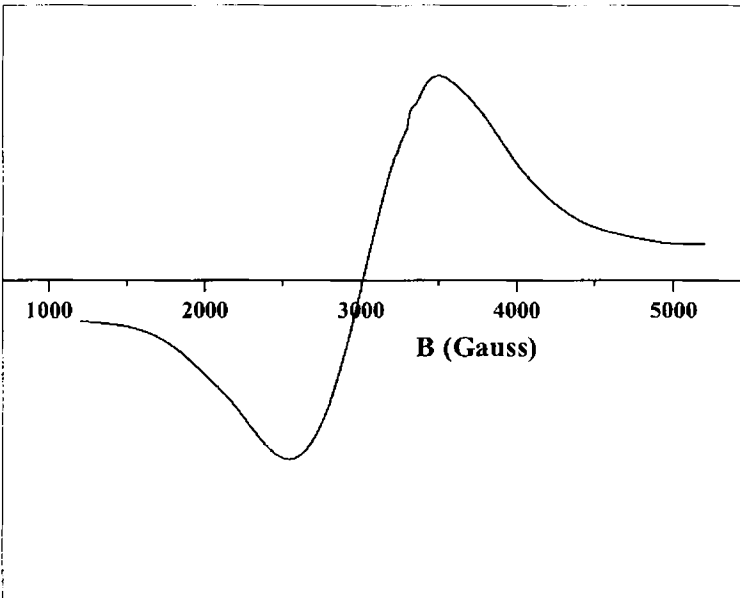
Figure 4.26 EPR spectra of EPDM gum vulcanisate
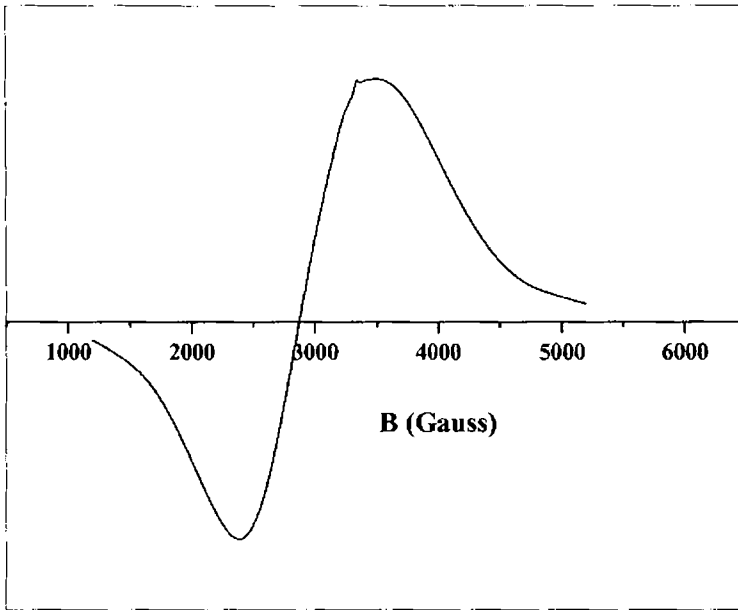
Figure 4.27 EPR spectra of RFC with 80 phr NiFe$_2$O$_4$
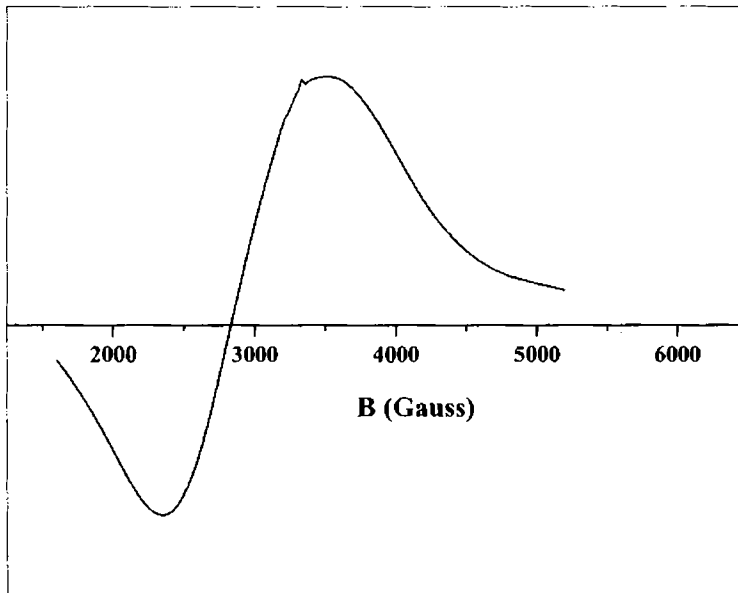
Figure 4.28 EPR spectra of RFC with 100 phr NiFe$_2$O$_4$
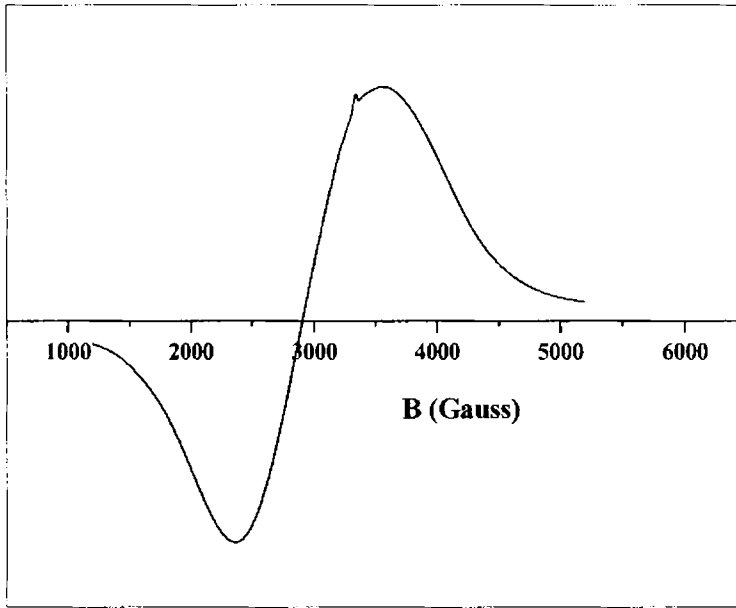
Figure 4.29 EPR spectra of RFC with 100 phr NiFe₂O₄ and 60 phr carbon black

From the analysis of the EPR data for RFCs with different loadings of nickel ferrite, the following can be inferred. The EPR signals have symmetrical line shape and deviations can be observed as the filler loading increases. The EPR signal of RFC with 100 phr nickel ferrite is slightly asymmetric as shown in figure 4.28. The g values and line width of the signals are tabulated in table 4.11.

Table 4.11 EPR parameters of NiFe₂O₄ and RFCs

Sample	'g'	Line width (G)
NiFe₂O₄	2.24	1380
E0	2.19	990
E40	2.24	1180
E60	2.27	1050
E80	2.26	1150
E100	2.27	1170
EB20	2.24	1140
EB60	2.24	1190

The small signal at about 3400 G in all the EPR signals is due to the presence of tetra cyano ethylene radical introduced into the cavity during the measurement, the 'g' value of which is 2.00277. 'g' values of the samples are calculated from the corresponding signals and are shown in table 4.11. 'g' value of nickel ferrite is approximately 2.24 and all RFCs have the same 'g' value. In the case of gum vulcanisate there are three possibilities for radical generation. (1) Due to the decomposition of dicumyl peroxide that is used as the curing agent. (2) Formation of radical sites by chain scission during processing. (3) From the catalysts used for the synthesis of EPDM rubber. The first two possibilities can be ruled out because of the fact that radicals generated from dicumyl peroxide can not be long lived as they get stabilised. Any radical formed during processing, cannot live long, since they combine together resulting in chain extension. According to the third option, a permanent signal is possible. Synthesis of EPDM rubber involves the use of Ziegler Natta catalyst which is a transition metal complex. The EPR signal of EPDM gum vulcanisate is due to the traces of this catalyst. A similar result is reported for polyisobutylene rubber [26].

The symmetrical line shape of RFCs in the EPR spectrum compliments the findings on dispersion of filler aggregates [27]. The asymmetrical nature of the EPR signal of RFC with 100 phr $NiFe_2O_4$, indicate the percolation limit of the filler in the elastomer medium. Asymmetrical line shape is expected for RFCs loaded with carbon black. Contrary to expectations, rather symmetrical signals are observed for them, which might be due to the reinforcing nature of the carbon black compared to the ferrite filler, which can be termed as semireinforcing. Insignificant change in line width also indicates the complete dispersion of ferrites within the matrix. These conclusions have complimenting evidences from SEM studies. Representative micrographs are shown in figures 4.30 to 4.32.

Figure 4.30 indicates that the filler is well dispersed at 80 phr loadings and the presence of agglomerates is not observed. Figure 4.31 is the SEM image and mapping picture of RFC with 100 phr $NiFe_2O_4$. An increase in the aggregate concentration can be clearly observed in this figure. The mapping picture gives an idea about the aggregate distribution. At some points increased concentration of the filler aggregates can be observed.

Figure 4.30 SEM image of RFC with 80 phr NiFe₂O₄
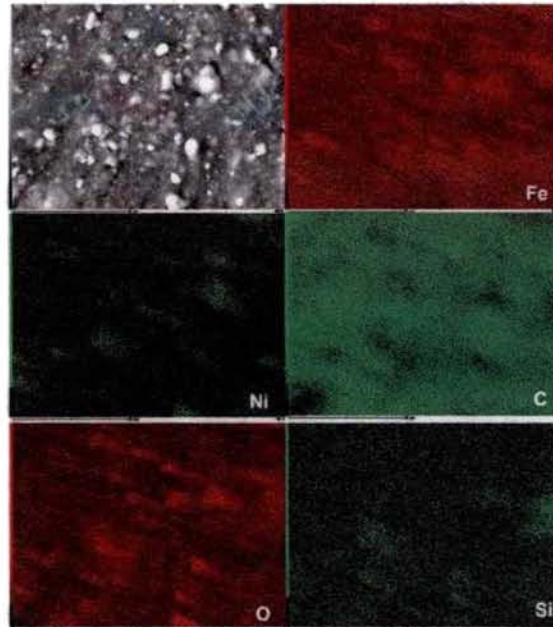
Figure 4.31 SEM image and mapping picture of RFC with 100 phr NiFe₂O₄

Figure 4.32 shows the SEM image of RFC with 100 phr NiFe$_2$O$_4$ and 60 phr carbon black at higher magnification. The presence of filler agglomerates is very clear in this micrograph. The presence of agglomerates as evidenced in the micrograph is

probably one of the reasons attributable to the reduced tensile strength of these composites at loadings greater than 80 phr.
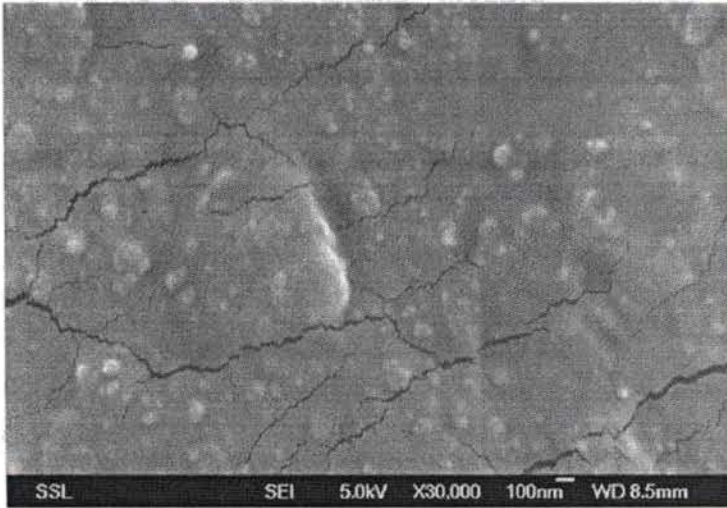
Figure 4.32 SEM image of RFC with 100 phr NiFe₂O₄ and 60 phr carbon black

4.9 Thermogravimetric analysis

Thermogravimetric analysis of gamma ferric oxide filled RFCs were carried out in the temperature range 30°C to 800°C. The thermograms of RFCs filled with γ-Fe_2O_3 are plotted in figure 4.33.
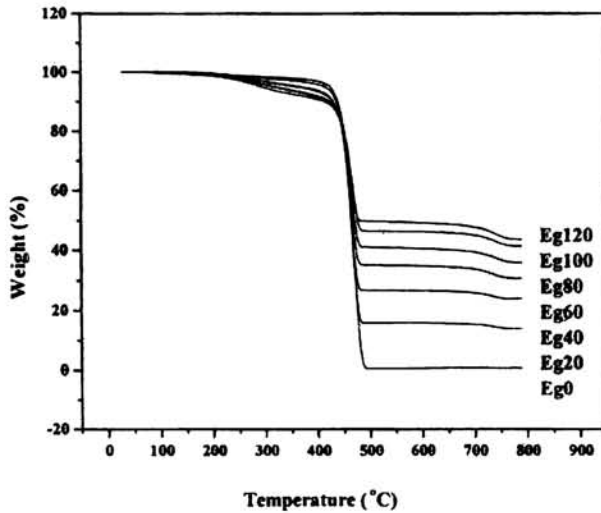
Figure 4.33 Thermograms of γ-Fe₂O₃ filled RFCs

Thermogravimetric data of γ-Fe_2O_3 filled RFCs is tabulated in table 4.12. From the figure 4.33 it can be seen that the onset of degradation temperature and temperature at maximum degradation of the RFCs shows insignificant change with increase in filler content. Moreover, the rate of degradation shows regular decrease with increase in filler loading. All these observations indicate the thermal stability of the RFCs.

Table 4.12 Characteristics of thermograms of γ-Fe_2O_3 filled RFCs

Sample	Onset degradation temperature (°C)	Temperature at maximum degradation (°C)	Rate of degradation (%/°C)	Weight loss at maximum degradation (%)	Residue (%)	Expected residue (%)
Eg0	379	470	2.95	96.9	0.90	-
Eg20	390	466	2.61	80.1	14.0	15.87
Eg40	386	463	2.21	67.5	24.1	27.03
Eg60	378	464	1.87	59.0	30.8	35.3
Eg80	391	464	1.54	50.8	36.0	41.7
Eg100	393	467	1.38	44.9	41.5	46.4

Thermal stability of the composites is not affected by the incorporation of ferrite fillers. Weight loss at maximum degradation and residue gives complementary information about the thermal degradation of the composites. Weight loss at maximum degradation decreases, where as, percentage of residue increases with loading. Weight loss at maximum degradation is due to the degradation of the rubber which decreases with increase in filler loading. However the residue obtained is slightly less than the calculated value. This may be due to the loss of some amount of ingredients during the processing of the composites.

4.10 Conclusion

Rubber ferrite composites were prepared by incorporating nickel ferrite and gamma ferric oxide separately into EPDM matrix. Composites with different loadings of carbon black along with ferrite were also prepared. For comparing the

processability and reinforcing nature of the ferrites, a set of carbon black filled EPDM composites were prepared under similar experimental conditions.

X-ray diffraction pattern of RFCs revealed that no structural changes occurred to the ferrite during the preparation of RFCs. Studies on cure characteristics of RFCs indicated that the addition of magnetic fillers reduced both scorch time and cure time. The maximum torque of RFCs decreased with the addition of the ferrite filler, where as it increased with the incorporation of carbon black. The processability studies revealed that the filler agglomeration occurred for nickel ferrite composites above 100 phr loading and for gamma ferric oxide composites above 60 phr loading. Cure kinetic studies showed first order kinetics for cure reactions of RFCs. The speed of cure reaction was found to increase with the addition of ferrites in both nickel ferrite and gamma ferric oxide based RFCs. The reinforcing effect of ferrites was less when compared to carbon black which shows that ferrites are semi reinforcing fillers. Addition of carbon black into RFC containing 100 phr nickel ferrite reduces mechanical properties. Morphological studies carried out on nickel ferrite filled RFCs revealed that filler dispersion in the matrix is uniform and the composite is homogeneous up to a loading of 100 phr.

References

1.   K.A. Malini, Ph.D.Thesis, Department of Physics, Cochin University of Science and Technology, Cochin, India, (2001).

2.   E.M. Mohammed, K.A. Malini, Philip Kurian and M.R. Anantharaman, Materials Research Bulletin, **37** (2002) 753.

3.   E.M. Mohammed, K.A. Malini, P.A. Joy, S.D. Kulkarni, S.K. Date, P. Kurian and M.R. Anantharaman, Plastics, Rubber and Composites, **31** (2002) 106.

4.   M.A. Soloman, Philip Kurian, M.R. Anantharaman and P.A. Joy, Indian Journal of Chemical Technology, **12** (2005) 582.

5.   M.A. Soloman, Philip Kurian, M.R. Anantharaman and P.A. Joy, Polymer-Plastic Technology and Engineering, **43** (2004) 1013.

6.   Maurice Morton, Rubber Technology, 3rd Edition, Van Nostrand Reinhold, NewYork, (1999).

7.   B.L. Lee, Rubber Chem.Technol., **52** (1979) 1019.

8.   H.M. da Costa, L.L.Y. Visconte, R.C.R. Nunes and C.R.G. Furtado, International Journal of Polymeric Materials, **53** (2004) 475.

9. C. M. Blow and C. Hepburn, Rubber Technology and Manufacture, 2nd Edition, Butterworths, London (1985).

10. A.A. Wazzan, International Journal of Polymeric Materials, 54 (2005) 783.

11. G. Mathew, C. Nah and J.M. Rhee and R.P. Singh, Journal of Elastomers and Plastics, 38 (2006) 43.

12. K. Fujimoto, T. Nishi and T. Okamoto, Int. Polym. Sci. Technol., 8 (1981) T/30.

13. G. Mathew, R.P. Singh, N.R. Nair and S. Thomas, J. Mater. Sci., 38 (2003) 2469.

14. A.I. Isayev and Brijesh Sujan, Journal of Elastomers and Plastics, 38 (2006) 291.

15. A.L.N. da Silva, M.C.G. Rocha, M.A.R. Moraes, C.A.R. Valente and F.M.B. Coutinho, Polym.Testing, 21 (2002) 57.

16. B.T. Poch, H. Ismail, E.H. Quah and P.L. Chin, J. Appl. Polym. Sci., 81 (2001) 47.

17. F.S. Deghaidy, Egypt. J. Sol., 23 (2000) 167.

18. S.H. Bidkar, A.G. Patil, U.R. Kapadi and D.G. Hundiwale, International Journal of Polymeric Materials, 55 (2006) 135.

19. K.A. Malini, E.M. Mohammed, S. Sindhu, P. Kurian and M.R. Anantharaman, Plastics, Rubber and Composites, 31 (2002) 449.

20. K.A. Malini, E.M. Mohammed, S. Sindhu, P.A. Joy, S.K. Date, S.D. Kulkarni, P. Kurian and M.R. Anantharaman, J. Mater. Sci., 36 (2001) 5551.

21. Shinzo Kohjiya and Yuko Ikeda, Rubber Chem. Technol., 73 (2000) 534.

22. M.T. Ramesan, Journal of Polymer Research, 11 (2004) 333.

23. J.S. Chiou and D.R. Paul, J. Polym. Eng. Sci., 26 (1986) 1218.

24. Aji P. Mathew, S. Packirisamy, M.G. Kumaran and Sabu Thomas, Polymer, 36 (1995) 4935.

25. J.L. Mateo, P. Bosch, J. Serrano and M. Calvo, European Polymer Journal, 36 (2000) 1903.

26. J.O. Brien, E. Cashell, G.E. Wardell and V.J. Mc Brierty, Rubber Chem. Technol., 50 (1977) 747.

27. Fracoise Boulic, Christian Brosseau, Yves Le Mest, Jean Loaec and Francois Carmona, J. Phys. D: Appl. Phys., 31 (1998) 1904.

Evaluation of Processability and Mechanical Properties of Neoprene Based Rubber Ferrite Composites

Polycrystalline ferrites are incorporated into elastomers to produce flexible magnets or rubber ferrite composites [1-4]. An appropriate selection of magnetic filler and matrix can result in RFCs with desired properties for different applications. Incorporation of ferrite modifies the dielectric and mechanical properties of the elastomer and at the same time makes them magnetic [5]. This chapter deals with the synthesis, processability studies and mechanical properties of neoprene based RFCs. Neoprene is a polar rubber characterised with appreciable ozone, weather and flame resistance and with medium oil resistance. The mechanical properties of neoprene based vulcanisates are comparable with that of natural rubber vulcanisates. The processability studies of the polymer composites are important since the products are to be moulded into the final finished shapes. This necessitates the evaluation of cure parameters like cure time, scorch time, maximum and minimum torque and different mechanical properties.

5.1 Synthesis of neoprene based rubber ferrite composites

Precharacterised nickel ferrite and gamma ferric oxide were incorporated into W grade neoprene rubber according to the recipe given in table 5.1. RFCs were prepared with ferrite fillers ranging from 40 to120 phr in steps of 20. A control compound was prepared without any filler. Mixing was carried out in a Brabender Plasticorder, Model PL 3S, at 50 rpm rotor speed and at 60°C, as per ASTM D3182-89 (2001). The mixed stock was homogenised using a two-roll mill at 0.8 mm nip gap and made in to sheets of 3 mm thickness.

Table 5.1 Recipe used for the preparation of $NiFe_2O_4$ and γ-Fe_2O_3 filled RFCs

Material	Loading (phr)
Neoprene	100
ZnO	5
MgO	4
Stearic acid	1
$NiFe_2O_4$ / γ-Fe_2O_3	X
Naphthaneic oil	5 % of X
NA22	0.5

Where X is 20,40,60,80,100 and 120 parts of nickel ferrite or gamma ferric oxide per hundred parts of neoprene rubber. The corresponding RFCs are represented as CRn and CRg respectively.

5.2 Cure characteristics

Cure characteristics of the RFCs were determined using a Rubber process analyser (RPA 2000 of Alpha technology) at a temperature of 160°C. From the RPA result, optimum cure time, scorch time and maximum and minimum torque values were determined.

5.2.1 Cure characteristics of $NiFe_2O_4$ filled neoprene based RFCs

Cure characteristics of RFCs based on $NiFe_2O_4$ filler and neoprene rubber is given in table 5.2. Cure time of the compounds increases with loading of the nickel ferrite. As the loading increases, the curatives may get adsorbed over the surface of the ferrite particles and its effective concentration may decrease. Consequently, the time required for the optimum cure increases. Scorch time of the compound increases with filler loading, which shows better processing safety. This may be due to adsorption of curatives over the active surface of the ferrite particles.

Table 5.2 Cure characteristics of NiFe$_2$O$_4$ filled neoprene based RFCs

Loading (phr)	Optimum Cure time, t$_{90}$ (minutes)	Scorch time, t$_{10}$ (minutes)	Maximum torque, D$_{max}$ (dNm)	Minimum torque, D$_{min}$ (dNm)
0	12.75	1.01	2.98	0.29
40	16.97	1.86	4.24	0.29
60	16.99	2.28	4.48	0.28
80	17.51	2.34	5.08	0.34
100	20.03	2.49	5.12	0.39
120	23.29	2.76	5.27	0.47

Maximum torque, which is a measure of the shear modulus increases markedly with increasing amount of NiFe$_2$O$_4$. Minimum torque, which gives a measure of the viscosity of the compound, increases with ferrite loading. Eventhough the minimum torque increases with filler content, it does not affect the processability of the compound. The increase in viscosity with addition of nickel ferrite is due to the occlusion of rubber within and between the filler aggregates and immobilisation of a layer of elastomer at the surface of the filler as seen in the case of EPDM based RFCs.

Wolf and Westlinning [6,7] proposed a mathematical expression in terms of rheometric data, which gives an idea about the bound structure of fillers in the vulcanisate, especially applicable for carbon black filled composites. By plotting the ratio of difference in maximum and minimum torque of the filled compound to that of the unfilled compound, a straight line is obtained, the slope of which is defined by Wolf as α$_F$ [8-11]

$$\frac{D_{max} - D_{min}}{D^0_{max} - D^0_{min}} - 1 = \alpha_F \frac{m_f}{m_p} \qquad 5.1$$

where D$^0_{max}$ and D$^0_{min}$ are the maximum and minimum torque of the unfilled compound and D$_{max}$ and D$_{min}$ are maximum and minimum torque of the filled compound. m$_f$ and m$_p$ are the mass of filler and mass of polymer in the compound and α$_F$ is filler specific constant which gives the final structure of the filler in the vulcanisate. The same expression is applied for RFCs and the dispersion of ferrite in the matrix is analysed.

Figure 5.1 shows the plot of $\dfrac{D_{max} \cdot D_{min}}{D_{max}^0 - D_{min}^0} - 1$ against m_f/m_p. The non-linear relationship of the relative torque to the filler loading indicates that the incorporation of nickel ferrite particles affect the crosslinking between the polymer chains.
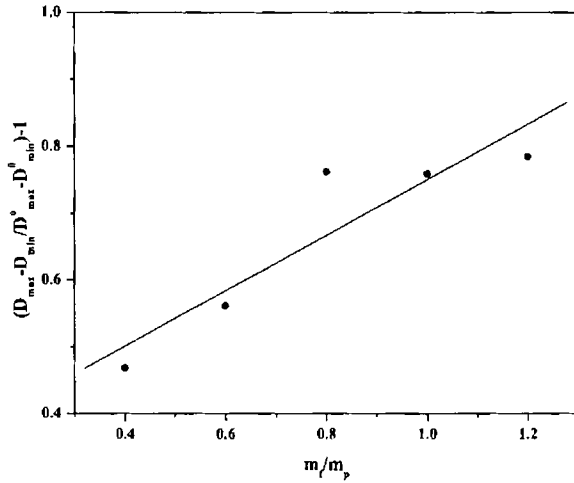
Figure 5.1 $\dfrac{D_{max} - D_{min}}{D_{max}^0 - D_{min}^0} - 1$ *against m_f/m_p*

Figure 5.2 shows the plot of Δ torque (D_{max}-D_{min}) against filler loading. Increase in Δ torque is linear at lower loadings, but at higher loadings deviation from linearity is observed.
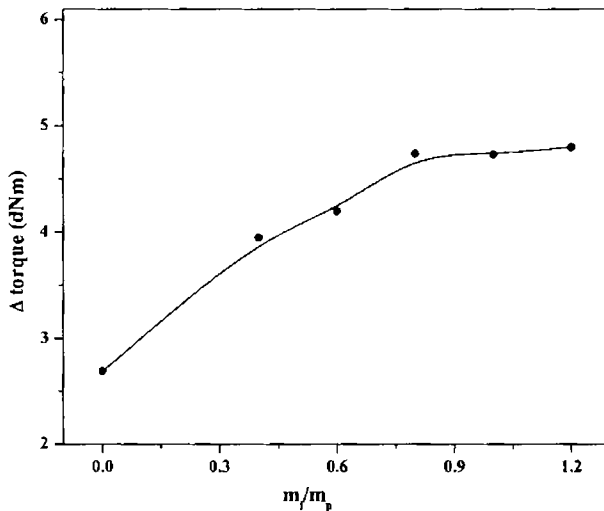
Figure 5.2 Variation of Δ torque with nickel ferrite loading

At lower filler concentration, the distance between the filler particle is high and the rubber chains are attached to single filler particle. This results in the formation of a gel like structure, which is uniformly dispersed through out the compound, resulting in a linear increase in Δ torque. As the filler loading increases, the filler-filler distance decreases. At this stage other than single segment attachments, inter particle attachment of the polymer chain occurs. Segmental mobility of the chain decreases further and a coherent gel type structure is formed and as a result, Δ torque deviates from linearity at higher filler loading.

Absolute value of α_F for each composite is calculated employing equation 5.1. The variation in α_F with filler loading is depicted in figure 5.3. The value of α_F decreases with nickel ferrite loading which indicates that even at higher loadings, nickel ferrite do not form agglomerates in the neoprene matrix.
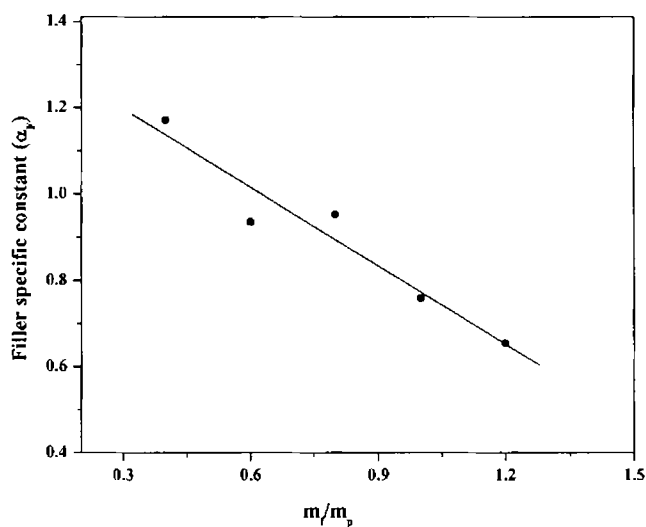
Figure 5.3 Variation of filler specific constant (α_F) against filler loading

5.2.2 Cure characteristics of γ-Fe₂O₃ filled neoprene based RFCs

Cure characteristics of γ-Fe$_2$O$_3$ filled RFCs are given in table 5.3. Initial increase in cure time is observed for composites containing gamma ferric oxide. Further addition of the filler does not produce any significant variation in cure time. These observations indicate that ferrite fillers do not activate or deactivate the curing reaction of neoprene rubber.

Table 5.3 Cure characteristics of γ-Fe₂O₃ filled neoprene rubber based RFCs

Loading (phr)	Optimum Cure time t_{90} (minutes)	Scorch time t_{10} (minutes)	Maximum torque, D_{max} (dNm)	Minimum torque, D_{min} (dNm)
0	12.75	1.01	2.98	0.29
40	16.45	1.39	4.58	0.32
60	16.67	1.48	5.40	0.37
80	16.23	1.46	6.35	0.45
100	16.99	1.59	7.72	0.66
120	16.68	1.71	9.37	1.07

The initial increase in cure time may be due to the adsorption of the curatives on the surface of the filler particles. Scorch time of the compound is found to increase with increase in ferrite loading. The processability of the compounds is not affected by the addition of ferrite fillers.

Both the maximum and minimum torque of the compounds increases with the filler loading. Figure 5.4 shows the variation of $\dfrac{D_{max-}D_{min}}{D_{max}^0 - D_{min}^0} - 1$ versus filler loading of the RFCs.
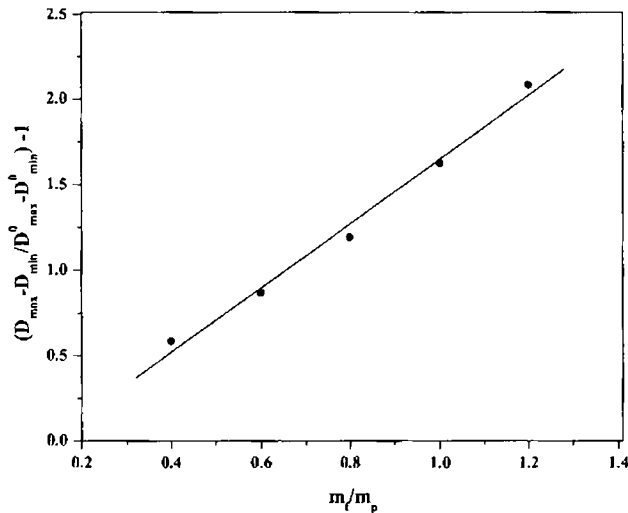
Figure 5.4 Variation of $\dfrac{D_{max-}D_{min}}{D_{max}^0 - D_{min}^0} - 1$ *against* m_f/m_p

The torque values increase linearly with filler loading. The Δ torque values of gamma ferric oxide filled RFCs shown in figure 5.5 are found to increase linearly with loading of gamma ferric oxide.
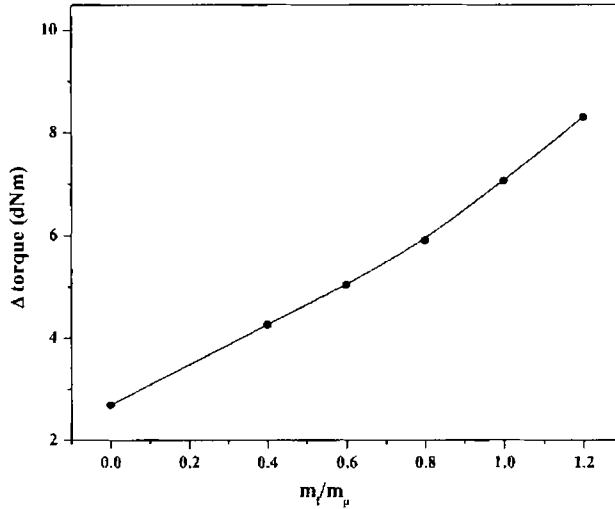
Figure 5.5 Variation of Δ torque with loading of gamma ferric oxide

The filler specific constant α_F is calculated and is plotted in figure 5.6. α_F decreases initially and then shows a sharp increase at higher loadings. This is quite
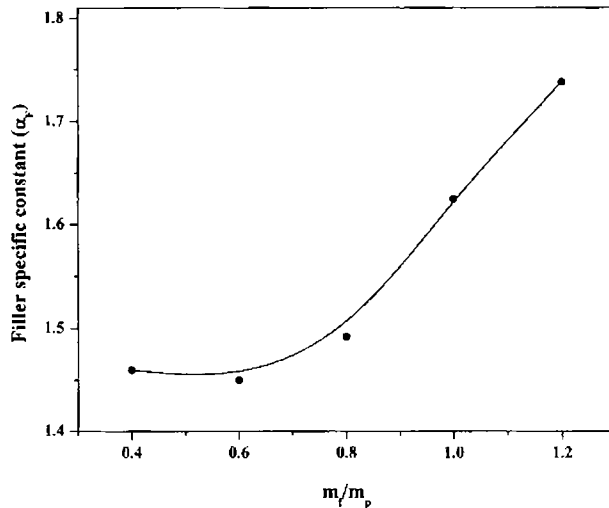
Figure 5.6 Variation of filler specific constant (α_F) against filler loading

115

opposite to that of nickel ferrite filled RFCs where α_F decreased with loading. Since α_F is a measure of the structure of fillers within the vulcanisate, the high α_F values for γ-Fe_2O_3 compared to $NiFe_2O_4$ indicates the presence of filler agglomerates in gamma ferric oxide filled RFCs.

5.3 Cure rate index and cure kinetics of $NiFe_2O_4$ filled neoprene based RFCs

5.3.1 Nickel ferrite filled RFCs
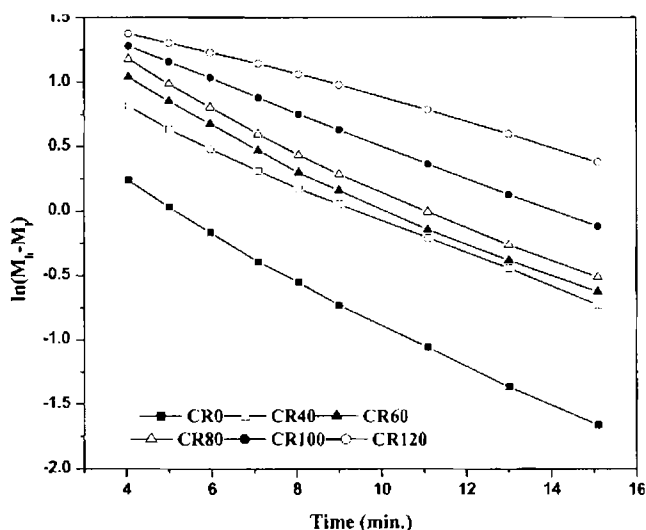
Figure 5.7 ln(M_h-M_t) vs time for $NiFe_2O_4$ filled RFCs

Kinetics of cure reactions of neoprene rubber based RFCs with different loading of nickel ferrite were determined from the torque values. Plot of ln(M_h-M_t) versus time is shown in figure 5.7. The linear nature of these graphs indicates that the cure reaction proceeds through first order kinetics.

From the slope of the straight lines, the rate constant of the cure reactions are determined and are shown in figure 5.8. Variation of cure rate constant is very similar to the variation of cure rate index given in the same figure. Speed of reaction is found to be slowing down on incorporation of 40 phr ferrite filler. Rate of cure reaction increases on further addition of the ferrite filler and decreases at higher filler loadings. Rate of cure reaction, which depends on the concentration of the rubber phase, is expected to decrease with filler loading.
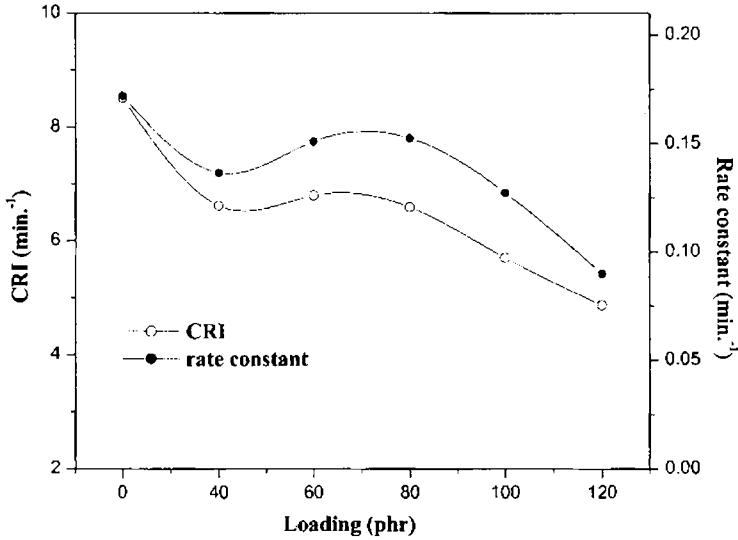
Figure 5.8 Cure rate index and cure rate constant of $NiFe_2O_4$ filled neoprene based RFCs

5.3.2 Gamma ferric oxide filled RFCs

A plot of $\ln(M_h-M_t)$ versus time of cure of the RFCs with $\gamma-Fe_2O_3$ filler is shown in figure 5.9 and are indicative of first order kinetics. The straight line plots confirm the first order kinetics of the cure reaction.
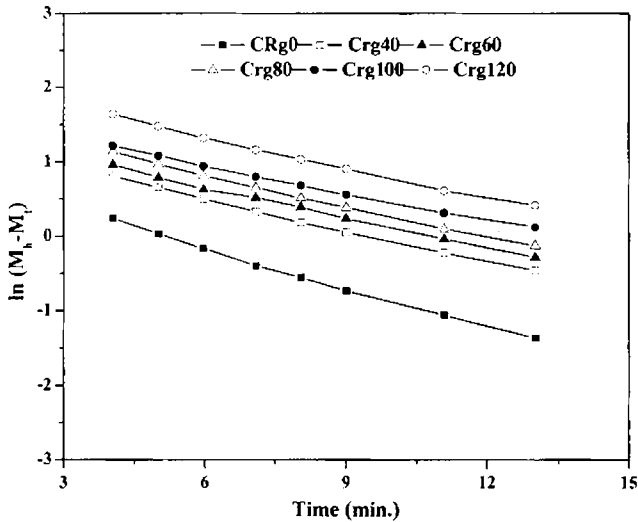
Figure 5.9 $ln(M_h-M_t)$ vs time for $\gamma-Fe_2O_3$ filled RFCs

117

The rate constants of the cure reactions obtained from the slope of the straight lines for various loadings of γ-Fe_2O_3 filler are plotted in figure 5.10. Variation of cure rate index with filler loading is also provided in figure 5.10.
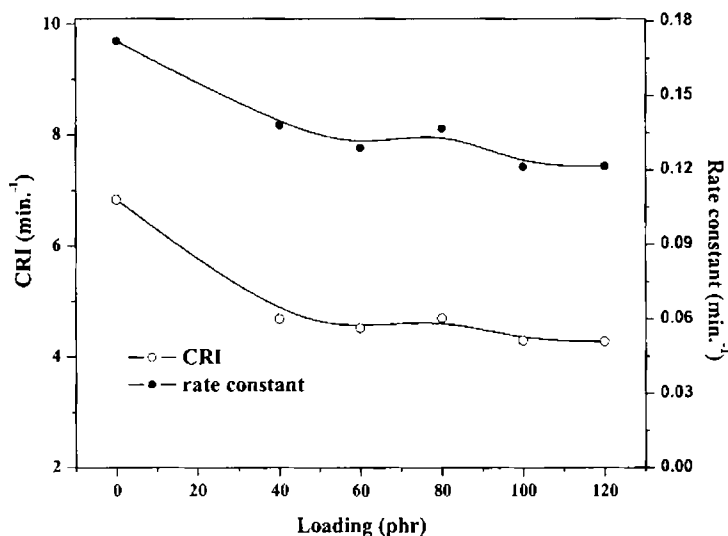
Figure 5.10 Cure rate index and cure reaction constant of
γ-Fe_2O_3 filled neoprene based RFCs

Both cure rate index and cure reaction constant decreases with loading, which indicates that the reaction progresses slowly with increase in filler loading. As the filler content increases the volume fraction of the rubber decreases. Hence, the rate of cure reaction, which depends on the concentration of the rubber phase, is decreased with increase in filler content.

5.4 Mechanical properties of neoprene based RFCs

5.4.1 Mechanical properties of $NiFe_2O_4$ filled RFCs

Mechanical properties of neoprene based RFCs filled with $NiFe_2O_4$ were measured and are presented in table 5.4. Tensile strength increases with loading and at higher loading decreases gradually. Tensile strength of RFC with 120 phr $NiFe_2O_4$ is about the same as that of the gum vulcanisate. All these observations point to the reinforcing character of the ferrite particles in the neoprene rubber matrix. Both surface area and specific activity of the filler are important factors in reinforcement.

Particle size contributes physically and surface activity contributes chemically towards reinforcement. The particle size of nickel ferrite used for the preparation of the RFCs is about 19 nm. As the particle size decreases, the interface area between the filler and the elastomer increases which leads to a better reinforcement. As the loading increases above 40 phr, a regular decrease in tensile strength is observed. As the filler loading increases, volume fraction of the rubber decreases, which decreases the tensile strength due to insufficient wetting of the filler.

Table 5.4 Mechanical properties of NiFe₂O₄ filled neoprene based RFCs

Loading (phr)	Tensile strength (MPa)	Tear strength (N/mm)	Elongation at break (%)	Modulus at 300% elongation (MPa)
0	13.99	35.16	1165	1.51
40	19.19	35.55	1290	2.07
60	18.59	36.69	1218	2.34
80	17.76	39.26	1194	2.53
100	15.59	40.28	1143	2.63
120	13.52	41.5	1092	2.72

Elongation at break of RFCs shows the same trend as in the case of tensile strength. Because of the fineness of nickel ferrite particles, an improvement in the stress bearing capacity of the polymer-filler interphase is observed. As the ferrite concentration increases, the interaction between the filler surface and the polymer phase decreases, hence elongation at break decreases.

Modulus at 300% elongation increases with increase in concentration of the ferrite. The increase in modulus with loading is due to the inclusion of rigid filler particles in the matrix. Bridging of rubber chains between the filler particles, results in an enhancement in modulus.

Tear strength of the RFCs is increased with increase in filler content as in the case of EPDM based RFCs. In the filled matrix, filler interacts with elastomer chains and create a barrier for the tear path and thus increases the tear strength [12].

Figure 5.11 shows the variation of hardness and resilience with loading of nickel ferrite. Hardness of the RFCs increases with nickel ferrite loading due to the decreased mobility of the elastomer chains. Resilience is found to decrease with increase in filler content. Resilience is directly related to the rubber content of the vulcanisate. As the rubber content decreases, damping characteristics of the vulcanisate decreases and the resilience decreases.
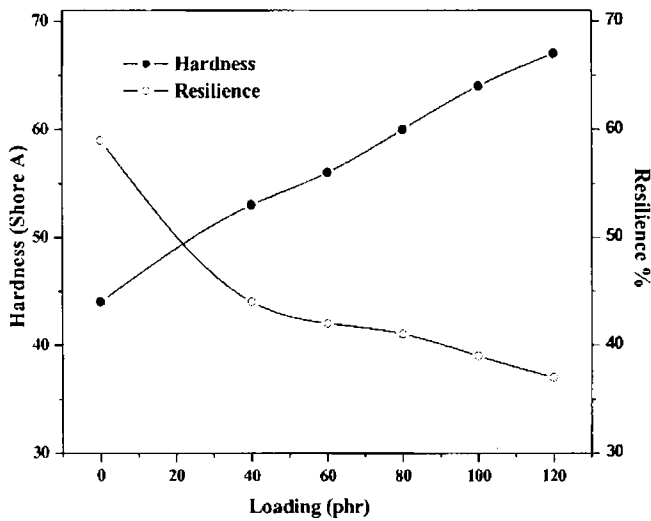
Figure 5.11 Variation of hardness and resilience of RFCs with NiFe$_2$O$_4$ loading

The decrease in rebound height with increase in filler loading is linear according to the equation

$$R_0 - R = A \frac{m_f}{m_p} \qquad\qquad 5.2$$

where R_0 is the rebound height of gum and R is that of the filled vulcanisate [8,13] and A is the filler specific constant that depends on the surface characteristics of the filler. The plot of R_0-R against m_f/m_p is a straight line as given in figure 5.12. The value of 'A' obtained from the slope of the straight line is 8.5.
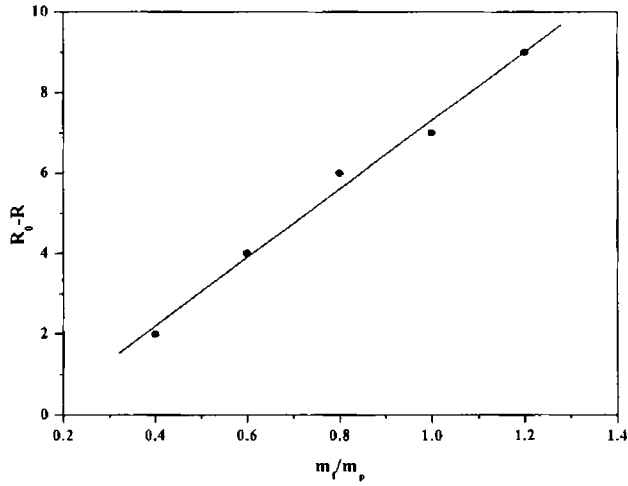
Figure 5.12 Variation of R_0-R against m_f/m_p

Figure 5.13 shows the variation in volume loss on abrasion with filler loading. As nickel ferrite is incorporated in neoprene, volume loss on abrasion decreases initially and then increases above 60 phr loading. The abrasion resistance increases up to 60 phr loading of nickel ferrite and shows a decrease at higher loadings.
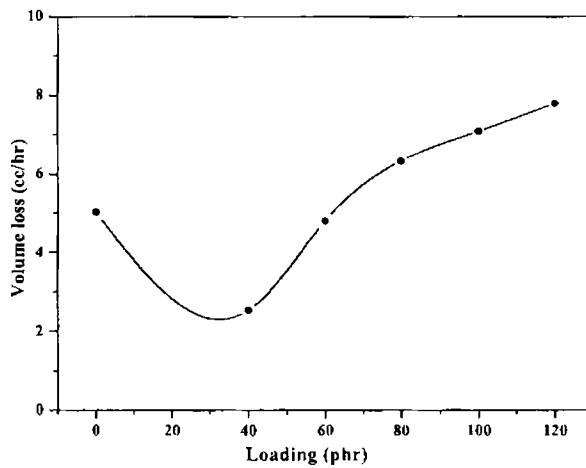
Figure 5.13 Variation of volume loss due to abrasion of $NiFe_2O_4$ filled RFCs

The increase in abrasion resistance of the RFCs may be due to the interaction between the neoprene matrix and filler that restricts the wearing of rubber during abrasion. At higher loadings, the filler-filler interactions overcome the rubber-filler interactions, leading to a reduced abrasion resistance.

121

5.4.2 Mechanical properties γ-Fe₂O₃ filled neoprene based RFCs

The mechanical properties of γ-Fe$_2$O$_3$ filled RFCs are tabulated in table 5.5.The tensile strength of the RFCs increases gradually with the increase in γ-Fe$_2$O$_3$ content upto 80 phr and decreases at higher loadings. Elongation at break shows an initial increase with loading and then decreases at higher loading. Modulus at 300% elongation of RFCs shows a regular increase with increase in filler addition.

Table 5.5 Mechanical properties of neoprene based RFCs with γ-Fe$_2$O$_3$ filler

Loading (phr)	Tensile strength (MPa)	Tear strength (N/mm)	Elongation at break (%)	Modulus at 300% elongation (MPa)	Resilience (%)
0	13.99	35.16	1165	1.51	59
40	17.94	37.53	1200	2.24	44
60	18.87	41.53	1165	2.81	42
80	19.11	45.78	1137	3.11	41
100	17.67	53.02	1058	3.57	39
120	12.26	58.04	626	4.70	37

Tear strength increases gradually with loading. Resilience of the composites as shown in table 5.5 gradually decreases as the volume fraction of the rubber decreases with increase in filler content.
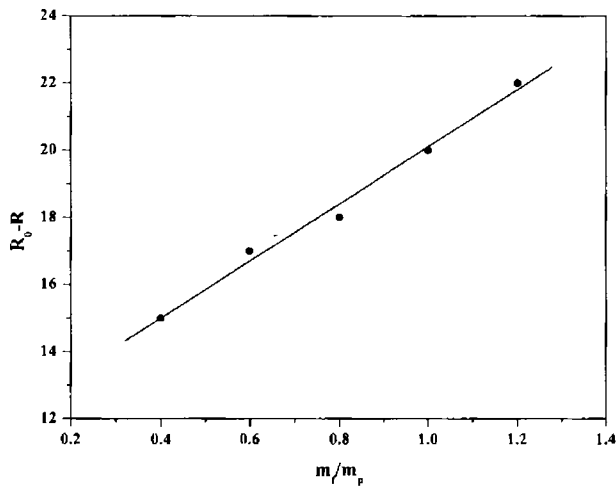
Figure 5.14 R_0-R against m/m_p of γ-Fe$_2$O$_3$ filled RFCs

The plot of R_0-R against m_f/m_p of γ-Fe$_2$O$_3$ filled RFCs as per equation 5.2 is a straight line and is shown in figure 5.14. The slope of the straight line is 8.5, which is a characteristic constant of the filler.

The improved mechanical properties of the RFCs show the semi reinforcing nature of these fillers. In order to compare the reinforcing effect of these two magnetic fillers in neoprene matrix, the reinforcing index values were calculated [14]. Figure 5.15 shows the reinforcing index of the neoprene based RFCs with filler loading.
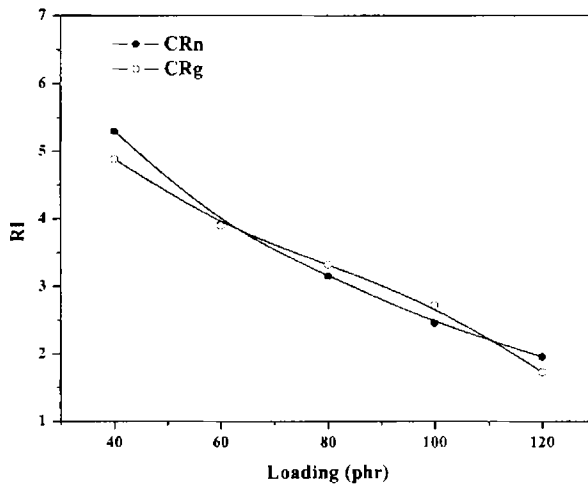
Figure 5.15 Reinforcing indexes of the RFCs with loading of NiFe$_2$O$_4$ and γ-Fe$_2$O$_3$.

The reinforcing index for both set of RFCs filled with NiFe$_2$O$_4$ and γ-Fe$_2$O$_3$ are almost identical. This may be due to the similar surface characteristics of both the fillers as supported by the filler specific constant obtained from the resilience. In both these cases the reinforcing index is found to decrease with loading. At lower loadings, nickel ferrite is found to have higher reinforcing index values compared to gamma ferric oxide. But at higher loadings, higher reinforcing index is obtained for the γ-Fe$_2$O$_3$ filled RFCs.

5.5 Swelling studies of neoprene based RFCs

Diffusion studies of the RFCs were carried out as explained in section 2.4.6, using toluene as the penetrant solvent and diffusion, sorption and permeation coefficients were calculated.

The sorption curves at room temperature are obtained by plotting percentage mole uptake of the penetrant against square root of time. The sorption curves of the nickel ferrite and gamma ferric oxide filled RFCs are shown in figures 5.16 and 5.17. The initial swelling rate is very high owing to the large concentration gradient. This keeps the polymer sample under intense solvent stress. As the concentration gradient decreases with advancing swelling, the swelling rate decreases and the concentration difference becomes negligible at equilibrium swelling. In both the cases, equilibrium mole% uptake decreases with increase in filler loading. The decrease in mole% uptake is due to the decrease in volume fraction of elastomer with loading of ferrites.
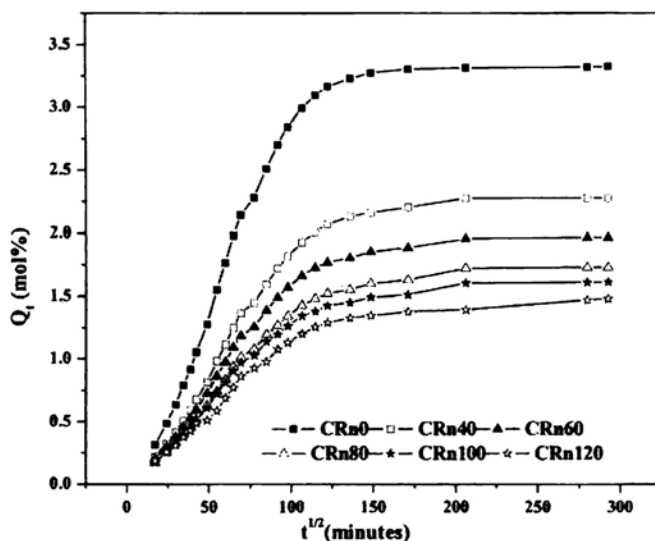
Figure 5.16 Sorption curves of neoprene based RFCs with NiFe$_2$O$_4$ filler

The transport mechanism of the penetrant through the rubber is analysed from the parameter 'n' determined using the equation,

$$\log Q_t/Q_\infty = \log k + n \log t \qquad 5.3$$

The value of n for different loadings for both the set of RFCs are given in table 5.6.
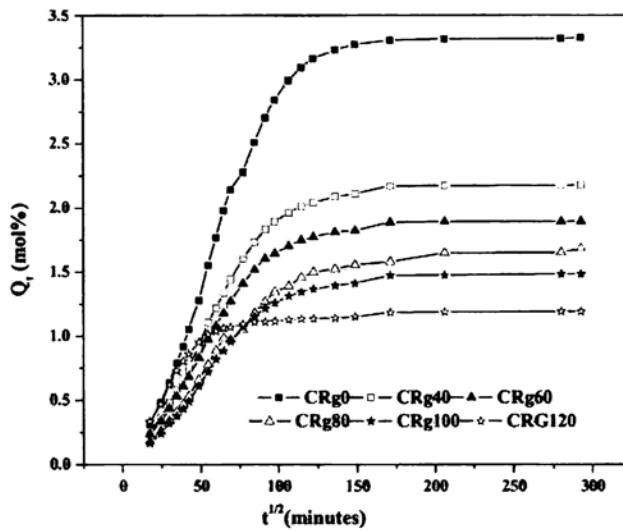
Figure 5.17 Sorption curves of neoprene based RFCs with γ-Fe₂O₃ filler

Table 5.6 The value of 'n' for NiFe₂O₄ and γ-Fe₂O₃ filled RFCs

Loading (phr)	'n' for NiFe$_2$O$_4$ filled RFCs	'n' for γ-Fe$_2$O$_3$ filled RFCs
0	0.68	0.68
40	0.63	0.62
60	0.61	0.61
80	0.59	0.60
100	0.58	0.60
120	0.52	0.54

Since the value of 'n' is between 0.5 and 1, the transport mechanism can be considered as anomalous where rearrangement of polymer molecules occurs at a comparable rate to that of the change of concentration [15,16]. The time taken by the rubber chains to respond to the swelling stress and to rearrange themselves to accommodate the solvent molecules is responsible for the anomalous behaviour of the sample. As the loading increases, the value of n decreases, which indicates that polymer relaxation increases compared to the rate of diffusion of penetrant molecules.

This is supported by the diffusion coefficient values. The diffusion coefficient values are found to decrease with loading for both the set of RFCs as shown in figure 5.18.
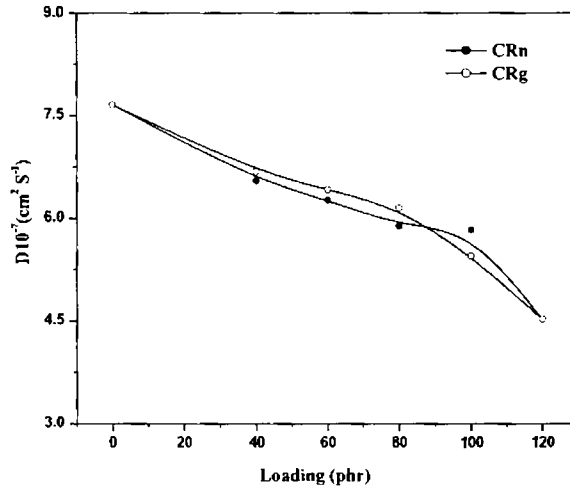
Figure 5.18 Variation of diffusion coefficients with loading for RFCs with $NiFe_2O_4$ and $\gamma\text{-}Fe_2O_3$

Diffusion process depends on the concentration gradient between the penetrant and sorption phase. As the loading increases, the concentration gradient decreases and hence coefficient of diffusion decreases.
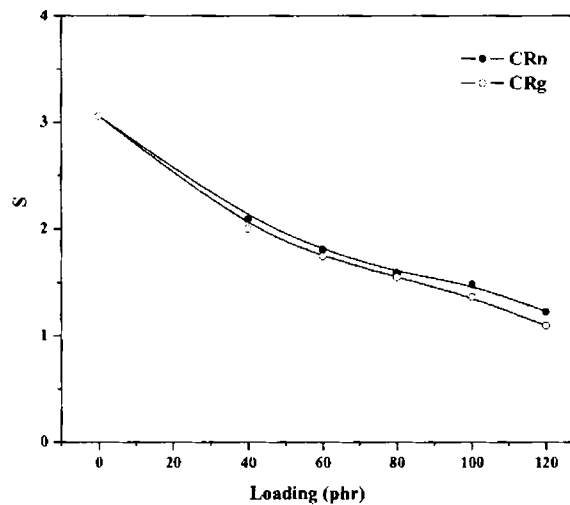
Figure 5.19 Variation of sorption coefficient of RFCs with loading

The variation of sorption and permeation coefficient for both set of RFCs is plotted in figures 5.19 and 5.20. Sorption and permeation coefficient for both set of

RFCs decreases with loading. The decrease in sorption coefficient is due to the decrease in volume fraction of absorbing phase with increase in loading. Since permeation is a collective process of diffusion and sorption, permeation coefficient also decreases with loading.
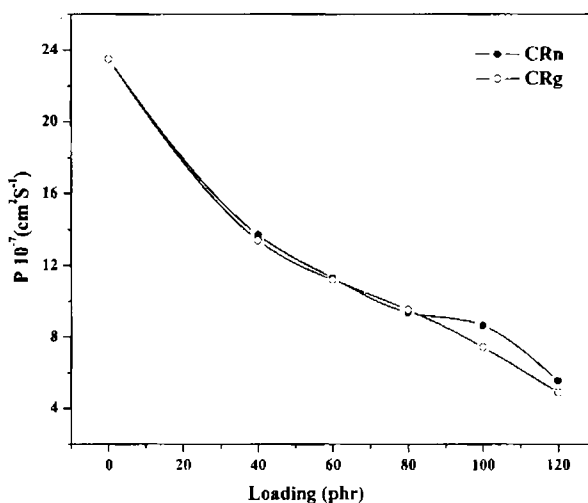
Figure 5.20 Variation of permeation coefficient of RFCs with loading

Diffusion, sorption and permeation coefficient for nickel ferrite and gamma ferric oxide filled RFCs have almost identical values. The identical swelling behaviour of both the set of RFCs indicates that the transport mechanism of penetrant molecules through neoprene matrix does not depend on the nature of the ferrite filler.

5.6 Crosslink density of RFCs

Crosslink density of the RFCs was determined as explained in section 2.4.6. The variation in crosslink density of RFCs with nickel ferrite and gamma ferric oxide loading is represented in figure 5.21.

Crosslink density decreases with loading for both set of RFCs. The decrease in CLD is due to the occlusion of the filler particles between the rubber chains. This is supported by the reinforcing index values for tensile strength of the RFCs which decreases with loading. Gamma ferric oxide filled RFCs are found to possess superior CLD at higher loadings. This is true for reinforcing index values too. Better mechanical properties of γ-Fe_2O_3 filled RFCs at higher loadings are because of their higher crosslink densities.

127
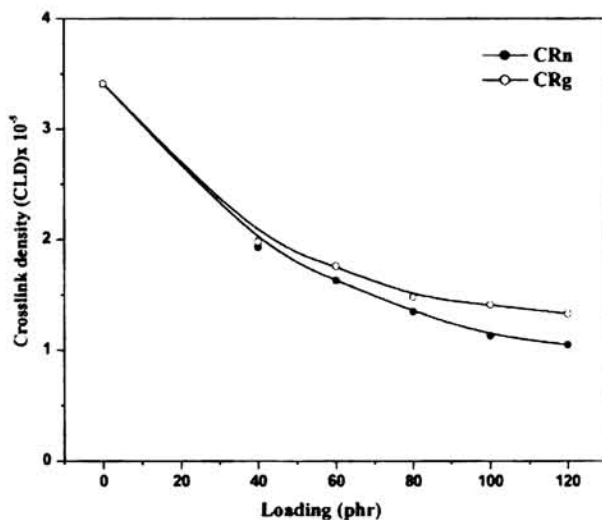
Figure 5.21 Variation of crosslink density of RFCs filled with NiFe$_2$O$_4$ and γ-Fe$_2$O$_3$

5.7 Morphology

5.7.1 Morphology of gamma ferric oxide filled RFCs
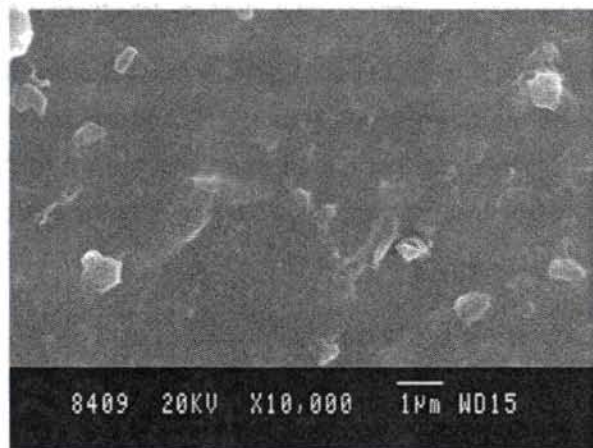
Figure 5.22 SEM image of tensile fractured surface of neoprene gum vulcanisate.

Dispersion of fillers in the neoprene matrix were analysed by subjecting these samples to Scanning electron micrograph studies. The micrographs are shown in figures 5.22 to 5.27.

The bright images obtained in figure 5.22 are due to the curatives added to the matrix that might not be utilised for the cure reaction.
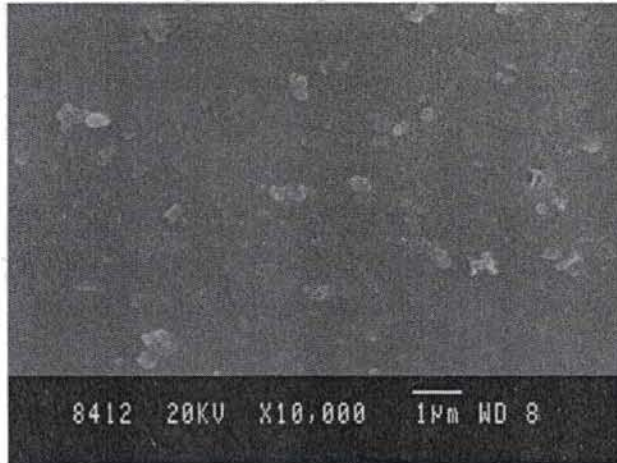
Figure 5.23 SEM image of tensile fractured surface of RFC with 40 phr γ-Fe$_2$O$_3$
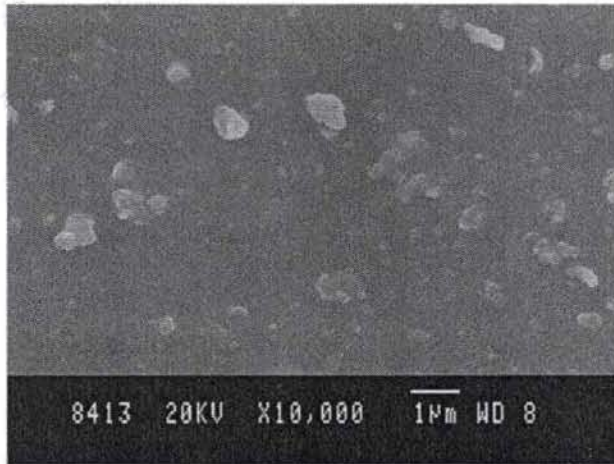
Figure 5.24 SEM image of tensile fractured surface of RFC with 60 phr γ-Fe$_2$O$_3$
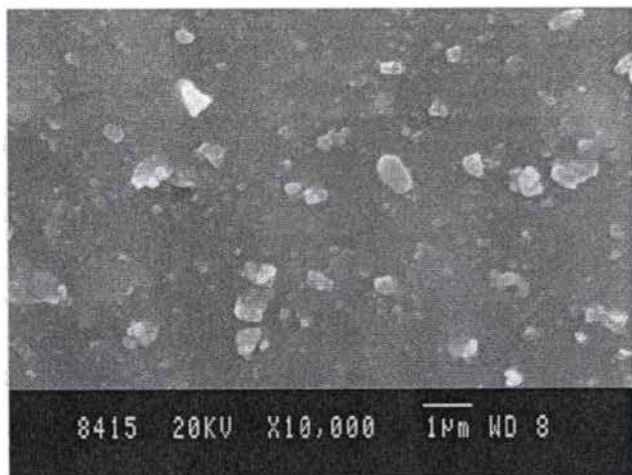
Figure 5.25 SEM image of tensile fractured surface of RFC with 80 phr γ-Fe₂O₃
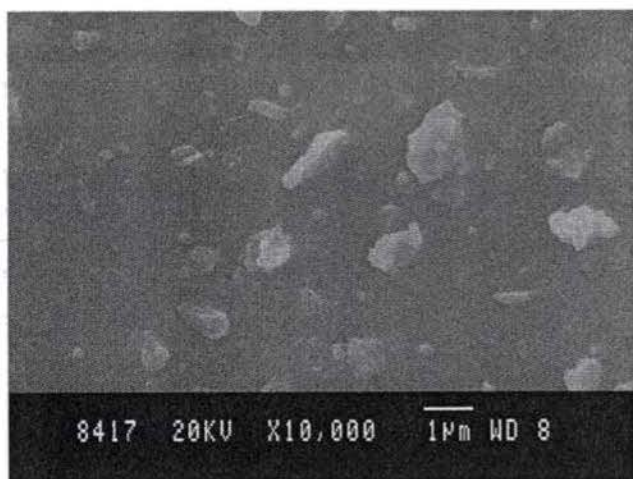
Figure 5.26 SEM image of tensile fractured surface of RFC with 100 phr γ-Fe₂O₃

Dispersion of the filler is complete up to a loading of 80 phr. At higher loadings, agglomeration of the filler occurs as is evident from figure 5.26. Topography of the fractured surface is found to be different for RFC with 120 phr of γ-Fe$_2$O$_3$. The rough topography at this high loading contributes to the poorer mechanical properties of the RFCs at higher loadings.
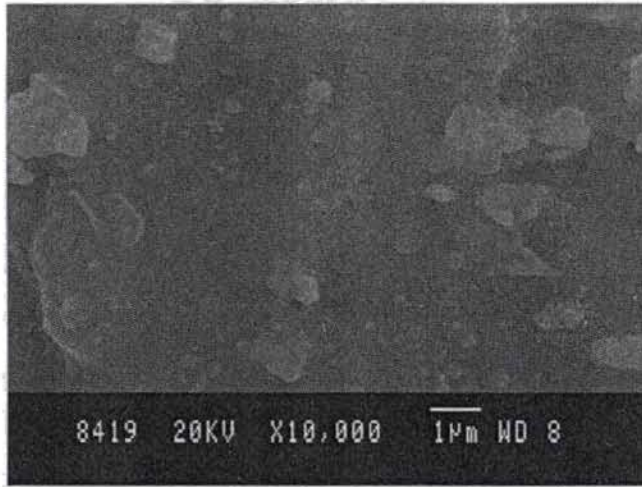
Figure 5.27 SEM image of tensile fractured surface of RFC with 120phr γ-Fe$_2$O$_3$

5.7.2 Morphology of nickel ferrite filled RFCs

SEM image of the tensile fractured surface of nickel ferrite filled RFCs are shown in figures 5.28 to 5.32.
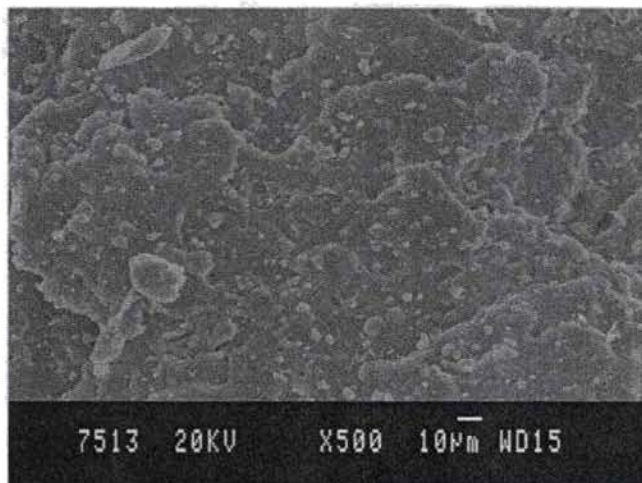
Figure 5.28 SEM image of tensile fractured surface of RFC with 40 phr NiFe$_2$O$_4$
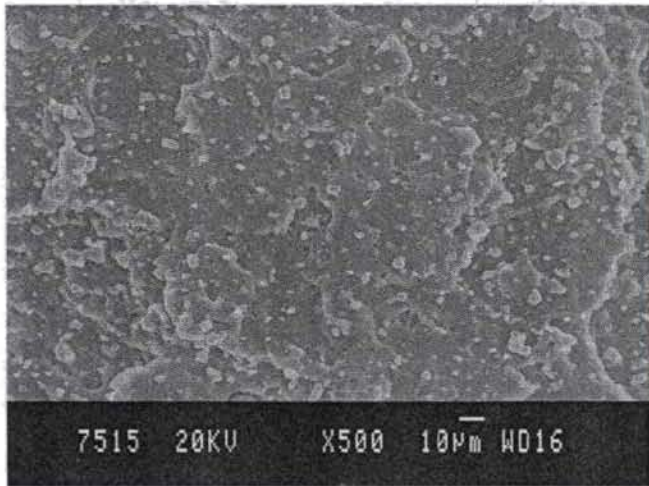
Figure 5.29 SEM image of tensile fractured surface of RFC with 60 phr NiFe₂O₄
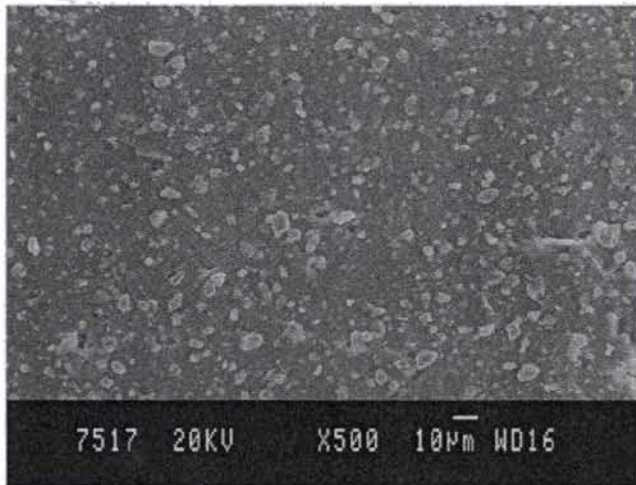
Figure 5.30 SEM image of tensile fractured surface of RFC with 80 phr NiFe₂O₄
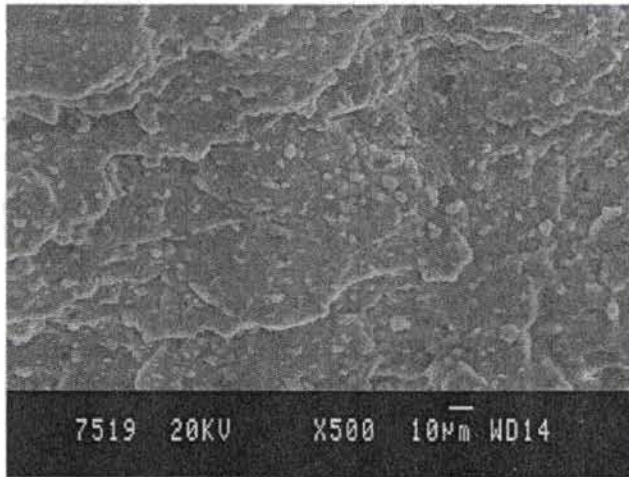
Figure 5.31 SEM image of tensile fractured surface of RFC with 100 phr NiFe₂O₄
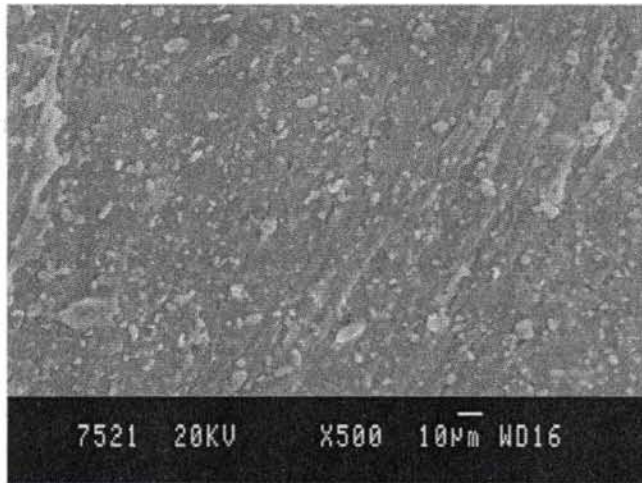
Figure 5.32 SEM image of tensile fractured surface of RFC with 120 phr NiFe₂O₄

Increased amount of filler content is visible from figures 5.28 to 5.32. Rough topography of the fractured surfaces explains and accounts for the delay in fracturing process. Due to the distribution of filler particles between rubber chains, at the initial stage of failure, stress distribution may be uniform. As failure progress, the stress distribution in the vulcanisate becomes non uniform, which results a rough topography.

5.8 Conclusion

Neoprene based rubber ferrite composites were prepared with nickel ferrite and gamma ferric oxide fillers. Cure time and scorch time of the nickel ferrite filled composites increased with the addition of the filler. For gamma ferric oxide filled RFCs, there was no significant variation in cure time, where as the scorch time increased gradually with increase in γ-Fe_2O_3 loading. Cure kinetic studies indicated that the cure reaction for RFCs with nickel ferrite and gamma ferric oxide follow first order kinetics. For γ-Fe_2O_3 filled RFCs a sharp decrease in cure rate index and cure reaction constant was observed at lower loadings. At higher filler content, the variation was less significant. The mechanical properties of the two set of RFCs were enhanced with the addition of the ferrite fillers. The reinforcing index for nickel ferrite and gamma ferric oxide was almost identical and in both the cases it decreased with the increase in filler content. Swelling studies for both the set of RFCs proved that the rate of diffusion of solvent molecules through the elastomer was comparable to that due to polymer relaxation. SEM images of the fractured tensile surface revealed that the dispersion was uniform and the composite was homogeneous. However, agglomeration was observed at high filler loadings. The cure kinetic studies and evaluation of mechanical properties of the RFCs indicated that both nickel ferrite and gamma ferric oxide function as reinforcing fillers in neoprene matrix. Studies on the cure characteristics revealed that the addition of these fillers did not affect the processability of the composites.

References

1. K.A. Malini, E.M. Mohammed, S. Sindhu, P.A. Joy, S.K. Date, S.D. Kulkarni, P. Kurian and M.R. Anantharaman, J. Mate. Sci., **36** (2001) 5551.

2. E.M. Mohammed, K.A. Malini, P.A. Joy, S.D. Kulkarni, S.K. Date, P. Kurian and M.R. Anantharaman, Plastics, Rubber and Composites, **31** (2002) 106.

3. M.R. Anantharaman, S. Jagathesan, S. Sindhu, K.A. Malini, C.N. Chinnasamy, A. Narayanasamy, P. Kurian and K.Vasudevan, Plast. Rubber compos. Process Appl., **27** (1998) 77.

4. M.R. Anantharaman, P. Kurian, B. Banerjee, E.M. Mohammed and M. George, Kautschuk Gummy Kunststoffe (Germany), **49** (1996) 424.

5.   M.A. Soloman, Philip Kurian, P.A. Joy and M.R. Anantharaman, International Journal of Polymeric Materials, **53** (2004) 565.

6.   Siegfried Wolf, Rubber Chem. and Technol., **69** (1996) 325.

7.   H.M. da Costa, L. L.Y. Visconte, R.C.R. Nunes, and C.R.G. Furtado, International Journal of Polymeric Materials, **53** (2004), 475.

8.   Gerard Kraus, Rubber Chem. and Technol., **51** (1978) 297.

9.   Maged S Sobhy, D. E. El-Nashar, Nabila A. Maziad, Egypt. J. Sol., **26** (2003) 241.

10. H. Westlinning and S. Wolf, Kautsch. Gummi Kunstst., **19** (1966) 470.

11. Siegfried Wolf and Meng-Jiao Wang, Rubber Chem. and Technol., **65** (1992) 329.

12. M.T. Ramesan, Journal of Polymer Research, **11** (2004) 333.

13. S. Wolf, Kautsch. Gummi Kunstst., **27** (1974) 511.

14. S. Kohjiya and Y. Ikeda, Rubber Chem. Technol., **73** (2000) 534.

15. R. Asaletha, M.G. Kumaran and Sabu Thomas, Polymers and Polymer composites, **6** (1998) 357.

16. V.G. Geethamma and Sabu Thomas, Polymer Composites, **26** (2005) 136.

Dielectric Properties of Nickel Ferrite Based Rubber Ferrite Composites

Polycrystalline ferrites possess high resistivity and low eddy current loss, which finds use in many high frequency applications [1-4]. Dielectric behaviour of ferrites markedly depends on several factors such as methods of preparation, grain size, crystal structure, ratio of Fe^{2+}/Fe^{3+} ions, defects in the crystal lattice and heat treatment given to the sample.

The dielectric behaviour of ferrites also depends on external factors such as frequency of the applied voltage, temperature, pressure and humidity. Since the properties of ferrites are very much dependent on the microstructure, composition and the processing variables, study of dielectric properties of these materials assumes significance. Dielectric permittivity is a consequence of polarisation mechanisms such as electronic, ionic, dipole and interfacial polarisation. So a systematic study on dielectric properties of ferrites provides valuable information on the behaviour of localised electric charge carriers within the system. Dielectric properties of polymers and polymer composites like those of other dielectric materials are usually expressed in terms of its resistivity, conductivity and complex permittivity. These quantities are functions of temperature and the type (ac/dc) and magnitude of the voltage applied. Frequency and temperature dependence of dielectric properties of RFCs throw light on the dielectric polarisation and shed light on the conduction mechanisms.

Many theories and semiemperical equations can be applied to the observed dielectric behaviour of the composites. These studies reveal valuable informations like filler matrix interaction, filler dispersion and percolation limit of the filler in the matrix. Dielectric permittivity of composites can be predetermined by applying different mixture equations in terms of its constituent dielectric components. Such investigations aid in tailoring the dielectric properties of the composites.

EPDM and neoprene based rubber ferrite composites were prepared by incorporating precharacterised nickel ferrite nanoparticles. The frequency and temperature dependence of dielectric properties of the nickel ferrite as well as nickel ferrite filled RFCs were studied. Different theoretical equations and mixture equations were applied to fit the observed dielectric data of the nickel ferrite and the corresponding RFCs.

6.1 Dielectric Measurements

The dielectric properties of the nickel ferrite and the RFCs were evaluated using a homemade cell and a LCR meter (model HP 4285A). The cell was standardised by using teflon pellets and lead. The fringe capacitance was eliminated by employing a procedure suggested by Ramasasthry *et al.* [5]. The samples were made in the form of a pellet having 12 mm diameter and 2 mm thickness. The capacitance of the sample was measured in the frequency range 0.1-8 MHz and in the temperature range 303-393 K. The relative permittivity and ac conductivity of the nickel ferrite were calculated using the formula

$$\varepsilon_r = \frac{Cd}{\varepsilon_0 A} \qquad\qquad 6.1$$

$$\sigma_{ac} = 2\pi f \tan\delta \; \varepsilon_0 \; \varepsilon_r \qquad\qquad 6.2$$

where C the capacitance of the sample, d the thickness, A the surface area, ε_0 the dielectric permittivity of air, f the frequency of the applied field and $\tan\delta$ is the loss factor. The complete experimental set up and details of the dielectric measurements are explained in section 2.5

The influence of frequency and temperature on the dielectric permittivity of polycrystalline nickel ferrite and corresponding RFCs were studied. These experimental values were then correlated into the theoretical values.

6.1.1 Frequency dependence of dielectric permittivity of nickel ferrite

Enormous literature exists on the dielectric studies on ferrites in different frequency regime [6-0]. The dielectric permittivity of nickel ferrite was determined in the frequency range 0.1-8 MHz and in the temperature range 303-393 K. Typical

graphs depicting the variation of dielectric permittivity with frequency is shown in figure 6.1.
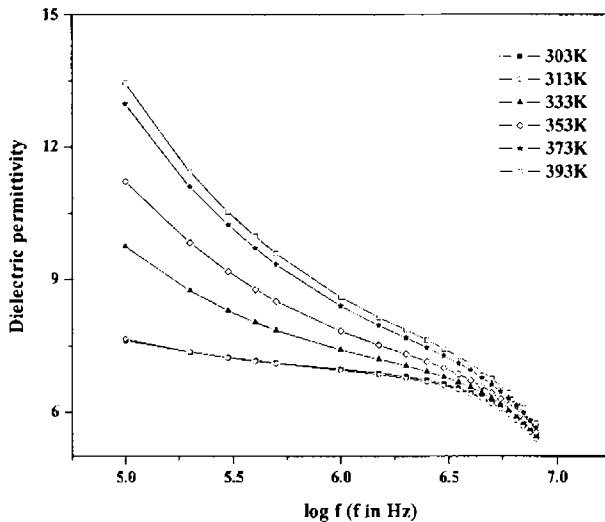
Figure 6.1 Variation of dielectric permittivity with frequency for $NiFe_2O_4$ at different temperatures

From figure 6.1, it can be seen that the dielectric permittivity decreases with increase in frequency. The decrease is rapid at lower frequencies and less rapid at higher frequencies. Finally, it reaches a constant value at all temperatures. This is the normal dielectric behaviour found in the case of ferrites. Mixed ferrites also exhibit a similar behaviour [11-13]. Dielectric behaviour of ferrites depends on their structure. In ferrites, the cations are surrounded by closely packed oxygen anions, which are isolated from each other, forming a heterogeneous structure as put forwarded by Maxwell-Wagner. In the Maxell-Wagner model, well conducting grains are separated by poorly conducting grain boundaries. The high values of dielectric permittivity at lower frequencies can be accounted by employing Koop's theory which is based on Maxwell-Wagner model for heterogeneous double layer dielectric structures [14-16].

The mechanism of dielectric polarisation in ferrites is similar to that of conduction process [17]. Under the application of an external ac electrical field, an electron exchange between +2 and +3 oxidation state occurs, resulting in local displacement of charge in the direction of the applied field. This electron exchange determines the net polarisation effect in ferrites. When the frequency of the applied ac

field is much smaller than the hopping frequency of electron between the adjacent +2 and +3 ions at the octahedral sites, the electron follows the field. Under such circumstances, the dielectric permittivity will be high. As the frequency of the applied ac field is increased, the hopping frequency of the electron between the two oxidation states lags behind the applied field, thus the dielectric polarisation as well as the dielectric permittivity decreases.

Equation 6.3 explains the variation of dielectric permittivity with frequency

$$\varepsilon'' = (r\text{-}r')(\varepsilon' \times \omega) \qquad\qquad 6.3$$

where ε' and ε'' are the real and imaginary parts of the dielectric permittivity and r and r' are the ac and dc conductivity respectively and ω is the frequency.

6.1.2 Effect of temperature on dielectric permittivity of nickel ferrite

Figure 6.2 shows the variation of dielectric permittivity with temperature at different frequencies. Dielectric permittivity increases as temperature increases which is the behaviour generally found in magnetic semiconductors like ferrites.
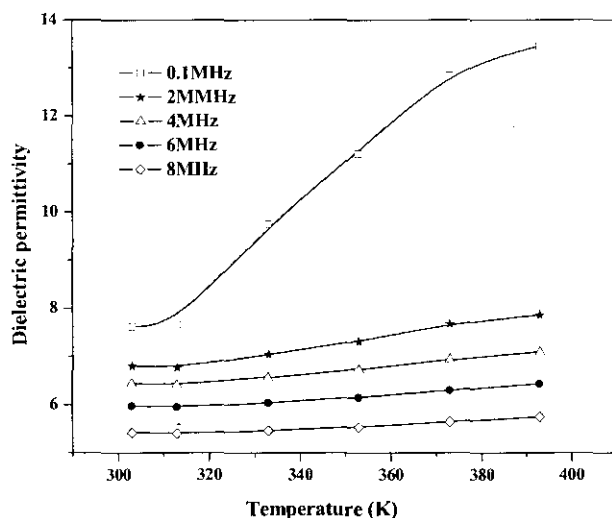
Figure 6.2 Variation in dielectric permittivity of NiFe$_2$O$_4$ with temperature

The increase in dielectric permittivity with temperature was observed for several mixed ferrites [18-20]. For ferrites, dielectric permittivity increases gradually with increasing temperature upto a particularlimit, which is designated as the dielectric transition temperature T_d. Beyond this temperature, the values of dielectric

permittivity for all the samples were found to decrease continuously [21,22]. The hopping of electrons between Fe^{2+} and Fe^{3+} ions is thermally activated on increasing the temperature. The hopping of these strongly localised electrons at the d-shell causes local displacements in the direction of the applied ac electric field which determines the dielectric polarisation in these materials. Therefore, dielectric permittivity, which is directly related to the polarisation, increases as the temperature increases.

The high dielectric permittivity found at low frequencies and high temperatures as shown in figure 6.2 may be explained due to the presence of permanent dipole moments, indicating a small effective charge separation. Such a small separation must be due to asymmetry in the fields experienced by either oxygen or metallic ions. In most cases, the atoms or molecules in the samples cannot orient themselves in low temperature regime. When the temperature raises, the orientation of these dipoles is facilitated and this increases the dielectric polarisation. But at very high temperatures, the chaotic thermal oscillations of molecules are intensified and the degree of orderliness of their orientation is diminished and thus the permittivity passes through a maximum value. In the present study, the maximum temperature of measurement is only 393 K and hence no decrease in dielectric permittivity is observed.

The variation of dielectric permittivity with temperature is more pronounced at low frequencies than at higher frequencies. At lower frequencies the temperature dependence is obeyed by an equation of the form

$$\varepsilon = \varepsilon_0 + A \exp (BT) \qquad\qquad 6.4$$

where ε and ε_0 are the dielectric permittivity at temperature T and 0 K and A and B are constants. For higher frequencies, the dielectric permittivity variation is nominal since the dipoles are not free to orient at higher frequencies and hence the orientation polarisation will be less at higher frequencies. Thus the total increase in polarisation will be less with the rise in temperature at higher frequencies. This explains the change in dielectric permittivity with temperature at higher frequencies.

6.1.3 Effect of frequency and temperature on dielectric permittivity of EPDM gum vulcanisate

Frequency dependence of dielectric permittivity of EPDM vulcanisate at selected temperatures is shown in figure 6.3. The measurements were conducted in the frequency range 0.1- 8 MHz. As the frequency increases the dielectric permittivity decreases gradually at lower frequencies and the decrease is more significant at higher frequencies.
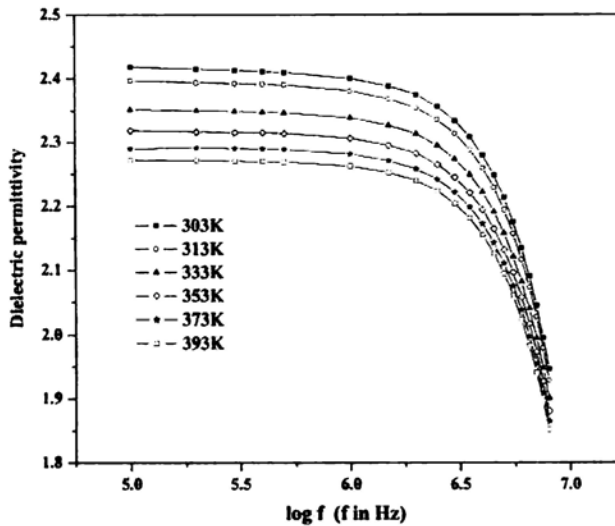
Figure 6.3. Variation of dielectric permittivity of EPDM gum vulcanisate with frequency

Dielectric behaviour of a polymeric material under the influence of an external electric field depends on the polarisation effect that occurs within the material. Total polarisation is the sum of the deformational polarisation and orientational polarisation. At low applied frequencies both the factors contribute to the total polarisation. As the frequency is increased the orientational polarisation becomes out of phase with the applied field, that is, the dipolar motion can no longer follow the rapid vibration in the electric field. So the dielectric permittivity of the polymeric materials decreases with increase in applied frequency.

The polarisation and hence the dielectric permittivity must be regarded as a complex quantity

$$\varepsilon^* = \varepsilon' \text{-i } \varepsilon'' \qquad\qquad 6.5$$

The complex dielectric permittivity ε^* is given by the Debye equation and is as follows

$$\varepsilon^* = \varepsilon_\alpha + \frac{\varepsilon_0 - \varepsilon_\alpha}{1 + i\varpi\tau} \qquad\qquad 6.6$$

Where ω is the angular frequency, ε_0 is the static dielectric permittivity and ε_α is the dielectric permittivity at infinite frequency. The real and imaginary components ε' and ε'' are given by [23-25]

$$\varepsilon' = \varepsilon_\alpha + \frac{\varepsilon_0 - \varepsilon_\alpha}{1 + (\varpi\tau)^2} \qquad\qquad 6.7$$

$$\varepsilon'' = \frac{(\varepsilon_0 - \varepsilon_\alpha)\varpi\tau}{1 + (\varpi\tau)^2} \qquad\qquad 6.8$$

According to equation 6.7, dielectric permittivity decreases with increase in frequency and the decrease is more pronounced at higher frequencies.
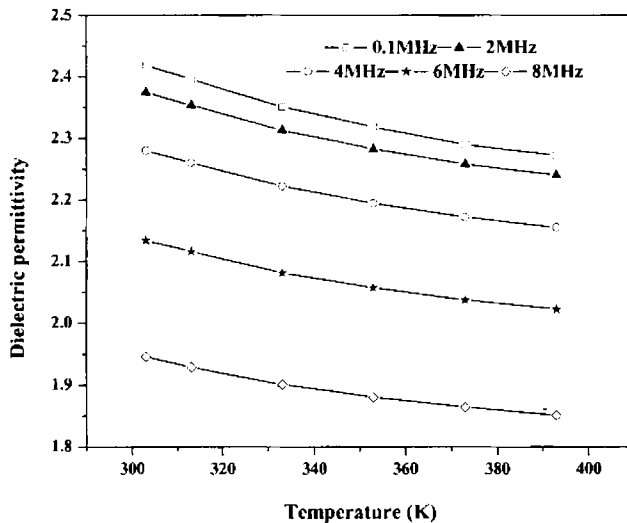
Figure 6.4 Effect of temperature on dielectric permittivity of EPDM gum vulcanisate

Effect of temperature on dielectric permittivity of EPDM gum vulcanisate at some selected frequencies is shown in figure 6.4. Dielectric permittivity of the EPDM

gum vulcanisate is found to decrease with increase in temperature. When temperature increases, due to thermal expansion of matter, the ratio of the number of molecules to the effective length of the dielectric diminishes. As a result dielectric permittivity decreases [26,27].

6.1.4 Frequency dependence of dielectric permittivity of nickel ferrite filled EPDM based RFCs

The dielectric properties of EPDM based RFCs containing different loadings of nickel ferrite were carried out in the frequency range 0.1-8 MHz and in the temperature range 303-393 K. The dependence of dielectric permittivity on various factors like frequency, temperature and loading of the nickel ferrite were studied and is reported here.

Effect of frequency on dielectric permittivity at some selected temperatures for EPDM based RFCs containing different loadings of nickel ferrite is represented in figures 6.5 to 6.10.
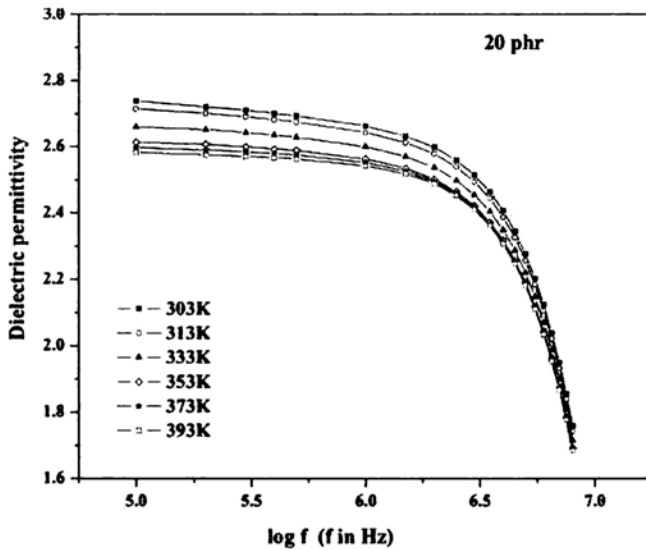
Figure 6.5 Dielectric permittivity versus log frequency of EPDM based RFC containing 20 phr NiFe$_2$O$_4$ at different temperatures
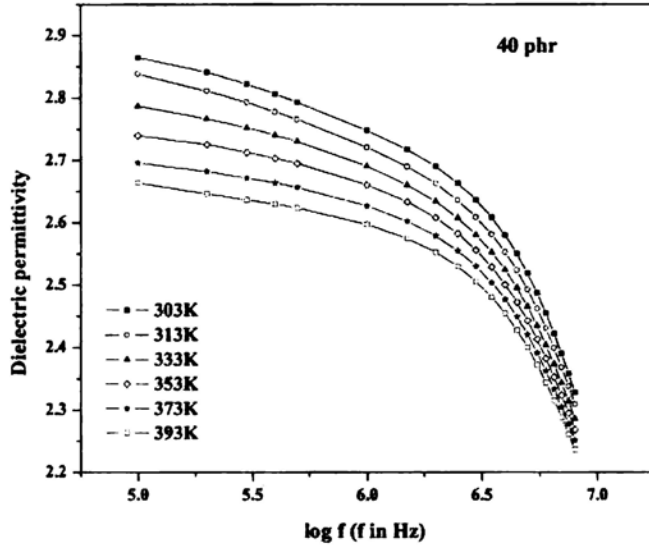
Figure 6.6 Dielectric permittivity versus log frequency of EPDM based RFC containing 40 phr NiFe$_2$O$_4$ at different temperatures
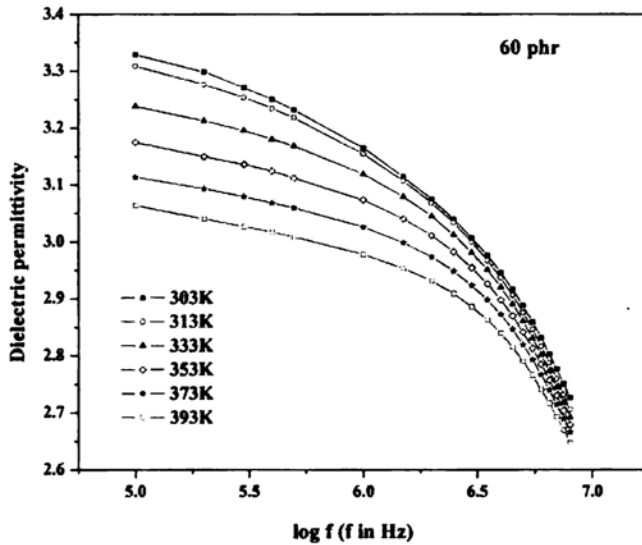
Figure 6.7 Dielectric permittivity versus log frequency of EPDM based RFC containing 60 phr NiFe$_2$O$_4$ at different temperatures
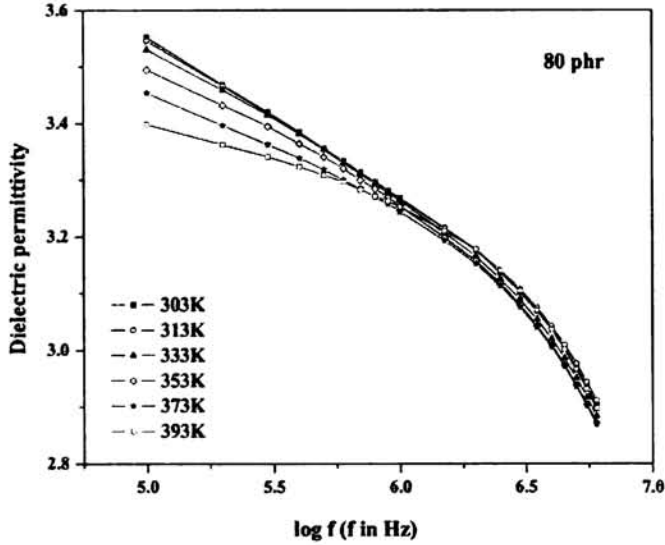
Figure 6.8 Dielectric permittivity versus log frequency of EPDM based RFC containing 80 phr NiFe₂O₄ at different temperatures
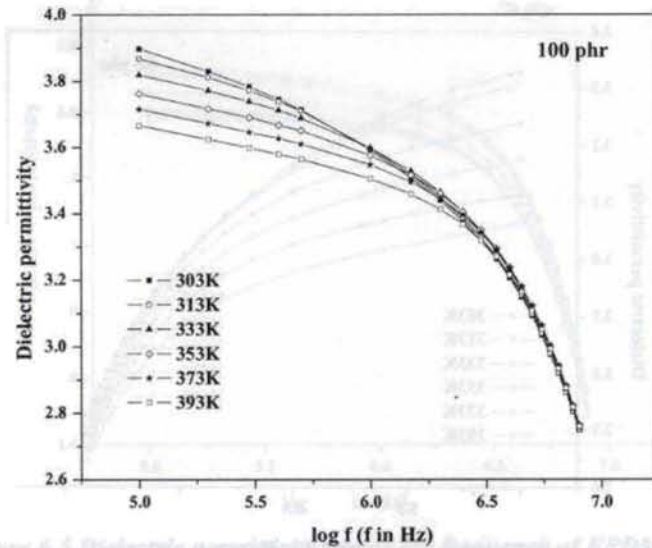
Figure 6.9 Dielectric permittivity versus log frequency of EPDM based RFC containing 100 phr NiFe₂O₄ at different temperatures
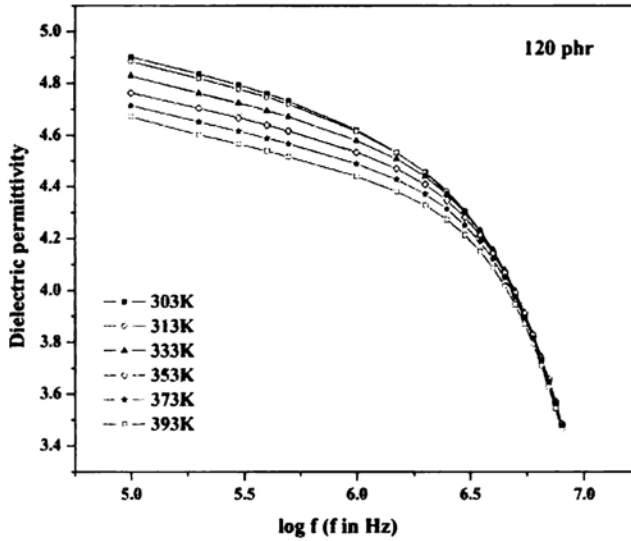
Figure 6.10 Dielectric permittivity versus log frequency of EPDM based RFC containing 120 phr NiFe₂O₄ at different temperatures

The variation pattern shows almost similar behaviour as that of the ceramic component. Absolute value of the dielectric permittivity of the composites is found to be greater than that of the gum vulcanisate, but less than that of the ceramic component. It can be seen that the dielectric permittivity decreases with frequency for composites containing different loadings of nickel ferrite. This behaviour is in accordance with Maxwell-Wagner theory of interfacial polarisation. As the frequency of applied field increases, interfacial polarisation decreases hence dielectric permittivity decreases.

6.1.5 Temperature dependence of dielectric permittivity of nickel ferrite filled EPDM based RFCs

Effect of temperature on dielectric permittivity of nickel ferrite filled EPDM based RFCs were carried out at selected frequencies and plotted in figures 6.11 to 6.16.
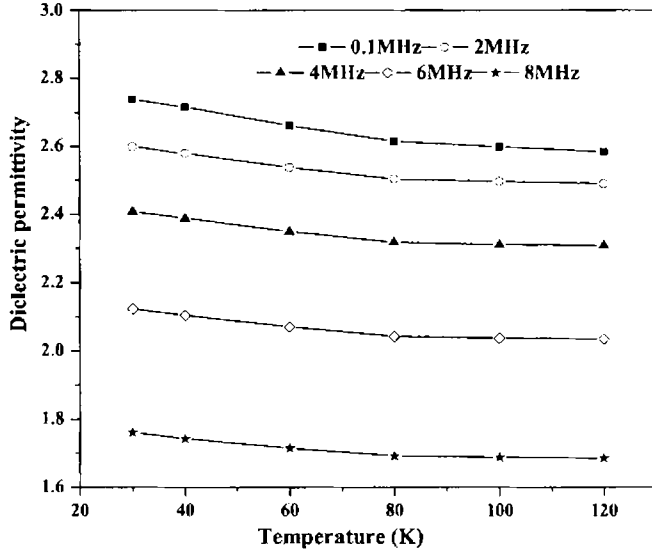
Figure 6.11 Temperature dependence of dielectric permittivity of EPDM based RFC with 20 phr $NiFe_2O_4$
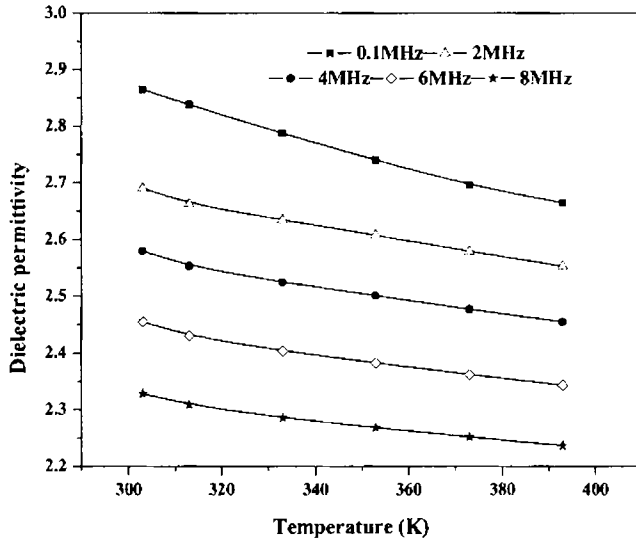
Figure 6.12 Temperature dependence of dielectric permittivity of EPDM based RFC with 40 phr $NiFe_2O_4$
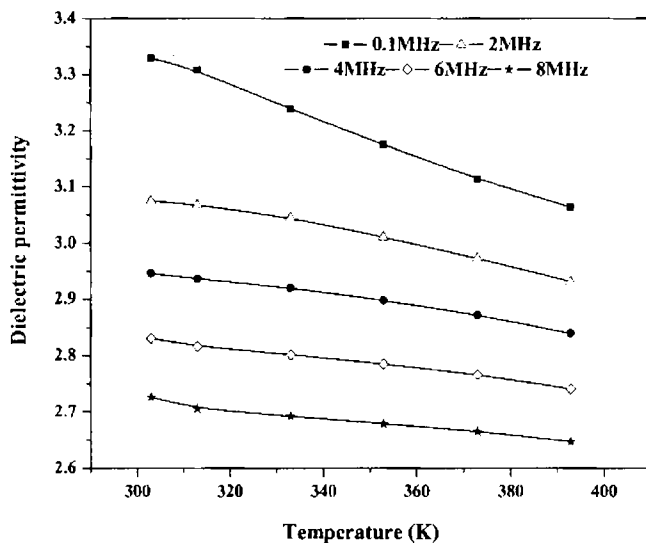
Figure 6.13 Temperature dependence of dielectric permittivity of EPDM based RFC with 60 phr NiFe₂O₄
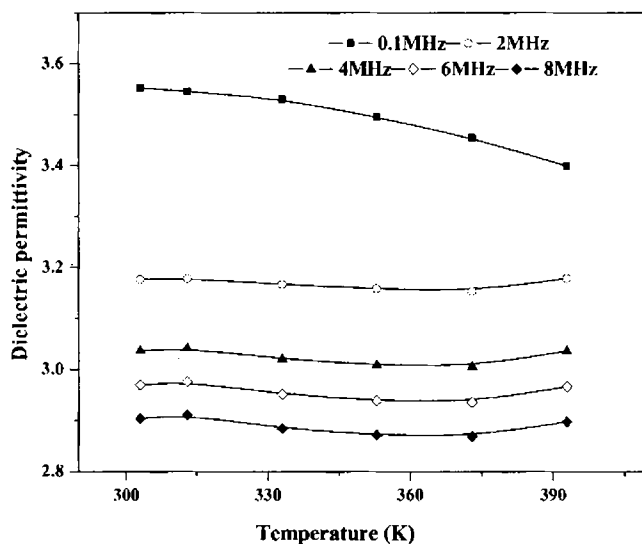
Figure 6.14 Temperature dependence of dielectric permittivity of EPDM based RFC with 80 phr NiFe₂O₄
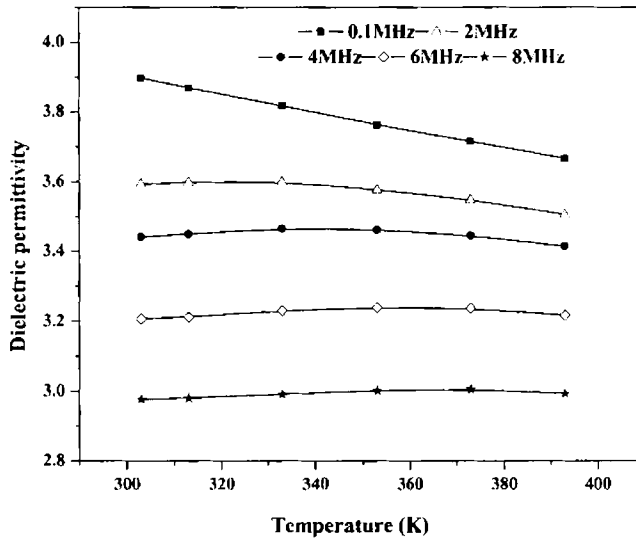
Figure 6.15 Temperature dependence of dielectric permittivity of
EPDM based RFC with 100 phr NiFe₂O₄

For RFCs containing $NiFe_2O_4$, upto 60 phr the dielectric permittivity is found to decrease with increase in temperature. This is due to the thermal expansion of the matrix. With increase in temperature, effective density of the dielectric material decreases, this decreases the dielectric permittivity. At higher loadings of $NiFe_2O_4$ (above 80 phr) the dielectric permittivity decreases with
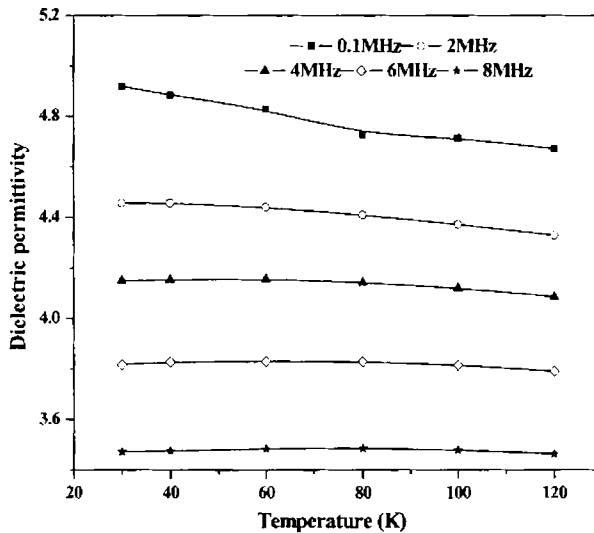
Figure 6.16 Temperature dependence of dielectric permittivity of
EPDM based RFC with 120 phr NiFe₂O₄

temperature at lower frequencies (0.1 MHz). But at higher frequencies, nominal increase in dielectric permittivity is observed with increase in temperature. At higher loadings, due to higher concentration of the ferrite in the matrix, the filler characteristics predominate over the thermal expansion of the matrix and hence dielectric permittivity increases.

6.1.6 Loading dependence of dielectric permittivity of EPDM based RFCs with nickel ferrite filler

Variation of dielectric permittivity with the loading of nickel ferrite was studied and is found to increase with increase in volume fraction of the ferrite. Figures 6.17 to 6.19 show the variation of dielectric permittivity with loading at different temperatures and at some selected frequencies. Maximum value of dielectric permittivity is observed for RFC with 120 phr nickel ferrite.
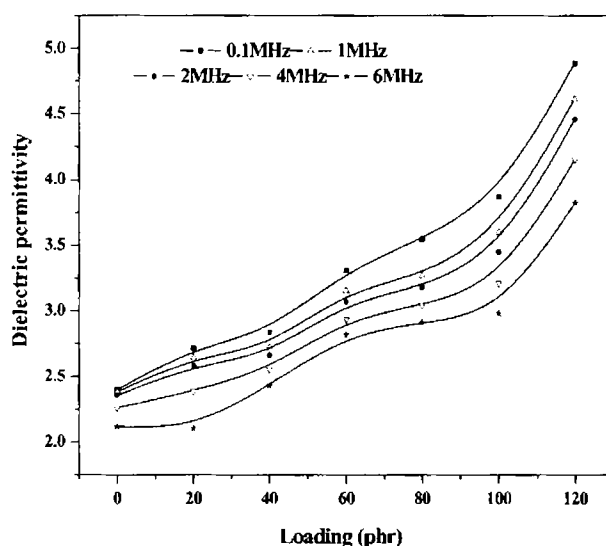
Figure 6.17 Dielectric permittivity versus loading of $NiFe_2O_4$ for EPDM based RFCs at 313 K
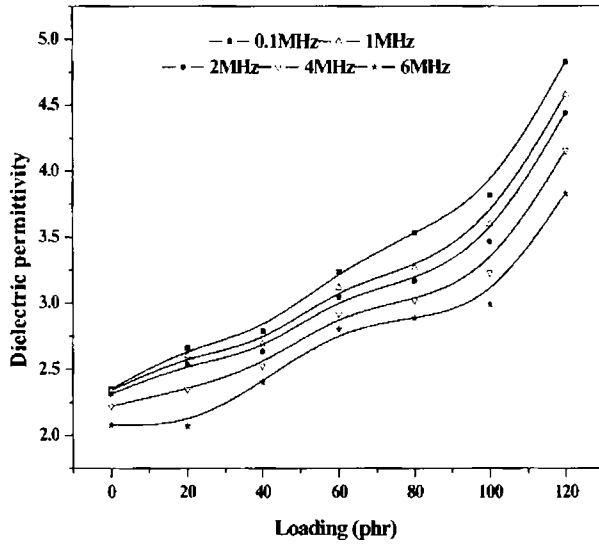
*Figure 6.18 Dielectric permittivity versus loading of NiFe$_2$O$_4$ for
EPDM based RFCs at 333 K*

Variation of dielectric permittivity with loading shows similar pattern at all the temperatures and frequencies studied. Thus it is clear from these studies that the dielectric permittivity of RFCs can be tuned by appropriate filler loading.
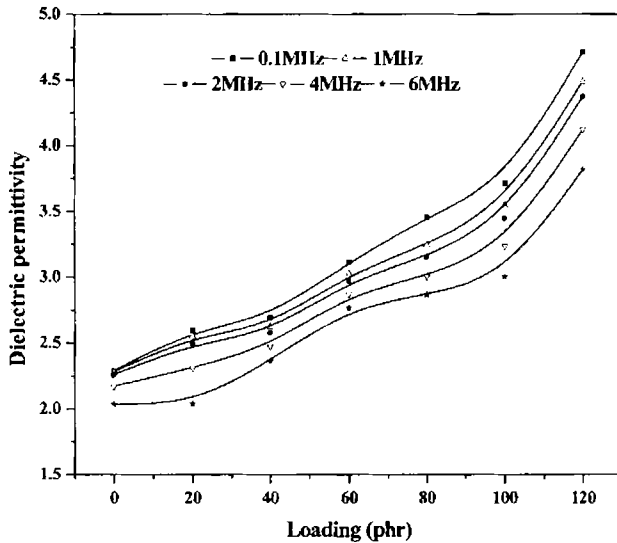
*Figure 6.19 Dielectric permittivity versus loading of NiFe$_2$O$_4$
for EPDM based RFCs at 373 K*

6.1.7 Tailoring of dielectric permittivity of rubber ferrite composites

The observed permittivity of RFCs can be predicted by knowing the permittivity of the host matrix and that of the ferrite by using the empirical equations 6.9 to 6.11, with certain modification. Among the different mixture equations used, the simplest one is the Lichtenecker equation [26,28-30] which can be written as

$$\log \varepsilon_{eff} = (1-V_f) \log \varepsilon_m + V_f \log \varepsilon_f \qquad 6.9$$

where ε_{eff} is the dielectric permittivity of the composite, V_f is the volume fraction of the filler, ε_m and ε_f are the dielectric permittivity of the matrix and the filler respectively.

The best known formula for ε_{eff} for a binary mixture is associated with Maxwell and Wagner. Maxwell developed the idea of effective conductivity of a binary system consisting of spheres of one conductivity distributed uniformly in a continuum of different conductivity. Wagner adopted Maxwell's expression to the dielectric case and the equation is as follows [31].

$$\varepsilon_{eff} = \varepsilon_m \frac{\left[1 - 2V_f \frac{(\varepsilon_m - \varepsilon_f)}{(2\varepsilon_m + \varepsilon_f)} \right]}{\left[1 + V_f \frac{(\varepsilon_m - \varepsilon_f)}{(2\varepsilon_m + \varepsilon_f)} \right]} \qquad 6.10$$

Another mixture equation of the form [32]

$$\varepsilon_{eff} = \frac{\varepsilon_m \varepsilon_f}{\varepsilon_m y_2 + \varepsilon_f y_1} \qquad 6.11$$

is also found to be useful in predicting the loading dependence of dielectric permittivity of the RFCs. In equation 6.11, y_1 and y_2 represent the weight fractions of the matrix and the filler respectively.

In the case of EPDM based RFCs the equations 6.9, 6.10 and 6.11 did not fit well with the experimental data. These equations are derived assuming that spherical shaped conducting/semiconducting particles are well distributed in

noncounducting medium. In the case of RFCs, deviations may occur due to the formation of agglomerates of ferrite particles within the matrix. Thus a modified version of these equations is employed to fit the experimental data. For convenience the logarithmic values were calculated and plotted along with experimental data.
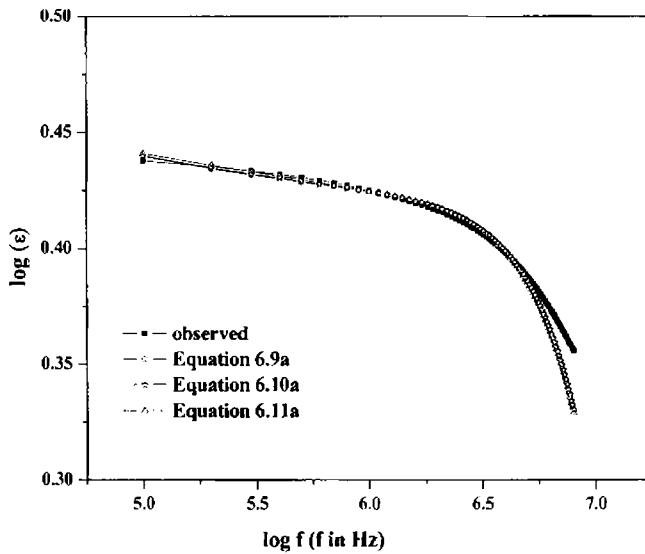
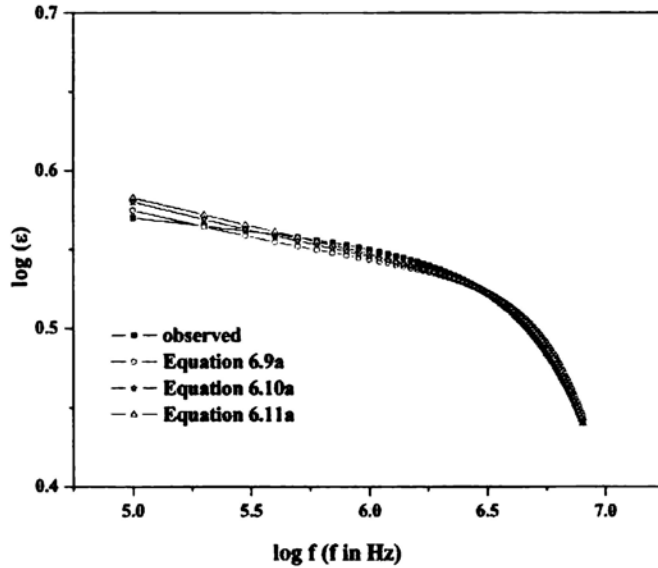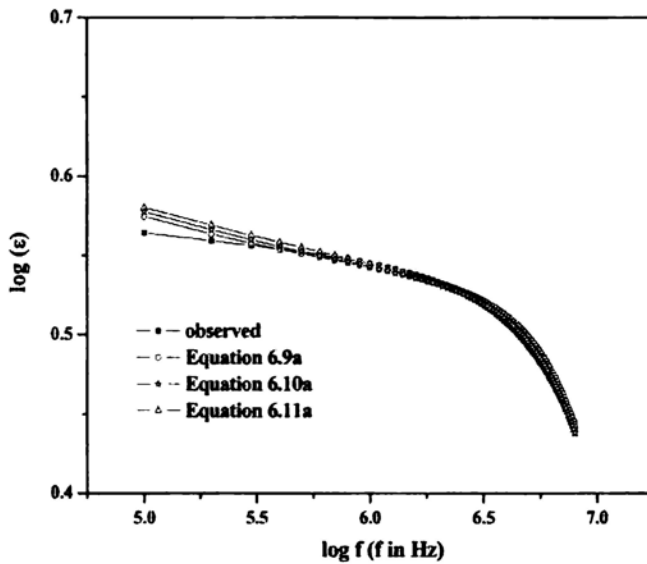*Figure 6.20 log ε versus log f for observed and calculated permittivity for RFC with 40 phr nickel ferrite at 353 K*

In the present study, the modified form of the equation 6.9 is used to calculate the dielectric permittivity of the RFC

$$\log \varepsilon_{eff} = (1\text{-}V_f)\,(\log \varepsilon_m)^k + V_f\,(\log \varepsilon_f)^k \qquad 6.9a$$

Equations 6.10 and 6.11 are also modified with an exponential factor and modified as

$$\log \varepsilon_{eff} = \log \varepsilon_m \frac{\left[1 - 2V_f \frac{\left(\varepsilon_m - \varepsilon_f\right)}{\left(2\varepsilon_m + \varepsilon_f\right)}\right]}{\left[1 + V_f \frac{\left(\varepsilon_m - \varepsilon_f\right)}{\left(2\varepsilon_m + \varepsilon_f\right)}\right]} + \log k \quad 6.10a$$

$$\log \varepsilon_{\text{eff}} = \log \frac{\varepsilon_m \varepsilon_f}{\varepsilon_m y_2 + \varepsilon_f y_1} + \log k \qquad\qquad 6.11a$$

Using equations 6.9a, 6.10a and 6.11a, log ε_{eff} is calculated and plotted against the log f. Figures 6.20 to 6.28 show the calculated permittivity of the RFCs along with that of the experimentally observed values. The calculated permittivity values are found to agree well with the experimentally observed results, in the whole frequency range 0.1-8 MHz.
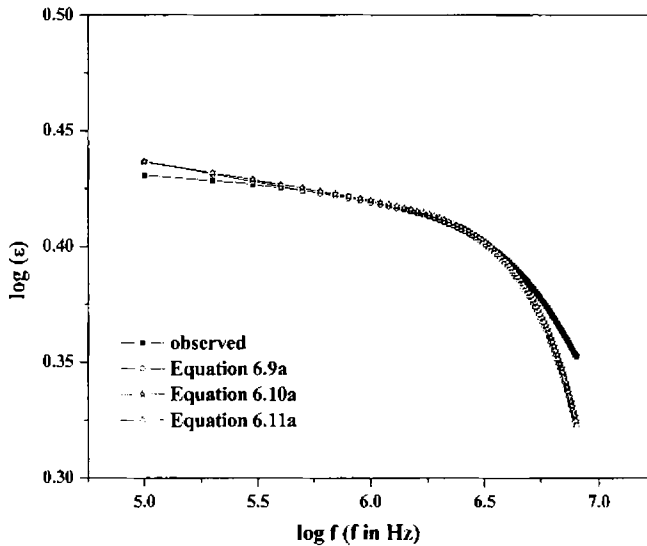
Figure 6.21 log ε versus log f for observed and calculated permittivity for RFC with 40 phr nickel ferrite at 373 K

The value of the newly introduced constant 'k' in equation 6.9a lies in the range 0.6 to 1 for RFCs with 40 to 120 phr nickel ferrite. The value of log k used in other two equations lies in the range 0.02 to 0.7. Value of k depends on several factors such as filler-matrix interaction and particle-particle interaction within the matrix. The marginal variation of the empirical constant may be due to the variation in these factors.
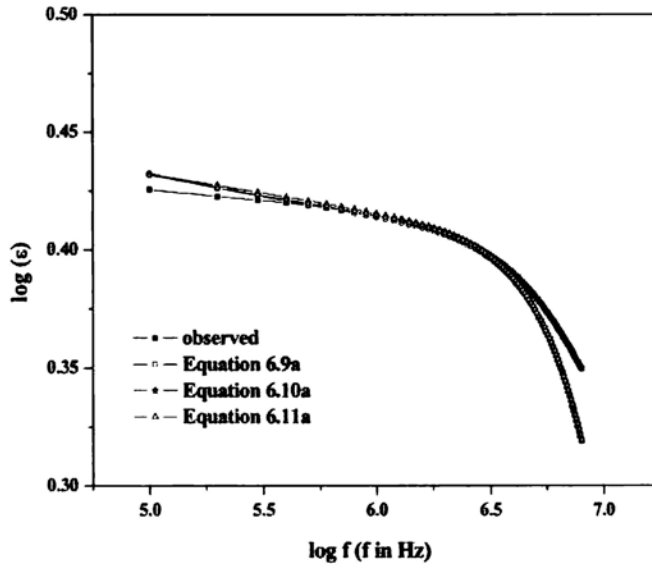
Figure 6.22 log ε versus log f for observed and calculated permittivity for RFC with 40 phr nickel ferrite at 393 K
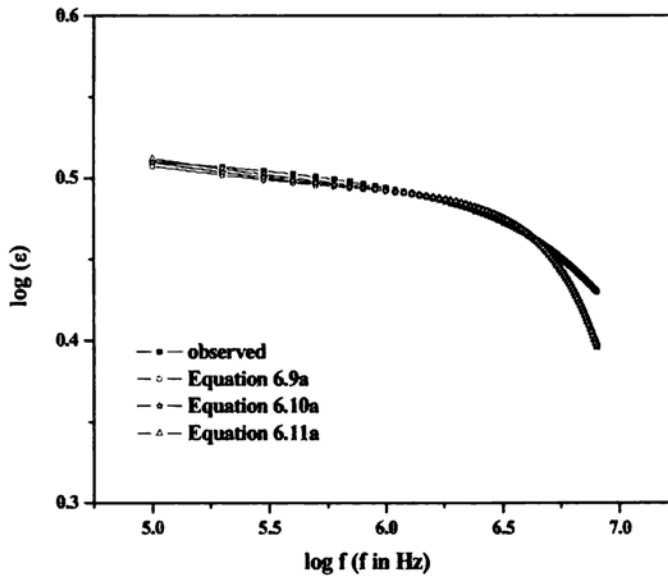
Figure 6.23 log ε versus log f for observed and calculated permittivity for RFC with 60 phr nickel ferrite at 333 K
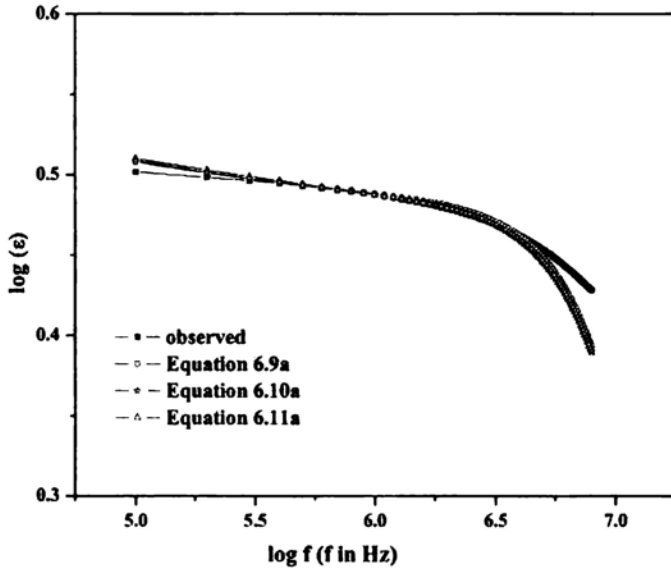
Figure 6.24 log ε versus log f for observed and calculated permittivity for RFC with 60 phr nickel ferrite at 353 K
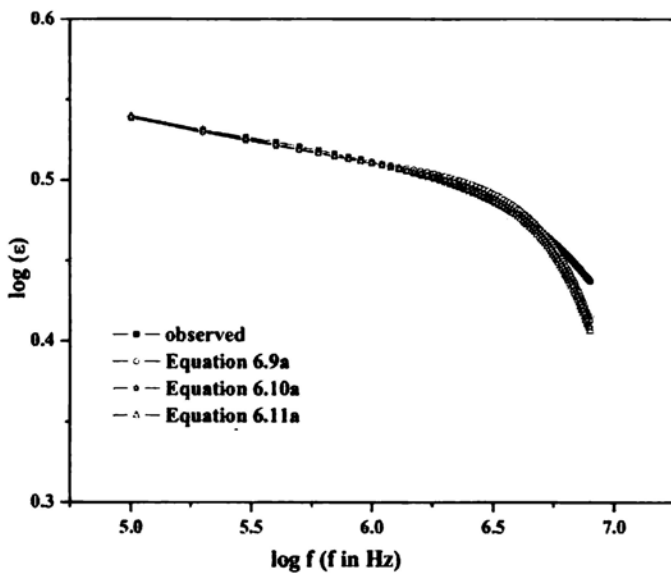
Figure 6.25 log ε versus log f for observed and calculated permittivity for RFC with 80 phr nickel ferrite at 373 K
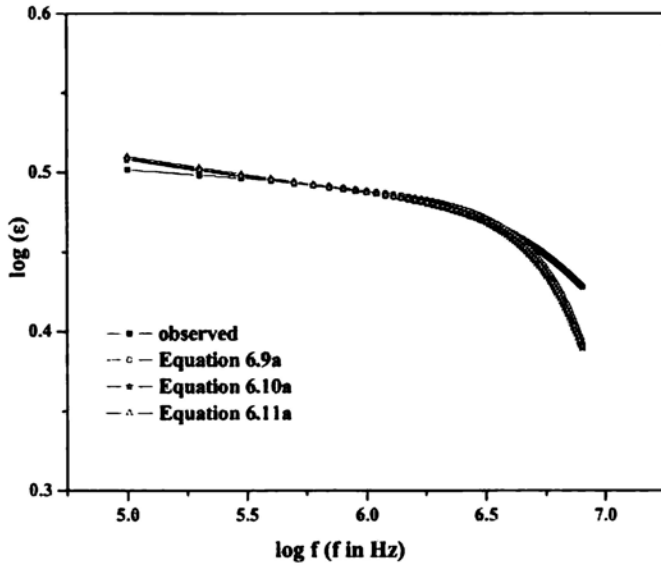
*Figure 6.26 log ε versus log f for observed and calculated permittivity
for RFC with 80 phr nickel ferrite at 393 K*

*Figure 6.27 log ε versus log f for observed and calculated permittivity
for RFC with 100 phr nickel ferrite at 373 K*

Figure 6.28 log ε versus log f for observed and calculated permittivity
for RFC with 100 phr nickel ferrite at 393 K

6.1.8 Dielectric properties of neoprene gum vulcanisate

The dielectric properties of neoprene gum vulcanisate were determined in the frequency range 0.1-8 MHz. The frequency and temperature dependence of dielectric permittivity of neoprene gum vulcanisate is shown in figures 6.29 and 6.30. The dielectric permittivity of neoprene gum vulcanisate is found to be 6.7 at 0.1 MHz, and it decreases with increase in frequency. The high dielectric permittivity of the neoprene vulcanisate compared to EPDM vulcanisate may be due to its polar nature and indicates that the neoprene rubber possess better dielectric characteristics than EPDM rubber.

The decrease in dielectric permittivity with frequency is due to the decrease in polarisation. At higher frequencies, the orientation polarisation lags behind the applied frequency and hence the total polarisation and the dielectric permittivity decreases with increase in frequency.
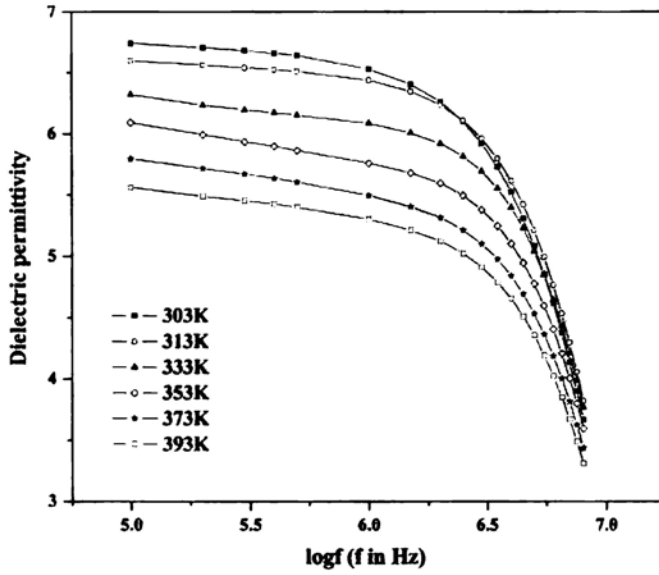
Figure 6.29 Frequency dependence of dielectric permittivity of neoprene gum vulcanisate
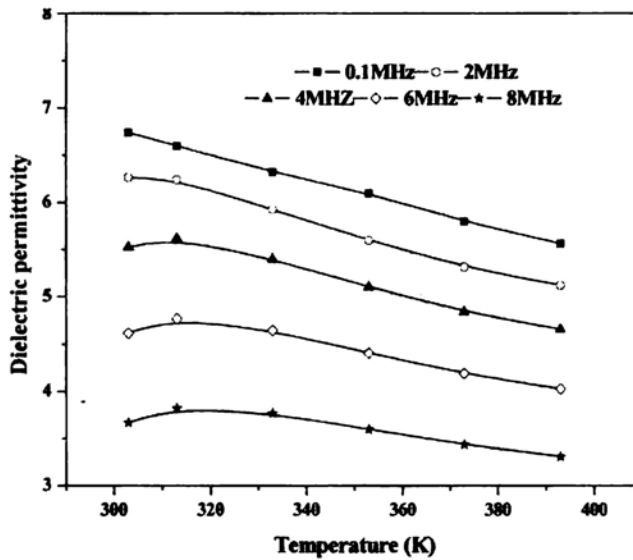
Figure 6.30 Effect of temperature on dielectric permittivity of neoprene gum vulcanisate

Another factor that affects the dielectric permittivity of the polymer is its crystallinity. The dielectric permittivity of semi crystalline polymer is the average of their respective values in the amorphous and crystalline phases.

Variation of dielectric permittivity of neoprene vulcanisate with temperature was determined in the temperature range 303-393 K and is shown in figure 6.30. Dielectric permittivity increases upto 333 K and then decreases with further increase in temperature. The initial increase in dielectric permittivity is more pronounced at higher frequencies.

The initial increase in dielectric permittivity at low temperature is due to the increase in polarity of the bond. But at very high temperature the increased polymer chain mobility decreases the density of the matrix and the dielectric permittivity decreases. These effects are more pronounced at higher frequencies.

6.1.9 Frequency dependence of dielectric permittivity of neoprene based RFCs filled with $NiFe_2O_4$

Effect of frequency on dielectric permittivity of neoprene based RFCs were studied in the temperature range 303-393 K. Figures 6.31 to 6.33 represent frequency dependence of dielectric permittivity of RFCs with different loadings of $NiFe_2O_4$ at 303 K, 333 K and 393 K respectively.

Frequency dependence of dielectric permittivity of neoprene based RFCs shows similar behaviour as in the case of EPDM based RFCs. In RFCs, the semi conducting ferrite is covered with the insulating materials and space charge polarisation occurs at the interfaces. This can also be explained by Maxwell-Wagner-Sillars theory [33], which accounts for the dielectric loss due to the interfacial polarisation of heterogeneous materials having the volume fraction of conductive filler lower than the percolation threshold. The interfacial polarisation can take place at lower frequency. As the frequency is increased, the time required for the interfacial charges to be polarised or for the dipoles to be arranged is delayed, thus the dielectric permittivity decreases with frequency.
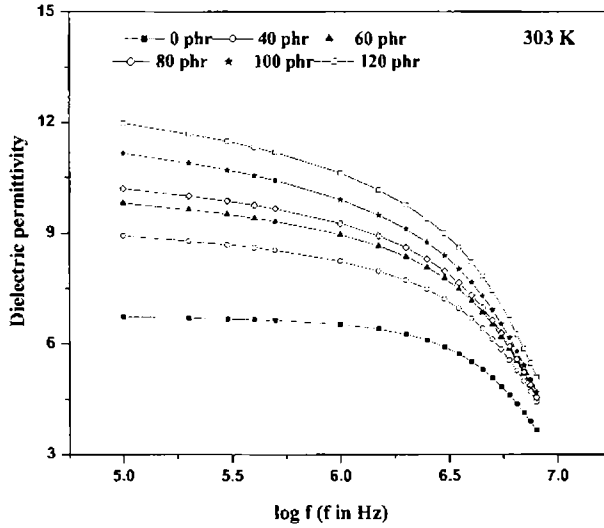
Figure 6.31 Effect of frequency on dielectric permittivity of neoprene based RFCs with different loadings of NiFe₂O₄ at 303 K
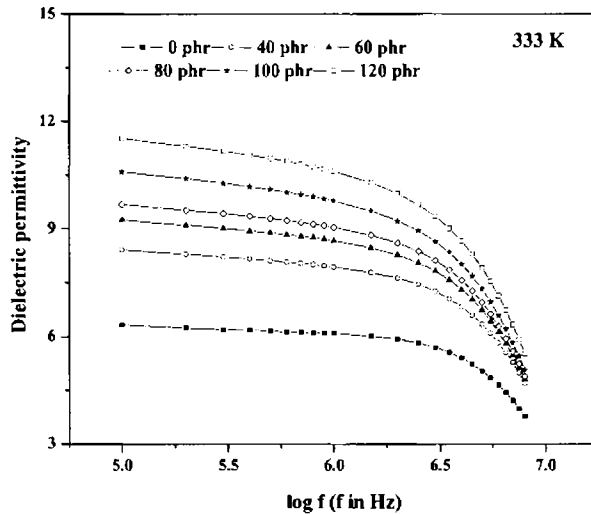
Figure 6.32 Effect of frequency on dielectric permittivity of neoprene based RFCs with different loadings of NiFe₂O₄ at 333 K
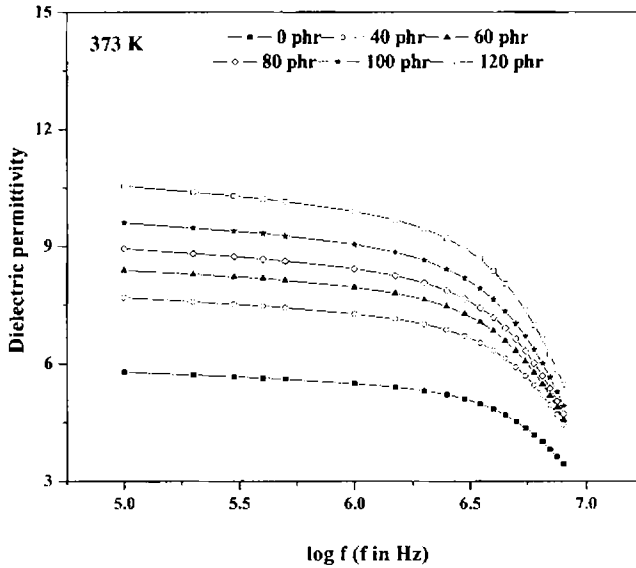
*Figure 6.33 Effect of frequency on dielectric permittivity of neoprene
based RFCs with different loadings of NiFe$_2$O$_4$ at 373 K*

6.1.10 Temperature dependence on the dielectric permittivity of neoprene based RFCs filled with NiFe$_2$O$_4$

Effect of temperature on the dielectric properties of neoprene based RFCs were studied and are plotted in figures 6.34 to 6.36.
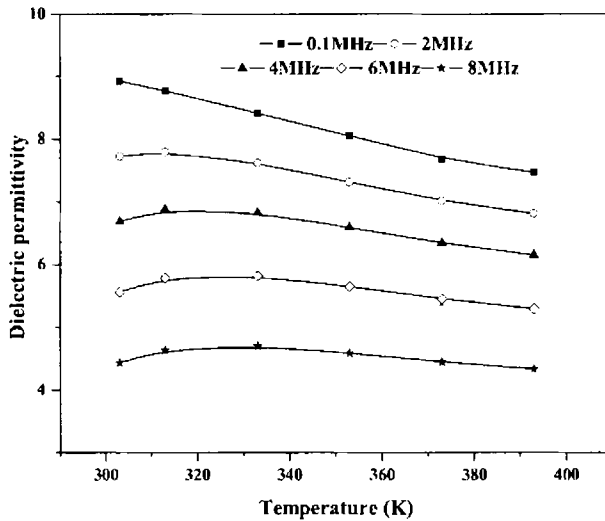
*Figure 6.34 Effect of temperature on dielectric permittivity of
neoprene based RFC containing 40 phr NiFe$_2$O$_4$*

163

For all the composites, the dielectric permittivity decreases with increase in temperature at lower frequency (0.1MHz). At higher frequencies dielectric permittivity increases as the temperature increases upto 333 K and then decreases with further increase in temperature.
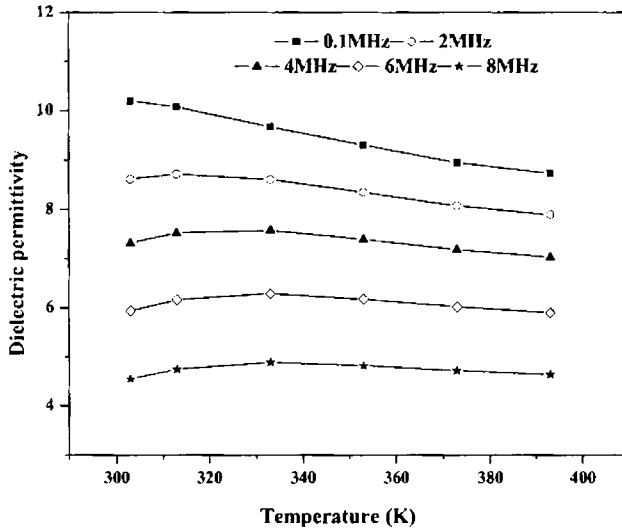
Figure 6.35 Effect of temperature on dielectric permittivity of neoprene based RFC containing 80 phr NiFe₂O₄
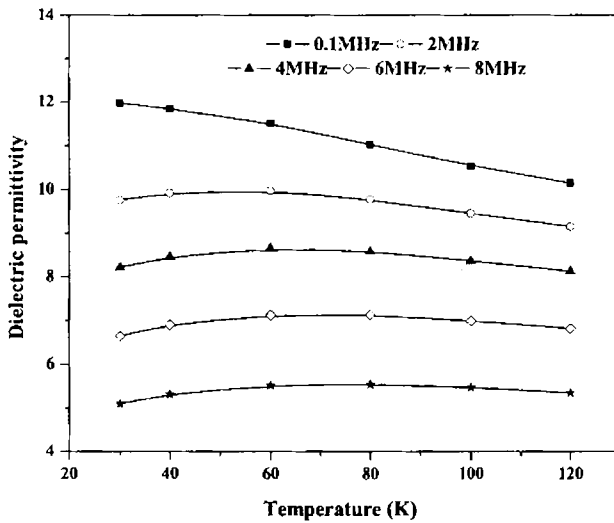
Figure 6.36 Effect of temperature on dielectric permittivity of neoprene based RFC containing 120 phr NiFe₂O₄

The initial increase in dielectric permittivity may be due to the increase in interfacial polarisation, which is facilitated by the increase in temperature. But at higher temperatures the density of the polymer matrix decreases which outweigh the increase in interfacial polarisation and thus the dielectric permittivity decreases.

6.1.11 Loading dependence of dielectric permittivity of neoprene based RFCs containing NiFe$_2$O$_4$

Variation of dielectric permittivity with loading of nickel ferrite in neoprene based RFCs is reported in figures 6.37 to 6.39. Dielectric permittivity is maximum for RFCs with 120 phr nickel ferrite. Dielectric permittivity of RFCs increased linearly with increase in volume fraction of the ferrite filler.
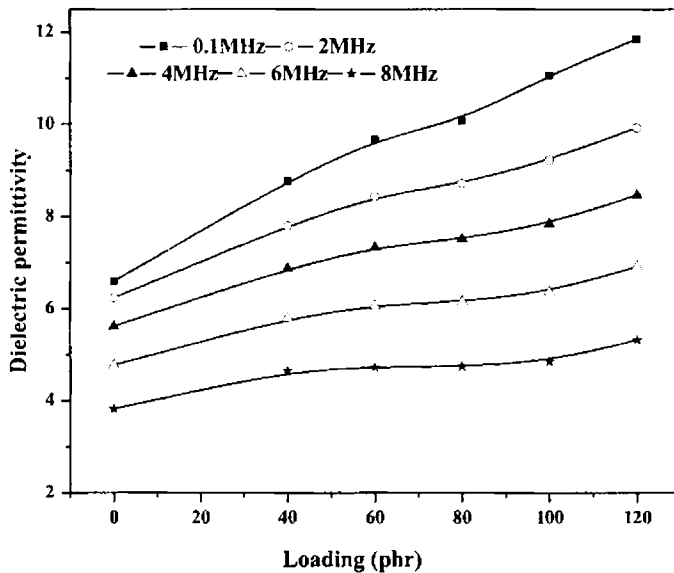
Figure 6.37 Dielectric permittivity versus loading of neoprene based RFCs with NiFe$_2$O$_4$ as filler at 313 K
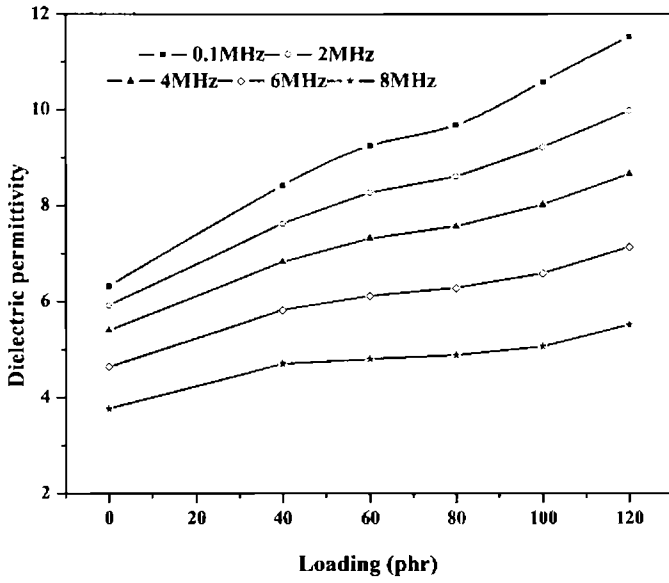
Figure 6.38 Dielectric permittivity versus loading of neoprene based RFCs with $NiFe_2O_4$ as filler at 333 K
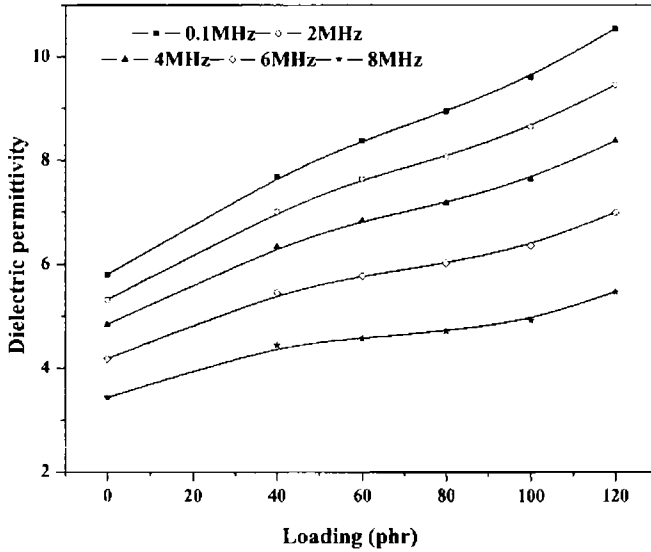
Figure 6.39 Dielectric permittivity versus loading of neoprene based RFCs with $NiFe_2O_4$ as filler at 373 K

6.2 ac Conductivity studies

Due to the magneto-dielectric properties, ferrites play an important role in the field of electronic industry. Ferrites are magnetic semiconductors with low mobility of charge carriers and an exponential dependence of electrical conductivity with temperature. Conventional theories like band theory can not be applied to explain the conductivity in ferrites. Conductivity in simple ferrites as well as in mixed ferrites can be explained by the hopping mechanism which involves hopping of electrons and holes between equivalent lattice cites [34].

Frequency and temperature dependence of ac conductivity of ferrites have provided a lot of information on the behaviour of bound electric charge carriers under an ac field, their mobility and mechanism of conduction [35,36]. Semiconducting behaviour of ferrite depends on the preparative conditions, sintering time and temperatures and the types of impurities [37,38].

The current passing through a sample of thickness h and cross-sectional area A can be determined from Ohm's law and has two components, the in-phase component I cos ϕ and the out-of-phase component I sin ϕ. The real and imaginary ac electrical conductivities are given by σ'_{ac} = (h/A) I cos ϕ and σ''_{ac} = (h/A) I sin ϕ respectively. The real part of ac electrical conductivity σ'_{ac} consists of two terms and can be written as

$$\sigma'_{ac} = \sigma_1(T) + \sigma_2(\omega) \qquad 6.12$$

$$\sigma_1(T) = \sigma_0 \exp[-E/kT], \quad \sigma_2(\omega) = B \, \omega^n \qquad 6.13$$

The first term, $\sigma_1(T)$ is related to drift electric charge carriers. It is frequency independent and temperature dependent, and is really the dc electrical conductivity. The second term, $\sigma_2(\omega)$, is related to the dielectric relaxation caused by bound charge carriers. k is the Boltzmann's constant and E is the activation energy in eV. σ_0, B and n are constants, where n is temperature dependent and ω is the angular frequency of the applied field [39].

The ac electrical conductivity of the ferrites and the EPDM and neoprene based RFCs was calculated from the data obtained from the dielectric measurements.

ac conductivity of the nickel ferrite and nickel ferrite loaded RFCs were estimated in the frequency range 0.1- 8 MHz and in the temperature range 303-393, K.

6.2.1 Frequency and temperature dependence of ac conductivity of $NiFe_2O_4$

Variation of ac conductivity of nickel ferrite with frequency at different temperatures was measured and plotted in figure 6.40. The ac conductivity initially increases with frequency, reaches a maximum, and then decreases at higher frequencies. This can be explained using Maxwell-Wagner two layers or the heterogeneous model of the polycrystalline structure of ferrites [40]. The heterogeneities of the material as described by the Maxwell-Wagner model consists of two layered capacitors, that is the well conducting grains are separated by layers of lower conductivity. The low-frequency ac conductivity is related to the resistive grain boundaries, where as the high frequency ac conductivity is due to the conductive grains [6].
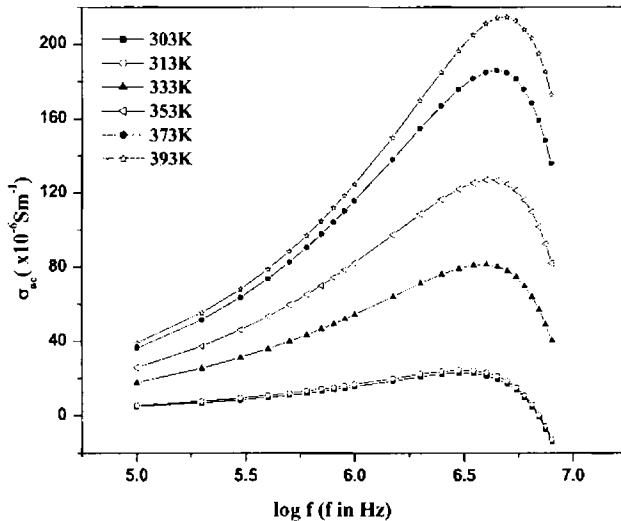
Figure 6.40 Variation of ac conductivity with logarithmic frequency of the applied field

Electrical conductivity in ferrites is due to the hopping of electrons (charge carriers) between Fe^{2+} and Fe^{3+} ions. As the frequency of the applied field increases, the hopping of the charge carriers also increases, thereby increasing the conductivity. In addition, the equations 6.2 and 6.13 explain the increase in σ_{ac} with increase in frequency. At very high frequencies, greater than 5 MHz, ac conductivity decreases

with further increase in frequency as the hopping of electron lags behind the applied frequency.
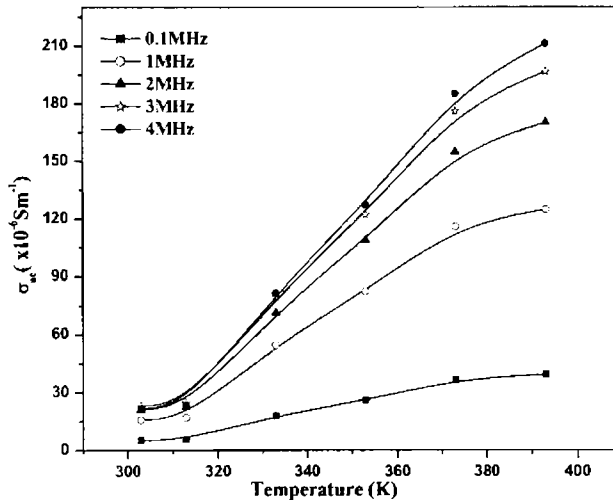
Figure 6.41 Effect of temperature on ac electrical conductivity of NiFe$_2$O$_4$

The effect of temperature on ac electrical conductivity of nickel ferrite is studied and plotted in figure 6.41. The temperature dependence on ac conductivity is studied in the range 303-393 K for different frequencies.

As the temperature increases, the conductivity increases, typical of magnetic semiconductors. The increase in conductivity with temperature can be related to the increase in the drift mobility of thermally activated electrons, which increases the hopping conduction. At low frequencies the variation is minimum, but at higher frequencies the variation is more rapid [41].

6.2.2 Frequency dependence of ac conductivity of EPDM based RFCs with NiFe$_2$O$_4$

Figure 6.42 shows the frequency dependence of ac conductivity of EPDM gum vulcanisate and the corresponding RFCs with different loading of NiFe$_2$O$_4$ at temperatures ranging from 303-393 K. Most of the polymeric materials are insulators and practically no conductivity is observed in unvulcanised elastomers. The ac conductivity observed in the vulcanised elastomers may be due to the different compounding ingredients added to it, which can act as carriers for conduction. Moreover, the semi crystalline polymer can be considered as a continuous matrix of

169
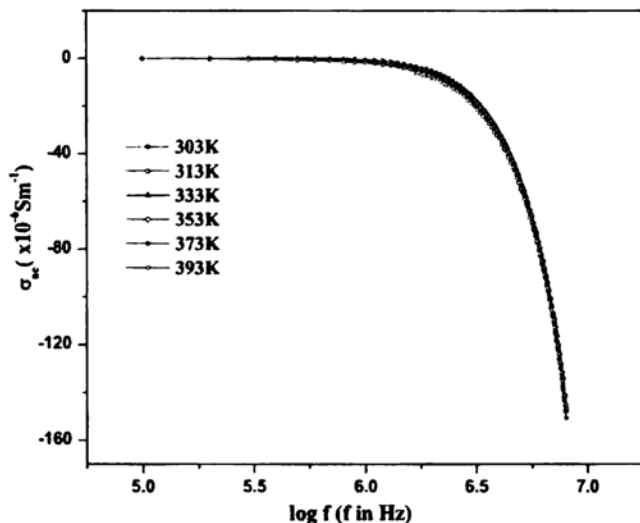
Figure 6.42 Variation of ac conductivity of EPDM gum vulcanisate
with logarithmic frequency

an amorphous polymer in which the crystalline regions are randomly distributed. The crystallite centers tend to lower the conductivity. Hence the structure can be considered similar to Maxwell-Wagner two layer model [42]. In the case of EPDM gum vulcanisate significant change in ac conductivity is not observed with frequency and temperature.
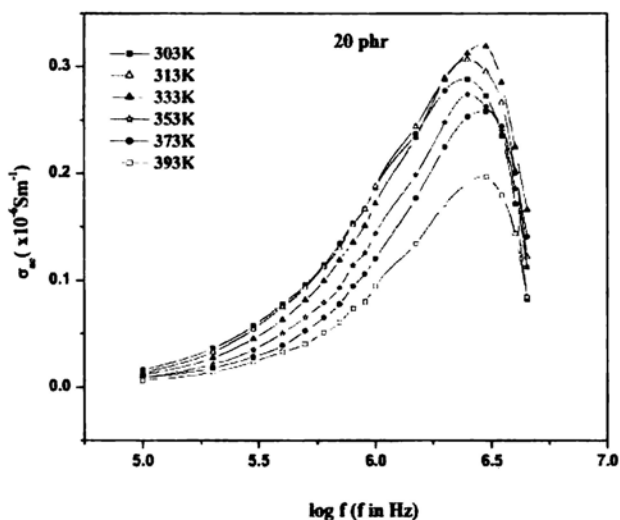
Figure 6.43 Effect of frequency on ac conductivity of EPDM
based RFC with 20 phr NiFe₂O₄

Effect of frequency on ac conductivity of the EPDM based rubber ferrite composites with different loading of nickel ferrite is shown in figures 6.43 to 6.45.
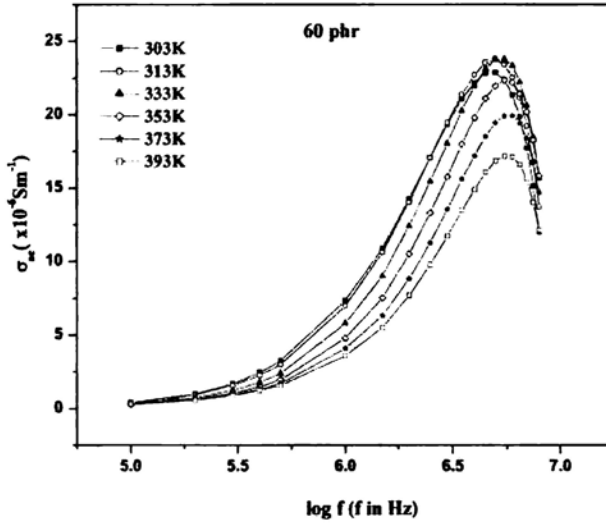
Figure 6.44 Effect of frequency on ac conductivity of EPDM based RFC with 60 phr NiFe$_2$O$_4$
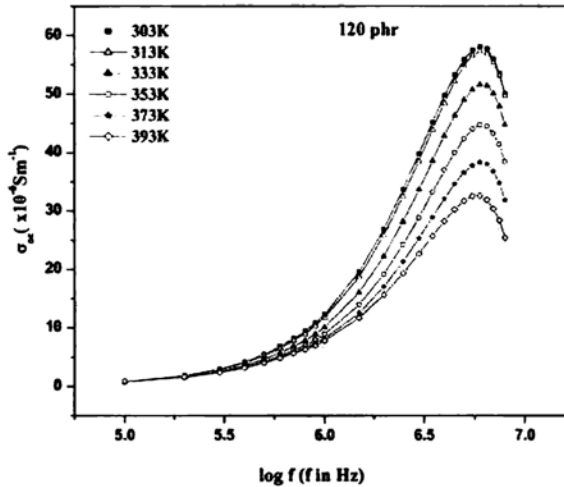
Figure 6.45 Effect of frequency on ac conductivity of EPDM based RFC with 120 phr NiFe$_2$O$_4$

With the incorporation of nickel ferrite, the ac conductivity increases with increase in frequency and drops after reaching a maximum at higher frequencies. The ac electrical conductivity of RFCs is due to the presence of fillers and the conduction mechanism is the same as that of the nickel ferrite. So the increase in ac conductivity

with frequency is due to the increase in hopping conduction. The RFCs with different loading of nickel ferrite exhibit similar frequency dependence at different temperatures.

6.2.3 Effect of temperature on ac electrical conductivity of EPDM based RFCs filled with $NiFe_2O_4$

Effect of temperature on ac conductivity at selected frequencies for RFCs with different loadings of nickel ferrite is shown in figures 6.46 to 6.48. At lower frequencies ac conductivity decreases with temperature. But at higher frequencies, a nominal increase in ac conductivity is observed upto 313 K and then decreases with further increase in temperature.
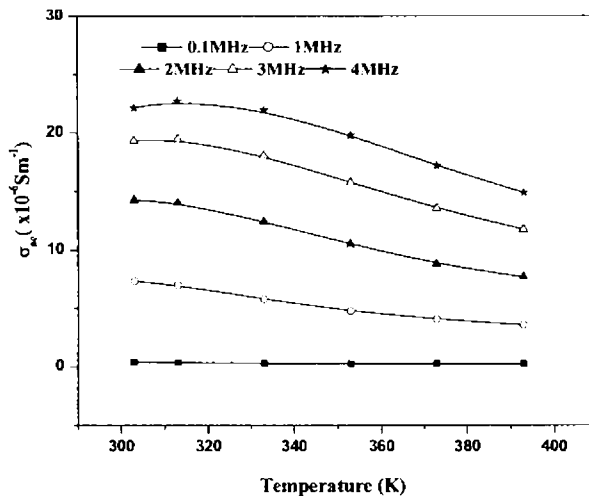
Figure 6.46 Effect of temperature on ac conductivity of EPDM based RFC with 60 phr $NiFe_2O_4$

Temperature dependence of ac conductivity of RFCs is quite similar to the temperature dependence of dielectric permittivity. The initial increase in conductivity at lower temperature is due to the increase in hopping conduction. But at very high temperatures, the segmental mobility of the polymer increase which may insulate the ferrite particles thus decreased ac conductivity is observed at high temperatures.
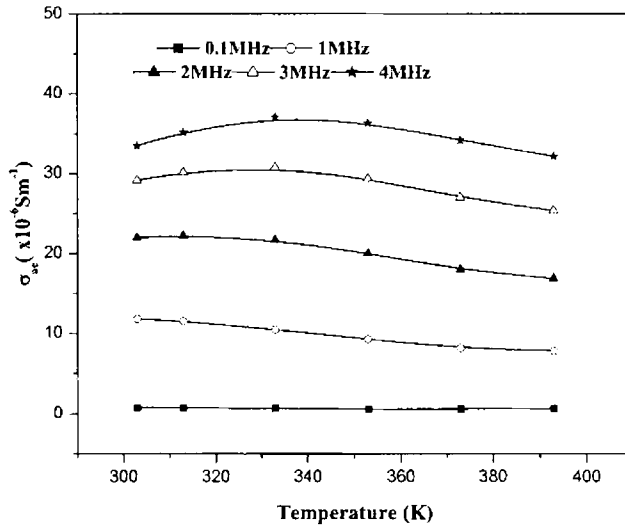
Figure 6.47 Effect of temperature on ac conductivity of EPDM based RFC with 80 phr NiFe₂O₄
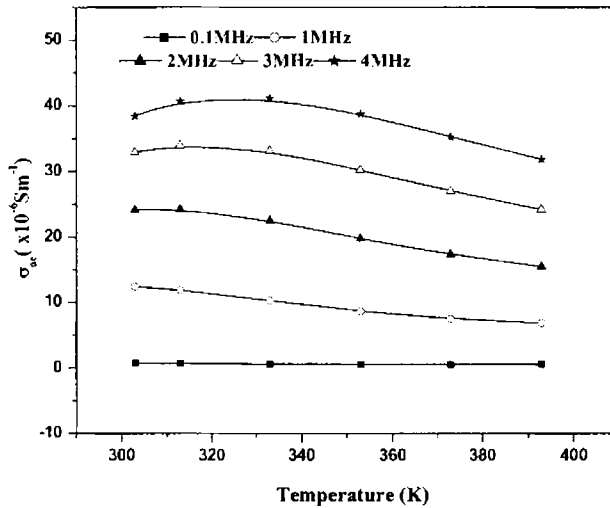
Figure 6.48 Effect of temperature on ac conductivity of EPDM based RFC with 100 phr NiFe₂O₄

6.2.4 Loading dependence of ac conductivity of EPDM based RFCs filled with NiFe₂O₄

Representative graphs for loading dependence of ac conductivity of RFCs at two different temperatures for some selected frequencies are shown in figures 6.49 and 6.50.
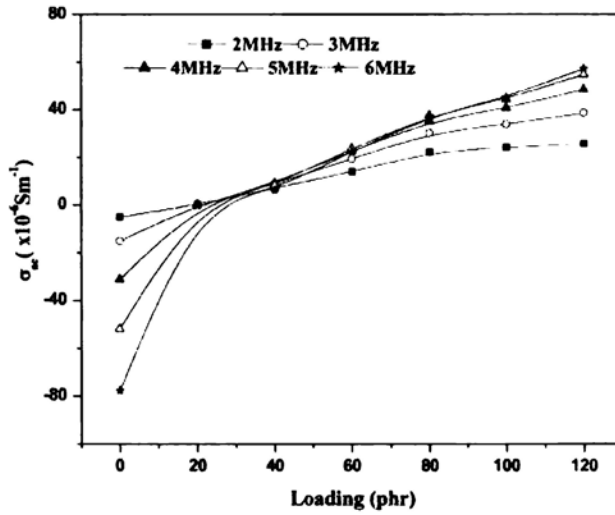
Figure 6.49 Loading dependence of ac conductivity of EPDM based RFCs with NiFe$_2$O$_4$ at 313 K
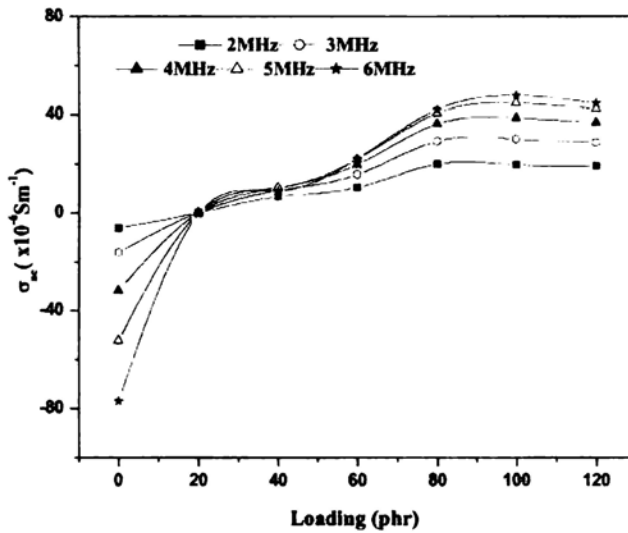
Figure 6.50 Loading dependence of ac conductivity of EPDM based RFCs with NiFe$_2$O$_4$ at 353 K

In nickel ferrite filled RFCs, an increase in ac conductivity is observed with increase in volume fraction of the filler. A maximum conductivity is observed for RFCs with 120 phr nickel ferrite. At lower loadings, the conductivity of the composites differs significantly from that of the gum vulcanisate. As the volume

fraction of the ferrite increases, a sharp increase in conductivity can be observed. This is due to the formation of a conductive path of ferrites within the rubber matrix.

6.2.5 Frequency dependence of ac conductivity of $NiFe_2O_4$ filled neoprene based RFCs

The ac conductivity of nickel ferrite filled neoprene based RFCs was estimated as explained in section 2.5.2. Frequency, temperature and loading dependence of RFCs were carried out in the frequency range 0.1-8 MHz and in the temperature range 303-393 K. Due to the presence of polar C-Cl bond in neoprene, ac electrical conductivity is found to be high for neoprene based RFCs compared to the EPDM based RFCs. However, the behaviour pattern with respect to the frequency and temperature is the same for EPDM and neoprene based RFCs. Representative graphs showing the effect of frequency on ac conductivity of neoprene based RFCs at three different temperatures are shown in figures 6.51 to 6.53.
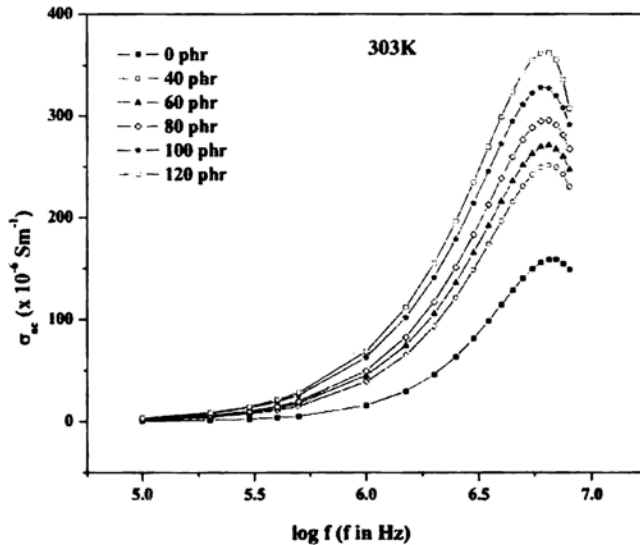
Figure 6.51 Effect of frequency on ac conductivity of neoprene based RFCs at 303 K
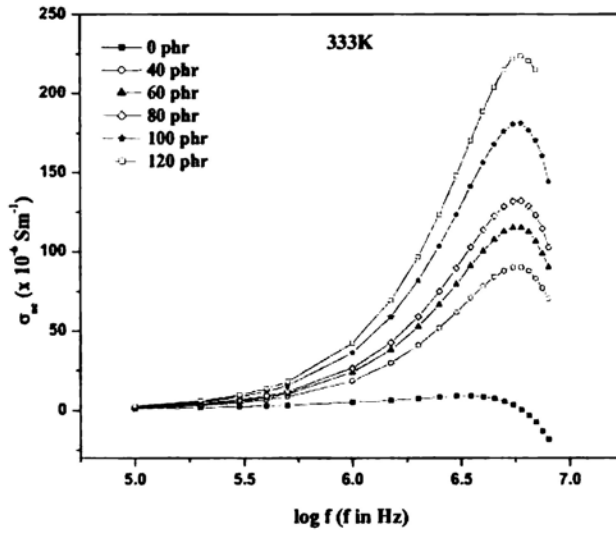
Figure 6.52 Effect of frequency on ac conductivity of neoprene based RFCs at 333 K
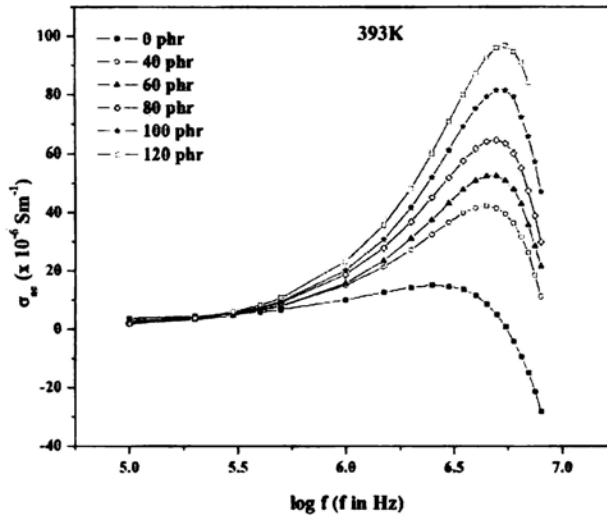
Figure 6.53 Effect of frequency on ac conductivity of neoprene based RFCs at 393 K

As the frequency increases the conductivity increases and drops at higher frequencies. The conductivity of gum vulcanisate is due to the different ingredients added for vulcanisation. Neoprene is a semi crystalline polymer. The semi crystalline polymer can be considered as a continuous matrix of an amorphous polymer in which the crystalline regions are randomly distributed. The crystallite centers tend to lower the conductivity. The elastomer can be visualised as a double layer which is made up of crystalline and non-crystalline centers, analogous to Maxwell-Wagner two layer

models. If the conduction is ionic, ion mobility through the crystalline region will be low and in the case of electronic conduction, the crystalline-amorphous interface may act as a trapping region. At lower frequencies, the crystalline-noncrystalline interface may be more active and as the frequency increases, the ions cross over to the interface leading to an increase in conductivity. High frequency limit is reached when applied frequency is greater than the hopping rate. Further increase in applied frequency leads to decrease in ac conductivity.

RFCs with different loading of nickel ferrite shows the same behaviour on frequency change. The conductivity increases with increase in frequency, reaches a maximum and then decreases at higher frequencies. However the rate of increase is higher for RFCs compared to the gum vulcanisate. The behaviour pattern is same at all the temperatures studied.

6.2.6 Temperature dependence of ac conductivity of neoprene based RFCs filled with NiFe$_2$O$_4$.

Effect of temperature on ac conductivity of neoprene based RFCs with different loadings of NiFe2O4 at selected frequencies are represented in figures 6.54 to 6.56.
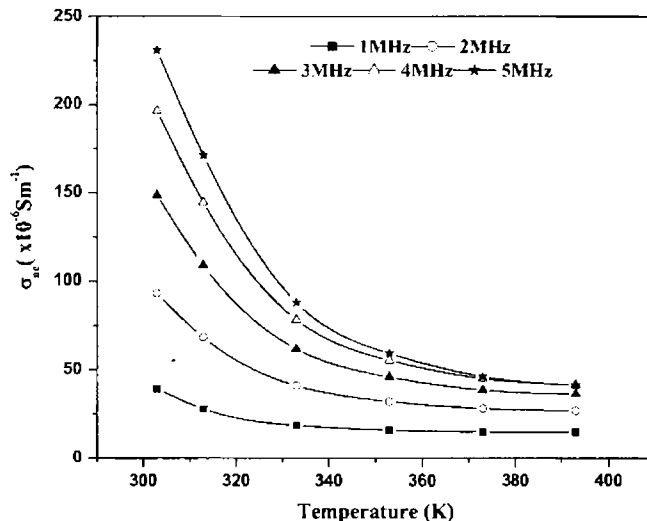
Figure 6.54 Effect of temperature on ac conductivity of neoprene based RFC with 40 phr NiFe$_2$O$_4$

As the temperature increases, ac conductivity of the RFCs decreases and becomes constant at very high temperature. Sharp decrease in conductivity is observed at lower temperatures, which attains a constant value at high temperatures.
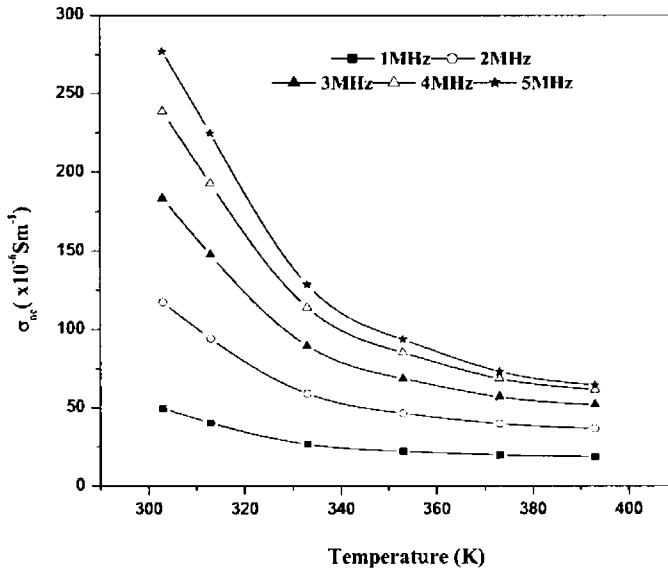
Figure 6.55 Effect of temperature on ac conductivity of neoprene based RFC with 80 phr NiFe₂O₄
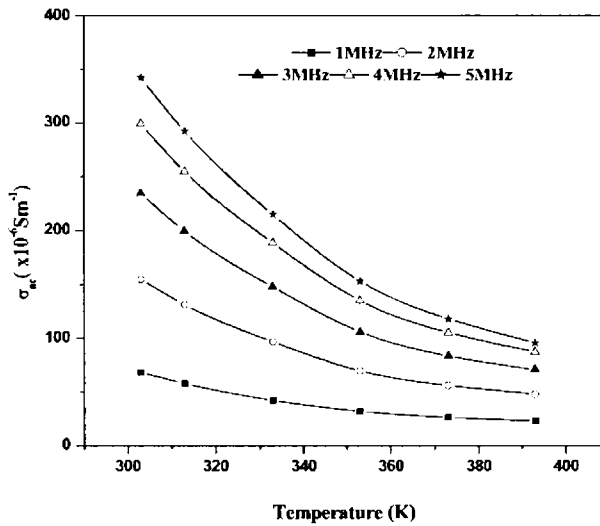
Figure 6.56 Effect of temperature on ac conductivity of neoprene based RFC with 120 phr NiFe₂O₄

As temperature increases, polymer chain mobility increases and volume of the matrix increases. As a result, the effective density of charge carriers in the matrix decrease which decreases the conductivity. At very high temperatures the conducting fillers are insulated by the matrix, so further decrease in conductivity becomes nominal.

6.2.7 Dependence of filler loading on ac conductivity

The effect of loading of $NiFe_2O_4$ on ac conductivity of neoprene based RFCs at different temperatures are shown in figures 6.57 to 6.59. The conductivity values were measured in the frequency range 0.1-8 MHz.
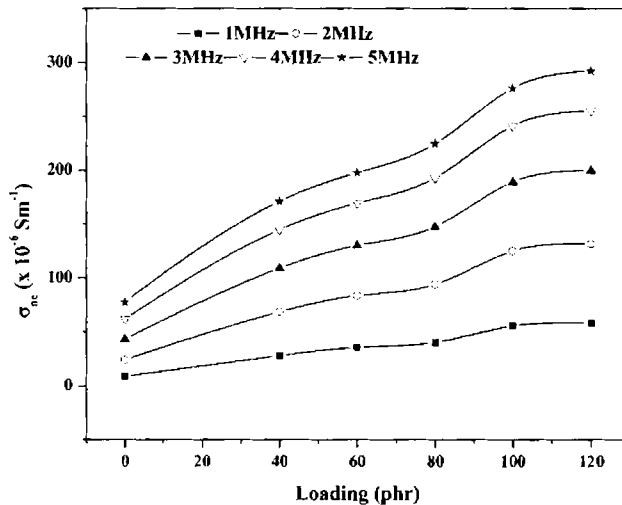
Figure 6.57 Variation in ac conductivity versus loading of $NiFe_2O_4$ in neoprene based RFCs at 313 K

As expected, the conductivity values of the RFCs increased with increase in volume fraction of semi conductive ferrite filler. Similar behaviour is observed at all temperatures and frequencies as evidenced by the figures 6.57 to 6.59. At higher concentrations of the filler, a conductive path of the ferrite particles may form, which increases the ac conductivity. Beyond the percolation limit, further increase in ac conductivity with ferrite concentration becomes nominal.
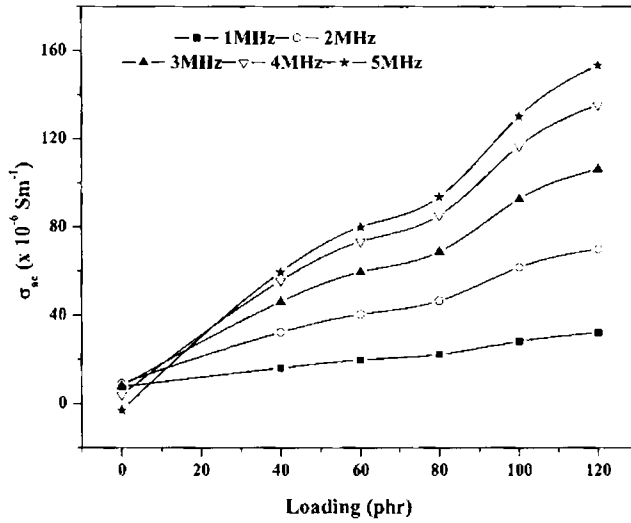
Figure 6.58 Variation in ac conductivity versus loading of $NiFe_2O_4$
in neoprene based RFCs at 353 K
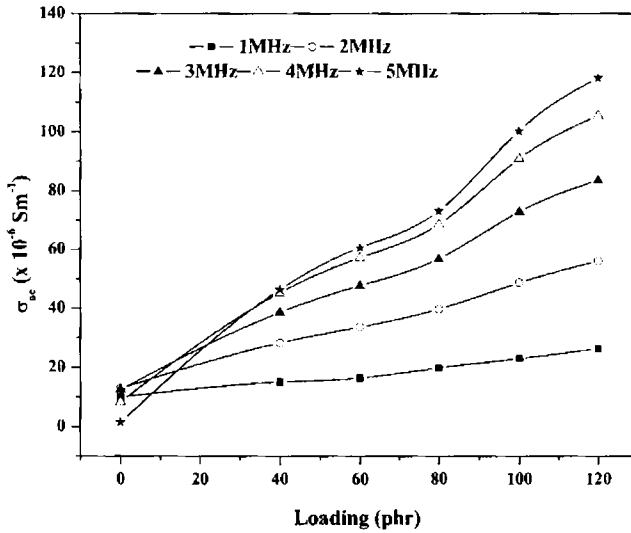
Figure 6.59 Variation in ac conductivity versus loading of $NiFe_2O_4$
in neoprene based RFCs at 373 K

6.3 Dielectric properties of carbon black filled EPDM based RFCs

RFCs find extensive applications because of its dielectric and microwave absorbing properties. The dielectric as well as microwave characteristics of RFCs can be improved by the incorporation of carbon black. Hence, EPDM based RFCs with

100 phr nickel ferrite was mixed with various loadings of carbon black ranging from 20 to 80 phr in steps of 20. The dielectric properties of these RFCs are studied in the frequency range 0.1-8 MHz. Effect of carbon black loading on dielectric permittivity and ac conductivity of these RFCs is also reported here.

Representative graphs showing the effect of frequency on dielectric permittivity and ac conductivity on carbon black filled RFCs is shown in figures 6.60 and 6.61. The frequency dependence of dielectric permittivity and ac conductivity is the same as that of the RFCs without carbon black. Dielectric permittivity decreases with increase in frequency as in the case of RFCs. The decrease in dielectric permittivity with frequency is due to the decrease in interfacial polarisation, which is explained by invoking Maxwell-Wagner theory of dielectrics.
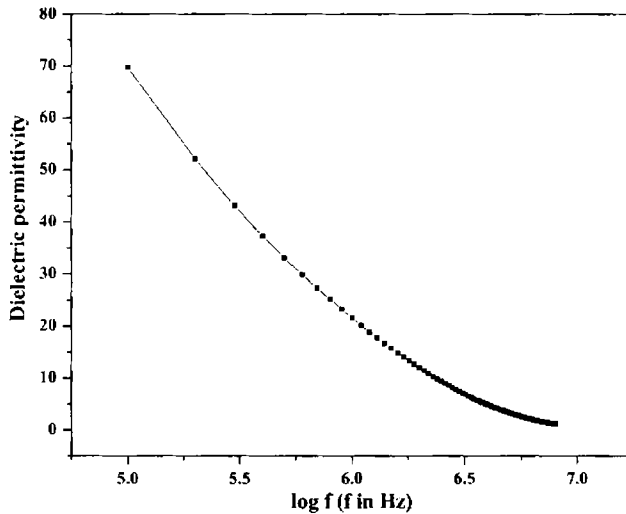
Figure 6.60 Dielectric permittivity versus logarithmic frequency of RFC with 100 phr NiFe₂O₄ and 60 phr carbon black at 303 K

As the frequency increases, the ac conductivity of the carbon black containing RFCs increases, attains a maximum and then decreases with further increase in frequency. The increase in ac conductivity with frequency can be attributed to the increase in hopping conduction as in the case of RFCs. At higher frequencies hopping conduction lags behind the applied frequency, hence conductivity decreases.
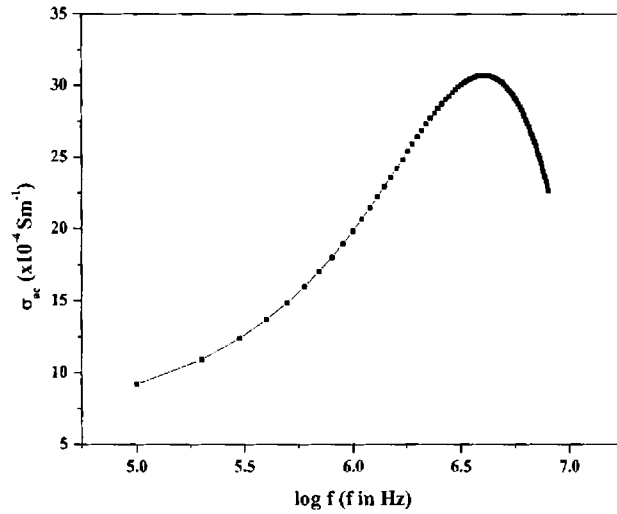
Figure 6.61 Effect of frequency on ac conductivity of RFC containing
100 phr NiFe$_2$O$_4$ and 60 phr carbon black at 303K

Loading dependence of dielectric permittivity and ac conductivity is shown in figures
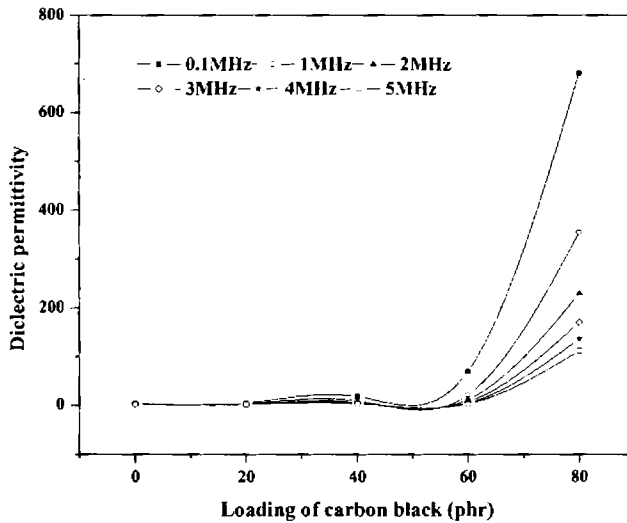6.62 and 6.63.

Figure 6.62 Dielectric permittivity versus loading of carbon black in
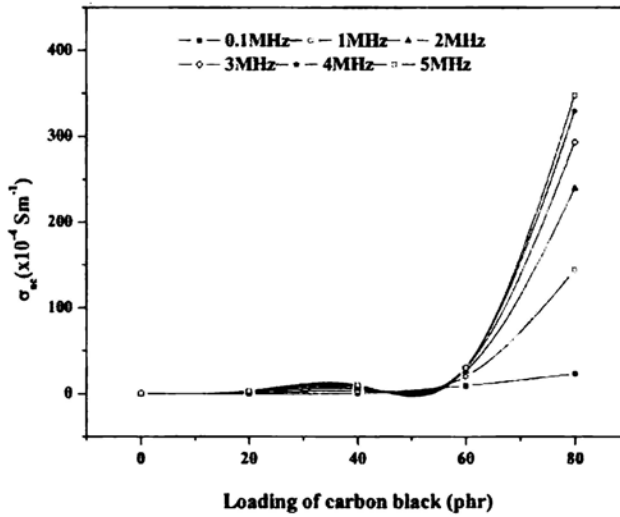*EPDM based RFC containing 100 phr of NiFe$_2$O$_4$ at various frequencies*

Figure 6.63 ac conductivity versus loading of carbon black in EPDM based RFC containing 100 phr of NiFe$_2$O$_4$ at various frequencies.

The dielectric permittivity of RFCs increases with the addition of carbon black. At 0.1 MHz frequency the dielectric permittivity of RFC with 100 phr nickel ferrite is 3.89 and it is increased to 680 at the same frequency with the addition of 80 phr carbon black. Similarly the conductivity of the RFCs is also enhanced by 2 orders of magnitude with the addition of 80 phr carbon black.

6.4 Conclusion

Precharacterised nickel ferrite at different loadings was incorporated into EPDM and neoprene matrix for preparing the rubber ferrite composites. The dielectric permittivity of the ferrite and the RFCs decreased with increase in applied frequency. For the ceramic filler, the dielectric permittivity was found to increase with temperature, where as for the RFCs, the dielectric permittivity decreased with temperature at lower frequencies. But at higher frequencies dielectric permittivity increased first and then decreased with further increase in temperature. In both EPDM and CR based RFCs the dielectric permittivity increased with increase in volume fraction of the ferrite and a maximum was obtained for RFC with 120 phr nickel ferrite. Neoprene based RFCs were having better dielectric properties compared to EPDM based RFCs.

Frequency and temperature dependence of ac electrical conductivity of nickel ferrite and EPDM and neoprene based RFCs were also studied. Dependence of frequency on the ac conductivity was same for nickel ferrite and the corresondimg RFCs. With the increase in frequency, ac conductivity increased and droped at higher frequencies. Compared to EPDM based RFCs neoprene based RFCs were found to have better ac conductivity. In both types of RFCs, the ac conductivity increased with increase in volume fraction of the filler and a maximum was obtained for the RFCs with 120 phr nickel ferrite. With increase in temperature, ac conductivity of the nickel ferrite increased. In the case of EPDM composites ac conductivity decreased with temperature at lower frequencies.

The frequency dependence of dielectric permittivity and ac conductivity of the carbon black containing RFCs was similar to that of the RFCs. The dielectric permittivity and ac conductivity of the RFCs were enhanced by the incorporation of carbon black. Since carbon black composites can function as microwave absorbers, the microwave absorption of RFCs can be modified with the incorporation of carbon black.

Different mixture equations were applied to calculate the dielectric permittivity of the RFCs and were found to agree with the observed values. The dielectric properties of the composites with different volume fractions of ferrite fillers can be predicted using the mixture equations. Thus the properties of RFCs can be tailored by employing one of these equations.

Refrences

1. A.A. Sattar, Egypt. J. Sol., **26** (2003) 113.
2. H. Igarash and K. Okazaki, J. Am. Ceram. Soc., **60** (1977) 51.
3. J. Kulikowski, J. Magn. Magn. Mater., **41** (1984) 56.
4. P. Ravindaranathan and K.C. Patil, J. Mater. Sci., **22** (1987) 3261.
5. C. Ramasastry and Syamasundra Rao, J. Phys. E. Sci. Instrum., **12** (1979) 1023.
6. M.A. EI Hiti, J. Magn. Magn. Mater., **192** (1999) 305.
7. M.H. Abdullah and A. N Yusoff, J. Mater. Sci., **32** (1997) 5817.
8. D. Ravinder and P. Vijaya Bhasker Reddy, Mater. Lett., **57** (2003) 4344.
9. M.A. EI Hiti, M.A. Ahmed, M.M. Mosaad and S.M. Attia, J. Magn. Magn. Mater., **150** (1995) 399.

10. C. B. Kolckar, P.N. Kamble, S.G. Kulkarni and A.S. Vaingankar, J. Mater. Sci., **30** (1995) 5784.

11. S.R. Kulkarni, C.M. Kanamadi and B.K. Chougule, Journal of Physics and Chemistry of Solids, **67** (2006) 1607.

12. Mathew George, Swapna S. Nair, Asha Mary John, P.A. Joy and M.R. Anantharaman, J. Phys. D: Appl. Phys., **39** (2006) 900.

13. M. EI Hiti, J. Phys. II (France), **6** (1996) 1307.

14. C. G. Koops, Phys. Rev., **83** (1951) 121.

15. J. Maxwell, Electricity and Magnetism, Volume 1 Section 328, Oxford University Press, London (1873).

16. K. Wagner, Ann. Phys., (Lipzig), **40** (1913) 817.

17. K. Iwavchi, J. Appl. Phys., **10** (1971) 1520.

18. O. Josyulu and J. Sobhanadri, Phys. Stat. Sol. (a), **59** (1985) 323.

19. M. EI Hiti and M. Ahmed, Mater. Sci. Technol., **14** (1998) 19.

20. S. Radhakrishna and K. Badarinath, J. Mater. Sci. Lett., **3** (1984) 867.

21. S.A. Olofa, J. Magn. Magn. Mater., **131** (1994) 103.

22. K.L. Yadav and R.N.P. Chowdhary, Mater. Lett., **19** (1994) 61.

23. Anne-Marie Jeffery and Dwight H. Damon, IEEE Transactions on Dielectrics and Electrical Insulation, **2** (1995) 394.

24. Kenneth S. Cole and Robert H. Cole, Journal of Chemical Physics, **9** (1941) 341.

25. A.M.Y. El-Lawindy, Egypt. J. Solids, **28** (2005) 97.

26. B. Tareev, Physics of Dielectrics, Mir Publishers, Moscow (1975).

27. M.R. Anantharaman, S. Sindhu, S. Jagatheesan, K.A. Malini and P. Kurian, J. Phys. D: Appl. Phys., **32** (1999) 1801.

28. K. Lichtenecker, Phys. Z, **10** (1908) 1005.

29. Hyung Do Choi, Hwan Woo Shim, Kwang Yun Cho, Hyuck Jae Lee, Chan Sik Park and Ho Gyu Yoon, J. Appl. Polym. Sci., **72** (1999) 75.

30. M.E. Achour, M. EL. Malhi, J.L. Miane, F. Carmona and F. Lahjomri, J. Appl. Polym. Sci., **73** (1999) 969.

31. K. W. Wagner, Arch Electrochem, **2** (1914) 371.

32. Mathew George, Ph.D thesis, Department of Physics, Cochin University of Science and Tecnology, Cochin (2004).

33. Kyoung Sik Moon, Hyung Do Choi, Ae Kyoung Lee, Kwang Yun Cho, Ho Gyu Yoon and Kwang S. Suh, J. Appl. Polym. Sci., **77** (2000) 1294.

34. B. Viswanathan and V.R.K Murthy, Ferrite materials, Narosa publishing House, New Delhi (1990).

35. A.M. Abdeen, J. Magn. Magn. Mater., **185** (1998) 199.

36. M.A. El Hiti, J. Magn. Magn. Mater., **164** (1996) 187.

37. S. Jankowski, J. Am. Ceram. Soci., **71** (1988) C-176.

38. P.V. Reddy, R. Satyanarayana and T.S. Rao, Phys. Stat. Sol. (a), **78** (1983) 109.

39. M.A. Ahmed, M.A. EI Hiti, M.K. EI Nimr and M.A. Amer, J. Magn. Magn. Mater., **152** (1996) 391.

40. P.K. Larsen and R. Metselaar, Phys. Rev. B, **8** (1973) 2016.

41. M.A. Hiti, J. Phys. D: Appl. Phys., **29** (1996) 501.

42. James M. Margolis, Conductive Polymers and Plastics, Chapmann and Hall, New York (1989).

Dielectric Properties of Gamma Ferric Oxide Based Rubber Ferrite Composites

Nano materials have been attracting a lot of attention because of their potential application as sensors, toners in photocopying, quantum electronic devices, smart windows and memory applications. Gamma ferric oxide commonly known as maghemite is an important magnetic material, which is the most commonly used one in magnetic recording and data storage devices. A single stage synthesis of γ-Fe_2O_3 in the nanometer range is very important for various applications such as high density data storage, magneto-optical devices, biocompatible ferrofluids for drug delivery and magnetic ink. Synthesis and magnetic properties of ferrites in different polymeric medium such as polyaniline, silica and poly pyrrole are studied and reported [1-3], where as the preparation and properties of magnetic composites based on γ-Fe_2O_3 in elastomer matrix is seldom reported in the literature.

In the present study, gamma ferric oxide in the nano regime was prepared by a low temperature sol-gel method and characterised. Precharacterised gamma ferric oxide is incorporated in EPDM and neoprene matrices to make RFCs at different loadings, ranging from 20 to 120 phr as explained in section 2.2.2. The dielectric properties of gamma ferric oxide and the corresponding RFCs were evaluated in the frequency range 0.1-8 MHz by subjecting them to dielectric permittivity studies. The effect of temperature on the dielectric properties was also investigated. The results are finally correlated.

7.1 Dielectric measurements of γ-Fe_2O_3

The electrical resistivity of metal oxides is relatively high when compared to that of the metals. The dielectric permittivity and ac conductivity of the gamma ferric oxide very much depend on its crystal structure. γ-Fe_2O_3 can be considered as a non-

stoichiometric defect magnetite (Fe_3O_4) with incomplete spinel cation site occupancy. The spinel structure consists of a frame work of cubic close packed layers of O^{2-} ions. The oxygen frame work encloses tetrahedral (fourfold coordination) as well as larger octahedral (sixfold coordination) interstices for cations, often referred to as the A and B positions. In a spinel structure, normally one out of three of the occupied interstices are tetrahedrally coordinated with oxygen and two out of three are octahedrally coordinated. In the cation-deficient spinel structure of maghemite, however, only five out of six of the total available positions are filled by Fe^{3+}, the remaining positions being vacancies [4-6]. The crystal structure of γ-Fe_2O_3 can be thought of as a vacancy ordered spinel having the formula $Fe^{3+}[(Fe^{3+})_{5/3}\square_{1/3}]O_4$ where vacancies are exclusively concentrated on the B sites.

The dielectric properties of the fillers as well as the RFCs were evaluated from dielectric permittivity measurements as per the details described in chapter 2.

7.1.1 Effect of frequency and temperature on dielectric permittivity of γ-Fe_2O_3

Effect of frequency on dielectric permittivity was studied and the details are shown in figure 7.1. The graph exhibits a sudden decrease in dielectric permittivity initially and reaches a constant value at higher frequencies. This behaviour is observed
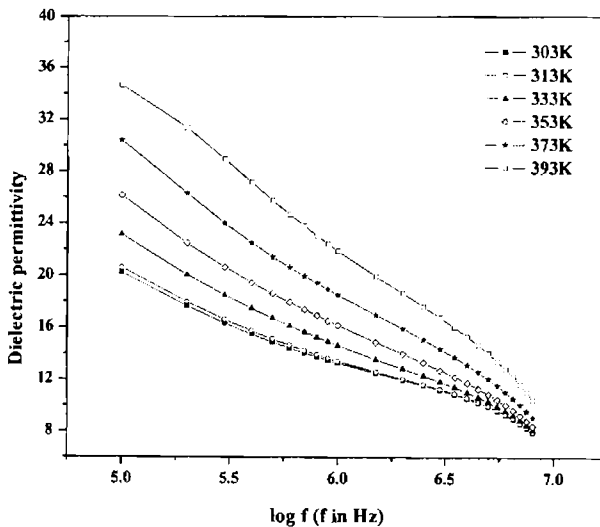
Figure 7.1 Effect of frequency on dielectric permittivity of
γ-Fe₂O₃ sample at different temperatures

at all temperatures. The dielectric properties of ceramic samples are influenced by various factors like method of preparation, sintering conditions, chemical compositions, ionic charge and grain size effect [7]. The observed variation in dielectric permittivity with frequency can be explained using Koop's phenomenological dispersion theory [8]. According to this model, the dielectric permittivity is the total effect of two layers as suggested by Maxwell-Wagner. Materials in which the individual grains are separated either by air gaps or by poorly conducting layers behave as inhomogeneous dielectric. One can trace the origin of polarisation in these materials to the heterogeneous structure exhibited by them [9]. The low conducting grains are active at low frequency. The effect of frequency on dielectric permittivity has been studied theoretically and verified for different ferrite systems [10,11]. The frequency dependence of dielectric permittivity, loss tangent and ac conductivity is given by the equation [12]

$$\varepsilon' = 4\pi\sigma'_{ac}/(\omega \tan\delta) \qquad\qquad 7.1$$

where ε' is the real part of dielectric permittivity, σ'_{ac} is the real part of ac electrical conductivity, ω is the angular frequency and $\tan\delta$ is the loss tangent. According to the above equation, dielectric permittivity, which is inversely proportional to the angular frequency, decreases with increase in frequency.
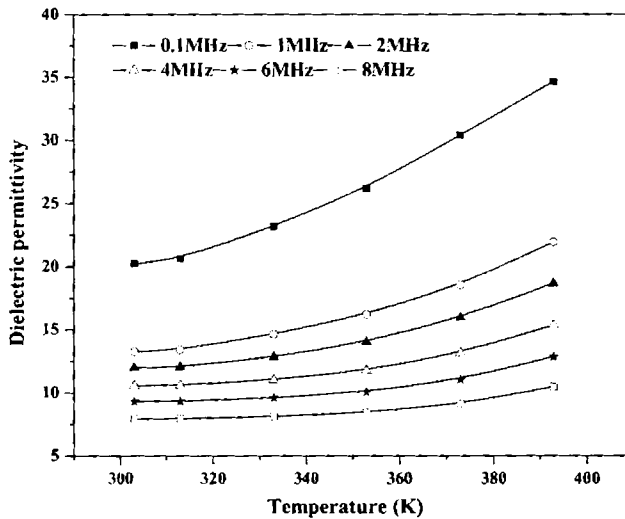
Figure 7.2 Effect of temperature on dielectric permittivity of γ-Fe$_2$O$_3$

Figure 7.2 shows the effect of temperature on dielectric permittivity of γ-Fe_2O_3 at selected frequencies. As in the case of nickel ferrite and other ferrite systems, the dielectric permittivity of γ-Fe_2O_3 increases with increase in temperature. Sharp increase in dielectric permittivity is observed at lower frequencies and especially at higher temperature. A maximum value of 34.6 was obtained at 393 K and at 0.1 MHz.

This behaviour may be attributed to the existence of strong correlation between conduction mechanism and dielectric polarisation in ferrites [13]. As the temperature increases, the number of charge carriers increases, resulting in an enhanced build-up of space charge polarisation and hence an increase in the dielectric properties. The presence of cation vacancies on the octahedral site is another important factor that contributes to the conductivity.

7.1.2 Effect of frequency and temperature on ac electrical conductivity of γ-Fe_2O_3

Effect of frequency and temperature on the ac conductivity of γ-Fe_2O_3 is given in figures 7.3 and 7.4 respectively. As the frequency increases, the conductivity increases, reaches a maximum and then decreases at higher frequencies. Conduction mechanism in ferrites was first explained by Verwey in 1947 [14,15].
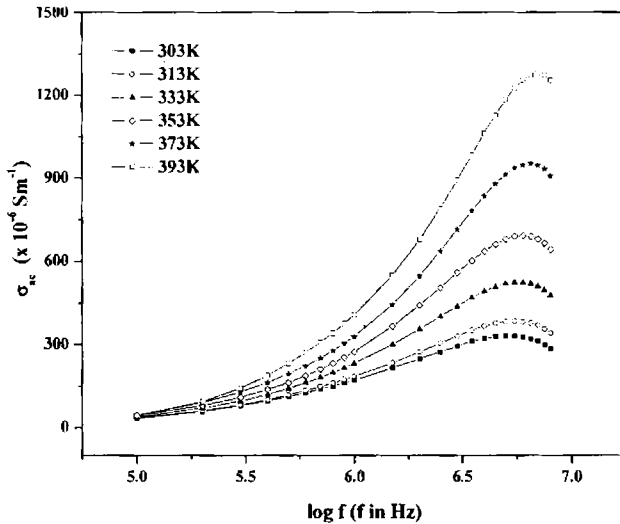
Figure 7.3 Variation of ac conductivity of γ-Fe_2O_3 with frequency

Conduction in ferrites is entirely due to an electron transfer between Fe^{2+} and Fe^{3+}. Thus increase in conductivity with frequency is due to the increase in hopping

conduction, which becomes maximum at a certain frequency, above which the frequency of hopping lags behind the applied frequency.
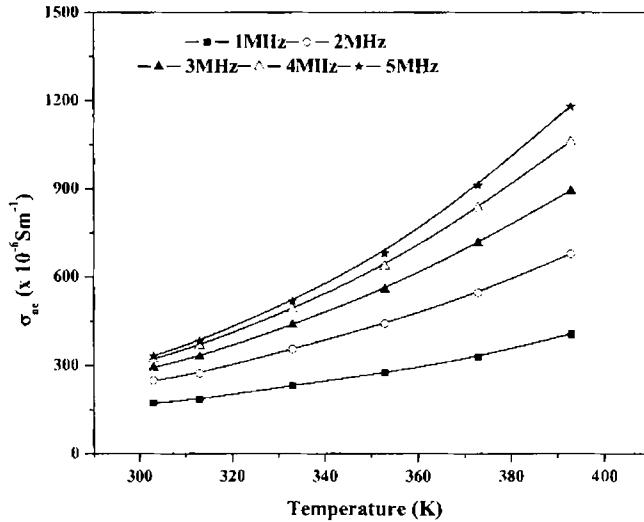
Figure 7.4 Variation of ac conductivity of γ-Fe₂O₃ with temperature

An increase in ac conductivity was observed for the sample with increase in temperature. As the temperature increases, the thermal activation of charge carriers increases leading to increase in hopping conduction.

7.2 Dielectric properties of γ-Fe₂O₃ filled neoprene based rubber ferrite composites

Dielectric properties of neoprene based rubber ferrite composites were measured in the frequency range 0.1 to 8 MHz. The dependence of dielectric permittivity on various factors like frequency, temperature and loading of the ferrite was studied.

7.2.1 Frequency dependence of dielectric permittivity of neoprene based RFCs with γ-Fe₂O₃

Representative graphs showing the frequency dependence of dielectric permittivity of RFCs at different temperatures are shown in figures 7.5 to 7.7. RFCs with different loadings of γ-Fe₂O₃ show identical response to the frequency. Dielectric permittivity is found to decrease with increase in frequency as in the case of the ferrite. In the presence of an applied field, any induced and permanent dipoles become

191

oriented in the electric field. Polarisation due to ionic conduction and the induction of a dipole moment of the molecule resulting from the distortion of electron cloud of
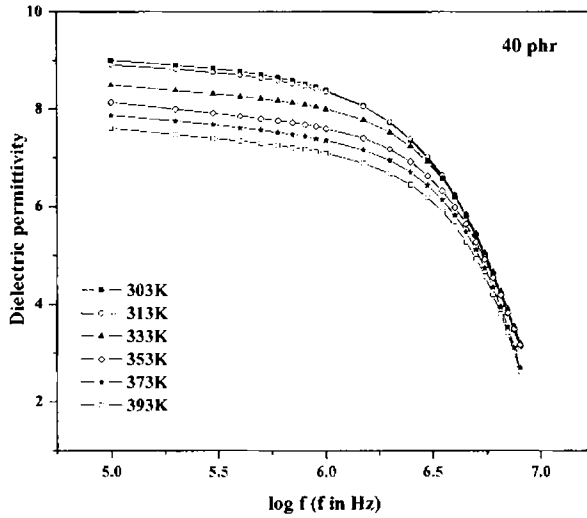
Figure 7.5 Effect of frequency on dielectric permittivity of neoprene based RFC with 40 phr γ-Fe₂O₃
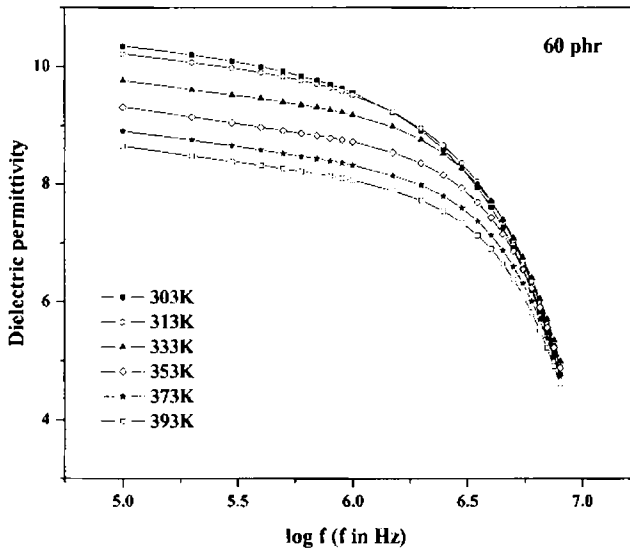
Figure 7.6 Effect of frequency on dielectric permittivity of neoprene based RFC with 60 phr γ-Fe₂O₃

individual atoms is nearly instantaneous, while polarisation due to the molecular motion and alignment of permanent dipoles in the electric field requires time. In addition to all these polarisation mechanisms, interfacial polarisation is also possible

which is due to the accumulation of charges at the interfaces. Hence, polarisation and conduction of current depend upon frequency, temperature and dielectric properties of the material [16].

In the case of rubber ferrite composites, the decrease in dielectric permittivity with frequency is due to the decrease in interfacial polarisation. The composite system can be considered as a heterogeneous system analogous to the Maxwell-Wagner double layer structure. At lower frequencies, the migration of charge carriers and induced polarisation will be high giving rise to high dielectric permittivity. At higher frequencies the migration frequency of charge carriers lags behind the applied field, where by decreasing the dielectric permittivity.
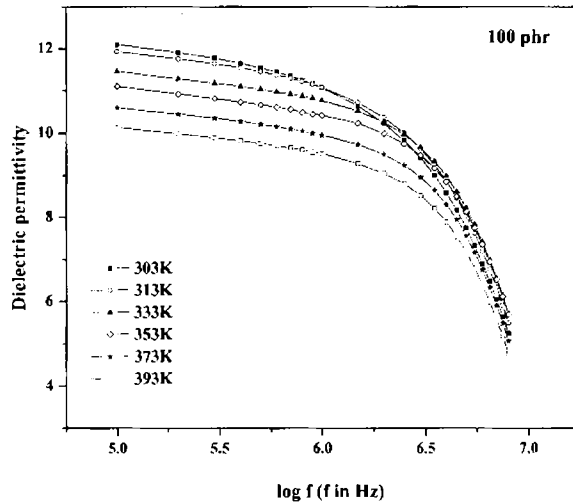
Figure 7.7 Effect of frequency on dielectric permittivity of neoprene based RFC with 100 phr γ-Fe₂O₃

7.2.2 Effect of temperature on dielectric permittivity of neoprene based RFCs filled with γ-Fe₂O₃

Representative graphs showing the effect of temperature on the dielectric permittivity of the RFCs at selected frequencies are shown in figures 7.8 to 7.10. Effect of temperature on dielectric permittivity of RFCs is slightly different from that of the gamma ferric oxide. For gamma ferric oxide, the dielectric permittivity is found to increase with increase in temperature.
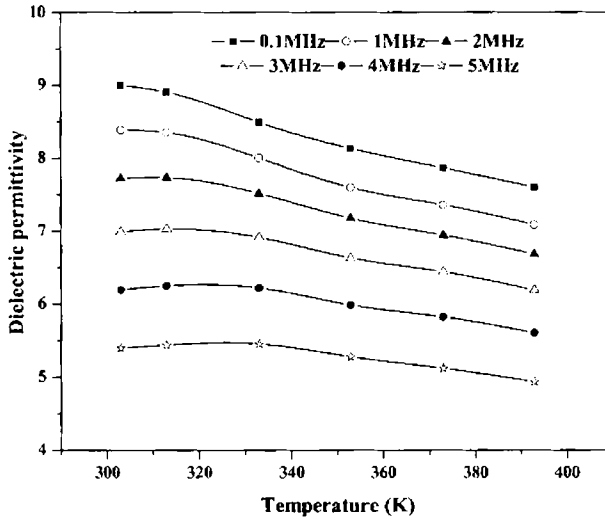
Figure 7.8 Effect of temperature on dielectric permittivity of neoprene based RFC with 40 phr γ-Fe_2O_3

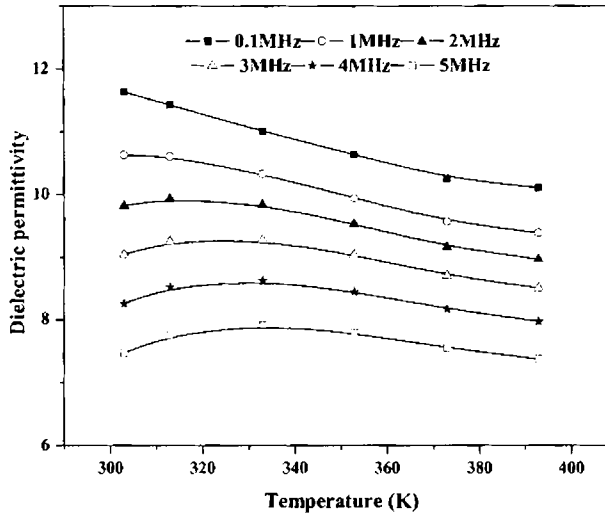*Figure 7.9 Effect of temperature on dielectric permittivity of neoprene based RFC with 80 phr γ-Fe_2O_3*

At lower frequencies, the dielectric permittivity of RFCs decreases with temperature. But at higher frequencies, the dielectric permittivity of RFCs is found to increase upto 333 K and then decrease at higher temperature. The initial increase is due to the increase in hopping of the charge carriers. At very high temperatures the polymer matrix expands, where by the ratio of the number of molecules to the

effective length of the dielectric diminishes and as a result, the dielectric permittivity decreases [17].
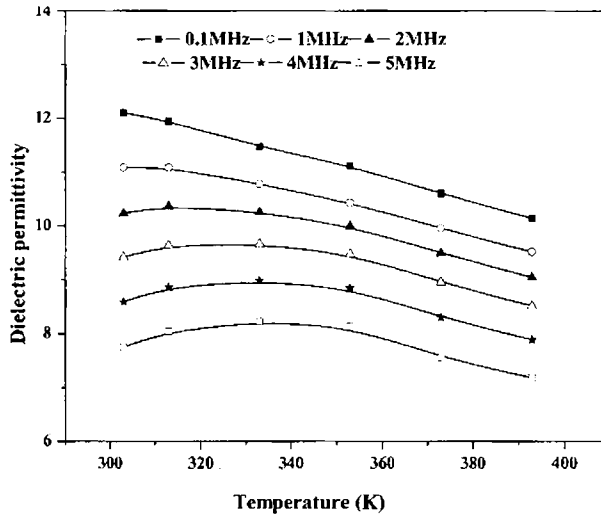
Figure 7.10 Effect of temperature on dielectric permittivity of neoprene based RFC with 100 phr γ-Fe₂O₃

7.2.3 Loading dependence of dielectric permittivity of neoprene based RFCs filled with γ-Fe₂O₃

Effect of ferrite concentration on the dielectric permittivity of the γ-Fe₂O₃ filled neoprene composites is shown in figure 7.11
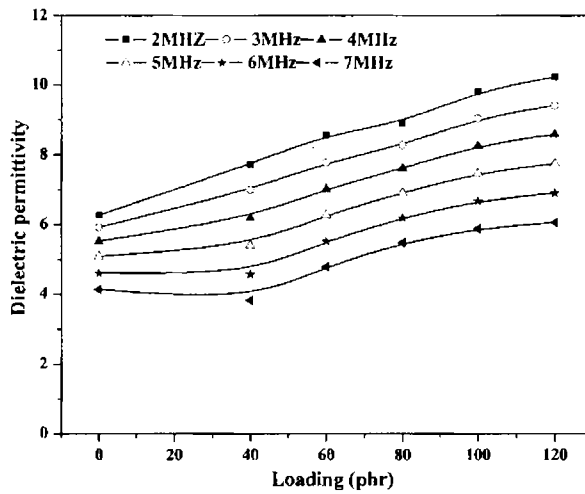
Figure 7.11 Loading dependence of dielectric permittivity of neoprene based RFCs at 303 K

The dielectric permittivity of RFCs depends on the nature of the matrix and ferrite filler, interaction of the filler with the matrix and percolation threshold. Ultimately, the value of dielectric permittivity depends on the amount of filler incorporated into the matrix. Dielectric permittivity of RFCs increases with increase in the volume fraction of the filler incorporated into the matrix. From figure 7.11, it can be inferred that the dielectric permittivity of the γ-Fe_2O_3 filled neoprene composites increases with increase in filler loading.

7.2.4 Tailoring of dielectric permittivity of γ-Fe_2O_3 filled neoprene based RFCs using the model equations

As explained in section 6.1.7, equations with certain modifications were applied to fit the observed dielectric data. Among the three modified equations 6.9a, 6.9b and 6.9c given in chapter 6, equation 6.9b and 6.9c were found to fit well the experimental data for γ-Fe_2O_3 filled neoprene composites.

The theoretical fit for various loadings of gamma ferric oxide is represented in figures 7.12 to 7.14.
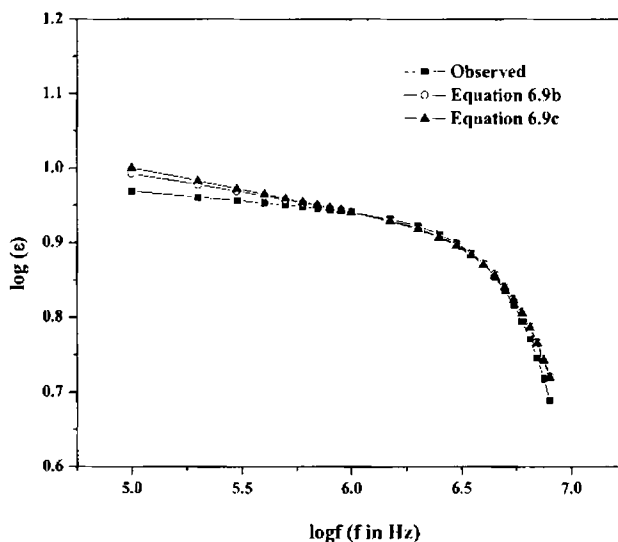
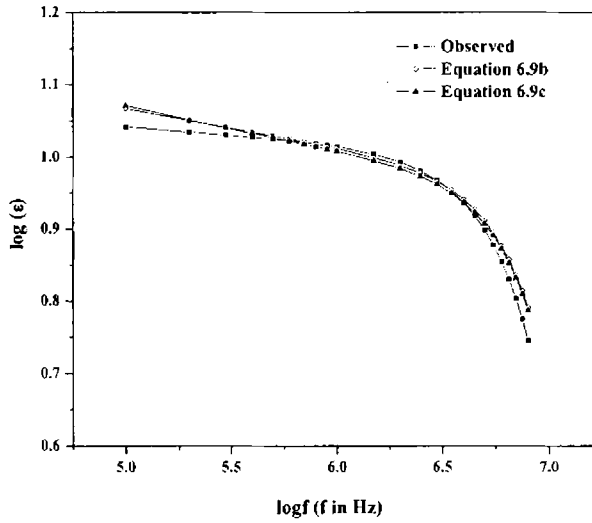*Figure 7.12 Theoretical fit for neoprene based RFCs with 60 phr γ-Fe_2O_3 at 353 K*

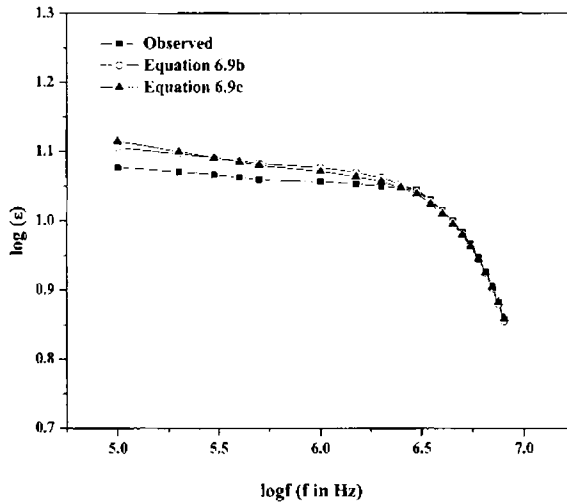*Figure 7.13 Theoretical fit for neoprene based RFCs with 80 phr γ-Fe_2O_3 at 333 K*

Figure 7.14 Theoretical fit for neoprene based RFCs with 100 phr γ-Fe_2O_3 at 313 K

7. 3   ac Conductivity of neoprene based rubber ferrite composites filled with γ-Fe_2O_3

Effect of frequency and temperature on ac electrical conductivity of neoprene based RFCs were studied and reported here.

7.3.1 Frequency dependence

Figures 7.15 to 7.17 show the variation of ac conductivity with frequency in the frequency range 0.1 to 8 MHZ, at different temperatures.
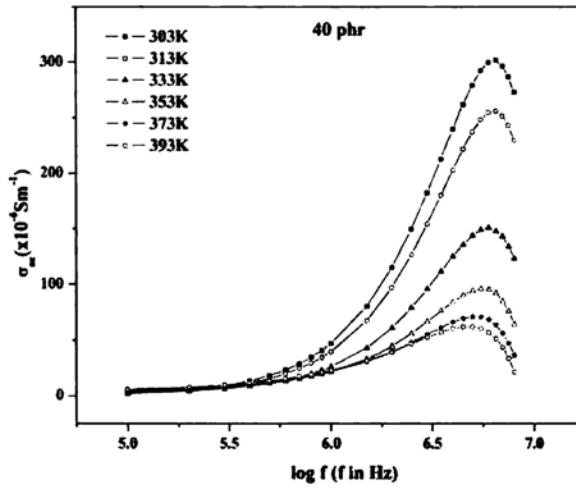
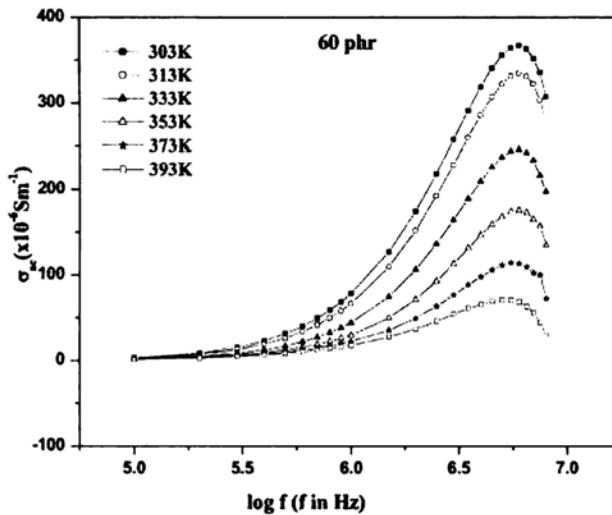*Figure 7.15 Effect of frequency on ac conductivity of neoprene based RFC with 40 phr γ-Fe₂O₃*

Figure 7.16 Effect of frequency on ac conductivity of neoprene based RFC with 60 phr γ-Fe₂O₃

As in the case of ferrite filler, the ac conductivity of the RFCs increases with frequency and after reaching a maximum value, it decreases at higher frequencies. The increase in ac conductivity with frequency is due to the increase in hopping of charge carriers. At higher frequencies migration frequency of charge carriers lags behind the applied frequency. Hence, after reaching a maximum value further decrease in ac conductivity with frequency is observed.
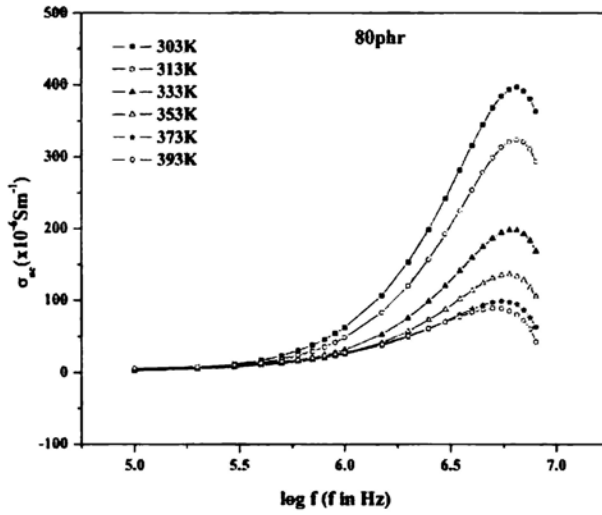
Figure 7.17 Effect of frequency on ac conductivity of neoprene based RFC with 80 phr γ-Fe$_2$O$_3$.

7.3.2 Temperature dependence

Effect of temperature on ac conductivity of the RFCs at selected frequencies is shown in figures 7.18 to 7.20.

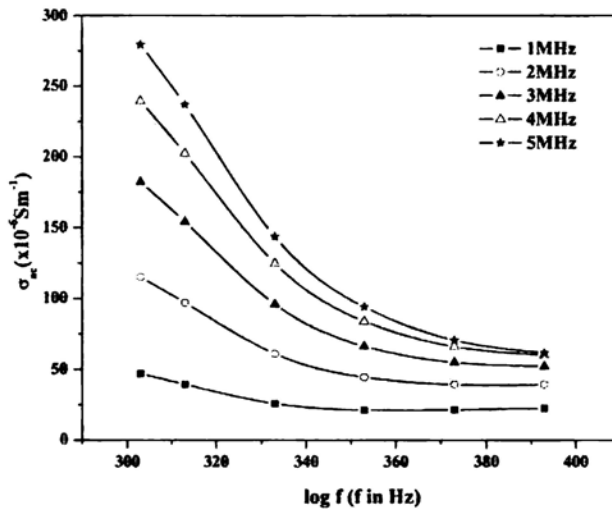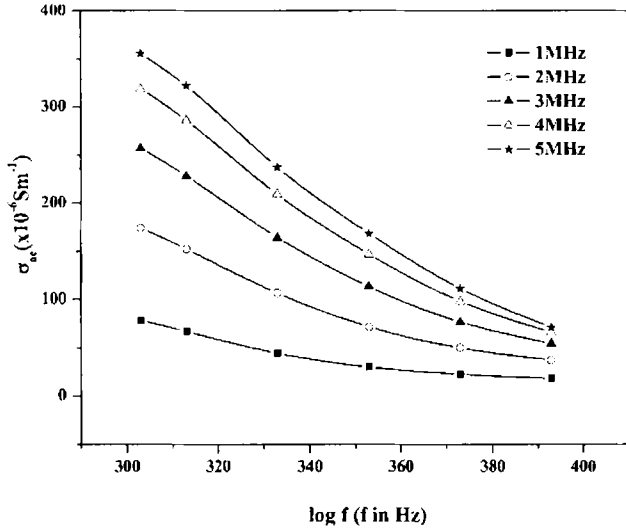*Figure 7.18 Effect of temperature on ac conductivity of neoprene based RFC with 40 phr γ-Fe$_2$O$_3$.*

Figure 7.19 Effect of temperature on ac conductivity of neoprene based RFC with 60 phr γ-Fe$_2$O$_3$.

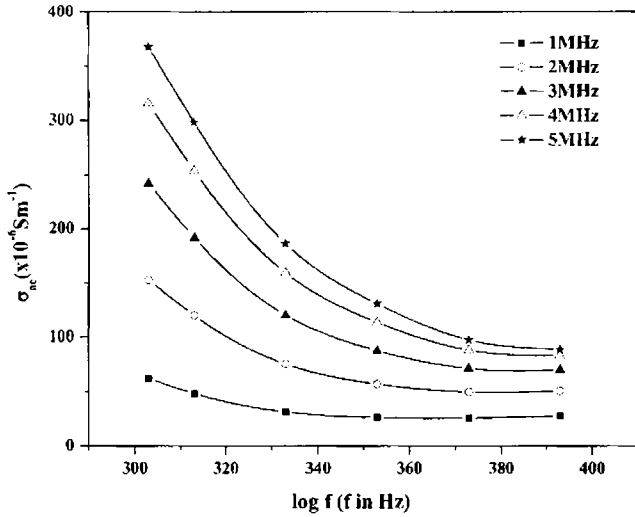*Figure 7.20 Effect of temperature on ac conductivity of neoprene based RFC with 80 phr γ-Fe$_2$O$_3$.*

Temperature dependence of ac conductivity of RFCs with different loadings of gamma ferric oxide is almost identical. As the temperature increases the ac conductivity decreases. At very high temperatures it remains constant. The decrease in ac conductivity is due to the decrease in density of the charge carriers, because as the temperature increases the polymer matrix expands and the effective volume of the matrix increases.

7.3.3 Effect of gamma ferric oxide concentration on ac conductivity of neoprene based RFCs

Figure 7.21 shows the effect of γ-Fe_2O_3 loading on the ac conductivity of the RFCs at selected frequencies. As the ferrite content increases the ac conductivity of the RFCs increases. The ac conductivity is increased from 2.86 x 10^{-6} Sm^{-1} for the gum vulcanisate at a frequency of 5 MHz and 373K to 440 x10^{-6} Sm^{-1} for the RFC with 120 phr of γ-Fe_2O_3. Proportionate increase is observed at different temperatures and frequencies.
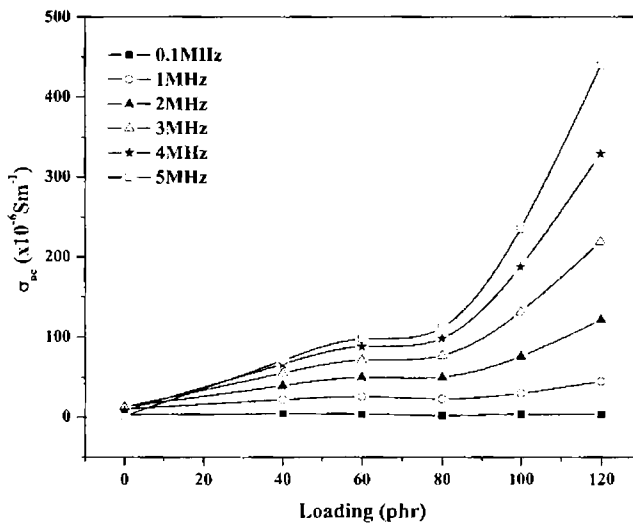

Figure 7.21 Loading dependence of ac conductivity of γ-Fe_2O_3 filled neoprene composites at 373 K.

7.4 Dielectric properties of EPDM based rubber ferrite composites filled with γ-Fe_2O_3

EPDM based RFCs with different loadings of γ-Fe_2O_3 ranging from 20 to 120 phr were prepared and the dielectric properties were determined in the frequency range 0.1 to 8 MHz at different temperatures. Frequency, temperature and loading dependence on the dielectric properties of the prepared RFCs were analysed and reported.

7.4.1 Frequency dependence on dielectric permittivity of EPDM based RFCs

Figures 7.22 to 7.24 represent the frequency dependence of dielectric permittivity of EPDM based RFCs at different temperatures. As in the case of nickel ferrite filled RFCs, the dielectric permittivity of γ-Fe_2O_3 filled EPDM composites decreases with increase in frequency. The decrease occurs when the jumping frequency of electric charge carriers could not follow the alteration of the applied ac electric field beyond a certain critical frequency.
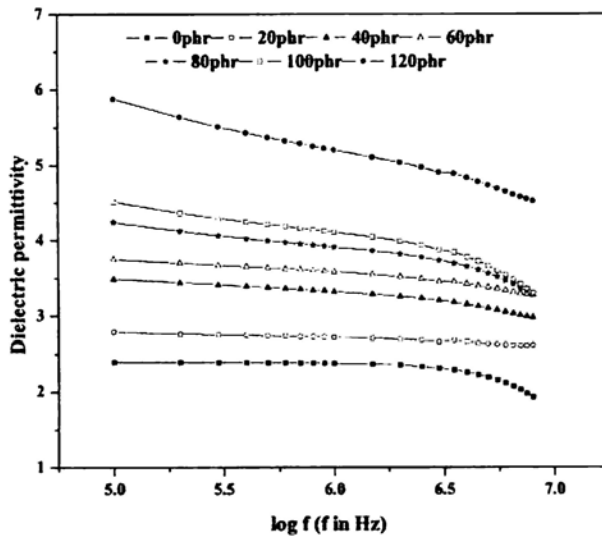

Figure 7.22 Effect of frequency on dielectric permittivity of EPDM based RFCs at 313 K
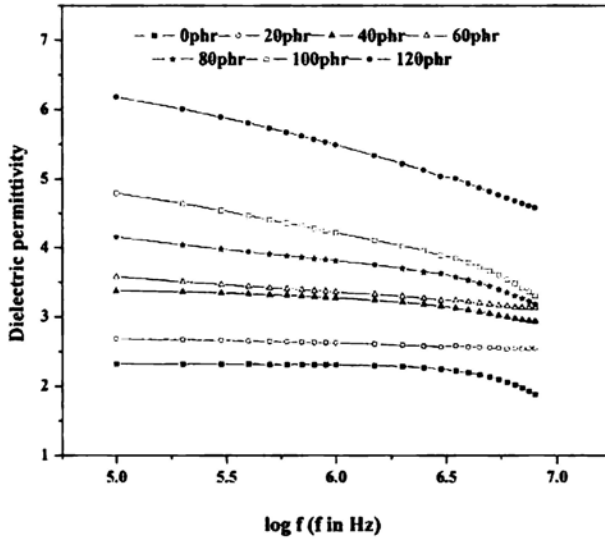
Figure 7.23 Effect of frequency on dielectric permittivity of EPDM based RFCs at 353 K
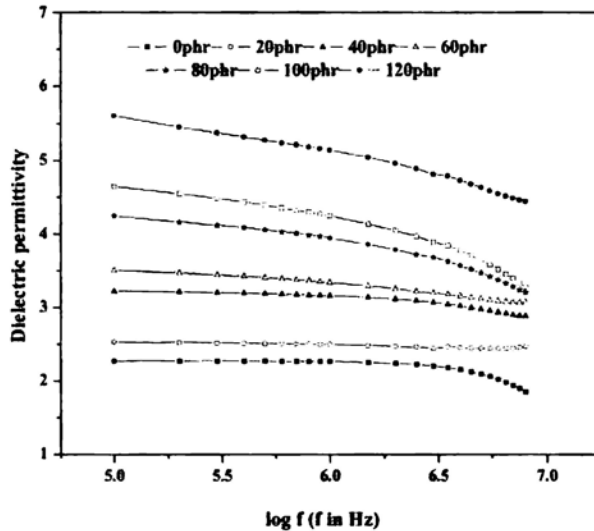

Figure 7.24 Effect of frequency on dielectric permittivity of EPDM based RFCs at 393 K

7.4.2 Effect of temperature on dielectric permittivity of EPDM based RFCs with γ-Fe_2O_3 filler

Effect of temperature on dielectric permittivity of EPDM based RFCs were carried out in the temperature range 303-393 K. Figures 7.25 to 7.27 show the effect

of temperature on the dielectric permittivity of RFCs with different loadings of γ-Fe_2O_3 at different frequencies.
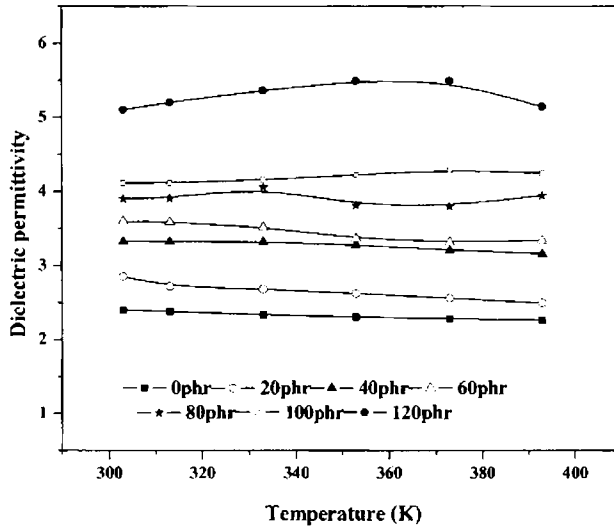

Figure 7.25 Effect of temperature on dielectric permittivity of EPDM based RFCs at 1MHz
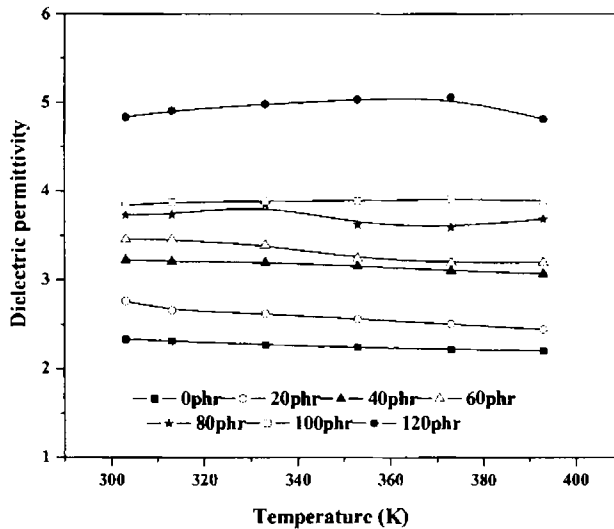

Figure 7.26 Effect of temperature on dielectric permittivity of EPDM based RFCs at 3 MHz
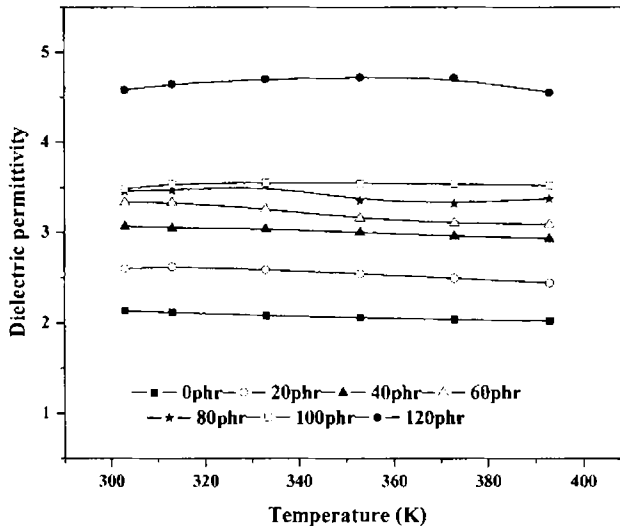
Figure 7.27 Effect of temperature on dielectric permittivity of EPDM based RFCs at 6 MHz

At lower loadings, the dielectric permittivity is found to decrease with temperature at all the measured frequencies. But at higher loadings of the ferrite, increase in dielectric permittivity is observed. The decrease in dielectric permittivity at lower filler loading is due to the decrease in density of charge carriers. But at very high filler concentrations, the characteristics of ferrite predominate over the matrix characteristics. So an increase in dielectric permittivity is observed at higher filler loading.

7.4.3 Loading dependence on the dielectric permittivity of EPDM based RFCs

Figures 7.28 to 7.30 show the effect of γ-Fe_2O_3 content on the dielectric permittivity of EPDM based RFCs at different temperatures. As expected the dielectric permittivity of the RFCs increases with increase in the ferrite content.
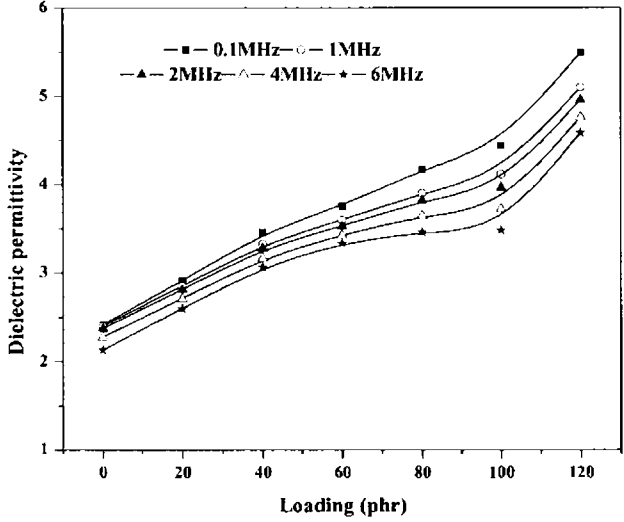
Figure 7.28 Loading dependence of dielectric permittivity
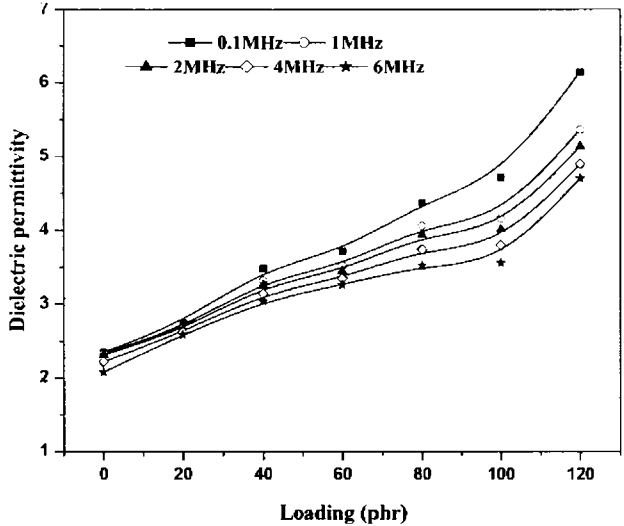*of EPDM based RFCs at 303 K*

Figure 7.29 Loading dependence of dielectric permittivity
of EPDM based RFCs at 333 K
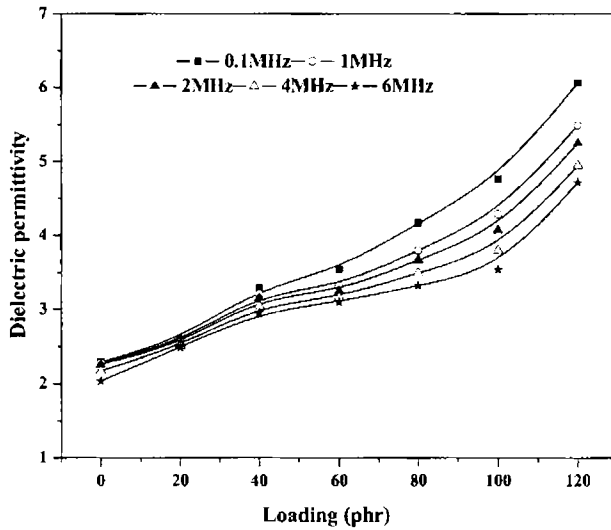
***Figure 7.30 Loading dependence of dielectric permittivity
of EPDM based RFCs at 373 K***

7.5 ac conductivity of EPDM based RFCs

Effect of various factors like frequency, temperature and loading on ac electrical conductivity of γ-Fe_2O_3 filled EPDM composites were analysed at different frequencies and temperatures.

7.5.1 Frequency dependence on the ac electrical conductivity of γ-Fe_2O_3 filled EPDM composites

Figures 7.31 to 7.33 show the variation of ac conductivity with frequency of EPDM based RFCs at different temperatures. The ac electrical conductivity is found to increase with increase in frequency and drops at some higher frequency. As the frequency of the applied field increases, migration of charge carriers increases between octahedral and tetrahedral site, which increases the ac conductivity. At very high frequency hopping of the charge carriers lags behind the applied field. Hence, after reaching a maximum, ac conductivity decreases with further increase in frequency.
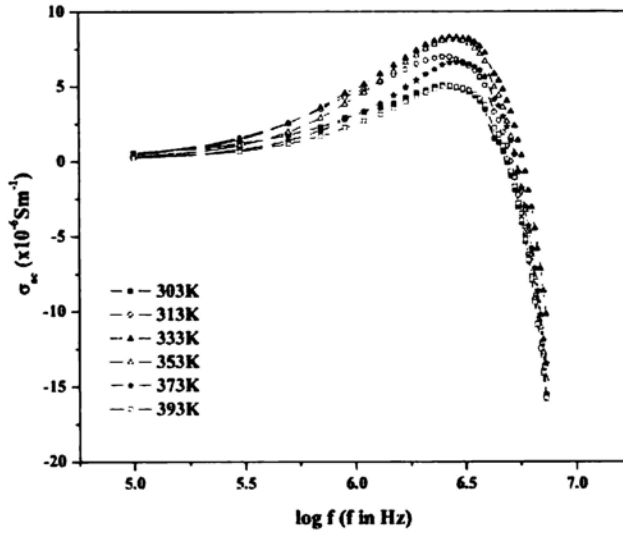
Figure 7.31 Effect of frequency on ac conductivity
of EPDM based RFC with 40 phr γ-Fe₂O₃
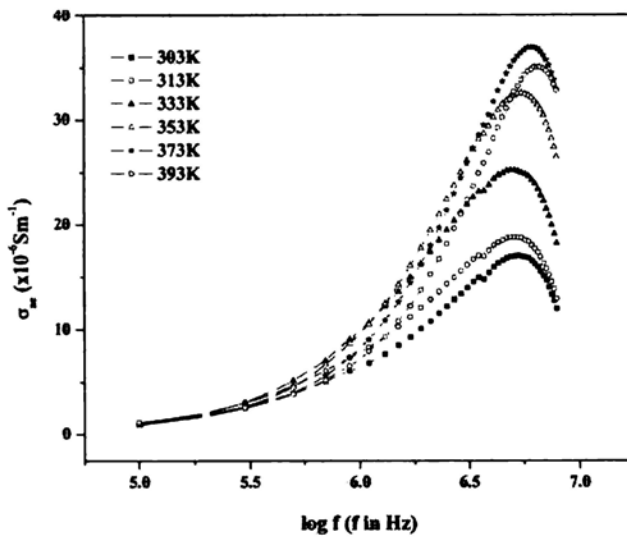
Figure 7.32 Effect of frequency on ac conductivity
of EPDM based RFC with 60 phr γ-Fe₂O₃
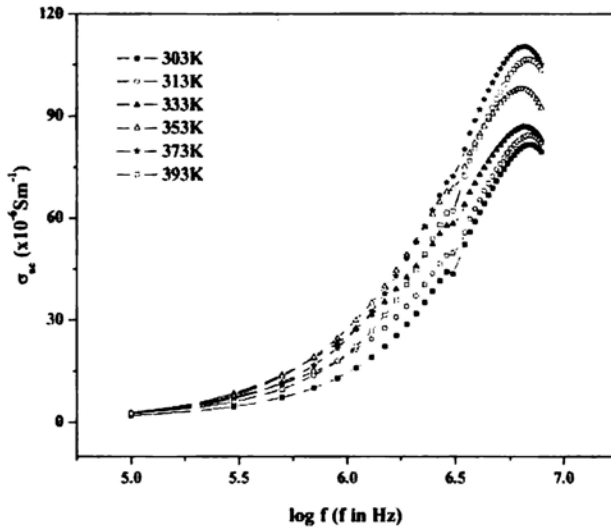
Figure 7.33 Effect of frequency on ac conductivity of
EPDM based RFC with 120 phr γ-Fe₂O₃

7.5.2 Temperature dependence of ac electrical conductivity of γ-Fe$_2$O$_3$ filled EPDM composites

Temperature dependence of ac electrical conductivity of EPDM based RFCs were done for different loadings of γ-Fe$_2$O$_3$. Figures 7.34 to 7.36 represent the variation of ac conductivity of the EPDM based RFCs containing different amounts of
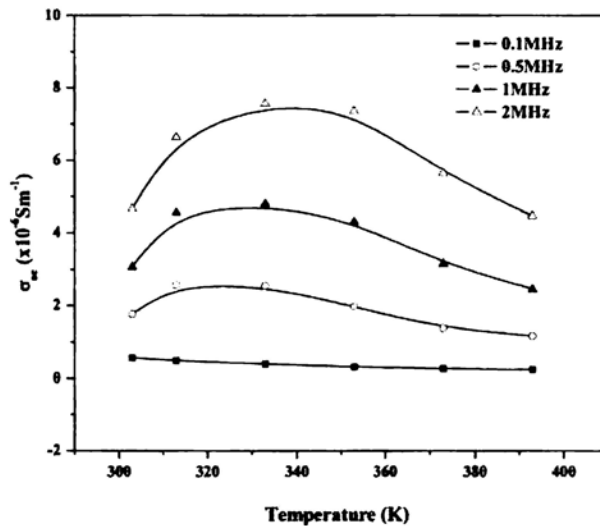
Figure 7.34 Effect of temperature on ac conductivity of
EPDM based RFC with 40 phr γ-Fe₂O₃

γ-Fe_2O_3. Effect of temperature on ac conductivity of EPDM based RFCs is found to be different from that of the neoprene based RFCs. For the EPDM based RFCs, ac conductivity increases upto 333 K and then decreases at higher temperatures and this is characteristics to the γ-Fe_2O_3. At high temperatures, the matrix expands and density of charge carrier decreases and the ac conductivity decreases.
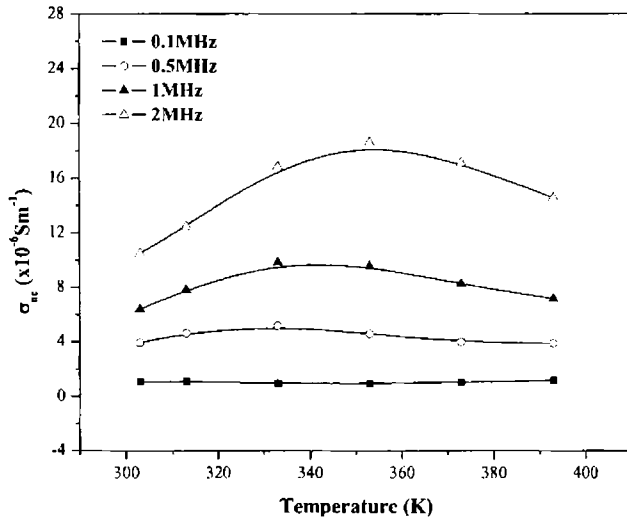
Figure 7.35 Effect of temperature on ac conductivity of EPDM based RFC with 60 phr γ-Fe_2O_3
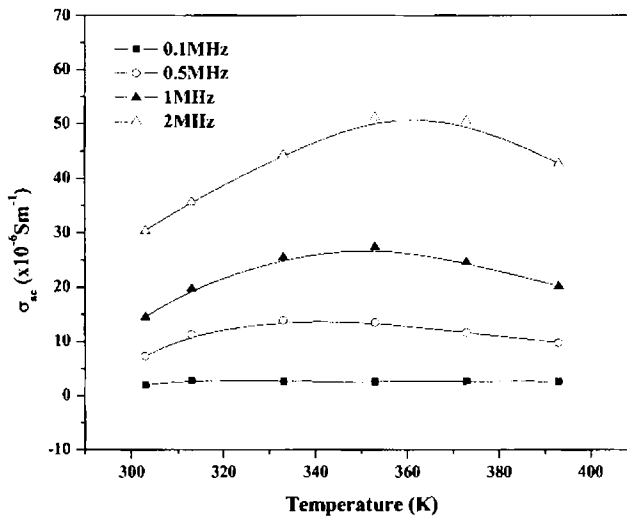
Figure 7.36 Effect of temperature on ac conductivity of EPDM based RFC with 120 phr γ-Fe_2O_3

7.5.3 Loading dependence of ac conductivity of EPDM based RFCs

Loading dependence of ac conductivity of EPDM based RFCs at selected frequencies and at different temperatures is shown in figures 7.37 to 7.39. The ac conductivity of the RFCs is found to increase with the ferrite content at the frequency and temperature range studied.
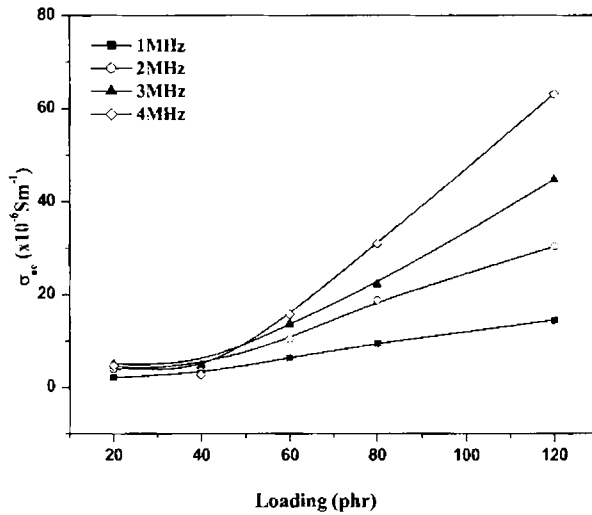
Figure 7.37 Variation of ac conductivity of EPDM based RFCs with the loading of γ-Fe₂O₃ at 303 K
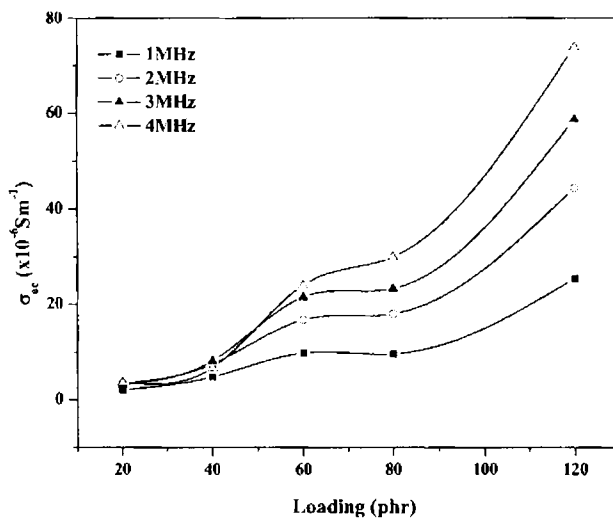
Figure 7.38 Variation of ac conductivity of EPDM based

211

RFCs with the loading of γ-Fe₂O₃ at 333 K
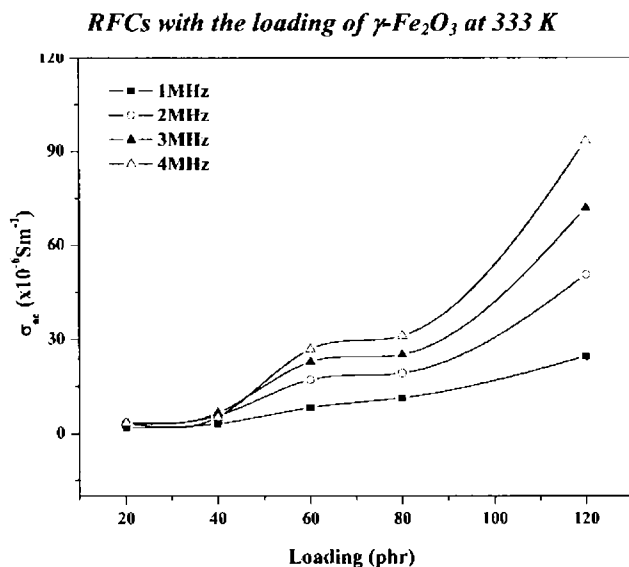
*Figure 7.39 Variation of ac conductivity of EPDM based
RFCs with the loading of γ-Fe₂O₃ at 373 K*

The ac conductivity of RFCs linearly increased with increase in volume fraction of the ferrite filler. At higher concentration of ferrite a conductive path of the ferrite particles may be formed which increases the ac conductivity.

7.6 Conclusion

Neoprene and EPDM based RFCs with different loadings of gamma ferric oxide was prepared and its dielectric properties were studied. Effect of frequency on the dielectric permittivity of the γ-Fe2O3 and the RFCs were carried out in the frequency range 0.1 to 8 MHz at different temperatures. The dielectric permittivity of both γ-Fe$_2$O$_3$ and RFCs decreased with increase in frequency. The dielectric permittivity of neoprene and EPDM based RFCs with gamma ferric oxide as the filler was found to decrease with increase in temperature. As the volume fraction of the ferrite increased, the dielectric permittivity was found to increase in both type of RFCs and a maximum value was obtained for RFC with 120 phr ferrite loading.

Frequency dependence of ferrite and the RFCs on the ac conductivity was identical. With increase in frequency, ac conductivity of the samples increased, and droped at higher frequencies. An increase in ac conductivity with temperature was observed for the gamma ferric oxide, where as a different behaviour was observed for

the RFCs. For the neoprene composites the values were found to decrease with temperature. EPDM based RFCs showed an increase in ac conductivity at higher frequencies and lower temperatures. The ac conductivity of RFCs increased with increase in volume fraction of ferrite. Higher dielectric permittivity was observed for neoprene based RFCs than the corresponding EPDM based RFCs.

References

1. Juan Carlos Aphesteguy and Silvia E. Jacobo, Physica B, **354** (2004) 224.
2. Daniel Niznansky, Jean Lue Rchspringer and Marc Drillon, IEEE Transactions on Magnetics, **30** (1994) 821.
3. Cecilia Albornoz, Elsa E. Sileo and Silvia E. Jacobo, Physica B, **354** (2004) 149.
4. Cor B. de Boer and Mark J. Dekkers, Geophys. J. Int., **144** (2001) 481.
5. D.H. Lindsley, Reviews in mineralogy, **3** (1976) L61.
6. Sung Yong An, In-Bo Shim and Chul Sung Kim, J. Appl. Phys., **97** (2005) 10Q909.
7. S.Verma, S.D. Pradhan, R.Pascicha, S.P. Sainkar and P.A. Joy, J. Am. Ceram. Soci., **88** (2005) 2597.
8. C.G. Koops, Phys. Rev., **83** (1951), 121.
9. Kozo Iwauchi, Japanese J. Appl. Phys., **10** (1971) 1520.
10. B. Kunar and G. Srivastava, J. Appl. Phys., **75** (1994) 6115.
11. J. Smit and H.P.J. Wijn, Ferrites, Philips Technical Library, (1959) Netherlands.
12. M.A. El Hiti, J. Magn. Magn. Mater., **164** (1996) 187.
13. A.M. Abo El Ata and S.M. Attia, J. Magn. Magn. Mater., **257** (2003) 165.
14. E.J. Verwey, P.W. Haayman and F.C. Romejin, J. Chem. Phys., **15** (1947) 181.
15. E.J. Verwey and E.L. Heilmann, J. Chem. Phys., **15** (1947) 174.
16. Joel R. Fried, Polymer Science and Technology, Prentice Hall PTR, New Jersey, (1995).
17. Frank E. Karasz, Dielectric properties of Polymers, Plenum Press, New York (1972).

Chapter 8

Microwave Characteristics of Rubber Ferrite Composites

With the proliferation of devices like cell phones, microwave ovens, wire lessnetworks and automatic control systems, electromagnetic interference has became a major concern of the environmental protection agencies world wide. It is thus imperative, not only to protect devices from electromagnetic interferences, but also to prevent harmful electromagnetic radiation emanating from the devices reaching the surrounding environment. This is a potential hazard as far as ecology is concerned. Hence strict regulations are enacted by nations to prevent pollution due to electromagnetic radiations.

As far as defense applications are concerned, development of microwave absorbers will play a key role in producing stealth aircrafts. So research activities in this area are of paramount importance to scientists and engineers alike. One way of producing microwave absorbers is to go for lossy dielectric materials. However, such alternatives are not without limitations. Basic electromagnetic theory tells us that the absorbing characteristic of a material is governed by the dielectric permittivity and the magnetic permeability. The absorbing characteristics are optimised for a minimum thickness and are dictated by the surface impedance equation.

Considering these requirements, the best way to fabricate a good microwave absorber is to synthesise a magnetic composite. Additives like graphite and carbon black can enhance the microwave absorbing properties and also aid to tune the bandwidth of absorption. Rubber ferrite composites can be good absorbers and ideal for applications in the frequency range 8-12 GHz.

Extensive study has been carried out to develop new microwave absorbing materials with high magnetic and electric loss [1-3]. Ferrites are excellent microwave absorbing materials because of their high specific resistance, large electrical resistivity, remarkable flexibility in tailoring the magnetic properties and ease of

preparation, low cost, low density and high magnetic loss [4,5]. Spinel ferrites such as Ni-Zn ferrites are found to be suitable microwave absorbers especially in the frequency range of 8-12 GHz (X-band) [6-8]. The major disadvantage of these ceramic materials is the difficulty in moulding complex shapes. However this can be overcome by making polymer bonded composites [9-14].

Ferrites as well as rubber ferrite composites absorb electromagnetic radiations due to various interactive loss processes of magnetisation and polarisation in the material. An electromagnetic wave will undergo a combination of reflection, absorption and transmission when it encounters a ferrite material [15-17]. The exact behaviour of the electromagnetic wave at the surface and in the bulk material critically depends on dielectric and magnetic properties of the material. The complex permeability (μ'-jμ'') and permittivity (ε'-jε'') of the constituent material of the microwave absorbers determine the reflection and attenuation characteristics of the test material [11,18-20]. Where μ' and μ'' are the real and imaginary parts of the magnetic permeability.

The normalised input impedance of a microwave absorbing layer backed by a reflector at the absorber surface (Z_{in}) is given by

$$Z_{in} = \frac{Z_i}{Z_0} = \left(\frac{\mu^*}{\varepsilon^*}\right)^{1/2} \tanh\left[j\frac{2\pi}{c}\left(\mu^*\varepsilon^*\right)^{1/2} fd\right] \qquad 8.1$$

where Z_i and Z_0 are the impedance of absorber and that of free space respectively, μ^* and ε^* are the relative permeabilities and permittivities of the medium respectively, c is the velocity of light in free space, f is the frequency of the microwave in free space and d is the thickness of the absorber. A perfect impedance match, ($Z_i = Z_0$) allows electromagnetic waves to propagate from the free space to the inside of the absorber without any reflection. Variations in matching of the two impedances give rise to reflections at the surface of the absorber. The process of absorption of microwaves within the material occurs as a result of various interactive processes taking place in the material because of magnetisation and polarisation. This requires the lossy or the imaginary parts of complex permeability and permittivity to be high. It is clear from equation 8.1 that the absorption depends on the thickness of the absorber. However

minimum sample thickness for maximum absorption also depends upon the permeability and permittivity of the material [21-23]. The reflection loss (RL) is related to Z_{in} and is as follows:

$$[dB] = -20\log\left(\frac{Z_{in}-1}{Z_{in}+1}\right) \qquad 8.2$$

where [dB] is the reflection loss. Lower the reflection loss, better the shielding effectiveness, since the amount of incident wave reflected is less [24]. Thus microwave absorbers can be designed by choosing an appropriate ferrite as filler. Generally, the thickness of the absorber is optimally reduced for maximum absorption. These criteria can be achieved by fabricating rubber ferrite composites, which can be moulded into any desired shape and thickness [25].

Microwave attenuation of the prepared rubber ferrite composites in X-band can be determined by cavity perturbation method. This is explained in section 2.8 in detail. Dielectric properties of the RFCs at X-band (8-12 GHz) and S band (2-4 GHz) frequencies were measured using a network analyser HP 8510C employing cavity perturbation method. For rectangular cavity, the TE_{10n} mode was excited, utilising the swept frequency option of the analyser. For odd modes, the position of maximum electric field coincides with the geometrical centre of the cavity while the even modes give the magnetic parameters.

Samples in the form of thin rectangular slices were introduced into cavity through a slot. Shift in resonant frequencies and change in quality factors were measured and the real and imaginary parts of the complex permittivity were calculated using the following equations [26,27]

$$\varepsilon_r^1 = \left(\frac{V_c}{2V_s}\right)\left[\left(\frac{f_c}{f_s}\right)-1\right]+1 \qquad 8.3$$

$$\varepsilon_r^{11} = \left(\frac{V_c}{4V_s}\right)\left[\frac{1}{Q_s} - \frac{1}{Q_c}\right] \qquad 8.4$$

where Vc and Vs are the volume of empty cavity and the sample respectively, f_c and Q_c are the resonance frequency and quality factor of the empty cavity and f_s and Q_s are the frequency and quality factor of the perturbed cavity with the sample. Insertion loss of the samples was measured by closely inserting the samples between the two

waveguides to coaxial adapters. From the measured parameters, other characteristics like loss tangent and heating coefficient were also calculated.

8.1 Microwave attenuation of rubber ferrite composites

Figure 8.1 shows the insertion loss (IL) of nickel ferrite filled EPDM composites in the X-band frequency, expressed in dB/cm. The microwave absorption of gum vulcanisate is about -14 dB/cm. Incorporation of ferrite filler improves the attenuation and a maximum value of -17 dB/cm is obtained for a loading of 120 phr of nickel ferrite.
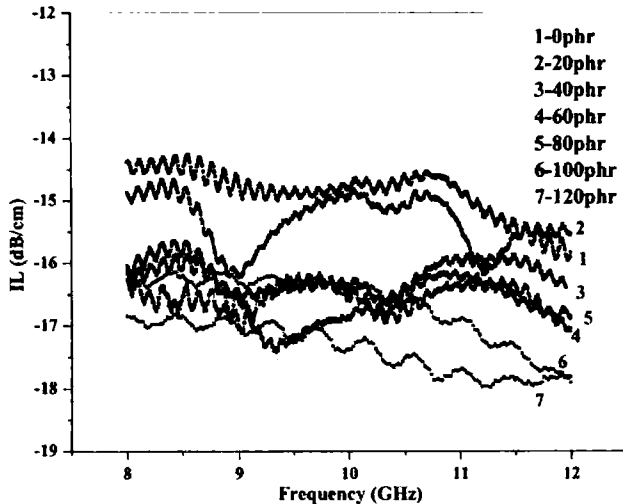
Figure 8.1 Microwave attenuation of NiFe₂O₄ filled EPDM composites

The insertion loss increases with increase in loading of the magnetic filler. This is due to the increased interaction of the magnetic filler with electromagnetic waves when the loading of the ferrite filler is increased. Attenuation in the material is achieved through dielectric conductive loss, magnetic loss or both.

Figure 8.2 shows the effect of both ferrite and carbon black on the insertion loss of carbon black (N330) containing RFCs. In figure 8.2, 0 phr indicates RFC with 100 phr $NiFe_2O_4$ and without carbon black. The addition of carbon black increases insertion loss and maximum absorption is observed over the entire X-band for sample with 100 phr $NiFe_2O_4$ and 80 phr carbon black.
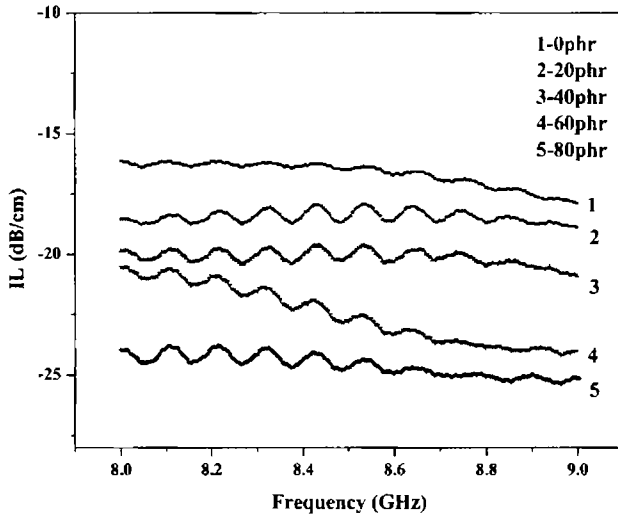
*Figure 8.2 Microwave attenuation of RFCs with 100 phr
NiFe₂O₄ and different loadings of carbon black*

Microwave attenuation increases from -14 dB/cm for the RFC with 100 phr $NiFe_2O_4$ to a value of -24 dB/cm for the RFC containing 100 phr $NiFe_2O_4$ and 80 phr carbon black. The increase in attenuation with the addition of carbon black can be attributed to the increase in interaction of the electromagnetic waves with carbon black.
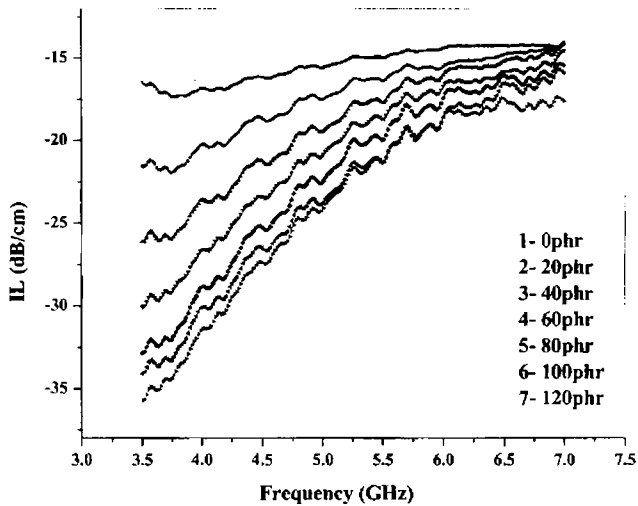
*Figure 8.3 Insertion loss of EPDM composites
with different loadings of carbon black*

A set of control composites containing carbon black alone was prepared as explained in section 4.1.1. The microwave attenuation of the control set was also measured and the frequency dependence of insertion loss is shown in figure 8.3.

Compared to the $NiFe_2O_4$ filled RFCs and carbon black containing RFCs, composites with only carbon black exhibit better attenuation characteristics. This is because of the presence of conductive carbon black filler.

Figure 8.4 represents the microwave attenuation characteristics of $NiFe_2O_4$ loaded neoprene composites. The microwave attenuation for the RFCs lies in the range of –17 to -18 dB/cm.
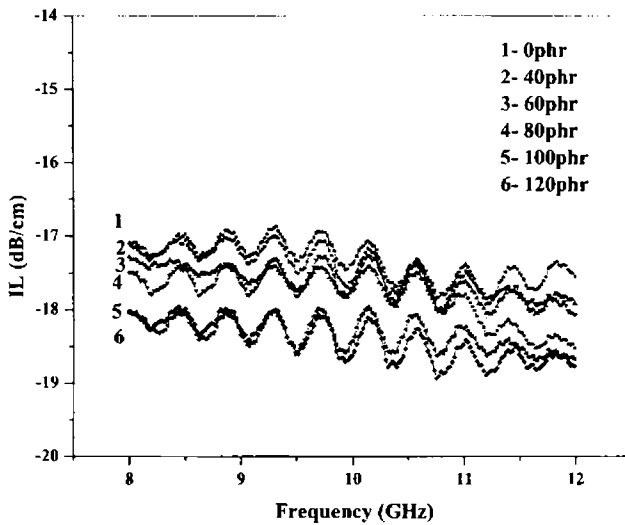
Figure 8.4 Microwave attenuation of $NiFe_2O_4$ filled neoprene composites

8.2 Permittivity measurements

The dielectric permittivity of the RFCs was determined in the X and S band frequencies by cavity perturbation technique. The permittivity values were also correlated with the ferrite loading. From the measured parameters the dielectric loss tangent and heating coefficient were also calculated.

8.2.1 Dielectric permittivity of EPDM based RFCs

Figure 8.5 and 8.6 shows the frequency dependence of the real part of permittivity of $NiFe_2O_4$ filled EPDM composites in X and S band respectively. In the

X band, dielectric permittivity decreases with increase in frequency where as, in S band it remains constant in the whole frequency range.
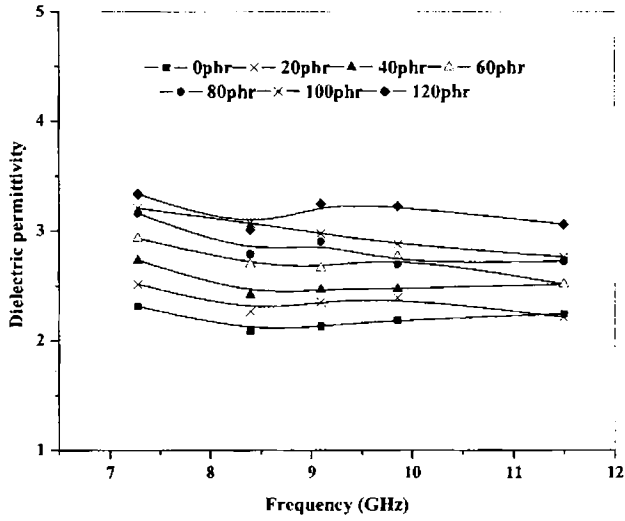
Figure 8.5 Dielectric permittivity of NiFe₂O₄ filled EPDM composites in X-band frequency.
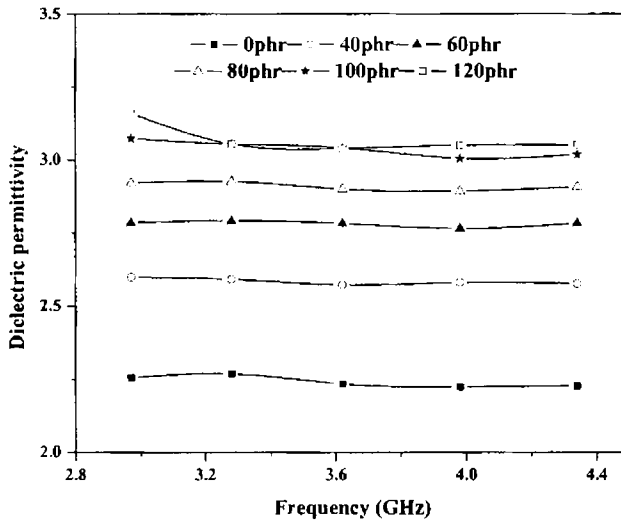
Figure 8.6 Dielectric permittivity of NiFe₂O₄ filled EPDM composites in S-band frequency.

221

The dielectric properties of polycrystalline ferrite-polymer composite arise mainly due to the interfacial polarisation along with contributions from ionic polarisation and intrinsic electric dipole polarisation. The interfacial polarisation results from the heterogeneous structure of ferrite comprising low conductivity grains separated by the higher resistivity grain boundaries [28]. Orientation polarisation which depends on the frequency of the applied field, contributes to dielectric permittivity. At high frequencies, orientation of dipoles faile to occur and this decreases the polarisability and leads to decrease in dielectric constant.
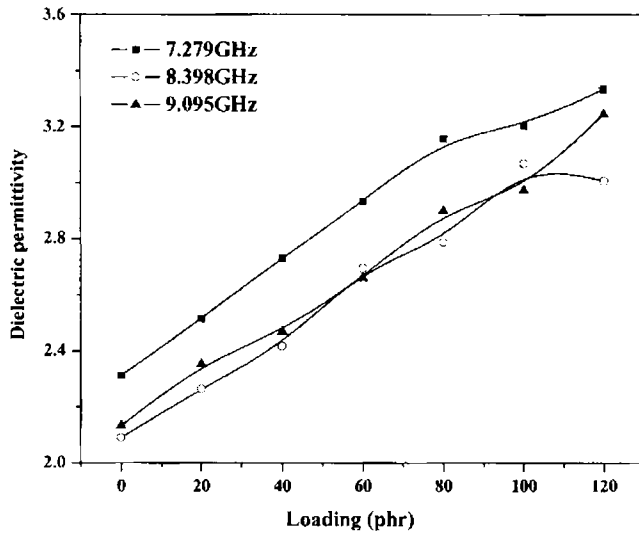
Figure 8.7 Loading dependence of dielectric permittivity of
EPDM based RFCs in X-band frequency

Figures 8.7 and 8.8 shows the loading dependence of dielectric permittivity of EPDM based RFCs in X and S band respectively. Dielectric permittivity depends on the volume fraction of the magnetic filler incorporated and hence increases with increase in ferrite content. Beyond 100 phr loading further increase in dielectric permittivity is not observed and this may be due to the attainment of percolation limit of filler.
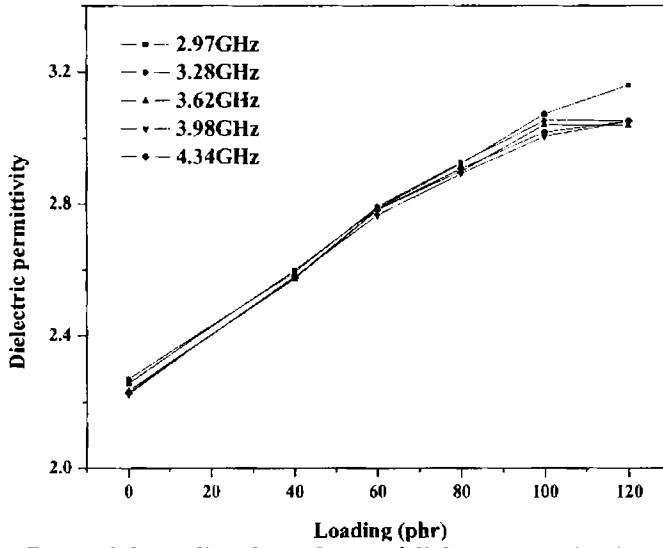
Figure 8.8 Loading dependence of dielectric permittivity of
EPDM based RFCs in S-band frequency

8.2.2 Loss tangent of EPDM based rubber ferrite composites

Figures 8.9 and 8.10 show the frequency dependence of tanδ in X and S band frequencies. Loss tangent value of all the RFCs shows similar behaviour. From figure 8.9, it is clear that RFCs exhibit higher tanδ values at 8.398 GHz and 10.66 GHz.
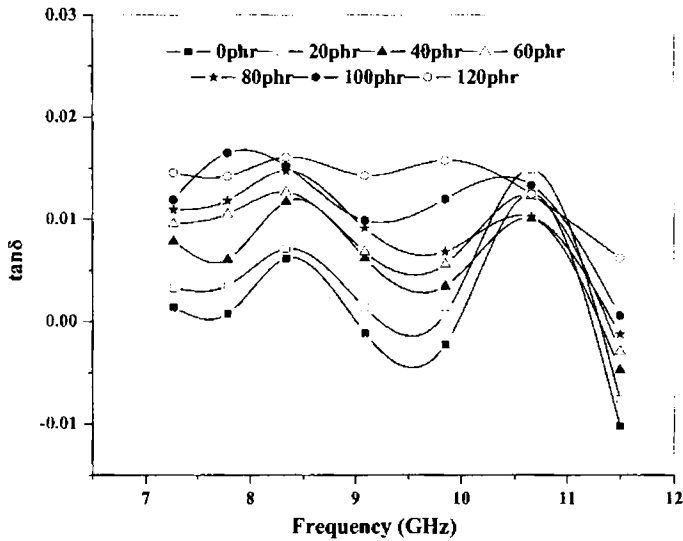
Figure 8.9 Loss tangent of NiFe$_2$O$_4$ filled EPDM
composites in X-band frequency.
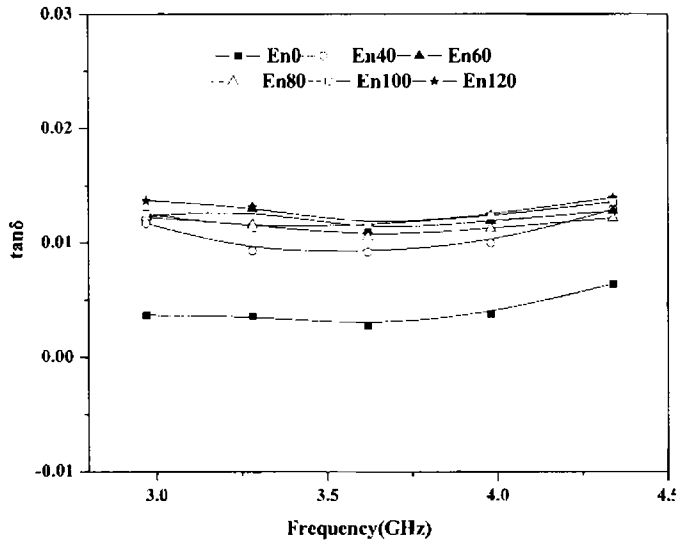
*Figure 8.10 Loss tangent of NiFe$_2$O$_4$ filled EPDM
composites in S-band frequency.*

As in the case of dielectric permittivity, loss tangent in S band does not change with frequency. Variation in tanδ with frequency can be taken as a function of relaxation process and the origin of this is due to the local motion of polar groups. At lower frequencies, the dipoles synchronise their orientation with the field. But as the frequency increases, the inertia of the molecule and the binding forces become dominant and this is the basis for high dielectric loss. Higher tanδ value observed at 8.398 GHz and 10.66 GHz may be a characteristic feature of these compounds. Since tanδ is a direct indication of microwave absorption, the RFCs loaded with nickel ferrite can act as better microwave absorbers at these frequencies.

Figures 8.11 and 8.12 shows the loading dependence of loss tangent in X and S band. As the ferrite content increases the tanδ value increases; above 100 phr loading, loss tangent remains constant with further increase in loading. The loss tangent value is increased from 0.00618 to 0.01605 at 8.4 GHz. In S-band, the loss tangent value is increased from 0.0027 to 0.0115 at 3.62 GHz.
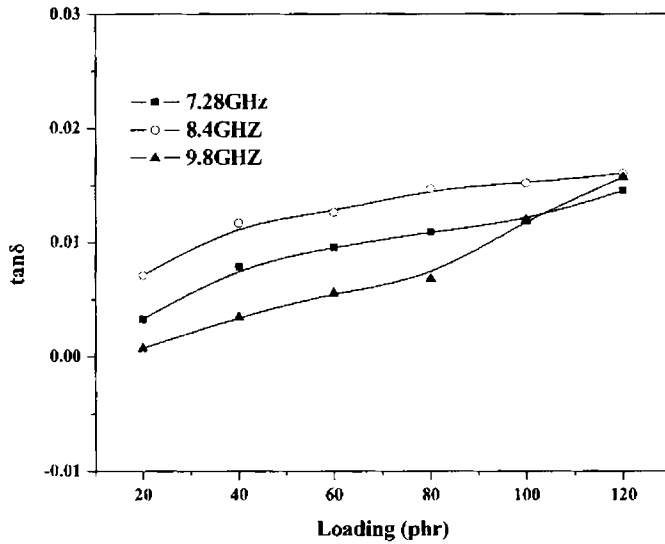
*Figure 8.11 Loading dependence of loss tangent of EPDM
based RFCs in X-band frequency*
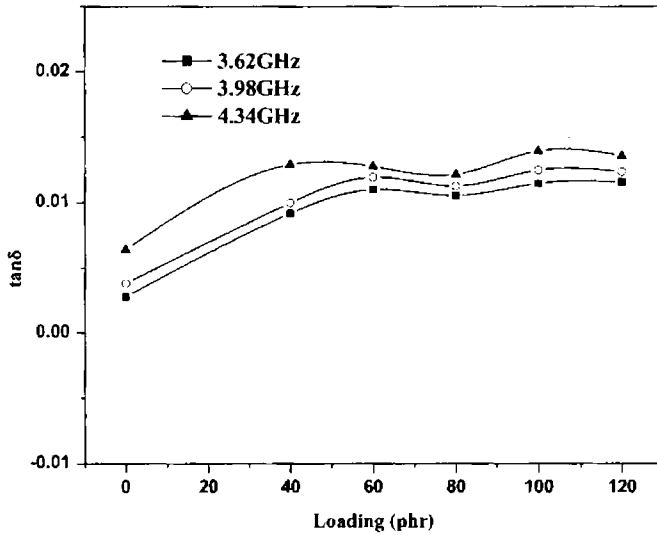
*Figure 8.12 Loading dependence of loss tangent of EPDM
based RFCs in S-band frequency*

8.2.3 Dielectric permittivity of carbon black filled RFCs in X-band

Microwave absorbing properties of RFCs are enhanced with the incorporation of carbon black. Improvement in dielectric permittivity and loss tangent are observed in X-band, with the additional loading of carbon black in RFCs. Figure 8.13 shows the

frequency dependence of dielectric permittivity of RFCs containing different loadings of carbon black. Dielectric permittivity decreases initially and then increases and a maximum value is obtained at 9.858 GHz.
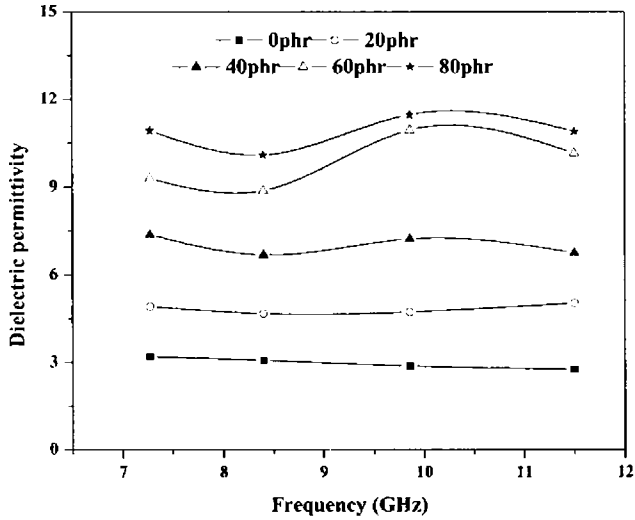
Figure 8.13 Frequency dependence of dielectric permittivity of RFCs containing carbon black in X-band

Figure 8.14 represents the dependence of dielectric permittivity with carbon black loading in RFCs. As the carbon black content increases, the dielectric
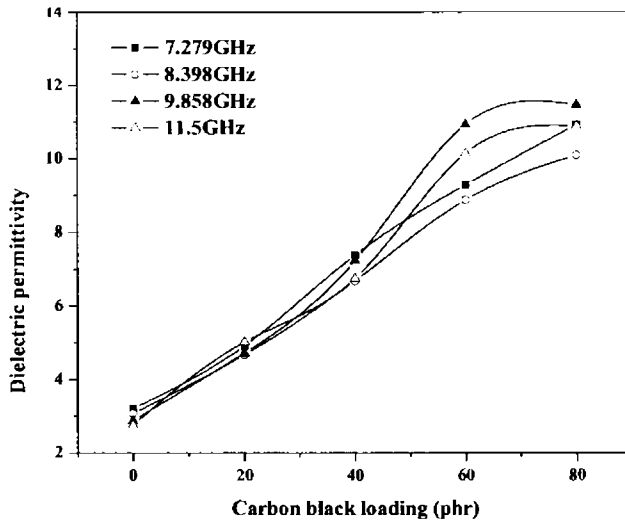
Figure 8.14 Loading dependence of dielectric permittivity of RFCs containing carbon black in X-band

permittivity increases and a maximum value is obtained for the RFC containing 80 phr carbon black. Dielectric permittivity of RFC with 100 phr nickel ferrite is 2.9. With the incorporation of 80 phr carbon black to this composite, dielectric permittivity is enhanced and a maximum value of 11 is obtained.

8.2.4 Loss tangent of carbon black filled RFCs in X-band

Figure 8.15 represents the frequency dependence of loss tangent of carbon black containing RFCs in X-band. Loss tangent does not change with frequency for RFCs containing different loadings of carbon black. But at higher loadings of carbon black, the loss tangent increases with frequency.
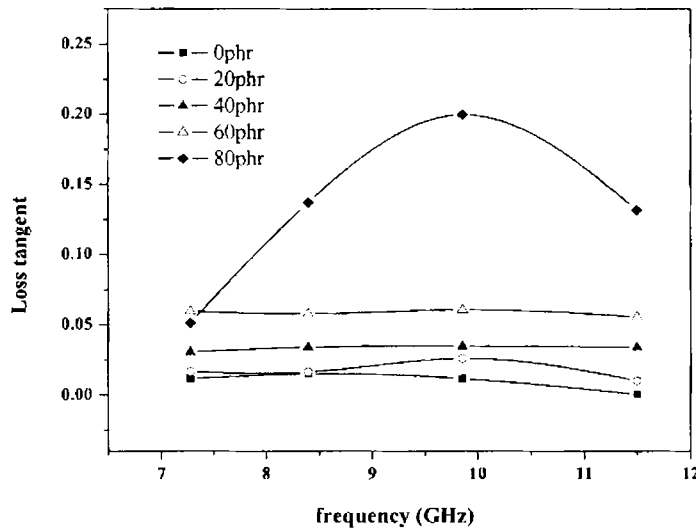
Figure 8.15 Frequency dependence of loss tangent of carbon black filled RFCs

Figure 8.16 shows the dependence of loss tangent on the carbon black content in RFCs at some selected frequencies. Loss tangent value increases with increase in carbon black loading. The value is improved from 0.012 for RFC containing 100 phr nickel ferrite to a value of 0.199 for RFC containing 100 phr nickel ferrite and 80 phr carbon black at 9.858 GHz.
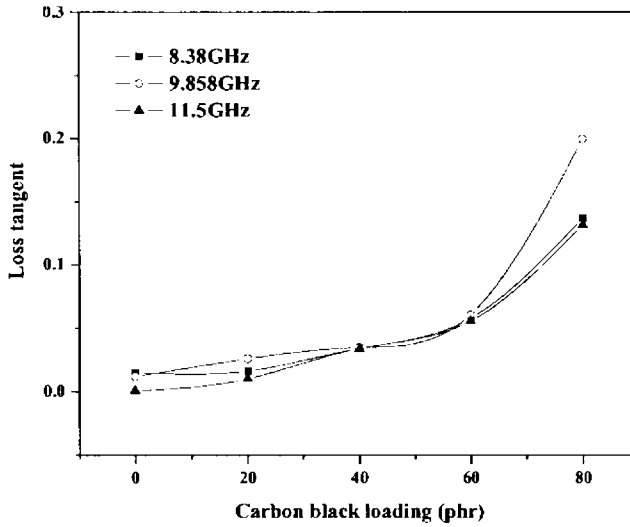
Figure 8.16 Loading dependence of loss tangent of carbon black filled RFCs

8.2.5 Dielectric permittivity and loss tangent of carbon black filled composites

Dielectric properties of the control set of composites with carbon black alone as the filler were done in X-band frequency. The frequency dependence of dielectric permittivity and loss tangent of the carbon black filled composites are shown in figures 8.17 and 8.18 respectively. The dielectric properties of carbon black composites are
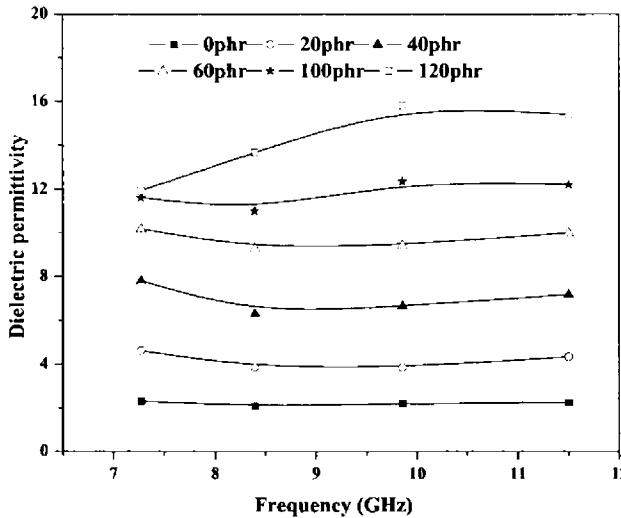
Figure 8.17 Frequency dependence of dielectric permittivity of carbon black composites in X-band

found to be higher than the RFCs and carbon black containing RFCs. A maximum value of dielectric permittivity of 16 is obtained at 9.858 GHz. At lower carbon black content, dielectric permittivity decreases with frequency, but at higher loadings improvement in dielectric constant with frequency is observed.
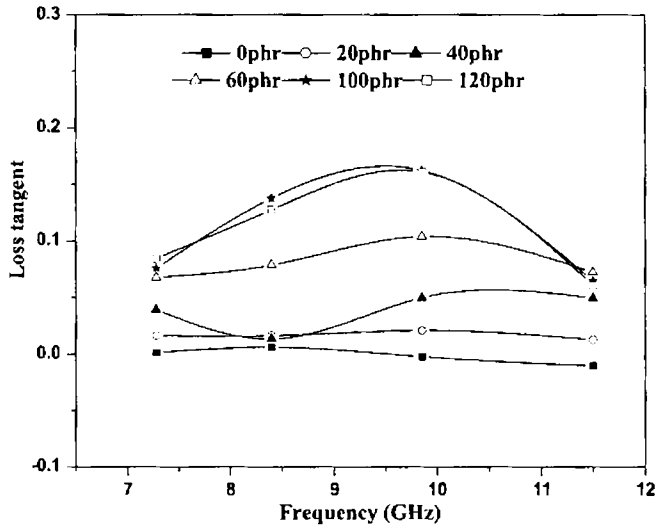
Figure 8.18 Frequency dependence of loss tangent of carbon black composites in X-band

The loss tangent value is also found to be high at 9.858 GHz frequency for the composites with different loadings of carbon black. A maximum value of 0.16 is obtained for the composites with 120 phr carbon black. On comparing the loss tangent of the carbon black composites with the values of RFCs and carbon black containing RFCs, higher values are obtained for the black filled RFCs.

8.2.6 Dielectric properties of $NiFe_2O_4$ filled neoprene based RFCs

Figures 8.19 and 8.20 represents the frequency dependence of dielectric permittivity and loss tangent of $NiFe_2O_4$ filled neoprene composites in S-band frequency. Dielectric permittivity of $NiFe_2O_4$ filled neoprene composites is found to be independent of the variation in frequency. Dielectric permittivity increases with increase in ferrite content. The dielectric permittivity of the gum vulcanisate is improved from a value of 3.5 to 4.4 for the RFC containing 120 phr nickel ferrite.
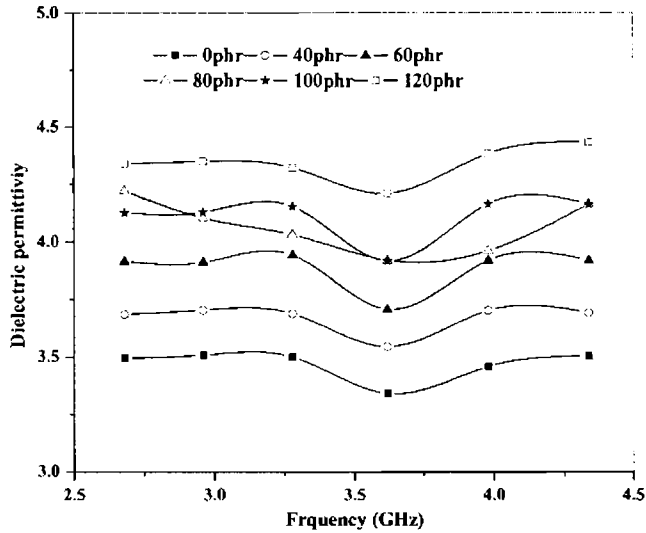
Figure 8.19 Frequency dependence of dielectric permittivity of NiFe₂O₄ filled neoprene composites in S-band frequency.
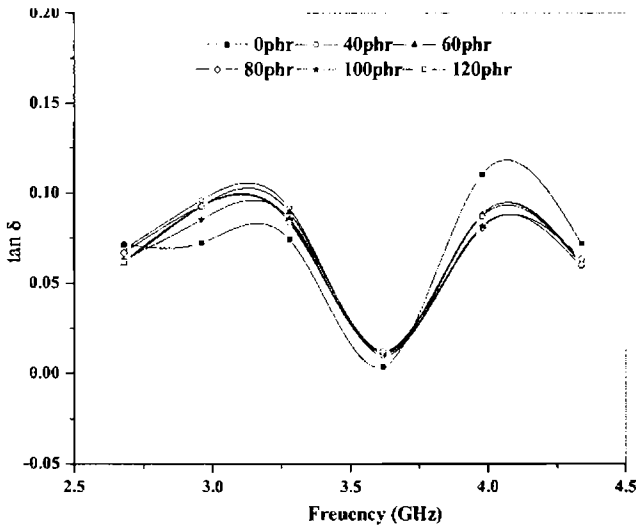
Figure 8.20 Frequency dependence of loss tangent of NiFe₂O₄ filled neoprene composites in S-band frequency.

Significant variation in loss tangent is not observed with frequency as well as with the change in ferrite content. At 3.62 GHz frequency a decrease in loss tangent is observed.

8.2.7 Heating coefficient of NiFe₂O₄ filled EPDM based RFCs

Heating coefficient (J) of the microwave absorbing materials can be calculated using the equation, $J = \dfrac{1}{\varepsilon_r \tan \delta}$ where ε_r is the permittivity of the material. Figures 8.21 and 8.22 represent the frequency and loading dependence of heating coefficient of NiFe₂O₄ filled EPDM composites. Higher heating coefficient values are observed at 9.86 GHz frequency.
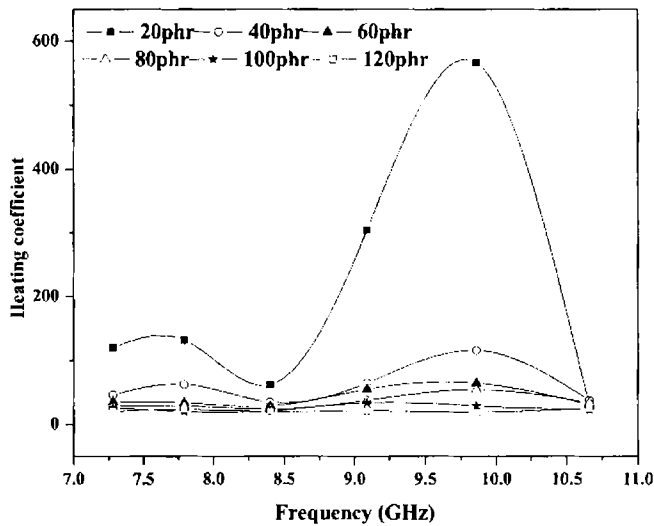
Figure 8.21 Frequency dependence of heating coefficient of EPDM based RFCs in X-band

From figures 8.21 and 8.22 it is clear that heating coefficient of RFCs decreases with loading. Lower the heating coefficient, better is the microwave attenuation. Hence as the loading increases the microwave attenuation of RFCs increases.
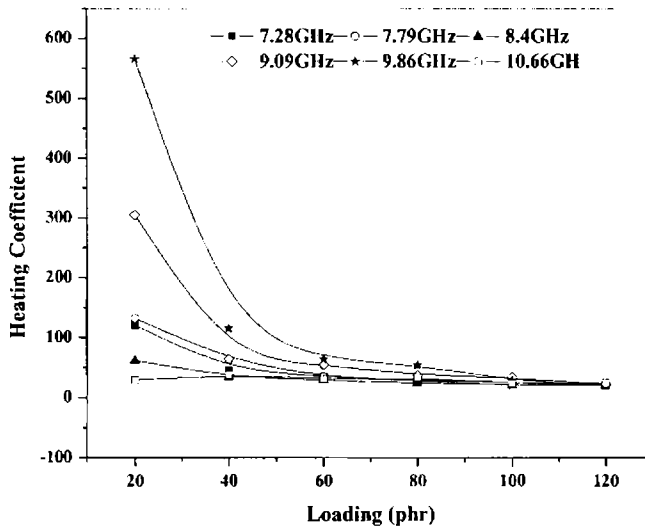
*Figure 8.22 Loading dependence of heating coefficient of
EPDM based RFCs in X-band*

8.2.8 Theoretical equations for the observed dielectric permittivity

The observed dielectric permittivity of the composites can be simulated by applying various empirical formulae. Different mixture equations can be applied to calculate the dielectric constant of the composites from that of the host medium and the well dispersed particles [29,30]. For very low particle concentration, all mixture laws give nearly the same results in frequent agreement with experiments. At very high filler concentration, these mixture equations generally disagree with experimental results. One of the best known mixture equations is developed by Maxwell and Wagner, which treatise the effective conductivity of a binary system consisting of spheres of one conductivity distributed uniformly in a continuum of different conductivity. The Maxwell-Wagner equation is given in section 6.1.7.

Maxwell Garnet theory (MG) is another important mathematical approach employed for modeling the permittivity of two component composite materials [31-34]. The permittivity of the composite is defined in terms of the permittivity of the components and the volume fraction of the filler. The composite is assumed to be consisting of spherical particles and are uniformly distributed through out a host medium. The effective permittivity is then given by,

$$\varepsilon_{eff} = \varepsilon_1 \frac{2\varepsilon_1(1 - V_f) + \varepsilon_2(1 + 2V_f)}{\varepsilon_1(2 + V_f) + \varepsilon_2(1 - V_f)} \qquad 8.5$$

where ε_1 and ε_2 are the dielectric permittivity of the medium and the filler respectively and V_f is the volume fraction of the filler.

MG theory breaks down for all frequencies when the permittivity of the filler is much larger than that of the host medium. By factorising ε_2 and applying the condition $\varepsilon_2 \gg \varepsilon_1$ equation (1) becomes,

$$\varepsilon_{eff} = \frac{\varepsilon_1(1 + 2f)}{(1 - f)} \qquad 8.6$$

The Maxwell Garnet equation was fitted for nickel ferrite filled EPDM based RFCs at different frequencies and shown in figures 8.23 to 8.27.
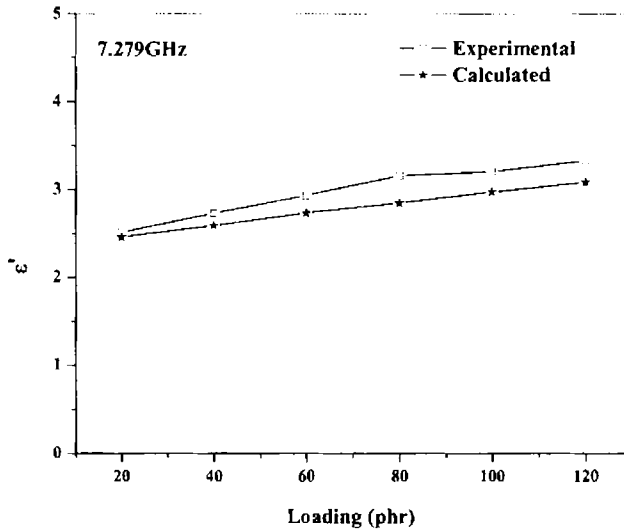
Figure 8.23 Fitted curves for effective permittivity of EPDM based RFCs at 7.279 GHz
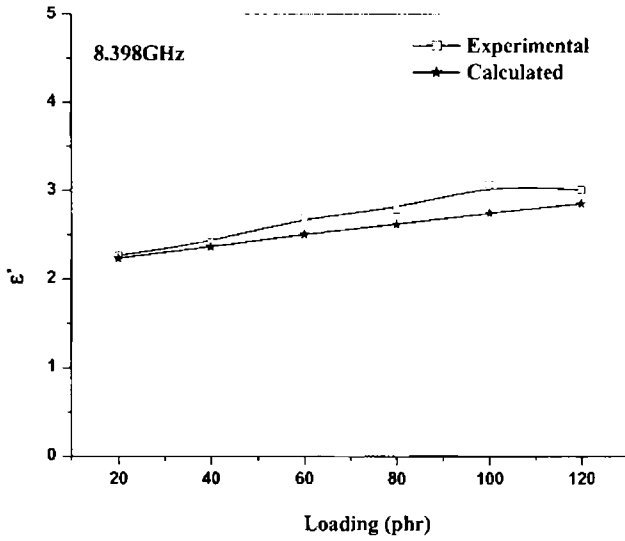
Figure 8.24 Fitted curves for effective permittivity of
EPDM based RFCs at 8.398 GHz
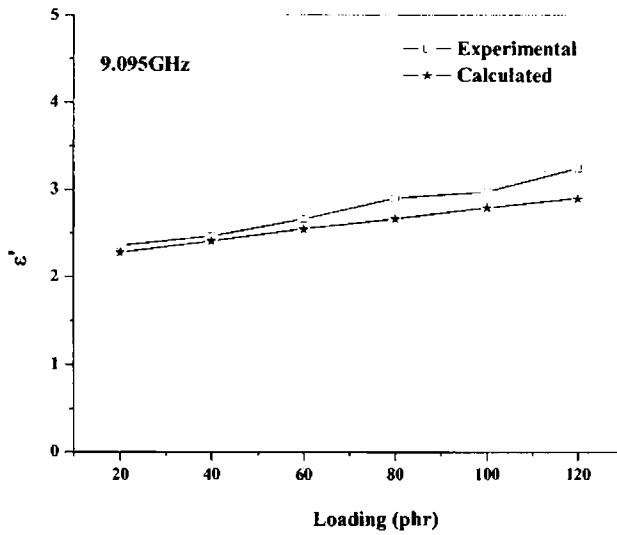
Figure 8.25 Fitted curves for effective permittivity of
EPDM based RFCs at 9.095 GHz
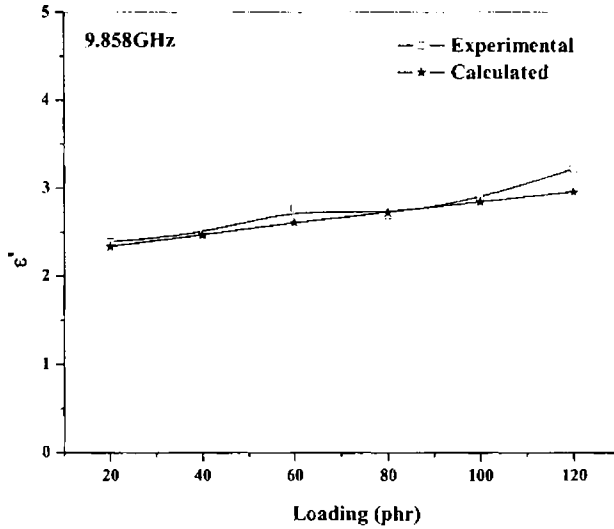
Figure 8.26 Fitted curves for effective permittivity of EPDM based RFCs at 9.858 GHz
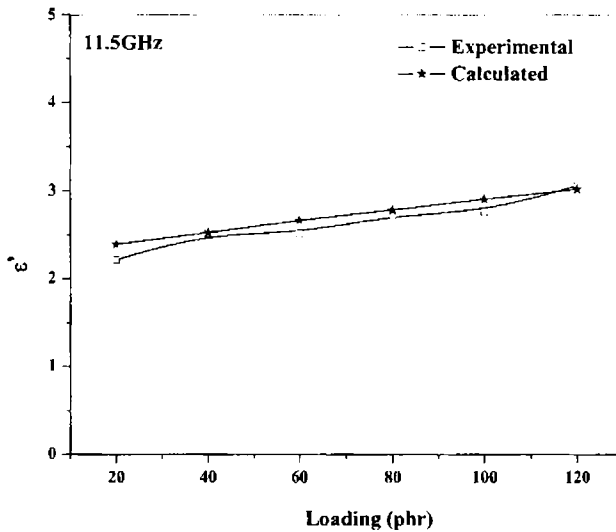
Figure 8.27 Fitted curves for effective permittivity of EPDM based RFCs at 11.5 GHz

At lower frequencies the equation is valid within a limit of about 10%. But at higher frequencies it is found to fit well with the experimental values. Deviation from the theoretical values especially for higher loadings can be accounted due to the assumptions made in MG equation. This equation is derived for composites of uniformly distributed spherical inclusions in a host medium. Another assumption is

that all the spherical particles are exposed to the same electric field. In RFCs due to agglomeration of filler particle, the particle size may not be strictly spherical and at higher loadings filler distribution also may not be homogeneous. Hence the deviation from the theoretical values is expected at higher loadings.

8.3 Conclusion

The microwave attenuation of EPDM and neoprene rubber based composites containing different volume fraction of nickel ferrite was done in the X-band frequency. The microwave attenuation was found to be increasing with incorporation of the ferrite in both the set of RFCs. But it was more significant in the case of EPDM based RFCs. Dielectric permittivity and loss tangent of the composites were measured by cavity perturbation method, both in X and S band frequencies. The variation in dielectric permittivity with frequency was not very pronounced in the case of RFCs within the X and S band. For the EPDM based RFCs, higher tanδ values were obtained at 8.398 GHz and 10.66 GHz. Compared to neoprene composites, EPDM composites were found to be better microwave absorbers. Both the dielectric permittivity and loss tangent increased with the volume fraction of the ferrite. The dielectric permittivity and tanδ values of the EPDM composites were improved with the additional loading of carbon black. Higher microwave attenuation characteristics were observed for carbon black containing RFCs. Heating coefficient of EPDM composites decreased with increase in filler content, which indicates better microwave attenuation of these composites. The effective permittivity of the composites were calculated by applying the Maxwell-Garnet equation and found to fit well with the observed values. Thus microwave properties of rubber ferrite composites can be tailored by the proper selection of the matrix and ferrite and can also modify with the incorporation of carbon black.

References
1. S. Ruan, B. Xu, H. Suo, F. Wu, S. Xiang and M. Zhao, J. Magn. Magn. Mater., **212** (2000) 175.
2. Praveen Singh, V.K. Babbar, A. Razdan, R.A. Puri and T.C. Goel, J.Appl. Phys., **87** (2000) 4362.
3. S.B. Cho, D.H. Kang and J.H. Oh, J. Mater. Sci., 31 (1996) 4719.

4. Z.W. Li, L.F. Chen, Y.P. Wu and C.K. Ong, J. Appl. Phys., **96** (2004) 534.

5. Gil M. Argentina and Paul D. Baba, IEEE Transactions on Microwave Theory and Technology, **MTT-22**, No.6 (June 1974).

6. Anjali Verma and Dinesh C. Dube, J. Am. Ceram. Soci., **88** (2005) 519.

7. Nutan Gupta, A. Verma, Subhash C. Kashyap and D.C. Dube, J. Magn. Magn. Mater., **308** (2007) 137.

8. T. Nakamura, J. Appl. Phys., **88** (2000) 348.

9. C.H. Peng, C.C Hwang, J. Wan, J.S. Tsai and S.Y. Chen, Mater. Sci. Eng. B, **117** (2005) 27.

10. A.Verma, A.K. Sexana and D.C. Dube, J. Magn. Magn. Mater., **263** (2004) 228.

11. Sung-Soo Kim, Sun-Tae Kim, Yeo-Choon Yoon and Kyung-Sub Lee, J. App. Phys., **97** (2005) 10F905.

12. W. Grunberger, B. Springmann, M. Brusberg, M. Schmidt and R. Jahnke, J. Magn. Magn. Mater., **101** (1991) 173.

13. J. Slama, A. Gruskova, R. Vicen, S. Vicenova, R. Dosoudil and J. Franek, J. Magn. Magn. Mater., **254-255** (2003) 642.

14. Magali Silveira Pinho, Maria Lusia Gregori, Regina Celia Reis Nunes and Bluma Guenther Soares, European Polymer Journal, **38** (2002) 2321.

15. V.T. Truong, S.Z. Riddell, and R.F. Muscat, J. Mater. Sci., **33** (1998) 4971.

16. P. Annadurai, A.K. Mallick, and D.K. Tripathy, J. Appl. Polym. Sci., **83** (2002)145.

17. Zhuangjun Fan, Guohua Luo, Zengfu Zhang, Li Zhou and Fei Wei, Materials Science and Engineering B, **132** (2006) 85-89.

18. Praveen Singh, V.K. Babbar, Archana Razdan, S.L. Srivastava, and T.C. Goel, Materials Science and Engineering B, **78** (2000) 70.

19. Xiangcheng Li, Rongzhou Gong, Zekun Feng, Junbing Yan, Xiang Shen and Huahui He, J. Am. Ceram. Soc., **89** (2006) 1450-1452.

20. S.S. Kim, S.B. Jo, K.K. Choi, J.M. Kim and K.S. Churn, IEEE Trans. Mag., **27** (1991) 5462.

21. A. Verma, R.G. Mendiratta, T.C. Goel and D.C. Dube, Journal of Electroceramics, **8** (2002) 203.

22. H.M. Musal Jr. and H. T. Hahn, IEEE Trans. Mag., **25** (1989) 3851.

23. Y. Naito and K. Suetaki, IEEE Transactions on Microwave Theory and Techniques, **MTT-19** (Jan 1971) 65.

24. Anna A. Barba, Gaetano Lamberti, Matteo d' Amore and Domenico Acierno, Polymer Bulletin, **57** (2006) 587.

25. Krishna Naishadham and Prasad K. Kadaba, IEEE Transactions on Microwave Theory and Techniques, 39 (July 1991) 1158.

26. S. M. Abbas, Mahesh Chandra, A.Verma, R. Chatterjee and T.C. Goel, Composites Part A, Applied Science and Manufacturing, **37** (2005) 2148.

27. Mukesh C. Dimri, Subhash C. Kashyap and D.C. Dube, Ceramic International, **30** (2004) 1623.

28. S.M. Abbas, A.K. Dixit, R. Chatterjee and T.C. Goel, J. Magn. Magn. Mater., **309** (2007) 20.

29. M.E. Achour, M. EI Malhi, J.L. Miane, F. Carmona and F. Lahjmori, J. Appl. Polym. Sci., **73** (1999) 969.

30. Hyung Do Choi, Hwan Woo Shim, Kwang Yun Cho, Hyuck Jae Lee, Chan Sik Park and Ho Gyu Yoon, J. Appl. Polym. Sci., **72** (1999) 75.

31. A.T. Ponomarenko, N. G. Ryvkina, V.S. Trakin, I.A. Tchmutin, A.L. Gusev and V.G. Shevchenko, International Scientific Journal for Alternative Energy and Ecology (ISJAEE), **3** (2002) 4.

32. J.H. Paterson, R. Devine and A.D. R. Phelps, J. Magn. Magn. Mater., **196-197** (1999) 394.

33. Mingzhong Wu, Haijun, Xi Yao and Liangying Zhang, J. Phys. D: Appl. Phys., **34** (2001) 889.

34. Kenneth Bober, Robert H. Giles and Jerry Waldman, International Journal of Millimeter Waves, **18** (1997) 101.

Magnetic Properties of $NiFe_2O_4$ and γ-Fe_2O_3 Based Rubber Ferrite Composites

Investigation on magnetic nanocomposites prepared by incorporating ferrites into elastomers are important not only from the fundamental point of view but also from the application perspective [1,2]. These composites are ideal templates to probe phenomenon such as particle-particle interaction in the matrix, particle-matrix interaction and their influence on the magnetic and microstructural properties.

Magnetic properties of spinel ferrites depend on a number of factors such as particle size, preparative conditions, heat treatment and the microstructure [3-8]. Both nickel ferrite and gamma ferric oxide are representatives of a large class of compounds called spinels. Nickel ferrite is an inverse spinel compound while γ-Fe_2O_3 is known to exhibit a vacancy ordered spinel with vacancies situated exclusively on the octahedral sites. Nickel ferrite and gamma ferric oxide is expected to exhibit interesting magnetic properties in the nano regime. The incorporation of these nano fillers into matrices like EPDM/CR will impart magnetic properties to the elastomer matrix.

Nickel ferrite nanoparticles exhibit anomalous magnetic behaviour [9-11] and they are found suitable for high frequency applications. The most important feature associated with the ferrite nanoparticles is the observed reduction in saturation magnetisation (M_s) compared to the bulk counter part [12-14]. The decrease in (M_s) with the decrease in particle size is associated with different reasons such as surface effects [15], spin canting [16] and dead layer formation [9,17-20].

Several studies were reported on the close relationship between structure and magnetic properties of different spinel ferrites [21-24]. The ferrimagnetism of spinel ferrites largely depends on the distribution of the metal ions in octahedral and tetrahedral lattice sites. As reported by Verma et al., the magnetic properties of nickel-

zinc ferrite system, like saturation magnetisation, coercivity (H_c) and magnetic remanence (M_r) are highly depend on the concentration of zinc ion in the tetrahedral site. The curie temperature of the system is also found to depend on the concentration and distribution of the cations between the octahedral and tetrahedral sites [25-27].

Tailoring of magnetic and mechanical properties of RFCs is also very vital as far as applications are concerned. Simple mixture equation can be formulated to foretell the magnetic properties of the RFCs. Evaluation of magnetic properties along with the modeling of these properties with known equations are significant.

Carbon black is added along with nickel ferrite/ gamma ferric oxide to enhance the microwave absorbing properties. The addition of carbon black in RFCs helps to tune the microwave properties by suitably modifying the dielectric property. So evaluation of magnetic properties of RFCs containing an optimum amount of magnetic filler together with the required amount of carbon black is also important. This is also taken up in this investigation.

Magnetic measurements of the $NiFe_2O_4$, γ-Fe_2O_3 and rubber ferrite composites containing these ferrites were carried out at room temperature using Vibrating sample magnetometer (VSM model EG&G PAR 4500) and the hysteresis loop parameters namely saturation magnetisation, remanent magnetisation and coercivity were determined.

9.1 Magnetic measurements of nickel ferrite and gamma ferric oxide

The hysteresis curve for nickel ferrite particles measured at room temperature is shown in figure 9.1. Parameters like saturation magnetisation and coercivity were determined from the hysteresis loop and are tabulated in table 9.1. The saturation magnetisation of the pristine nickel ferrite filler is found to be 39 emu/g which is less than the reported M_s value of the bulk sample (~55 emu/g) [28,29]. The coercivity of the prepared sample is ~100 Oe which is also less than the reported coercivity of bulk sample (130 Oe). The deviation in magnetic properties arises due to a number of factors. The structure of the particles could be changed by the presence of lattice defects or by a change in the distribution of the constituent ions between the tetrahedral sites and octahedral sites. In the present study, M_S of the samples is lower

than that of the bulk value, which rules out the absence of mixed spinel structure. In the inverse spinel structure, the net magnetisation comes from the Ni^{2+} moments in the B sites as the Fe^{3+} moments from the A and B sites cancel each other. In the mixed spinel structure some Ni^{2+} ions occupy the tetrahedral site, and in that case the net magnetisation will be higher than that of inverse spinel structure [30,31].
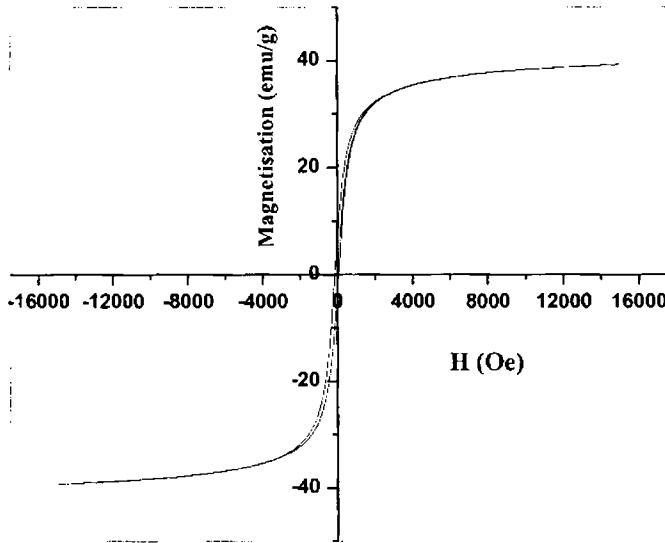
Figure 9.1 Hysteresis loop for NiFe₂O₄

The anomalous decrease in M_s for the prepared nickel ferrite than the bulk may be due to fine size effect and surface effects. Saturation magnetisation of particles decreases with particle size due to surface spin disorder. In fine particle systems since the surface to volume ratio is large, the ratio of number of surface spins to the total number of spins increases. This may lead to misalignment of surface spins resulting in surface anisotropy and deviation from the bulk properties. Another source of surface spin disorder for the fine particle nickel ferrite is due to broken exchange bonds that destabilise magnetic order giving rise to spin-frustration [32-34].

As the particle size decreases, coercivity increases, reaches a maximum value and then decreases after reaching a specific particle size [25,35,36]. As the particle size decreases, number of domains and domain walls decreases. The magnetisation/demagnetisation caused by domain wall movement requires less energy than that required by domain rotation. The number domain walls decreases with

241

decrease in grain size and the contribution of wall movement to magnetisation /demagnetisation is lower than that of domain rotation. Thus samples having lower grain size are expected to have high coercivity. In this particular study, the average particle size of the prepared nickel ferrite sample is higher than the critical diameter below which the coercivity shows a decreasing tendency with the decrease in particle size. Thus the coercivity of the prepared nickel ferrite was found to less than that of its bulk counter part.

Similar results are also observed for gamma ferric oxide particles. Figure 9.2 represents the hysteresis loop for the γ-Fe_2O_3. The saturation magnetisation of the prepared γ-Fe_2O_3 is found to be about 52 emu/g and the coercivity is 123 Oe, where as the corresponding values for the bulk sample is 75 emu/g and 300 Oe respectively. The magnetic characteristics of gamma ferric oxide particles are given in table 9.1. The decrease in M_s observed for γ-Fe_2O_3 is due to the fine size effect. Formation of non-magnetic alpha phase is also observed as revealed by X-ray diffraction, which also results in a reduction in magnetic properties.
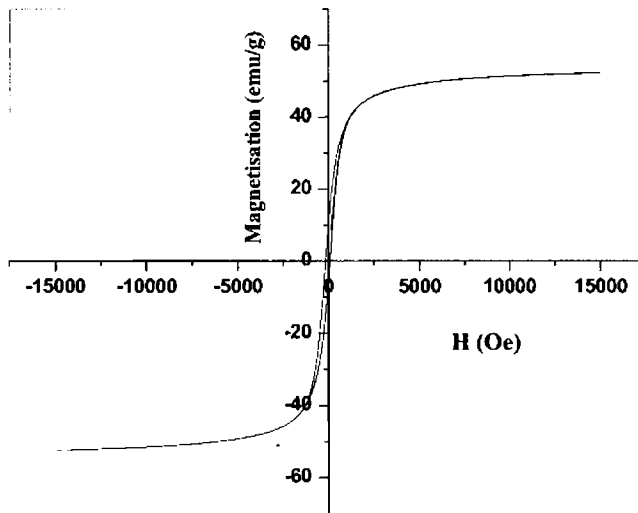
Figure 9.2 Hysteresis loop for γ-Fe_2O_3

The presence of superparamagnetic iron oxide could be another reason for the reduced magnetisation of γ-Fe_2O_3. The occurrence of superparamagnetic iron oxide along with ferrimagnetic iron oxide in the compound can considerably reduce the net coercive force of the compound. Magnetisation alone can't reveal the presence of

superparamagnetic components in a compound and techniques like Mossbauer spectroscopy is necessary to identify the presence of superparamagnetic components.

Table 9.1 Magnetic characteristics of NiFe$_2$O$_4$ and γ-Fe$_2$O$_3$

Sample	Saturation Magnetisation M$_s$ (emu/g)	Coercivity H$_c$ (Oe)	Magnetic Remanence M$_r$ (emu/g)	M$_r$/M$_s$
NiFe$_2$O$_4$	39	101	5.3	0.13
γ-Fe$_2$O$_3$	52	123	8.1	0.16

9.2 Magnetic measurements of NiFe$_2$O$_4$ based RFCs

Rubber ferrite composites containing different loadings of NiFe$_2$O$_4$ and γ-Fe$_2$O$_3$ were prepared using EPDM and CR and the VSM analysis of these samples was carried out as in the case of ferrites.

9.2.1 Magnetic properties of EPDM based RFCs with nickel ferrite filler

Figure 9.3 represents the hysteresis loops for EPDM based RFCs containing 20,40,60,80,100 and 120 phr of NiFe$_2$O$_4$. From the hysteresis loop, the hysteresis loop parameters like M$_s$, H$_c$ and M$_r$ were evaluated and tabulated in table 9.2.
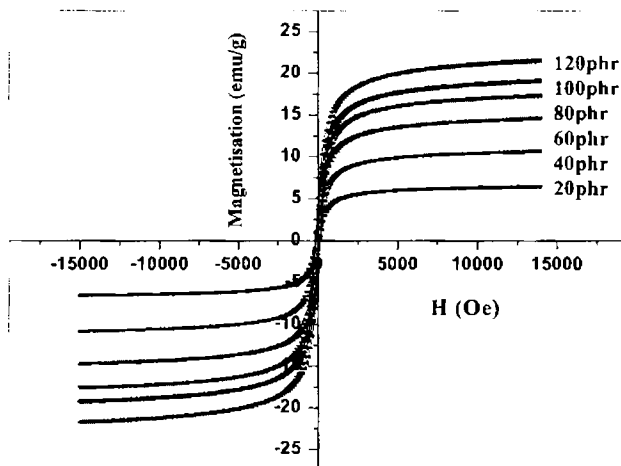
Figure 9.3 Hysteresis loops for EPDM based RFCs with different loadings of NiFe$_2$O$_4$

Saturation magnetisation and magnetic remanence of the EPDM based RFCs, increases with increase in ferrite content. Coercivity of the composite does not alter with variation in ferrite loading.

Table 9.2 Magnetic characteristics of NiFe₂O₄ filled EPDM composites

NiFe$_2$O$_4$ Loading (phr)	Saturation Magnetisation, M$_s$ (emu/g)	Coercivity, H$_c$ (Oe)	Magnetic Remanence, M$_r$ (emu/g)	M$_r$/M$_s$
20	7	126	1.3	0.20
40	11	126	2.0	0.18
60	15	126	2.9	0.20
80	17	126	3.1	0.18
100	19	126	3.6	0.19
120	22	126	4.3	0.20

The coercivity of the RFCs is higher than that of the nickel ferrite filler. Coercivity of the ceramic samples mainly depends on sintering conditions and particle size. The average particle size of the ferrite within the matrix may be different from that of the powder sample due to some degree of agglomeration. Another reason for the variation in coercivity between the ceramic and composites may be due to the interaction of the filler with the matrix. Since coercivity is a mass independent phenomena, change in coercivity of RFCs with ferrite loading is not observed.

Since saturation magnetisation of RFCs is a filler specific phenomenon, the M$_s$ value of RFCs can be tailored with the proper selection of the type and amount of the magnetic filler within the matrix. If the M$_s$ value of the ferrite is known, a simple mixture equation of the general form (equation 9.1) involving the weight fractions of the filler can be employed to calculate the M$_s$ of the composites.

$$M_{RFC} = W_1M_1 + W_2M_2 \qquad 9.1$$

Where M$_{RFC}$ is the saturation magnetisation of the composite, W$_1$ and W$_2$ are the weight fractions of the filler and polymer, M$_1$ and M$_2$ are the saturation magnetisation of the filler and the polymer respectively. Since the matrix used for the preparation of RFCs is non magnetic, equation 9.1 can be reduced to the following form [37,38]

$$M_{RFC} = W_1 M_1 \qquad\qquad 9.2$$

Figure 9.4 shows the variation in magnetisation values of $NiFe_2O_4$ filled EPDM composites with loading of the ferrite. The corresponding calculated values of M_s are also plotted.
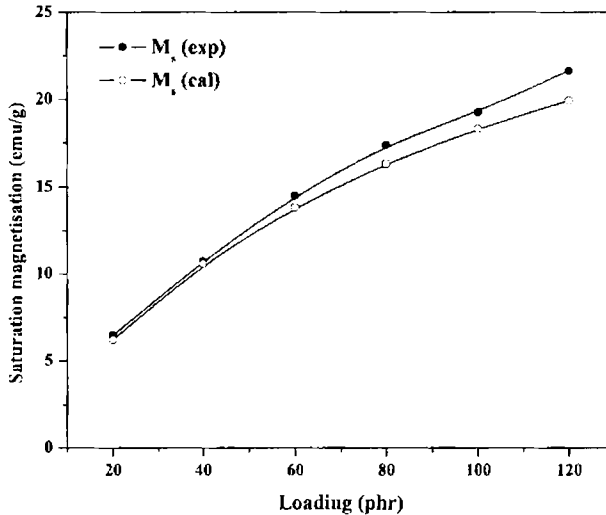
Figure 9.4 Experimental and calculated values of saturation magnetisation of NiFe₂O₄ filled EPDM composites

From figure 9.4, it is clear that the calculated values are in good agreement with the experimental values especially at lower loadings. The slight variation, observed at higher loadings may be due to the deviation from the ideal dispersion of the filler within the matrix. Agglomeration of the filler particles occurs at higher loadings as evidenced from the physicomechanical studies of the RFCs.

9.2.2 Magnetic properties of neoprene based RFCs containing NiFe₂O₄ filler

VSM analysis of neoprene based RFCs containing different loadings of $NiFe_2O_4$ ranging from 40 to 120 phr were done at room temperature. Figure 9.5 represents the hysteresis loops for the neoprene based RFCs containing different amounts of $NiFe_2O_4$.
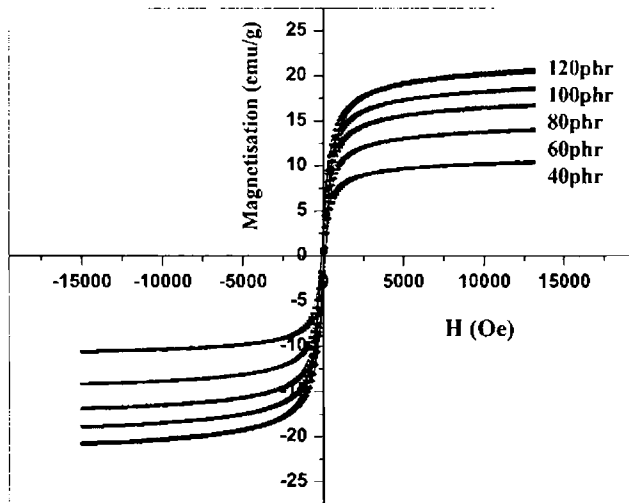
Figure 9.5 Hysteresis loops for neoprene based RFCs with different loadings of NiFe₂O₄

The magnetic parameters calculated from the hysteresis loops of the composites are given in table 9.3. From table 9.3, it is observed that the M_s and M_r of the composites increase with increase in ferrite content. Coercivity of the neoprene based RFCs remain constant as in the case of EPDM based RFCs.

Table 9.3 Magnetic characteristics of NiFe₂O₄ filled neoprene composites

NiFe₂O₄ Loading (phr)	Saturation Magnetisation, M_s (emu/g)	Coercivity, H_c (Oe)	Magnetic Remanence, M_r (emu/g)	M_r/M_s
40	10	115	2.1	0.21
60	14	115	2.8	0.20
80	17	115	3.5	0.21
100	19	115	3.7	0.19
120	21	115	3.8	0.18

Coercivity of neoprene based RFCs is different from that of the NiFe₂O₄ filled EPDM based RFCs. The difference in H_c between the ferrite and the RFCs gives indications of possible interaction between the ferrite and the rubber matrix. Small difference in coercivity is observed between EPDM and CR based RFCs, which may

be due to the difference in interaction of nickel ferrite filler with these matrices. However, the difference is insignificant, which indicates that there is only physical interaction between the ferrite and the matrices.
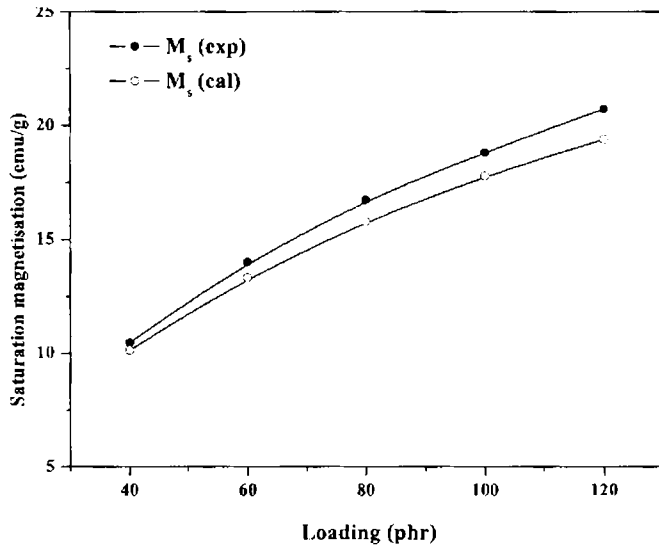
Figure 9.6 Experimental and calculated values of saturation magnetisation of NiFe₂O₄ filled neoprene composites

Saturation magnetisation value of the $NiFe_2O_4$ filled neoprene based RFCs are calculated using equation 9.1 and plotted along with the experimental values in figure 9.6. At lower filler contents, the calculated and experimental values agree well, but at higher loadings, deviations are observed.

A comparison of M_s of EPDM and neoprene based RFCs containing same amount of nickel ferrite is given in figure 9.7. For the same loading of nickel ferrite the M_s of EPDM and neoprene based RFCs were almost same and this is expected since saturation magnetisation depends only on the weight fraction of the ferrite in the matrix.
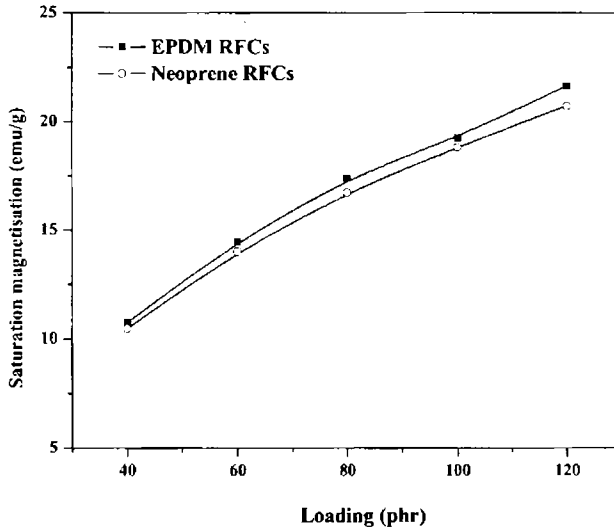
Figure 9.7 Comparison of M_s value of $NiFe_2O_4$ filled
EPDM and neoprene based RFCs

9.2.3 Effect of carbon black on the magnetic properties of RFCs containing $NiFe_2O_4$

Figure 9.8 shows the hysteresis loops of EPDM based RFCs containing different loadings of carbon black and 100 phr $NiFe_2O_4$. Magnetic properties of composites containing different loadings of carbon black were evaluated from the corresponding hysteresis loops.
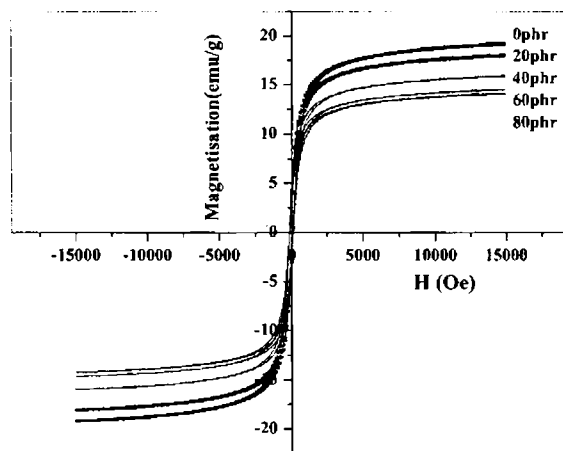
Figure 9.8 Hysteresis loops for EPDM based RFCs containing
100 phr $NiFe_2O_4$ and different loadings of carbon black.

The different magnetic parameters like M_s, H_c and M_r of the carbon black filled RFCs are given in table 9.4. From table 9.4, it is clear that the magnetic properties like M_s and M_r were found to decrease with increase in carbon black loading. Since carbon black is non magnetic, as the carbon black content increases the weight fraction of magnetic filler in the matrix decreases. The carbon black containing

Table 9.4 Magnetic properties of carbon black filled RFCs

Carbon black Loading (phr)	Saturation Magnetisation, M_s (emu/g)	Coercivity, H_c (Oe)	Magnetic Remanence, M_r (emu/g)	M_r/M_s
0	19	115	3.7	0.19
20	18	123	3.6	0.20
40	16	123	3.3	0.21
60	15	123	3.1	0.21
80	14	123	2.7	0.19

RFCs are still sufficiently magnetic, and are useful for application as flexible magnetic composites with improved mechanical properties. Moreover, additional loading of carbon black is expected to modify the microwave absorption property of these composites.
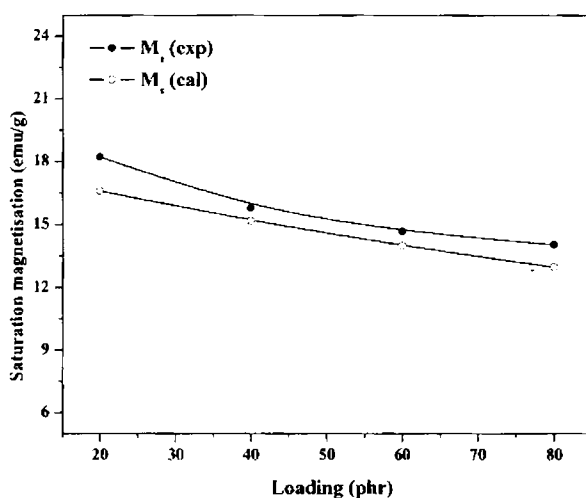
Figure 9.9 Experimental and calculated values of saturation magnetisation of carbon black containing RFCs

Figure 9.9 shows the comparison of the observed and calculated saturation magnetisation value of RFCs containing carbon black. Experimental M_s value found to be slightly greater than the calculated value. As the ferrite content increases, agglomeration of the filler particles occurs and the effective particle size increases. Thus the calculated value of the saturation magnetisation deviates from the experimental values.

9.3 Magnetic properties of γ-Fe_2O_3 filled RFCs

Precharacterised gamma ferric oxide was incorporated into EPDM and CR matrix to prepare the corresponding RFCs.

9.3.1 Magnetic properties of γ-Fe_2O_3 filled EPDM based RFCs

Hysteresis loops for EPDM based RFCs with various loading of γ-Fe_2O_3 are represented in figure 9.10.
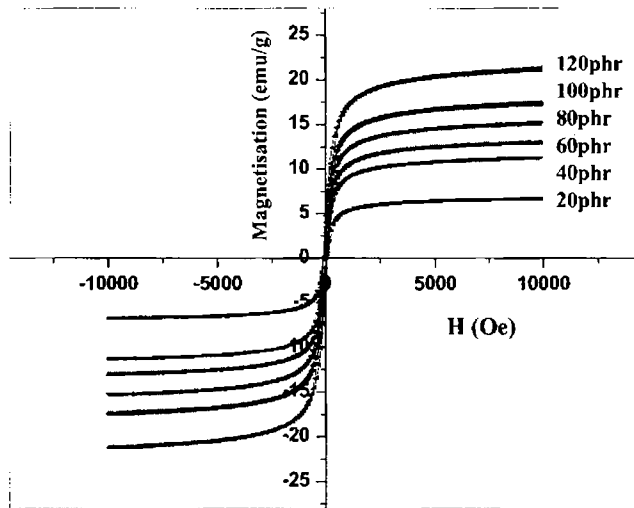
Figure 9.10 Hysteresis loops of γ-Fe₂O₃ filled EPDM composites

Figure 9.11 shows the variation of M_s and M_r with loading. Saturation magnetisation and magnetic remanence of EPDM based RFCs increases with increase in ferrite content. The increase in M_s and M_r is proportional to the increase in loading of the magnetic filler in the composites.
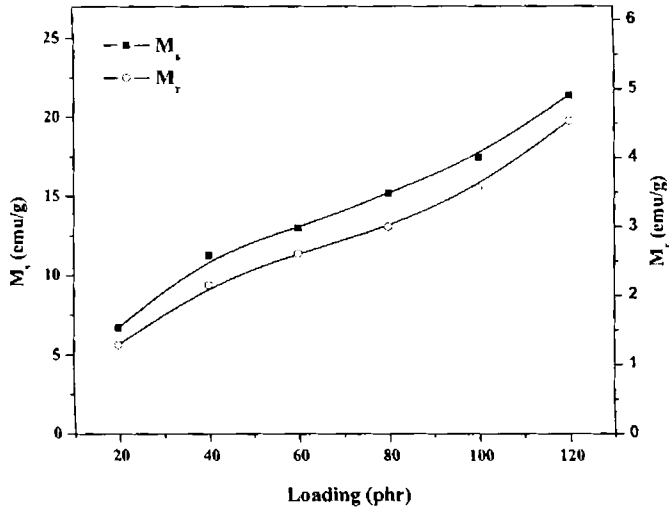
Figure 9.11 Loading dependence of M_s and M_r of γ-Fe₂O₃ filled EPDM composites

Figure 9.12 shows the variation of coercivity with the change in loading of γ-Fe₂O₃. Significant change in coercivity with the increase in the filler content is not observed. But slightly higher values are obtained for the RFCs compared to gamma ferric oxide.
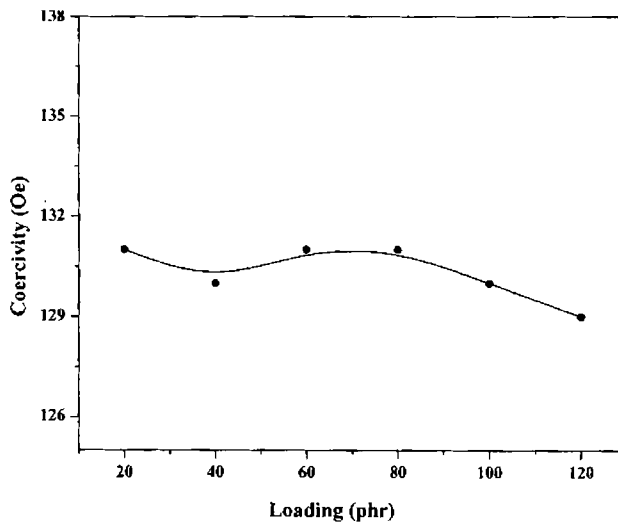
Figure 9.12 Variation of coercivity of EPDM composites with loading of γ-Fe₂O₃

251

9.3.2 Magnetic properties of γ-Fe₂O₃ filled Neoprene based RFCs

Neoprene based RFCs containing different loadings γ-Fe$_2$O$_3$ were prepared and magnetic measurements were done using Vibrating sample magnetometer. The hysteresis loops for neoprene based RFCs containing different loadings of γ-Fe$_2$O$_3$ are shown in figure 9.13.
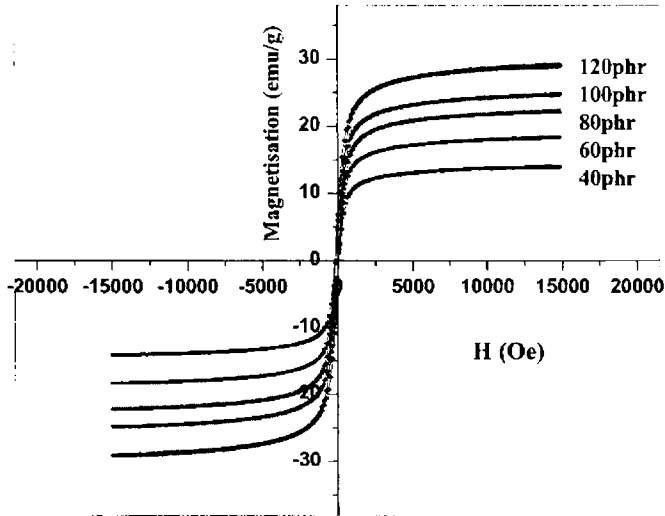
Figure 9.13 Hysteresis loops of γ-Fe₂O₃ filled neoprene composites

The magnetic characteristics calculated from the hysteresis loops are given in table 9.5. The saturation magnetisation and magnetic remanence increased with increase in ferrite loading. The increase in M$_s$ is proportional to the increase in ferrite content. The difference in H$_c$ between the filler and the RFCs are less significant.

Table 9.5 Magnetic properties of γ-Fe₂O₃ filled neoprene based RFCs

γ-Fe₂O₃ Loading (phr)	Saturation Magnetisation, M$_s$ (emu/g)	Coercivity, H$_c$ (Oe)	Magnetic Remanence, M$_r$ (emu/g)	M$_r$/M$_s$
40	14	125	2.9	0.21
60	18	125	3.0	0.16
80	22	124	4.2	0.18
100	25	123	5.1	0.21
120	29	122	6.0	0.21
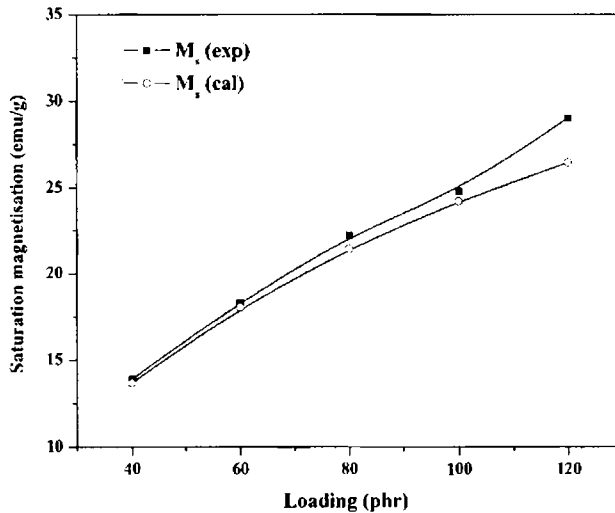
*Figure 9.14 Experimental and calculated values of saturation
magnetisation of γ-Fe₂O₃ filled neoprene composites*

The calculated and experimental M_s values are plotted in figure 9.14. The observed M_s agrees well with the calculated values at lower loadings and a slight deviation is observed at higher loadings, which may be due to filler agglomeration.

9.4 Conclusion

Rubber ferrite composites were prepared using nickel ferrite and gamma ferric oxide as the filler and EPDM and neoprene as the host matrix. Magnetic parameters of the ferrites as well as that of the RFCs were measured using vibrating sample magnetometer. The saturation magnetisation of the prepared ferrites in the nanoregime was found to be less than that of the corresponding bulk samples. Coercivity of the nano ferrites was also found to be less than the bulk counter cousins. Saturation magnetisation and magnetic remanence of the prepared RFCs were found to be proportional to the loading of the ferrites. A simple mixture equation based on M_s and the weight fraction of filler was employed to calculate the M_s of the RFCs. The calculated magnetisation was found to be in agreement with the observed values especially at lower filler concentrations. The coercivity values of different set of RFCs were found to be independent of filler loading, but deviations were observed from that of the pure ferrites. The insignificant change in coercivity as well as linear dependence of M_s and M_r of RFCs, can be used to tailor the magnetic properties of the RFCs.

Effect of carbon black on the magnetic properties of EPDM based RFCs were studied. Magnetic properties of RFCs were found to decrease with increase in carbon black content. Coercivity values were found to be unaffected by the change in carbon black loading. Since carbon black modifies the microwave absorption properties of the RFCs, materials with desired microwave and magnetic properties can be prepared by adjusting the amount of carbon black and the ferrite.

References

1. M.R. Anantharaman, S. Jagatheesan, S. Sindhu, K.A. Malini, C.N. Chinnasamy, A. Narayanasamy, P. Kurian and K.Vasudevan, Plastics, Rubber and Composites Processing and Applications, **27** (1998) 77.

2. M.A. Soloman, Philip Kurian, M.R. Anantharaman and P.A. Joy, Polymer- Plastics Technology and Engineering, 43 (2004) 1013.

3. J.P. Chen, C.M. Sorensen, K.J. Klabunde, G.C. Hadjipanayis, E. Devlin and A. Kostikas, Physical Review B, **54** (1996) 9288.

4. Vuk Uskokovic, Miha Drofenik and Irena Ban, J. Magn. Magn. Mater., **284** (2004) 294.

5. M.E. Rabanal, A. Varez, B. Levenfeld and J.M. Torralba, Journal of Materials Processing Technology, **143-144**, (2003) 470.

6. Manisha V. Rane, D. Bahadur, S.D. Kulkarni and S.K. Date, J. Magn. Magn. Mater., **195** (1999) L256.

7. K. Kondo, T. Chiba and S. Yamada, J. Magn. Magn. Mater., **254-255** (2003) 541.

8. M. Muroi, R. Street, P.G. McCormick and J. Amighian, Phys. Rev. B, **63** (2001) 184414.

9. A.H. Morrish and K. Haneeda, J. Appl. Phys., **52** (1981) 2496.

10. A.E. Berkowitz, J.A. Lahut, I.S. Jacobs, L.M. Levinson and D.W. Forester, Phys. Rev. Lett., **34** (1975) 594.

11. C.N. Chinnasamy, A. Narayanasamy, N. Ponpandian, K. Chattopadhyay, K. Shinoda, B. Jeyadevan, K. Tohji, K. Nakatsuka, T. Furubayashi and I. Nakatani, Phys. Rev. B, **63** (2001) 184108.

12. C. Caizer and M. Stefanescu, J. Phys. D: Appl. Phys., **35** (2002) 3035.

13. J. Moulin, Y. Champion, J. M. Greneche and F. Mazaleyrat, J. Magn. Magn. Mater., **254-255** (2003) 538.

14. Z.X. Tang, C.M. Sorensen, K.J. Klabunde and G.C. Hadjipanayis, Phys. Rev. Lett., **67** (1991) 3602.

15. E.C. Sousa, C.R. Alves, R. Aquino, M.H. Sousa, G.F. Goya, H.R. Rechenberg, F.A. Tourinho and J. Depeyrot, J. Magn. Magn. Mater., **289** (2005) 118.

16. Q.A. Pankhurst and R.J. Pollard, Physical Review Letters, **67** (1991) 248.

17. R.H. Kodama, A.E. Berkowitz, E.J. McNiff, Jr. and S. Foner, Phys. Rev. Lett., **77** (1996) 394.

18. J.M.D. Coey, Phys. Rev. Lett., **27** (1971) 1140.

19. Y. Yamamoto and A. Makino, J. Magn. Magn. Mater., **133** (1994) 500.

20. N. Moumen, P. Veillet and M.P. Pileni, J. Magn. Magn. Mater., **149** (1995) 67.

21. S.A. Ghodake, U.R. Ghodake, S.R. Sawant, S.S. Suryavanshi and P.P Bakare, J. Magn. Magn. Mater., **305** (2006) 110.

22. V. Sepelak, S. Wibmann and K.D. Becker, J. Magn. Magn. Mater., **203** (1999) 135.

23. A.E. Virden and K.O'Grady, J. Magn. Magn. Mater., **290-291** (2005) 868.

24. Shannon A. Morrison, Christopher L. Cahill, Everett E. Carpenter, Scott Calvin, Raja Swaminathan, Michael E. McHentry and Vincent G. Harris, J. Appl. Phys., **95** (2004) 6392.

25. A.Verma, T.C. Goel, R.G. Mendiratta and P. Kishan, J. Magn. Magn. Mater., **208** (2000) 13.

26. S.T. Mohmud, A.K.M. Akther Hossain, A.K.M. Abdul Hakim, M. Seki, T. Kawai and H. Tabata, J. Magn. Magn. Mater., **305** (2006) 269.

27. M. Zheng, X.C. Wu, B.S. Zou and Y.J. Wang, J. Magn. Magn. Mater., **183** (1998) 152.

28. V. Sepelak, M. Menzel, I. Bergmann, M. Wiebcke, F. Krumeich and K. D. Becker, J. Magn. Magn. Mater., **272-276** (2004) 1616.

29. A. Kale, S. Gubbala, R.D.K. Misra, J. Magn. Magn. Mater., **277** (2004) 350.

30. D. Makovec, A. Kosak and M. Drofenik, Nanotechnology, **15** (2004) S160.

31. A.E. Berkowitz, R. H. Kodama, Salah A. Makhloul, F. T. Parker, F. E. Spada, E. J. McNiff Jr. and S. Foner, J. Magn. Magn. Mater., **196-197** (1999) 591.

32. Xavier Battle and Amilcar Labarta, J. Phys. D: Appl. Phys., **35** (2002) R15.

33. Mathew George, Swapna S. Nair, Asha Mary John, P.A. Joy, M.R. Anantharaman, J. Phys. D: Appl. Phys., **39** (2006) 900.

34. Hongxia Wang, Faling Zhang, Wei Zhang, Xianjie Wang, Zhe Lu, Zhegnan Qian, Yu Sui, Dawei Dong and Wenhui Su, Journal of Crystal Growth, **293** (2006) 169.

35. A.C.F.M. Costa, E. Tortella, M.R. Morelli and R.H.G.A. Kiminami, J. Magn. Magn. Mater., **256** (2003) 174.

36. M.S. Seehra and A. Punnoose, Solid State Communications, **128** (2003) 299.

37. M.R. Anantharaman, K.A. Malini, S. Sindhu, E.M. Mohammed, S.K. Date, S.D. Kulkarni, P.A. Joy and Philip Kurian, Bull. Mater. Sci., **24** (2001) 623.

38. K.A. Malini, E.M. Mohammed, S. Sindhu, P.A. Joy, S.K. Date, S.D. Kulkarni, P. Kurian and M.R. Anantharaman, J. Mater. Sci., **36** (2001) 5551.

Conclusion

Polymers are increasingly finding applications in various devices, which have become an integral part of our day to day life. Man's urge to develop newer materials for newer devices has resulted in explosive research activity in this area. He has been combining the benevolent properties of different constituents to make composite materials whose properties are extremely different from their parent materials. Thus the search for new composite materials with superlative performance characteristics for different applications has been a canonical attribute of scientists and engineers. So tremendous amount of research is carried out in this area of composites with a view to removing obsolescence and invent newer materials with novel properties. Polymer chemists have been contributing a great deal to the synthesis of composites, comprising of polymers and various other inorganic compounds. At the same time the boundary between various disciplines has started slowly melting and physicists are also venturing into this area for understanding various phenomenons occurring at the interfaces and also for delving into the mechanism of improved magnetic, dielectric and mechanical properties of these composites. Such an understanding at the fundamental level enables engineers to tailor make the composites for specific applications. Thus the role physics in strengthening the hands of polymer chemists is very significant and dominant.

The dawn of 21st century saw the advent of fresh new technology called nano technology. With the birth of nano science and nano technology, it is possible to modify chemical, physical and mechanical properties of materials by manipulating the size of particles. Combining the good properties of nano materials, with that of polymers can often results in nano composites for specific applications. The demand for such polymer nano composites is increasingly going up, because of the various challenges posed by the polymer industry as well as man made factors influencing the ecology of the universe. For example, indiscriminate use of microwave devices has

thrown up fresh new challenges to develop efficient microwave absorbers. Such a task has become imminent because of stricter environmental regulations. Development of efficient microwave absorbers in the form of emulsions can find aerospace applications in the form of stealth coatings for air crafts and other devices.

Synthetic rubbers like EPDM and neoprene provide a lossy dielectric platform. This is one of the criteria of a good microwave absorber. Synthetic rubber along with ingredients like carbon black and nano ferrites will combine to form ideal composites suited for such applications. These are generally called RFCs with natural rubber or synthetic rubber as one of the constituents and ferrites as the secondary component. Often carbon black or graphite is added to improve the dielectric properties. This work also is aimed at synthesising RFCs based on spinel ferrites and EPDM and neoprene rubber.

As has been mentioned earlier, a lot more has to be understood at the fundamental level especially, the factors determining physicomechanical, dielectric and magnetic properties. So the role of physics and chemistry in understanding the various properties of these composites assume significance. Not only synthesising RFCs but also probing the various mechanisms leading to improved properties is yet another objective in this particular investigation. The salient conclusions and inferences drawn out of this investigation are discussed in the ensuing paragraphs. Finally the scope for carrying out further research in this area is also brought out.

Precursor fillers belonging to inverse spinel ferrites namely nickel ferrite and gamma ferric oxide were synthesised in the nano regime. Bulk quantities of these fillers were prepared and homogenised using high energy ball milling. Prior to incorporation in polymer matrices, they were thoroughly characterised using X-ray diffraction technique and Transmission electron microscopy. They were found to be pure without any detectable impurities and evaluation of particle size by XRD and TEM indicates that they lie in the nano regime (19-25 nm). Further, the hysteresis loop parameters of these fillers were evaluated and found to be having the required magnetic characteristics.

The pre characterised fillers were employed for synthesising ferrite composites with rubber. The impregnation of fillers in rubber matrices has to be

according to a specific recipe. The evaluation of cure characteristics is vital for further processing of these composites especially for moulding. Parameters like cure time and scorch time of RFCs with different fillers like nickel ferrite and gamma ferric oxide were determined. It has been found that the cure time and scorch time of EPDM based RFCs with various ferrite fillers decreases with increase in ferrite concentration. The incorporation of carbon black in the matrix also evokes a similar response with respect to cure time and scorch time. It has also been found that the maximum torque for EPDM based RFCs were found to diminish with increase in filler concentration, where as the minimum torque was found to increase with increase in filler concentration. It has been found that compounds are processable and scorch safe. Further, from the maximum and minimum torque values, it has been inferred that the filler particles are expected to agglomerate over and above 100 phr. In the case of gamma ferric oxide composites agglomeration is expected at about 60 phr and above. Confirmatory and complementary evidences for these observations have been obtained from the data on the mechanical properties of these composites. SEM micrographs of composites at these loadings also indicated the fact that the agglomeration really starts above 80 phr loading.

In the case of neoprene based RFCs, the cure time and scorch time for both nickel ferrite and gamma ferric oxide filled composites were found to be increasing with increasing ferrite content.

In order to analyse kinetics of cure reaction, cure rate index and cure reaction constants were computed. In the case of EPDM based RFCs, these values were found to be increasing with increase in ferrite content. Thus it can be inferred that incorporation of ferrites promotes the cure reaction of EPDM. However in the case of neoprene based RFCs, speed of cure reaction, as indicated by the cure rate index and cure reaction constant, is found to decrease with increase in ferrite content.

Sorption studies conducted on EPDM and neoprene based RFCs with toluene as a solvent indicates the rate of polymer chain relaxation is comparable to penetration of solvent molecules, especially at lower filler loadings. This has received supportive evidence from morphology studies conducted by scanning electron microscopy. It has been found that incorporation of nano ferrite fillers modifies the mechanical properties

namely tensile strength, tear strength, hardness and modulus at 300% elongation. This is observed in the case of both EPDM and neoprene based RFCs. The enhancement in mechanical properties of RFCs with ferrites indicates the semi reinforcing nature of the ferrite fillers. However addition of carbon black, which is normally reinforcing, along with nickel ferrite has not contributed significantly in increasing the mechanical properties and on the contrary decreases the mechanical properties. This is probably because; the rubber has penetrated into the semi reinforcing ferrite filler without leaving any 'structure' for carbon black.

It has been found that dielectric permittivity decreases with increase in frequency of applied field. It was also noticed that composites are stable upto a temperature of 393 K with no visible signs of degradation. The variation of dielectric permittivity with frequency, temperature and with loading was studied in detail. For ceramic samples the dielectric permittivity found to increase with increase in temperature. In the case of RFCs marginal decrease in dielectric permittivity with temperature was observed.

The ac conductivity of the ceramic filler, gum vulcanisate and corresponding composites were found to increase with increase in frequency and then decreases at higher frequencies. The ac conductivity of the ceramic fillers increased with increase in temperature where as in the case of RFCs it decreased with increase in temperature.

Both dielectric constant and ac conductivity of the RFCs, mainly depends on volume fraction of ferrite filler incorporated into it. As the volume fraction of ferrite increased, the dielectric constant and ac conductivity of RFCs also increased. The variation of permittivity with concentration of filler was fitted with semiempirical equations. The theoretical fit and experimental curve was in good agreement.

The microwave attenuation measurements of nickel ferrite filled EPDM and neoprene based composites were carried out in the X and S band. In the case of EPDM and neoprene based RFCs dielectric permittivity increased with increase in filler concentration. The addition of carbon black in these composites helped to modify dielectric permittivity as well as the loss tangent. Heating coefficient of EPDM composites decreased with ferrite content, which is an indication of increased microwave attenuation. The effective permittivity of the composites were calculated

based on Maxwell-Garnet equation and were found to be fitting well with that of the experimental values.

The magnetic properties of these composites were evaluated and they were found to be having appropriate magnetic characteristics. It has been found that the saturation magnetisation of RFCs can be manipulated by varying the weight fractions of the ferrite filler. A simple mixture equation is good enough to predict the saturation magnetisation of RFCs. The coercivity, which is an important parameter as far as applications are concerned, remained by and large the same, as that of the ferrite filler.

Generally it can be concluded that good quality RFCs can be synthesised, starting from precursor materials. Dielectric, magnetic and mechanical properties can be modified by selecting appropriate filler and the weight percentage of filler. The addition of carbon black along with nickel ferrite, though does not improve the mechanical properties, is found to improve the dielectric permittivity substantially.

The microwave attenuation in the X and S band can be increased by incorporating carbon black in the matrix along with nickel ferrite. A thorough study involving the evaluation of permeability and permittivity, together at low and high frequencies would have enabled to fabricate a thin absorber, by employing surface impedance equations. This has not been possible because of various limitations. This is one of the lacunae of the present investigation. So this gives scope for further studies in evaluating the microwave absorbing properties of RFCs. Further more the role of carbon black in tailoring the band width of absorption could not be pointed out. This is yet another drawback which warrants further investigations.

Microwave absorbing emulsions, much sought after, especially for aerospace applications. The state of Kerala, where this piece of investigation is carried out, is fondly called the land of latex. Hence a systematic investigation into the various aspects of the microwave absorption of an emulsion, based on latex and nano ferrite fillers along with carbon black, for tuning the band width, is a worth while research proposition that can be pursued further.

There is ample scope for carrying out extensive investigations on nanocomposites, based on thermoplastics/nylon and with various magnetic fillers like NdFeB and SmCo. From a fundamental angle a lot more is to understood from physics

point of view. Various intricating phenomena taking place at the interface of the polymer and filler, polymer-polymer and filler-filler interfaces needs to understand properly. At increased surface to volume ratio, these interactions play a very dominant role in determining the overall properties of the composites. It would be interesting to carry out a similar study delving into the interactions taking place at the nano scale in these composites. This assumes importance from a theoretical perspective. Though it has been found that inert fillers like nickel ferrite, becomes semi reinforcing in the nano regime, much light could not be shed on the semi reinforcing properties exhibited by these fillers in the nano regime. This is a fit case for a systematic study.

List of Abbreviations

ASTM	American Society for Testing and Materials
BET	Brunauer-Emmet-Teller
CLD	Crosslink Density
CR	Chloroprene
CRI	Cure Rate Index
CVC	Chemical Vapour Condensation
D	Diffusion Coefficient
DCPD	Dicyclopentadiene
EPDM	Ethylene Propylene Diene Rubber
EMI	Electromagnetic Interference
ENB	Ethylidene norbornene
EPR	Electron Paramagnetic Resonance Spectroscopy
ESR	Electron Spin Resonance Spectroscopy
FTIR	Fourier Transform Infrared Spectroscopy
GMR	Giant Magneto Resistance
HAF	High Abrasion Furnace Black
H_c	Coercivity
HEBM	High Energy Ball Milling
HRTEM	High Resolution Transmission Electron Microscopy
Hz	Hertz
ICP	Inductively Coupled Plasma-atomic Electron Spectrometry
ISDN	Integrated Services Digital Network
kN	kilo Newton
LCR	Inductance, Capacitance and Resistance Meter
min.	minutes
MPa	Mega pascal
MRI	Magnetic Resonance Imaging
M_r	Magnetic remanence
M_s	Saturation magnetisation
NdFeB	Neodymium Iron Boron
nm	Nano meter

NR	Natural Rubber
P	Permeation coefficient
Phr	Parts per hundred rubber
ppm	Parts per million
RAM	Random Access Memory
RFCs	Rubber Ferrite Composites
RI	Reinforcing Index
RPA	Rubber Process Analyser
rpm	Rotations per minute
S	Sorption coefficient
SAED	Selected Area Electron Diffraction
SEM	Scanning Electron Microscopy
SmCo	Samarium Cobalt
TCNE	Tetra Cyano Ethylene
TEM	Transmission Electron Microscopy
UTM	Universal Testing Machine
VSM	Vibrating Sample Magnetometer

List of Symbols

α_F	Filler specific constant
β	Full width at half maximum
χ	Magnetic Susceptibility
$\tan\delta$	Loss tangent
ε'	Real part of dielectric permittivity
ε''	Imaginary part of dielectric permittivity
φ	Magnetic flux
λ	Wavelength
μ'	Real part of magnetic permeability
μ''	Imaginary part of magnetic permeability
ρ	Density
σ_{ac}	ac conductivity
ω	Angular frequency
A	Area
C	Capacitance
E_a	Energy of activation
f	Frequency
Q_c	Quality factor of the cavity
Q_s	Quality factor of the sample
V_c	Volume of the cavity
V_s	Volume of the sample
Z_{in}	Input impedance

List of Publications

1. **Prema. K. H**, Philip Kurian, P.A. Joy and M. R. Anantharaman, Physicomechanical and Magnetic Properties of Neoprene Based Rubber Ferrite Composites, Polymer Plastics Technology and Engineering. (Accepted).

2. **Prema. K. H**, Philip Kurian, Suma M.N, Manoj Joseph and M. R. Anantharaman, Permittivity Characteristics in the X and S Band Frequencies of Microwave Absorbers Based on Rubber Ferrite Composites, Journal of Elastomers and Plastics. (Communicated).

3. **Prema K. H**, Philip Kurian, Sanoj M.A, and M. R. Anantharaman, Effect of Carbon Black on the Mechanical and Dielectric Properties of Rubber Ferrite Composites, Progress in Rubber, Plastics and Recycling Technology. (Communicated).

Conference papers

1. **Prema. K. H**, Philip Kurian, Sanoj. M.A, and M. R. Anantharaman, Dielectric properties of carbon black loaded rubber ferrite composites. International Seminar, Asia Rub Tech Expo 2006 Kochi, November 23-25 (2006).

2. **Prema. K. H**, Philip Kurian, and M. R. Anantharaman., Effect of Ferrite Fillers on Cure Kinetics and Dielectric Behaviour of RFCs. National Seminar in Frontiers in Organic Chemistry (FOCY 2007), Dept. of Chemistry, Calicut University, January 11-12 (2007).

3. **Prema. K. H** and M. R. Anantharaman., Development of Rubber Ferrite Composites with Appropriate Dielectric Characteristics for High Frequency Applications. 19th Kerala Science Congress, Kannur, Janury 29-31 (2007).

4. **Prema. K. H,** Philip Kurian, Vijutha Sunny and M. R. Anantharaman, Effect of Magnetic Nano Particles on Cure Characteristics and Mechanical Properties of Neoprene Rubber. International Conference on Nanomaterial & its Applications (ICNA-2007), Dept.of Chemistry, NIT Tiruchirappalli, February 4-6 (2007).

5. **Prema. K. H,** Philip Kurian, and M. R. Anantharaman, Fabrication of New Dielectric Materials Based on Gamma Ferric Oxide and Neoprene Rubber. International Conference on Materials for the Millennium (Mat Con 2007), Dept. of Applied Chemistry, CUSAT, Kochi, March 1-3 (2007).

6. **Prema. K. H,** Philip Kurian, and M. R. Anantharaman., Preparation and Characterisation of Nickel Ferrite and Gamma Ferric Oxide. National Conference on Smart Electronics (NCSE 2007) CMET Thrissur, March 8-9 (2007).